Out-of-equilibrium dynamics and thermalization of weakly interacting disordered Bose gases

Thibault Scoquart

To cite this version:

Thibault Scoquart. Out-of-equilibrium dynamics and thermalization of weakly interacting disordered Bose gases. Quantum Physics [quant-ph]. Sorbonne Université, 2021. English. NNT : 2021SORUS472 . tel-03828484

HAL Id: tel-03828484

https://theses.hal.science/tel-03828484

Submitted on 25 Oct 2022

SCIENCES
SORBONNE
UNIVERSITÉ

Laboratoire Kastler Brossel
Physique quantique et applications

THÈSE DE DOCTORAT
DE SORBONNE UNIVERSITÉ

Spécialité : Physique

École doctorale : ED 564 : « Physique en Île-de-France »

réalisée

au Laboratoire Kastler Brossel

présentée par

Thibault Scoquart

pour obtenir le grade de :

DOCTEUR DE SORBONNE UNIVERSITÉ

Sujet de la thèse :

Dynamique hors d'équilibre et thermalisation des gaz de Bose désordonnés en interaction faible

soutenue le 7 décembre 2021

devant le jury composé de :

M.	Thomas Bourdel,	Examinateur
M.	Nicolas Cherroret,	Co-directeur de thèse
M.	Dominique Delande,	Directeur de thèse
M.	Nicolas Dupuis,	Examinateur
M.	Thierry Giamarchi,	Rapporteur
M$^{\text{me}}$	Anna Minguzzi,	Rapportrice

Contents

Introduction

In 1995, the first experimental realizations of a Bose-Einstein condensate [1, 2] opened a new era for low-energy quantum physics. These experiments, indeed, constituted the starting point of the field of quantum simulations, aimed at realizing, in a nearly ideal fashion, single and many-body Hamiltonians for quantum gases. From this perspective, cold atoms present many assets. One of the most interesting is perhaps the possibility, using external laser fields, to engineer a large variety of optical potentials. This allows, for example, to restrict the atomic motion in certain directions thanks to confining potentials so to study low-dimensional physics [3–5]. This also offers the possibility to load the atoms in optical lattices, allowing for an experimental simulation of paradigmatic theoretical problems, such as the Hubbard model [6]. Likewise, atomic clouds can be subjected to spatially disordered potentials, for example obtained by reflection of a laser on a rough plate [7, 8]. This particular feature makes cold atoms suitable candidates to study intriguing phenomena, such as Anderson [9, 10] or weak localization [11, 12], responsible for the inhibition of transport due to quantum interference in disordered systems. While we will give a more complete history of this physics in chapter 1, let us, at this stage, already point out the decisive advantages of cold atoms for exploring disorder-related phenomena: the possibility to greatly control the statistical properties of the (optical) disorder, the access to local and in situ observables, and the possibility to realize time-resolved experiments in conditions close to those of a truly isolated system. In the 2000s, these assets ultimately allowed for a precise and direct observation of Anderson localization of atomic matter waves in one dimension in 2008 [13, 14], and shortly after by explorations of the Anderson phase transition in three dimensions [15, 16]. A few years earlier, the critical properties of this transition were thoroughly characterized for atoms in temporal forms of optical disorder – a system called the quantum kicked rotor – [17–19]. All these works were complemented, more recently, by very precise measurements of coherent backscattering [20–23], a spectacular interference precursor of Anderson localization.

In addition to the possibility to design external potentials for the atoms, in cold-atom experiments atom-atom interactions can also be controlled to a broad extent thanks to the technique of Feshbach resonances [24], at least for certain atomic species. Combined with the presence of a disorder potential, this brings the so-called "dirty-boson" problem [25, 26] within reach of systematic experimental investigations. At a general level, the physics of interacting *and* disordered quantum gases is a vast topic, which has stimulated an intense research activity since the beginning of the century [27]. A representative example of this is perhaps the long-lasting interest for the *equilibrium* properties of disordered interacting Bose gases at low temperature. The topic was introduced by early theoretical predictions of the existence of an low-temperature, insulating "Bose glass" phase in one dimension [25], whose precise properties have been the subject of a number of works, up to nowadays [28–35]. The existence of such an insulating phase has, since then, been generalized to higher dimensions [33, 36–41]. These theoretical works on the Bose glass were supported by successful experimental realizations, mainly based on cold atoms in optical lattices [42–46], but also in magnetic insulators, for instance [47–49]. The presence of disorder also affects the finite temperature superfluid-to-normal fluid transitions, typically associated with condensation phenomena of interacting Bose gases [50–54]. One of the most fascinating is perhaps the Berezinskii-Kosterlitz-Thouless (BKT) transition [55, 56], a general, two-dimensional phase transition of topological origin, which has been extensively studied in the context of cold atoms [57–63]. The BKT mechanism relies on the pairing of topological defects called vortices, which propagate freely in the normal phase. The question of how the presence of disorder affects these pairings, and by extension the emergence of superfluidity was quickly raised, and has recently been the topic of a growing number of theoretical [52, 64, 65], numerical [54, 66] and experimental [67, 68] works.

In parallel to studies of quantum gases at equilibrium, in the recent years there was a considerable interest in the *out-of-equilibrium* properties of interacting quantum systems. From a theoretical point of view, one of the main questions in this field is to understand how the notion of thermalization of classical interacting systems translates to the context of isolated many-body quantum systems. In the classical case, thermalization is intrinsically linked to the notion of ergodicity, which is the ability for a system to explore uniformly all the accessible phase space, thus allowing for a universal statistical description of its equilibrium. Provided that the system has a sufficient number of degrees of freedom, and does not display an extensive number of conserved quantities, dynamical chaos ensures ergodicity, and leads to thermalization toward an equilibrium state that maximizes entropy [69–71]. In many-body quantum systems, the evolution is unitary and the spectrum discrete, such that classical notions of chaos and ergodicity are not easily generalizable. Early attempts by Von Neumann [72] predicted that under suitable conditions, quantum systems should thermalize, without providing a precise picture of the thermalization mechanism. It was then shown, both theoretically [73, 74] and experimentally [75–77], that a generic quantum many-body system indeed relaxes towards a state well described by statistical mechanics. Better, the thermalization of such systems was proven to occur simultaneously at the level of individual eigenstates [73], meaning that, at thermal equilibrium, the statistical average of an observable can be readily obtained by its average over a single energy eigenstate. Formally, the commonly accepted picture is that occurrence of thermalization is governed by the Eigenstate Thermalization Hypothesis (ETH) [78–80], first introduced in [81, 82], which provides sufficient conditions for a local observable $\hat{O}$ to evolve towards a thermal value predicted by statistical mechanics. In a thermal many-body quantum system, all the physically relevant local observables are thus expected to follow the ETH, which was verified by numerical experiments for a large variety of systems [83–86]. Once again, cold-atom experiments turned out to be very suitable candidates to explore non-equilibrium quantum physics. Indeed, as stated above, imaging techniques allow for in situ measurements in these systems and, most importantly, time-resolved experiments can be carried out using “quench protocols” where a parameter of the Hamiltonian is changed suddenly, starting, e.g., from a state of thermal equilibrium [87–89].

In the context of out-of-equilibrium interacting systems, another important notion is integrability. In a classical picture, a system is said to be integrable if it has a sufficient number of conserved quantities to prevent the appearance of ergodic behavior [90]. As a consequence, the stationary expectation values of physical observables differ from the predictions of statistical mechanics, and the system does not thermalize in the sense previously defined. A quantum system having, in general, an infinite set of conserved quantities, the classical notion of integrability cannot be obviously generalized to the quantum case. However, some quantum models, for example the Lieb-Liniger model [91], or the Bose-Hubbard model [92], are known to be integrable[1], and exhibit a sufficiently large set of conserved quantities to prevent them from reaching true thermal equilibrium. In fact, quantum systems described by integrable models quickly relax toward exotic non-thermal steady states, which can be described by the so-called generalized Gibbs Ensembles (GGE) that maximize entropy [95–97], associated with an effective, “temperature-like” thermodynamic variable for each relevant conserved quantity. Another property of quantum integrable models is that they are exactly solvable, and thus allow for for precise predictions, which can be experimentally verified, as was done successfully in [89, 98] to probe the existence of GGE. The existence of non-thermal steady states for integrable systems raises an interesting question : what is the steady state of the system if a small perturbation of the Hamiltonian brings the system slightly away

---

[1] The precise definition of quantum integrability is rather involved. In short, a quantum model is said to be integrable if it has a infinite number of conserved quantities with certain locality properties. These quantities constrain the dynamics of the system in a way similar to the classical case discussed above. The interested reader can find further details in [93, 94].

from integrability ? In this case, the stationary non-thermal state described by the GGE becomes metastable, and the system exhibits a non-trivial dynamics characterized by two well-separated time scales [99]. Over a relatively short time scale, the system relaxes toward the metastable non-thermal state (which closely ressembles the final steady state in the integrability limit), before undergoing its asymptotic relaxation toward a true thermal state. The intermediate dynamical evolution for near-integrable systems is called prethermalization [80, 98, 100–104], and has been observed in cold-atoms experiments [75, 89, 105].

In the presence of sufficiently strong disorder, Anderson localization is known to induce a breakdown of thermalization in interacting many-body quantum systems. This effect, coined many-body localization (MBL), has been the object of a huge research activity over the past 15 years [80, 106–109], triggered by the pioneering works [110, 111] in the context of interacting electrons in disordered conductors. Many-body localized systems violate the ETH, and constitute the only known class of non-integrable systems that do not reach thermal equilibrium. This implies that they retain a certain memory of the initial state, even at finite temperature, which is an interesting perspective for the development of quantum information technologies [112]. Signatures of many-body localization have now been reported on several occasions in cold-atom experiments [80, 113–115], and more recently on an array of superconducting qbits [116]. In these experiments, the strength of disorder and interactions is typically very large. The fate of localization in a regime of weaker interactions have also been studied, essentially in the context of the subdiffusive spreading of wave packets in disorder [117–120] and the thermalization problem in one-dimensionsal disordered chains [121]. Generally speaking, however, the regime of weak interactions has received much less attention, even though it could provide some interesting and analytically accessible insight on precursor mechanisms for many-body localization, in particular in higher dimensions.

In this thesis, we present our theoretical contribution to this problem, mainly restricting ourselves to the case of weak disorder. Our perspective is focused on the out-of-equilibrium dynamics of a two-dimensional, weakly interacting disordered Bose gas. In the first chapter, we set our theoretical basis for the effect of disorder in the non-interacting case. Precisely, we derive the time evolution of the momentum distribution of a Bose gas after a disorder quench by means of a diagrammatic transport theory. This distribution exhibits a strong signature of weak localization known as the coherent backscattering (CBS) effect. Then, in the second chapter, we add the ingredient of particle interactions, treated within a classical-field approach, and consider a quench in both disorder and interactions. Adapting the diagrammatic theory of the first chapter for interactions weaker than the disorder, we develop a kinetic theory that describes the time-evolution of both the diffusive and the CBS modes of the gas.

The short-time consequences of the kinetic theory are confronted to ab initio simulations of the disordered Gross-Pitaeskii equation in chapter 3, where we also present a quantitative description of the destruction of CBS by interactions. In chapter 4, the opposite regime of interactions stronger than the disorder is explored. We find that at relatively short times, the spatial correlations of the gas decay algebraically within a light-cone. We relate this behavior to the establishment of prethermalization in the presence of disorder. Finally, in chapter 5, we study the long-time thermalization of the gas following the quench, for arbitrary values of the disorder and interactions. Using our simulations of the Gross-Pitaevskii equation, we construct the disorder-temperature equilibrium phase diagram of the 2d disordered Bose gas a long time after the quench, and relate it with the preceding out-of-equilibrium dynamics. Using the phase diagram, we also study the effect of disorder on characteristic features of the Berezinskii-Kosterlitz-Thouless transition.

Chapter 1

Matter waves in disordered media

From the music going out of a speaker, to the light that reaches your eyes as you read this sentence, most of the physical phenomena that we experience can be described in terms of wave propagation. But the ubiquity of the concept of wave is not limited to our direct perception of the environment: ever since the early stages of quantum theory, in the beginning of the last century, waves constitute one of the most fundamental aspect of modern physics and technology. Whether they are mechanical or electromagnetic, classical or of quantum origin, the behavior of waves is always affected by the medium they propagate in. Therefore we would like to describe as accurately as possible how waves propagate in a given medium. Nowadays, the propagation of electromagnetic waves in a perfectly homogeneous medium or the electronic motion in a perfect crystal are well-understood. In the real world however, there is no such thing as perfect order. The particles that form a fluid are permanently agitated by their interaction with one another. The most perfect crystal has defects or impurities within its atomic structure. Any real medium displays a certain degree of spatial heterogeneity that we call disorder. If the disorder affects a parameter that controls the wave propagation, such as the refractive index for electromagnetic waves, any sudden change of this parameter will be seen as an obstacle for the waves, and they will be scattered as they approach it. In a medium containing a large number of such obstacles, the physics of wave propagation over large distances can become very complex, as the wave at any given point of space is the superposition of many partial waves scattered from various positions and with random momenta. In this case, we say that the waves propagate in the so-called multiple scattering regime. In addition, provided that, inside the medium, the waves display a certain degree of phase coherence, interference phenomena may occur and add to the complexity of the problem. This physical picture encompasses a lot of situations which occur at length scales spanning several orders of magnitude. Some of the most famous examples include the conduction of electrons (seen as a quantum-mechanical wave) in a disordered semiconductor, the propagation of seismic waves inside the earth's crust, the scattering of sunlight inside clouds or through a glass of milk, etc... The disorder being, by essence, a *random* occurrence of a lack of regularity, physicists cannot hope to give a meaningful and consistent description of these systems by looking at every specific sample – or realization – of a disordered medium (not to mention the formidable complexity of this task). Rather, the main focus should be to derive properties that are common to all disordered systems. This essentially means that, for disorder-related phenomena, we have to resort to a stochastic description of the physics at play, where the expectation values of all physical quantities are expressed as an ensemble average over a large number of realizations of the disorder. With this approach, the – random – properties of wave transport are linked to the statistical properties of the disorder: its distribution and spatial correlations. For this reason, in the rest of the manuscript, we will denote the ensemble average of a physical observable O over many[1] realizations of the disorder by $\overline{O}$.

1.1 Diffusion and localization of electrons

In this section, we give a qualitative and historical picture of the main mesoscopic phenomena induced by coherent multiple scattering of electrons. Since we will be ultimately interested in ultracold atomic gases, our goal here is not to give an exhaustive picture of the physics of electronic transport in the presence of disorder, but rather to introduce two of its most important concepts, Anderson (or strong) localization, and weak localization, in their historical context.

1.1.1 Incoherent diffusive transport

When a wave propagates in a disordered medium, it is likely to experience a certain number of successive scattering events, which will progressively randomize its direction of propagation. Within a classical picture, this process, called multiple scattering, essentially consists in a random walk, which suggests that, for a long enough sequence, the wave should exhibit diffusive behavior: after a time t, the wavefront is typically at a distance $\sqrt{Dt}$ from its starting point, where D is the classical diffusion coefficient. In a semiconductor, where the collective motion of the conduction electrons can be described in terms of electronic matter waves, this picture is typically valid at high temperature, where thermal fluctuations dramatically decrease the electronic phase coherence, and prevent the occurence of quantum interference between multiply scattered waves. In this regime, the electronic transport is indeed diffusive

---

[1] Note that the number of disorder realizations required to obtain a meaningful averaged value can vary a lot depending on the quantity we are looking at. As we will see, this is especially relevant when one wants to perform numerical simulations (see chapter 3). Note also that some quantities are self-averaging: in a single sample of sufficient size, they display typical values equal to their ensemble average. The most common example is the conductance of a disordered material, which follows Ohm's law in the classical limit where the electronic motion is diffusive.

(or incoherent), and the conductivity σ, which relates the electronic current to the electric field, follows the well-known Drude result [122, 123]

$$\sigma = \frac{ne^2\tau}{m}, \tag{1.1}$$

where n,m and e are respectively the electronic density, mass and elementary charge, and τ is defined as the average time between two electron scattering events. Drude developed the first microscopic picture for the macroscopic Ohm's law. But this purely classical approach has to be corrected for systems in which the quantum nature of electrons plays a role.

1.1.2 Anderson localization

If the propagating waves now presents a certain degree of phase coherence over the size of the system, multiple scattering can induce interference phenomena that may break down this simple, classical picture, sometimes in a spectacular fashion. The consequences of coherent multiple scattering on conducting electrons in a disordered solid have been a central research topic in the end of the last century [124]. Indeed, when the size of the conductor becomes comparable to the distance over which electrons can maintain their phase coherence L_ϕ, the effects of quantum interference have to be taken into account, and can affect the electronic motion through the conductor in a multitude of ways. The study of such phenomena is coined as mesoscopic physics [125]. The most striking example of mesoscopic effect is perhaps the phenomenon of Anderson, or strong, localization, predicted in 1958 by P. W. Anderson in his famous seminal paper [9]. In this paper, Anderson shows that, in a three-dimensional (3d) conductor where a disorder potential models the presence of defects in the crystalline atomic structure, the accumulation of destructive interference induced by coherent multiple scattering can lead to a complete absence of diffusion. Provided that the disorder is strong enough, the square modulus of the electronic wavefunction exhibits an exponential decay, controlled by the so-called localization length ζ_{loc}[2]

$$|\psi(\boldsymbol{r})|^2 \propto e^{-r/\zeta_{loc}}. \tag{1.2}$$

In other words, electronic transport is practically frozen, and the conductor turns into an insulator. This phenomenon has been and still is the subject of intensive research, both from the physical and mathematical point of view [127–129]. Since then, Anderson localization has been predicted to be a universal property of coherent waves in a random environment, and as such, it should be observed in any disordered system crossed by coherent waves [130, 131]. The experimental observation of Anderson localization, however, turns out to be quite challenging in condensed matter systems: electron-electron interactions, as well as their uncontrolled

---

[2] Note that in equation (1.2) we did not put an average value over the density: Anderson localization is so robust that the exponential decay of the wavefunction can be observed from sample to sample, with a statistically equivalent disorder [126].

coupling to the phononic excitations of the crystalline structure induce decoherence between the propagating waves and prevent the onset of localization. Morover, in condensed matter experiments, it is difficult to perform direct measurements of local observables in the bulk of the solid. The property (1.2), for instance, cannot be directly verified, and one can only probe the indirect consequences of localization on conduction properties. Nevertheless, indirect signatures of Anderson localization in 3d solids have been observed around the 1970's, through the vanishing of electron conductivity in suitable experimental conditions [132].

1.1.3 Weak localization

Another important consequence of coherent multiple scattering of electrons in disordered conductors is known as weak localization. It was theoretically described in 1979 by Gor'kov [11] as a small reduction of the classical Drude-Boltzmann conductivity, controlled by the electronic coherence length L_ϕ [133]. Unlike Anderson localization, whose precise analytic description in terms of interference between multiply scattered partial waves is out of question due to its complexity, the small weak localization correction is a consequence of an enhanced probability for the electrons to return at a point previously explored due to a well-identified interference process between counter-propagating wave amplitudes (we will come back to this point in more details in the next sections). For this reason, weak localization is easier to observe experimentally, as it can be turned on and off by applying a perturbation that introduces a dephasing between the two counter-propagating amplitudes. This was done noticeably in 2d thin films [134], based on a principle that is reminiscent of the famous experiments demonstrating the Aharonov-Bohm effect [135]. In the presence of a perpendicular magnetic field, two counter-propagating amplitudes that follow the same scattering sequences acquire additional phases – proportional to the magnetic flux in the surface that they enclose – of opposite sign, thus breaking the constructive interference responsible for weak localization. The alteration of weak localization by dephasing mechanisms has also been confirmed experimentally in the presence of other physical phenomena, such as spin-orbit coupling [136–138], magnetic impurities [139, 140] or electron-phonon scattering [141]. Due to its strong dependence on L_ϕ, weak localization correction remains nowadays an interesting tool to evaluate the extent of electronic coherence in disordered materials [142–144].

1.2 Localization of classical waves

As already discussed, the observation of both strong (Anderson) and weak localization for electronic matter waves in disordered conductors is a real challenge, due to a large number of uncontrolled parameters, and the difficulty to measure local observables. In addition, conduction experiments are usually stationary in time, which prevents any insight of the dynamical aspects of localization. Finally, they offer a poor control over the characteristics of the disorder, which has to be directly engineered in several different samples.

1.2.1 Anderson localization

At the end of the 20th century, the quest for the observation of Anderson localization led experimentalists to consider different experimental platforms, which would not suffer from these drawbacks. These experiments were motivated by early works on the possibility of strong localization of classical waves [130, 145, 146]. There is, nevertheless, a trade-off of experimental limitations compared to conduction experiments. Indeed, classical waves usually suffer from a high absorption in dielectric materials, and their nature prevents the formation of bound states in potential wells, as is the case for matter waves. Nevertheless, the use of classical waves provided a number of remarkable achievements, such as the successful probing of localization in 1d and 2d for microwaves [147, 148], ultrasounds [149, 150], but also for light [151–154].

1.2.2 Weak localization

In the context of electronic transport, the weak localization correction manifests itself as a very small correction to global transport quantities such as the conductivity. It has, however, much more spectacular consequences in measurements where the incoming and outgoing directions of the scattered waves $\boldsymbol{k}_{in}$ and $\boldsymbol{k}_{out}$ can be resolved: the constructive interference between counter-propagating paths then leads to an increase of the wave density in the exact backscattering direction $\boldsymbol{k}_{out} = -\boldsymbol{k}_{in}$. Performing such an experiment is particularly suitable in optics and other classical-wave experiments, where one can easily shine a disordered medium with a plane-wave of well-defined momentum, and look at the reflective angular profile. This effect, known as coherent backscattering (CBS), was first described theoretically in the middle of the 1980's [12, 155, 156], and observed in a wide range of different wave experiments, starting with optics [157–159], but also with microwaves [160, 161] and ultrasounds [162, 163]. Occurences of CBS effects have even been spotted directly in nature, for instance for affecting the emission spectrum of satellites of Saturn [164], or explaining the opposition effect of the moon [165].

1.3 Probing localization with ultracold atoms

At the beginning of the 90's, the development of laser cooling for atomic gases [166–168] and the subsequent first experimental platforms for ultracold atoms, initially designed for the direct observation of Bose-Einstein condensation in a controlled environment [1], offered a new perspective to a number of long-lasting experimental limitations both in condensed-matter and classical-wave systems. Similarly to electrons, the collective motion of ultracold atoms can be described by coherent matter waves, which makes them excellent candidates to reproduce condensed-matter quantum phenomena.

1.3.1 Experimental evidence of localization of matter waves

The coherent backscattering of cold atoms, in particular, was probed in an optics-like configuration where an ultracold Bose gas was initially given a finite average velocity, and its subsequent dynamics in the presence of disorder probed in momentum space. This configuration, originally introduced in [169], turned out also to be useful to explore other interference phenomena like coherent forward scattering [170], to achieve an echo spectroscopy of coherent transport in disorder [22, 171] or to monitor the thermalization and dynamical formation of condensates in momentum space [172]. In a typical ultracold Bose gas experiment designed to probe wave localization phenomena, the gas is initially prepared as a condensed atomic cloud (BEC) in a magnetic trap. At the initial time, the trap is (quasi-)instantaneously turned off, and the atomic cloud evolves freely in an optical disorder potential, where it experiences coherent multiple scattering. This expansion can be confined to a selected direction of space, usually by superimposing on the disorder potential an harmonic laser potential that confines the atomic motion in a certain geometry. This is yet another proof of the formidable modularity of ultracold atoms as an experimental platform. Then, at a chosen measurement time t, the disorder is switched off, and various imaging techniques give access to the spatial density or velocity distribution of the atomic cloud. The full experiment can then be repeated to obtain a temporal picture of the physics at play (and perform a disorder averaging, if required !). This kind of protocol allowed for the direct observation of Anderson localization of atomic matter waves in 1d in 2008 [13, 14], following a number of preliminary theoretical works on the topic [173–175]. The same observations were then performed in 3d a few years later [15, 16]. All of these experiments reported evidence of the temporal freezing of the diffusive motion of the atomic cloud. Surprisingly, the first observations of the consequences of weak localization for atomic matter waves were only made a few years later, in 2012, when the Coherent Backscattering peak was observed in the *average* momentum distribution of a two-dimensional Bose gas initially prepared in a state with a very narrow momentum distribution [21]. To achieve this, after preparing the gas in a condensed state, its density is reduced by a quick release of the trap followed by switching on for a short duration a “larger” harmonic potential (δ-kick cooling). As a consequence of the low spatial density of the gas, interactions can be neglected, and the cloud has a very narrow momentum dispersion. The application of a magnetic field gradient then gives the atoms an average finite momentum $\boldsymbol{k}_0$, without changing the momentum dispersion. Thus, the momentum distribution of the initial state, shown in the first image of Fig. 1.1, is a peak centered at $\boldsymbol{k}_0$, with a small width $\Delta\boldsymbol{k}$. In the language of matter waves, this corresponds to a very extended wave packet, close to a plane-wave state of well defined momentum $\boldsymbol{k}_0$.

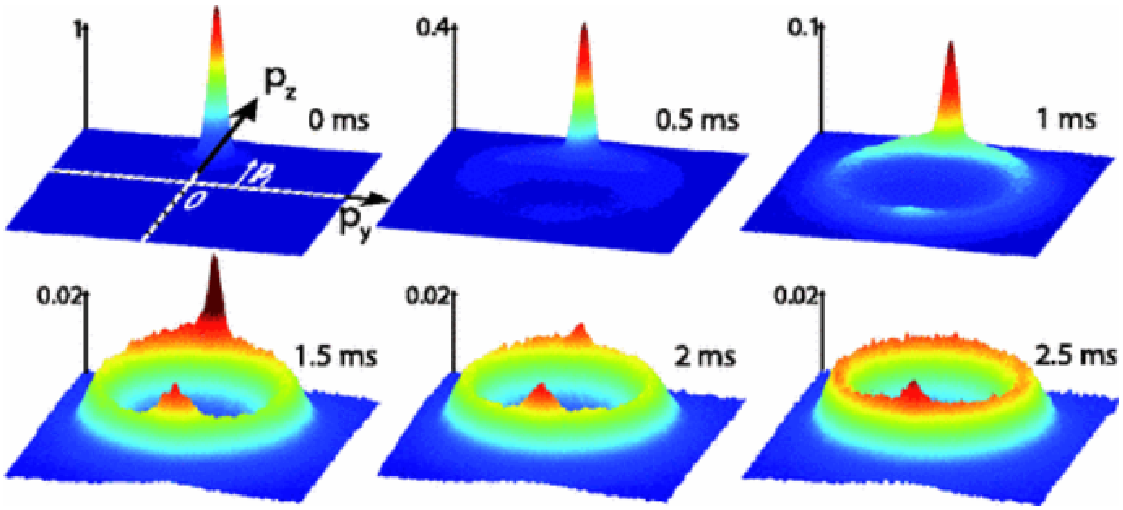

Figure 1.1 – Momentum distribution of an ultracold gas of ^{87}Rb in a two-dimensional geometry, obtained by time-of-flight imaging after it has evolved in a speckle optical potential. The results are averaged over 20 experimental runs. Starting from an initially narrow state in momentum space, similar to a plane-wave $|\boldsymbol{k}\rangle$, the momentum distribution displays a diffusive ring that grows anisotropically – a consequence of the potential's finite correlation length –, supplemented with a peak around the backscattering direction, the CBS peak. The corresponding scattering mean free time was experimentally measured: $\tau = 0.33 \pm 0.02ms$. Adapted from [21].

The gas is then released in a two-dimensional speckle potential and, at measurement time t, its momentum distribution is recorded by a time-of-flight experiment [6, 176]: the potential is switched off, causing the atoms to fall freely under the action of gravity and, after waiting a sufficiently long time, the atomic spatial distribution is directly proportional to the momentum distribution of the cloud at the moment of release. A simple fluorescence imaging of the cloud then gives direct access to this quantity. This measurement scheme being obviously destructive, the experiment has to be repeated to obtain the time-resolved momentum density of Fig. 1.1. After a short intermediate regime, the two main features of the momentum distribution are revealed :

- An isotropic ring of radius $\boldsymbol{k}_0$, which corresponds to the diffusive atoms, whose direction of propagation is randomized by multiple scattering. The scattering being elastic – there is no transfer of energy to or from the wave during a scattering event –, one would expect that the momentum $|\boldsymbol{k}|$ of an initial plane-wave is conserved during the multiple scattering, yielding an infinitely thin diffusive ring. In fact, the reason for the finite width of the ring is twofold: first, the momentum dispersion $\Delta\boldsymbol{k}$ of the initial wave packet is finite, but, more importantly, the disorder induces a certain 'width' in the dispersion relation of the matter wave: in a disorder potential, translational invariance of the system is broken, and plane-waves are not anymore eigenstates of the Hamiltonian. As a consequence, a plane-wave of well-defined wavevector $\boldsymbol{k}$ does not have a well-defined energy (due a finite lifetime), which broadens the width of the diffusive ring. If the disorder potential constitutes a weak perturbation of the free-space Hamiltonian, the energy dispersion around the free-space value $\epsilon(\boldsymbol{k}) = k^2/2m$ and the ring is is nevertheless small.
- The CBS peak, around the backscattering direction $-\boldsymbol{k}_0$. The peak has a rather large angular width, and a relatively small amplitude compared to the height of the diffusive ring. These two effects, also linked to the width of momentum distribution of the initial state $\Delta\boldsymbol{k}$, will become clearer as we present the theory of the non-interacting CBS for matter waves in the next sections.

In the rest of this chapter, we present a detailed theoretical description of the observed results of this particular experiment, making use of a diagrammatic quantum transport theory. This approach will serve as starting point for the next chapter, where the particle interactions will be added.

1.4 Coherent multiple scattering of matter waves: an intuitive picture

In this section, we give an intuitive picture of coherent multiple scattering of matter waves in a spatially disordered potential. The aim is to provide a qualitative explanation for localization phenomena, and to introduce some concepts that will be useful to understand the quantitative diagrammatic theory that is presented in the next section.

1.4.1 Single scattering

Let us consider a classical particle of kinetic energy ϵ_0, trapped in a two-dimensional disordered potential V. If the energy ϵ_0 is larger the typical height of the energetic barriers formed by the potential, it will 'fly' above those obstacles, and have a ballistic motion. On the other hand, if the particle meets potential barriers larger than ϵ_0, it will get trapped in the resulting potential well. Things are different for a quantum particle, whose evolution is described by the Schrödinger equation

$$\left[i\hbar\frac{\partial}{\partial t} - \mathcal{H}\right]|\psi(t)\rangle = 0, \qquad \mathcal{H} = \frac{p^2}{2m} + V(\boldsymbol{r}), \tag{1.3}$$

where $\psi(\boldsymbol{r},t) = \langle\boldsymbol{r}|\psi(t)\rangle$ is the wavefunction of the particle, such that $|\psi(\boldsymbol{r},t)|^2$ is the probability density to find the particle at point $\boldsymbol{r}$ at time t. In this case, we know that the particle can tunnel through a potential barrier, but also be reflected by a very small potential hill. Essentially, any spatial fluctuation of the disorder potential produces reflected and a transmitted wave components. One occurrence of this process is what we will call a single scattering event in the following. The result of a scattering event will heavily depend on the relative values of the de Broglie wavelength λ of the wave, and the typical size σ of the potential hill. For a disorder potential, σ coincides with the correlation length of the potential, usually defined through the characteristic extent of its correlation function $\overline{V(\boldsymbol{r})V(\boldsymbol{r}')}$. Of course, scattering of matter waves is an elastic process. This means that an incoming momentum component maintains its energy after the scattering process, only its direction being altered.

1.4.2 Scattering mean free time

In a multiple scattering process, a central quantity is the scattering mean free time τ, defined as the average time between two consecutive scattering events on the potential. The mean free time corresponds to the inverse of the transition rate between two eigenstates $|\boldsymbol{k}\rangle$ and $|\boldsymbol{k}'\rangle$ of the free-space Hamiltonian $\mathcal{H}_0 = p^2/2m$. Assuming that the disorder potential V acts as a weak perturbation of the Hamiltonian, the mean free time is given by the Fermi golden rule :

$$\frac{\hbar}{\tau} = 2\pi \int \frac{\mathrm{d}\boldsymbol{k}'}{(2\pi)^d}\, \overline{|\langle\boldsymbol{k}|V|\boldsymbol{k}'\rangle|^2}\, \delta(\epsilon_{\boldsymbol{k}} - \epsilon'_{\boldsymbol{k}}). \tag{1.4}$$

Assuming that one detects the propagating wave at a time t after it was released in a disorder potential, one can then identify three different regimes of transport:

- If $t < \tau$, no scattering event has occurred on average. The momentum distribution of the cloud corresponds to the free-space evolution of the initial state during time t. This is called the ballistic regime.
- When $t \simeq \tau$, only one scattering event has occurred on average. This is the single scattering regime. The direction of propagation of the initial wave is not yet randomized, and the wave propagation is only slightly affected by the disorder.
- When $t \gg \tau$, a lot of scattering events have occurred. This is the multiple scattering regime, where the memory of the initial condition is generally lost. If no mechanism breaking the phase of the wave occurs from $t = 0$ to t, interference effects such as weak or Anderson localization can occur.

Occasionally in the manuscript, we will also use the spatial counterpart of τ, the mean free path ℓ, i.e. the average distance covered by a wave between two consecutive scattering events. Both quantities are linked by the relation

$$\ell = v\tau \tag{1.5}$$

where $v = \hbar k/m = h/m\lambda$ is the group velocity of the plane-wave $|\boldsymbol{k}\rangle$. Both τ and ℓ depend on the energy ϵ in general. However, since scattering is elastic, if the initial momentum distribution of the waves is peaked around a given value k_0, and if the disorder strength is weak enough, the energy dispersion remains small, and one usually perform the on-shell approximations $\tau(\epsilon) = \tau(\epsilon_0 = k_0^2/2m)$ and $\ell(\epsilon) = \ell(\epsilon_0 = k_0^2/2m)$. A more precise definition of the weak-disorder regime will be given in the following.

1.4.3 Decomposition over scattering sequences

In the multiple scattering regime $t \gg \tau$, an intuitive picture of the effect of wave multiple scattering can be given. Consider a particle initially placed at point $\boldsymbol{r}$, with a well-defined momentum $\boldsymbol{k}$. According to the superposition principle, the complex wavefunction $\psi(\boldsymbol{r}', t)$ at point $\boldsymbol{r}'$ after a time t is the sum over all probability amplitudes p to travel from $\boldsymbol{r}$ to $\boldsymbol{r}'$ during the time t.

$$\psi(\boldsymbol{r}', t) = \sum_{\text{paths } p} \psi_p = \sum_{\text{paths } p} |\psi_p| e^{i\delta_p} \tag{1.6}$$

where ψ_p is the partial complex amplitude associated with the multiple scattering path p of length $\mathcal{L}_p$. In the second equality, we introduce the phase $\delta_p \sim k\mathcal{L}_p$. Consequently, the average density of the gas $n_{\boldsymbol{r}'}(t)$ at time t reads:

$$n_{\boldsymbol{r}'}(t) = \overline{\Big|\sum_{\text{paths } p} \psi_p\Big|^2} = \overline{\sum_{\text{paths } p} \psi_p\, \psi_p^*} + \overline{\sum_{\text{paths } l \neq p} \psi_l\, \psi_p^*\, e^{i(\delta_l - \delta_p)}}. \tag{1.7}$$

The first term in the right-hand side of (1.7) is formed by the pairs of amplitudes that travel through the same scattering sequences in the same order. It describes a propagation where the complex amplitudes do not interfere, and their intensity simply adds up. This is the classical, diffusive picture of multiple scattering we have mentioned above. The second term is formed by pairs of amplitudes that go through different multiple scattering paths. It encapsulates all the possible interference effects between partial waves in the medium. For a given pair of multiple scattering sequences, $\delta_l - \delta_p \sim k(\mathcal{L}_l - \mathcal{L}_p)$. The two partial amplitudes travel at the same velocity $v = \ell/\tau$, and must reach the final point at the same time t. Thus, a pair of multiple scattering paths from the expansion (1.7) cannot be radically different: the path length difference between the two is of the order of few ℓ. The phase factor also fluctuates from one disorder realization to another, thus the interference contribution to the density will always vanish when taking the ensemble average, provided that $k\ell$ is large enough. In this case, we are left with the incoherent contribution – the first term of (1.7) – only, and the wave propagates diffusively. In the opposite case $k\ell \leq 1$, quantum interference is not negligible, and we are in the so-called strong disorder regime. As it turns out, in this regime of strong disorder, coherent effects completely dominate wave propagation. In fact, as the mean free path becomes comparable to the wavelength $\lambda = 2\pi/k$, the description of matter-wave propagation as a ballistic motion successively interrupted by independent scattering events breaks down: the waves are constantly scattered, and there is almost no propagation. As a consequence, the physics of wave propagation in strong disorder is a very complex problem, which cannot be easily tackled analytically. We are in the regime where Anderson localization of the matter wave is expected. In 1960, Ioffe and Regel [177] proposed a precise criterion for the onset of Anderson localization in an infinite space. In 3d, it is consistent with the result we obtained from our simple description in the last paragraph:

$$k\ell \leq C, \quad (d = 3) \tag{1.8}$$

with C a non-universal parameter of the order of 1.

For a matter wave, the Ioffe-Regel criterion defines an energy threshold

$$E \simeq E_c \tag{1.9}$$

known as the mobility edge. This strict criterion portrays Anderson localization as a phase transition between a diffusive phase, where waves are extended over the whole space at high energies, and a localized phase, where waves are confined in small regions of space at low energies. The existence of this phase transition was formalized by the celebrated scaling theory of localization [10], which provoked a surge of interest in the phenomenon of localization. In the context of electronic transport through a disordered conductor for example, the transition separates a conducting phase from an insulating phase. The Anderson transition in dimension 3 is very hard to describe theoretically, mainly because ressuming all the interference terms in expression (1.7) is an impossible task. Several theoretical descriptions such as the self-consistent theory of localization, first developed by Vollhardt and Wölfle [178, 179] allowed for significant advances, such as the prediction of a subdiffusive regime for the wave at the onset of the transition, but a precise analytic prediction for the value of the critical exponent, for example, is still lacking. Nevertheless, the phase transition has been observed more or less successfully in various wave experiments [180, 181], but noticeably with cold atoms in a very specific setup: the atomic kicked rotor [17, 19, 182]. In 1d and 2d geometries however, it turns out that Anderson localization is generically present, and all eigenstates of a disordered Hamiltonian are localized, as predicted by the scaling theory of localization [10]. The mobility edge E_c cannot be defined, and our reasoning from last paragraph does not seem to apply. This seems to be in direct contradiction with the conclusions of the experiment we described in the last section, where weak localization and a diffusive behavior was observed in 2d. In fact, while it is true that all eigenstates are localized in 2d, the localization length in this case grows as $\ell \exp(\pi k\ell/2)$ [183, 184]: in the limit $k\ell \gg 1$, the localization length is so large that the effect of Anderson localization can be neglected in first approximation. In a typical experiment of cold atoms in a 2d configuration, ζ_{loc} is at best several times the size of a typical sample, which prevented the observation of strong localization of atomic matter waves, until very recently [185]. Over the size of the atomic cloud, the effects of strong localization are however usually negligible, and the matter waves effectively display a diffusive behavior.

1.4.4 Counter-propagating amplitudes and weak localization

In 2d and 3d systems, the effects of Anderson localization are negligible in the weak disorder limit $k\ell \gg 1$. The simple description of coherent multiple scattering given by equation (1.7) suggests that no interference effect can survive the disorder average, as the phase factor $\delta_l - \delta_p \sim k(\mathcal{L}_l - \mathcal{L}_p)$ will fluctuate between large values from one realization to another, and thus vanish with the ensemble average. It turns out, however, that a specific interference term always survives the disorder average. It corresponds in fact to configurations where the partial amplitudes ψ_l and ψ_r follow the same multiple scattering path but in reverse order. One can see that in this case, provided that the sequence forms a closed loop, each amplitude accumulates the same phase during its propagation and the resulting phase difference vanishes for all disorder realizations. Moreover, one can see that if the system is time-reversal invariant, this coherent contribution is unchanged by reversing one of its amplitude, and is thus equal to its incoherent, diffusive counterpart. Consequently, this type of scattering sequence enhances by a factor 2 the probability for a given particle to return at the origin.

1.5 Quantum transport theory for matter waves in a random potential

In this section, we recall the main lines of the quantum transport theory describing weak localization of non-interacting matter waves in the presence of disorder, focusing on the 2d experimental situation of Fig. 1.1. In particular, we derive expressions for both the incoherent (diffusive ring) and coherent (CBS peak) components of the average momentum distribution of the gas by means of a diagrammatic expansion. The presentation of this well-known formalism, mostly inspired by [125], is meant as an introduction to the next chapter, where this theory will be modified to account for particle interactions. In the weak disorder limit, the effects of strong localization are negligible in 2d and 3d, and analytic expressions of the gas density can be obtained by performing a perturbative expansion in powers of the disorder strength using the Green's function formalism. This formalism will allow us not only to write this expansion in a simple way, but also to perform easily the average over disorder realizations. Using this expansion, we will derive the average probability density to find the initial wave at a given point (in position or momentum space), from which we infer a formula for the average momentum distribution $n_{\boldsymbol{k}}(t)$ at time t. Here and in the rest of the thesis, we focus on a two-dimensional disordered Bose gas, although the results of chapters 1, 2 and 3 are, to a large extent, generalizable to the 3d case. In the rest of the chapter, we set $\hbar = 1$.

1.5.1 Green's function for the propagation of matter waves

As already stated, we want to describe the propagation of a matter wave formed by the collective motion of a Bose-Einstein condensate of N atoms, released in a spatially disordered potential V. In the absence of interactions, the evolution of the condensate can be described by the single-particle complex wavefunction $\psi(\boldsymbol{r}, t) = \langle \boldsymbol{r} | \psi(t) \rangle$, which obeys the Schrödinger wave equation:

$$\left[i \frac{\partial}{\partial t} - \mathcal{H} \right] |\psi(t)\rangle = 0, \tag{1.10}$$

where $\mathcal{H} = \mathcal{H}_0 + V = \frac{\hat{p}^2}{2m} + V$. We will denote by $\mathcal{V}$ the volume of the system, supposed large enough to be considered infinite.

Green's Function of a linear operator

The Green's function formalism in a very powerful tool to perform perturbative calculations. For this reason its use is widespread, from high-energy physics to condensed-matter theory. The Green's function G associated to a linear differential operator $\mathcal{L}$ is the solution of the equation

$$\mathcal{L}G(x, y) = \delta(x - y). \tag{1.11}$$

It represents the response of the operator to a point-like source. Since any function g can be seen as an infinite superposition of Dirac delta-functions (because $\int \mathrm{d}y\, \delta(x-y)g(y) = g(x)$ by definition), the solutions of the differential equation $\mathcal{L}f = g$, can be conveniently written as:

$$f(x) = \int \mathrm{d}y\; G(x, y)\; g(y). \tag{1.12}$$

Therefore, the knowledge of G is sufficient to express simply the response of the linear operator $\mathcal{L}$ to any source term.

Green's Function for the Schrödinger equation

In our case, we wish to find the Green's function for the linear operator $\mathcal{L} = i\frac{\partial}{\partial t} - \mathcal{H}$, i.e the solution of the equation

$$\left[i\frac{\partial}{\partial t} - \mathcal{H}\right] G(\boldsymbol{r}, \boldsymbol{r}', t, t') = \delta(\boldsymbol{r} - \boldsymbol{r}')\delta(t - t'). \tag{1.13}$$

The Schrödinger's equation (1.10) should be complemented with an initial condition, the state $|\psi_0\rangle$ of the condensate at $t = 0$, when the BEC is released from the trap:

$$\left[i\frac{\partial}{\partial t} - \mathcal{H}\right] |\psi\rangle = \delta(t)\, |\psi_0\rangle\,. \tag{1.14}$$

On the one hand, using Eq. (1.12), it follows that, in real space representation ,

$$\psi(\boldsymbol{r}, t) = \int \mathrm{d}\boldsymbol{r}' G(\boldsymbol{r}', \boldsymbol{r}, t, 0)\psi_0(\boldsymbol{r}'). \tag{1.15}$$

On the other hand, we know that the temporal evolution (in bra/ket notation) $|\psi(t)\rangle$ of an initial state $|\psi_0\rangle$ is described by the unitary evolution operator $\hat{U}(t) = e^{-i\mathcal{H}t}$:

$$|\psi(t)\rangle = \hat{U}(t)\, |\psi_0(0)\rangle = e^{-i\mathcal{H}t}\, |\psi_0\rangle\,, \tag{1.16}$$

such that

$$\psi(\boldsymbol{r}, t) = \langle \boldsymbol{r}|\psi(t)\rangle = \int \mathrm{d}\boldsymbol{r}'\; \langle \boldsymbol{r}|e^{-i\mathcal{H}t}|\boldsymbol{r}'\rangle\, \langle \boldsymbol{r}'|\psi_0\rangle\,. \tag{1.17}$$

By identifying expressions (1.15) and (1.17), we arrive at our definition of the Green's function for the Schrödinger equation:

$$G(\boldsymbol{r}', \boldsymbol{r}, t) \equiv G(\boldsymbol{r}', \boldsymbol{r}, t, 0) = \langle \boldsymbol{r} | e^{-i\mathcal{H}t} | \boldsymbol{r}' \rangle \,, \tag{1.18}$$

and the associated Green's operator

$$\hat{G}(t) \equiv e^{-i\mathcal{H}t}. \tag{1.19}$$

This operator contains all the information on the system evolution. Its knowledge allows a priori to derive the time-evolution of any observable. In what follows, we will mostly use the Fourier transform – with respect to time and space – of the Green's function,

$$G(\boldsymbol{k}', \boldsymbol{k}, \epsilon) \equiv \langle \boldsymbol{k} | \frac{1}{\epsilon - \mathcal{H}_0 \pm i0^+} | \boldsymbol{k}' \rangle = \int \mathrm{d}t \, \mathrm{d}\boldsymbol{r} \, e^{i\epsilon t} e^{-i(\boldsymbol{r}'.\boldsymbol{k}' - \boldsymbol{r}.\boldsymbol{k})} G(\boldsymbol{r}', \boldsymbol{r}, t). \tag{1.20}$$

Advanced and retarded Green's functions

In the derivation of the last paragraph, we omit to specify the sign of the time t. As a consequence, the Green's operator (1.19) describes the evolution of ψ_0 at $t = 0$ to an arbitrary time t, positive or negative. To take into account the causality of the real physical system, we usually define the retarded (R) and advanced (A) Green's operators, which describe respectively the evolution towards the positive and negative times:

$$\begin{aligned} \hat{G}^R(t) &\equiv -i\theta(t) e^{-i\mathcal{H}t} \\ \hat{G}^A(t) &\equiv i\theta(-t) e^{-i\mathcal{H}t}. \end{aligned} \tag{1.21}$$

Their Fourier transforms with respect to time read:

$$\hat{G}^{R/A}_\epsilon = \int_{-\infty}^{+\infty} -i\theta(t) e^{i(\epsilon - \mathcal{H})t} = \frac{1}{\epsilon - \mathcal{H} \pm i\eta}, \tag{1.22}$$

where $\eta \to 0$ is a small imaginary part necessary for convergence of the first integral at long times. Note that equality (1.22) implies the following relation between the advanced and retarded Green's functions :

$$(G^R_\epsilon(\boldsymbol{k}', \boldsymbol{k}))^* = G^A_\epsilon(\boldsymbol{k}, \boldsymbol{k}'). \tag{1.23}$$

In order to lighten the notations, in what follows, we will omit the subscripts R and A they are not necessary, and simply denote by $\hat{G}$ (G) the retarded Green's operator (function). In these cases, the equivalent expressions for the advanced Green'soperator (function) follow easily from relation (1.23).

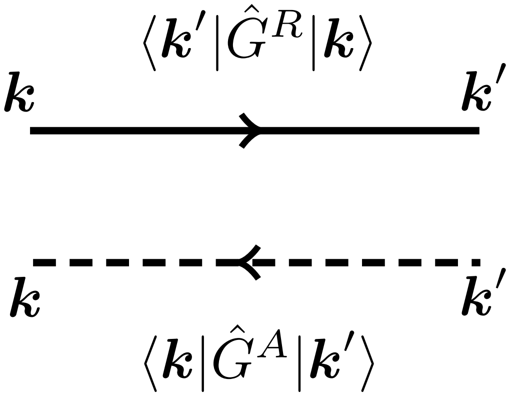

Figure 1.2 – Conventions for the diagrammatic representation of the Green's functions, used throughout this manuscript. Solid lines refer to $\langle \boldsymbol{k}' | \hat{G}^R_\epsilon | \boldsymbol{k} \rangle = G^R_\epsilon(\boldsymbol{k}, \boldsymbol{k}')$, and dashed lines to $\langle \boldsymbol{k} | \hat{G}^A_\epsilon | \boldsymbol{k}' \rangle = G^A_\epsilon(\boldsymbol{k}', \boldsymbol{k})$. For solid (dashed) lines, arrows coincide with the (opposite of the) direction of propagation. The value of the corresponding energies ϵ will be specified directly on the diagrams when they are not obvious. In the rest of the manuscript, we will use these notations to describe both free-space and averaged Green's functions.

Diagrammatic convention

We introduce in Fig. 1.2 our convention for the representation of the retarded and advanced Green's functions $G^R_\epsilon(\boldsymbol{k}, \boldsymbol{k}')$ and $G^A_\epsilon(\boldsymbol{k}', \boldsymbol{k})$ that will be used in diagrams throughout this manuscript.

1.5.2 Average Green's function

In this subsection we compute the disorder average of the Green's function for the Schrödinger equation (1.10). This function encodes the average effect of the disorder on the dynamics.

Born series

The convenience of the Green's function formalism becomes obvious when one tries to express the operator $\hat{G}$, associated with $\mathcal{H}$, as a function of the operator $\hat{G}_0$, associated with $\mathcal{H}_0$ (we omit the R/A subscripts for clarity here):

$$\begin{aligned}
\hat{G} &= \frac{1}{\epsilon - \mathcal{H}_0 - V + i\eta} = \frac{\epsilon - \mathcal{H}_0 + i\eta}{(\epsilon - \mathcal{H}_0 - V + i\eta)(\epsilon - \mathcal{H}_0 + i\eta)} \\
&= \frac{1}{\epsilon - \mathcal{H}_0 + i\eta} + \frac{V}{(\epsilon - \mathcal{H}_0 - V + i\eta)(\epsilon - \mathcal{H}_0 + i\eta)} \\
&= \hat{G}_0 + \hat{G}_0 V \hat{G}, \qquad (1.24)
\end{aligned}$$

which is the Lipmann-Schwinger equation. Iteration of equation (1.24) yields an infinite series expansion in powers of the operator V, known as the Born series:

$$\hat{G} = \hat{G}_0 + \hat{G}_0 V \hat{G}_0 + \hat{G}_0 V \hat{G}_0 V \hat{G}_0 + \dots \tag{1.25}$$

Expansion for the average Green's function

Using the definition (1.19) and the fact that $\mathcal{H}_0$ is diagonal in momentum space we can conveniently write the free-space Green's functions as:

$$G_0^{R/A}(\boldsymbol{k}, \boldsymbol{k}', \epsilon) = \langle \boldsymbol{k} | \frac{1}{\epsilon - \mathcal{H}_0 \pm i\eta} | \boldsymbol{k}' \rangle = \frac{(2\pi)^d \delta(\boldsymbol{k} - \boldsymbol{k}')}{\epsilon - \epsilon_{\boldsymbol{k}} \pm i\eta}, \tag{1.26}$$

where $\epsilon_{\boldsymbol{k}} = k^2/2m$ is the free-space dispersion relation for a particle of mass m. This function is the propagator in free space from a state $|\boldsymbol{k}\rangle$ to the state $|\boldsymbol{k}'\rangle$ at energy ϵ. $\hat{G}_0$ being obviously diagonal in momentum space – as a consequence of translational invariance –, we will from now use the notation $G_0(\boldsymbol{k}, \epsilon)$, formally defined by :

$$G_0(\boldsymbol{k}, \boldsymbol{k}', \epsilon) = (2\pi)^d \delta(\boldsymbol{k} - \boldsymbol{k}') G_0(\boldsymbol{k}, \epsilon). \tag{1.27}$$

Once the free-space Green's function is known, the full Green's function $G_\epsilon(\boldsymbol{k}, \boldsymbol{k}')$ is expressed as an infinite series using Eq. (1.25):

$$\begin{aligned} G_\epsilon(\boldsymbol{k}, \boldsymbol{k}') = {} & (2\pi)^d \delta(\boldsymbol{k} - \boldsymbol{k}') G_0(\boldsymbol{k}, \epsilon) + G_0(\boldsymbol{k}, \epsilon) \langle \boldsymbol{k} | V | \boldsymbol{k}' \rangle G_0(\boldsymbol{k}', \epsilon) \\ & + G_0(\boldsymbol{k}, \epsilon) \left[\int \frac{\mathrm{d}\boldsymbol{k}''}{(2\pi)^2} G_0(\boldsymbol{k}'', \epsilon) \langle \boldsymbol{k} | V | \boldsymbol{k}'' \rangle \langle \boldsymbol{k}'' | V | \boldsymbol{k}' \rangle \right] G_0(\boldsymbol{k}', \epsilon) + \dots \end{aligned} \tag{1.28}$$

At this stage, an important reminder is in order: the disorder operator V is a random variable, such that the full Green's function is a random variable as well. For a given realization of the disorder potential $V(\boldsymbol{r})$, we can expect that it will be very complicated, and not necessarily informative on the physics of a generic disordered system. For this reason, we will adopt a statistical description and focus on quantities that are *averaged* over a large number of realizations of the disorder. This strategy is not only simpler to handle, but it also allows to showcase universal properties of disordered systems, rather than sample-to-sample phenomenology. We denote the disorder average by the notation $\overline{X}$ for any random variable X. For convenience, we also set the origin of energies to $\overline{V}$; this causes the second term in Eq. (1.28) to vanish when we take the disorder average. We are left with:

$$\begin{aligned} \overline{G_\epsilon(\boldsymbol{k}, \boldsymbol{k}')} = {} & (2\pi)^d \delta(\boldsymbol{k} - \boldsymbol{k}') G_0(\boldsymbol{k}, \epsilon) \\ & + G_0(\boldsymbol{k}, \epsilon) \left[\int \frac{\mathrm{d}\boldsymbol{k}''}{(2\pi)^d} G_0(\boldsymbol{k}'', \epsilon) \overline{\langle \boldsymbol{k} | V | \boldsymbol{k}'' \rangle \langle \boldsymbol{k}'' | V | \boldsymbol{k}' \rangle} \right] G_0(\boldsymbol{k}', \epsilon) + \dots \end{aligned} \tag{1.29}$$

We assume the disorder operator V to be local, such that $\langle \boldsymbol{r}|V|\boldsymbol{r'}\rangle = \delta(\boldsymbol{r}-\boldsymbol{r'})V(\boldsymbol{r})$. Therefore, its Fourier transform can be written in the form $\langle \boldsymbol{k}|V|\boldsymbol{k'}\rangle = V(\boldsymbol{k}-\boldsymbol{k'})$. We then define the two-point correlation function of the disorder V:

$$\overline{\langle \boldsymbol{r}|V|\boldsymbol{r}\rangle \langle \boldsymbol{r'}|V|\boldsymbol{r'}\rangle} = \overline{V(\boldsymbol{r})V(\boldsymbol{r'})} \equiv \mathcal{C}(\boldsymbol{r}-\boldsymbol{r'}). \tag{1.30}$$

The correlator in Eq. (1.29) can be expressed as a function of its Fourier transform :

$$\overline{\langle \boldsymbol{k}|V|\boldsymbol{k''}\rangle \langle \boldsymbol{k''}|V|\boldsymbol{k'}\rangle} = (2\pi)^d\delta(\boldsymbol{k}-\boldsymbol{k'})\,\tilde{\mathcal{C}}(\boldsymbol{k''}-\boldsymbol{k}), \tag{1.31}$$

Substituting this into Eq. (1.29), we finally obtain :

$$\begin{aligned}\overline{G_\epsilon(\boldsymbol{k},\boldsymbol{k'})} &= (2\pi)^d\delta(\boldsymbol{k}-\boldsymbol{k'})G_0(\boldsymbol{k},\epsilon)\left[1+G_0(\boldsymbol{k},\epsilon)\int\frac{\mathrm{d}\boldsymbol{k''}}{(2\pi)^d}G_0(\boldsymbol{k''},\epsilon)\tilde{\mathcal{C}}(\boldsymbol{k''}-\boldsymbol{k})+\dots\right]\\ &= (2\pi)^d\delta(\boldsymbol{k}-\boldsymbol{k'})\overline{G_\epsilon(\boldsymbol{k})}.\end{aligned} \tag{1.32}$$

We can see that, similarly to the free-space Green's function, $\overline{G}$ is diagonal in momentum space. Indeed, taking the disorder average restores the translationnal invariance of the system. From now on, we only need to work with the diagonal version of $\overline{G}$:

$$\overline{G_\epsilon(\boldsymbol{k})} = G_0(\boldsymbol{k},\epsilon)\left[1+G_0(\boldsymbol{k},\epsilon)\int\frac{\mathrm{d}\boldsymbol{k''}}{(2\pi)^d}G_0(\boldsymbol{k''},\epsilon)\tilde{\mathcal{C}}(\boldsymbol{k''}-\boldsymbol{k})+\dots\right] \tag{1.33}$$

Dyson equation

The development (1.33) of the average Green's function in powers of the potential V is at the core of the perturbative calculations in random potentials. In order to manipulate it and construct a consistent perturbation theory, it is nevertheless useful to rearrange it. By analyzing higher-order terms in Eq. (1.25), one observes that, for a general random potential V, a lot of terms of the type $\overline{VG_0VG_0VG_0\dots}$ will arise after taking the disorder average. In the momentum space representation, they will yield very complicated expressions involving intricate convolutions of high-order correlation functions with G_0 functions. To describe them, it is convenient to use a diagrammatic representation. Each of these expressions can be represented as a diagram. Some examples are drawn in Fig. (1.3): one can see that, at each order in V, it is possible to enumerate the number of terms that we will obtain in the expansion, by counting the possible arrangements of “impurity” lines, which represent correlators of the disorder potential. If, for each order, we only keep diagrams that are not simple concatenations of previously drawn, lower-order diagrams, we are left with a collection of so-called “irreducible” diagrams (for instance, the second term in Eq. (1.33) corresponds to the only irreducible diagram of order 2). By this process, we can reduce the infinite series

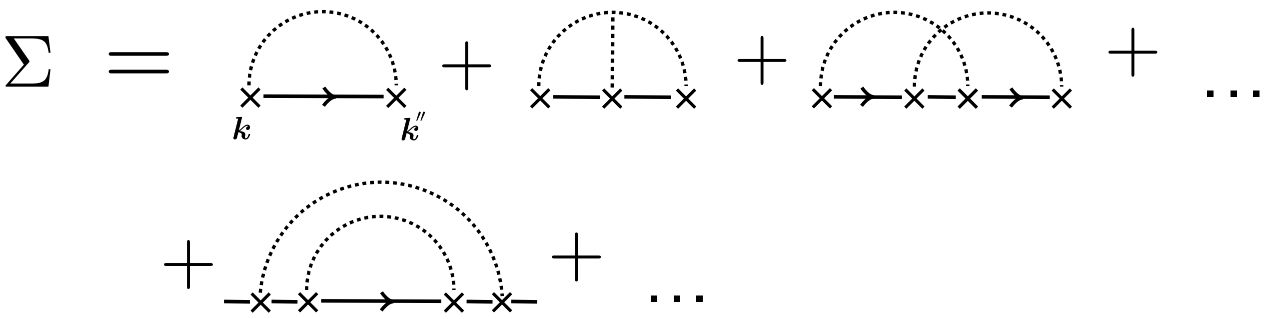

Figure 1.3 – Diagrammatic representation of the self-energy. Solid lines denote the free Green's function $\langle \boldsymbol{k}|\hat{G}_0^R(\epsilon)|\boldsymbol{k}''\rangle$, in accordance with our convention, Fig. 1.2. The dashed lines represent correlations of the potential in momentum space (for example, in the first diagram it represents $\tilde{\mathcal{C}}(\boldsymbol{k}-\boldsymbol{k}''))$. In the first row are some examples of irreducible diagrams of increasing order. The first one corresponds to the term within brackets in Eq. (1.33), and the only irreducible diagram of order 2, all of the second order diagrams being generated by its concatenations.

to a basis of diagrams that generate it by iteration. This means, in particular, that if we call $\Sigma(\boldsymbol{k},\epsilon)$ the sum of all irreducible diagrams, the expansion (1.33) can be simply written as

$$\overline{G_\epsilon(\boldsymbol{k})} = G_0(\boldsymbol{k},\epsilon)\left\{1+\sum_{n=1}^{+\infty}\left[\Sigma(\boldsymbol{k},\epsilon)G_0(\boldsymbol{k},\epsilon)\right]^n\right\}, \tag{1.34}$$

which, after summation of the geometric series, reduces to

$$\overline{G_\epsilon(\boldsymbol{k})} = G_0(\boldsymbol{k},\epsilon)\left\{1+\Sigma(\boldsymbol{k},\epsilon)\overline{G_\epsilon(\boldsymbol{k})}\right\}. \tag{1.35}$$

Equation (1.35) is called the Dyson equation and Σ is the self-energy. The role of the latter becomes clearer when we recast the previous expression as:

$$\overline{G_\epsilon(\boldsymbol{k})} = \frac{G_0(\boldsymbol{k},\epsilon)}{1-\Sigma(\boldsymbol{k},\epsilon)G_0(\boldsymbol{k},\epsilon)} = \frac{1}{\epsilon-\epsilon_{\boldsymbol{k}}-\Sigma(\boldsymbol{k},\epsilon)}. \tag{1.36}$$

In this form, the full average Green's function has an expression similar to the free-space Green's function G_0, except for the self-energy Σ, a complex quantity that encapsulates the effect of the disorder potential on the single particle evolution. Note that, since the self-energy is defined through diagrams that use either G_0^R or G_0^A, Σ also exists in its retarded Σ^R and advanced Σ^A versions.

Born approximation

Computing exactly the self-energy is in general not possible, as it involves an infinite number of diagrammatic classes. However, when the disorder potential V is weak enough (the exact condition in our case will be defined shortly), we can use the so-called Born approximation [186]: In the self-energy expansion of Fig. (1.3), we only keep the first term. Within the Born approximation, Eq. (1.36) becomes

$$\overline{G_\epsilon(\boldsymbol{k})} = G_0(\boldsymbol{k},\epsilon)\left[1+\overline{G_\epsilon(\boldsymbol{k})}\int\frac{\mathrm{d}\boldsymbol{k}''}{(2\pi)^d}G_0(\boldsymbol{k}'',\epsilon)\tilde{\mathcal{C}}(\boldsymbol{k}''-\boldsymbol{k})\right], \tag{1.37}$$

and the corresponding self-energy (remember expansion (1.33)) reads:

$$\Sigma(\boldsymbol{k},\epsilon) = \int\frac{\mathrm{d}\boldsymbol{k}''}{(2\pi)^d}G_0(\boldsymbol{k}'',\epsilon)\tilde{\mathcal{C}}(\boldsymbol{k}''-\boldsymbol{k}). \tag{1.38}$$

Mean free time

The physical meaning of Σ becomes apparent after switching to the time domain. We want to compute:

$$\overline{G(\boldsymbol{k},t)} = \int\frac{\mathrm{d}\epsilon}{2\pi}\frac{1}{(\epsilon-\Sigma'(\boldsymbol{k},\epsilon))-\epsilon_{\boldsymbol{k}}-i\Sigma''(\boldsymbol{k},\epsilon)}e^{-i\epsilon t}, \tag{1.39}$$

where $\Sigma = \Sigma' + i\Sigma''$, which can be done using contour integration. Assuming that Σ is a smooth function of the energy, the integrand has a trivial pole at $\epsilon = \epsilon_{\boldsymbol{k}}+\Sigma'(\boldsymbol{k},\epsilon_{\boldsymbol{k}})+i\Sigma''(\boldsymbol{k},\epsilon_{\boldsymbol{k}})$, which is either in the upper or lower half of the complex plane, depending of the sign of the imaginary part of $\Sigma(\boldsymbol{k},\epsilon_{\boldsymbol{k}})$. In the "causal" (retarded) situation with $t>0$, we can only use the residue theorem in the lower half plane.[3] As a consequence, the result is non-zero if and only if $\Sigma''^R < 0$. We find:

$$\overline{G^R(\boldsymbol{k},t)} = -i\theta(t)e^{-i(\epsilon_{\boldsymbol{k}}+\Sigma'^R(\boldsymbol{k},\epsilon_{\boldsymbol{k}}))t}\times e^{\Sigma''^R(\boldsymbol{k},\epsilon_{\boldsymbol{k}})t}. \tag{1.40}$$

Comparing this formula with the definitions (1.21) of the free-space Green's operators, one understands that the real part of the self-energy Σ' encodes an energy shift, while its imagi-

---

[3] To use the residue theorem, we choose the usual half-circle contour followed by ω in the complex plane. As the radius of this circle goes to infinity, we need to use Jordan's lemma to ensure that the integral over the contour is equal to our original integral: for an integrand of the form $e^{ia\epsilon}f(\epsilon)$, it applies only in the lower (upper) half of the complex plane if $a<0$ ($a>0$).

nary part Σ'' is a decay rate, which corresponds to the lifetime τ of a plane-wave propagating through the disorder:[4]

$$\tau \equiv -\frac{1}{2|\Sigma''|}. \tag{1.41}$$

Furthermore, using Eq. (1.38), we have:

$$\Sigma''(\boldsymbol{k}, \epsilon) = -\pi \int \frac{\mathrm{d}\boldsymbol{k}''}{(2\pi)^d} \tilde{\mathcal{C}}(\boldsymbol{k}'' - \boldsymbol{k}) \delta(\epsilon - \epsilon_{\boldsymbol{k}''}), \tag{1.42}$$

where we used the Sokhotski–Plemelj theorem $\frac{1}{x+i0^+} = PV\frac{1}{x} - i\pi\delta(x)$. From Eq. (1.41), we infer:

$$\frac{1}{\tau_\epsilon(\boldsymbol{k})} \equiv 2\pi \int \frac{\mathrm{d}\boldsymbol{k}''}{(2\pi)^d} \tilde{\mathcal{C}}(\boldsymbol{k}'' - \boldsymbol{k}) \delta(\epsilon - \epsilon_{\boldsymbol{k}''}). \tag{1.43}$$

Noticing that $\tilde{\mathcal{C}}(\boldsymbol{k}'' - \boldsymbol{k}) = \overline{|\langle \boldsymbol{k}|V|\boldsymbol{k}'\rangle|^2}$, we see that this definition coincides with the Fermi Golden rule (1.4).

Mean free path

Associated to the mean free time, we can introduce the mean free path ℓ_ϵ. Its definition follows from the expression of the average Green's function in position space (for simplicity we neglect here the real part of the self energy):

$$\overline{G}(\boldsymbol{r}, \boldsymbol{r}', \epsilon) = G_0(\boldsymbol{r}, \boldsymbol{r}', \epsilon)\ e^{-\frac{|\boldsymbol{r}-\boldsymbol{r}'|}{\ell_\epsilon}} \tag{1.44}$$

with

$$\ell_\epsilon(\boldsymbol{k}) \equiv -\frac{k}{2m\Sigma''(\boldsymbol{k}, \epsilon)} = \frac{k}{m}\tau_\epsilon(\boldsymbol{k}), \tag{1.45}$$

which is nothing more than the product of the mean free time by the group velocity $v_g = k/m$.

Weak disorder criterion

We now have everything needed to formulate the weak disorder criterion, which specifies the validity of the Born approximation. By studying the self-energy series, whose first few terms are depicted in Fig. 1.3, one can see that the first diagram, the self-energy at the Born approximation, is of order $1/k\ell_\epsilon(\boldsymbol{k})$ [125] (we will show this explicitly for a specific type of disorder potential in the next subsection). The higher-order irreducible diagrams, on the

---

[4] The factor 2 stems is added so that this definition of τ coincides with the Fermi golden rule (1.4). It stems from the fact that the self-energy deals with $|\boldsymbol{k}\rangle$, while the Fermi golden rule deals with $|\,|\boldsymbol{k}\rangle\,|^2$.

other hand, are all of order $(k\ell_\epsilon(\boldsymbol{k}))^{-n}$ [125]. As a consequence, the natural choice for the weak disorder criterion is :

$$k\ell_\epsilon(\boldsymbol{k}) \gg 1. \tag{1.46}$$

For the matter waves within this regime, most of the observables are accessible analytically, and complicated disorder-induced phenomena, such as Anderson localization, are negligible in 2d and 3d (see the discussion at the end of Sec. 1.4.3).

1.5.3 Model for the disorder potential

The theory we developed so far is quite general and is valid for any disorder potential. From this point however, the results we present are vastly dependent on the properties of the disorder. As already stated, most experiments aiming at observing mesoscopic phenomena with cold atoms use optical speckle as the disordered potential for the atoms, mainly because it is easy to generate [21]. The choice of a speckle distribution for the potential is however not essential to the observation of localization effects. Rather, it makes the theoretical description of these phenomena more involved. Indeed, speckles are spatially correlated, with a correlation length σ, which makes wave scattering processes display an anisotropy controlled by the ratio λ/σ. Moreover, due to their specific probability distribution, all high-order correlation functions of a speckle potential are non-vanishing, in contrast with a Gaussian distributed potential for example, for which all correlation function of odd order vanish. This reduces the precision of the Born approximation [187], as the first neglected diagrams in the self-energy expansion of Fig. 1.3 in the case of speckle are of order 3, while they are of order 4 for a Gaussian-distributed potential.

Gaussian uncorrelated disorder

In what follows and throughout the thesis (with the exception of chapter 5), we will discuss the case of a Gaussian-distributed disorder potential with zero average ($\overline{V} = 0$), and a spatial correlation function

$$\mathcal{C}(\boldsymbol{r} - \boldsymbol{r}') = \gamma\delta(\boldsymbol{r} - \boldsymbol{r}'), \tag{1.47}$$

such that the Fourier transform $\tilde{\mathcal{C}}$ of $\mathcal{C}$ reads [125]

$$\tilde{\mathcal{C}}(\boldsymbol{k}) = \gamma \int \mathrm{d}(\boldsymbol{r} - \boldsymbol{r}') e^{-i\boldsymbol{k}.(\boldsymbol{r}-\boldsymbol{r}')}\delta(\boldsymbol{r} - \boldsymbol{r}') = \gamma, \tag{1.48}$$

the parameter γ measuring the strength of the disorder. The distribution of such a potential reads

$$\mathbb{P}[V(\boldsymbol{r})]\mathcal{D}V(\boldsymbol{r}) = \sqrt{\frac{\mathcal{V}}{2\pi\gamma}} \exp\left(-\frac{1}{2\gamma}\int \mathrm{d}\boldsymbol{r} V(\boldsymbol{r})^2\right) \mathcal{D}V(\boldsymbol{r}). \tag{1.49}$$

Mean free time in the Born approximation

Using equations (1.38) and (1.48), we can express the (retarded) self-energy in the Born approximation as

$$\Sigma(\boldsymbol{k},\epsilon) = \gamma\int \frac{\mathrm{d}\boldsymbol{k}''}{(2\pi)^d} G_0^R(\boldsymbol{k}'',\epsilon) = \gamma\int \frac{\mathrm{d}\boldsymbol{k}''}{(2\pi)^d}\frac{1}{\epsilon-\epsilon_{\boldsymbol{k}''}+i0^+}, \tag{1.50}$$

which yields

$$\Sigma(\boldsymbol{k},\epsilon) = \gamma\left[\int \frac{\mathrm{d}\boldsymbol{k}''}{(2\pi)^d} PV\left(\frac{1}{\epsilon-\epsilon_{\boldsymbol{k}''}}\right) - i\pi\int \frac{\mathrm{d}\boldsymbol{k}''}{(2\pi)^d}\delta(\epsilon-\epsilon_{\boldsymbol{k}''})\right]. \tag{1.51}$$

The first integral, which represents the real part of the self-energy, is divergent for dimensions $d > 1$. This unphysical result is characteristic of a δ-correlated potential [125]. In the rest of this chapter, we will neglect this real part, as it constitutes a simple constant shift of the energies, known to be small in the weak disorder limit.

The imaginary part, in turn, yields:

$$\Sigma''(\epsilon) = -\pi\gamma\int \frac{\mathrm{d}\boldsymbol{k}''}{(2\pi)^d}\delta(\epsilon-\epsilon_{\boldsymbol{k}''}) = -\pi\gamma\nu_\epsilon. \tag{1.52}$$

The second equality follows from the definition of the density of states per unit volume, that we call ν_ϵ. Note, in passing, the simple relationship between the Green's function and the free-space density of states.

$$\nu_\epsilon = -\frac{1}{\pi}\int \frac{\mathrm{d}\boldsymbol{k}''}{(2\pi)^d}\Im\left[G_0^R(\boldsymbol{k}'',\epsilon)\right]. \tag{1.53}$$

Replacing the free-space Green's function by the average Green's function in this equation yields the averaged density of states per unit volume $\overline{\nu_\epsilon}$, which contain the disorder corrections, encoded in the self-energy. These corrections are of order $1/k\ell_\epsilon(k)$, so we can safely neglect them in the weak disorder limit, and consider that $\overline{\nu_\epsilon} = \nu_\epsilon$. In the Born approximation, Σ'' does not have an explicit dependence in $\boldsymbol{k}$. We deduce from equation (1.52) the mean free time and the mean free path in a Gaussian uncorrelated disorder potential

$$\frac{1}{\tau_\epsilon} = -2\,\Sigma''^{R}(\epsilon) = 2\pi\gamma\nu_\epsilon, \tag{1.54}$$

and

$$\frac{1}{\ell_\epsilon(k)} = \frac{m}{k\tau_\epsilon} = \frac{2\pi m\gamma\nu_\epsilon}{k}. \tag{1.55}$$

In the specific case of a 2d system (widely used in the rest of this thesis), the free-space density of states for unit volume is independent of the (positive energy) [125]:

$$\nu_\epsilon = \frac{1}{2\pi}\theta(\epsilon), \tag{1.56}$$

so that:

$$\tau_\epsilon = \frac{1}{\gamma} \qquad \text{and} \qquad \ell_\epsilon = \frac{k}{m\gamma}. \tag{1.57}$$

Spectral function

A central object for the description of the dynamics of matter waves in a disorder potential is the spectral function, defined as:

$$A_\epsilon(\boldsymbol{k}) \equiv 2\pi\overline{\langle\boldsymbol{k}|\delta(\epsilon-\mathcal{H})|\boldsymbol{k}\rangle}. \tag{1.58}$$

From this definition, it is clear that

$$\int \frac{\mathrm{d}\epsilon}{2\pi} A_\epsilon(\boldsymbol{k}) = 1. \tag{1.59}$$

Thus $A_\epsilon(\boldsymbol{k})$ can be viewed as the probability density for a plane-wave $|\boldsymbol{k}\rangle$ to have energy ϵ in the presence of disorder. When the disorder is absent, the spectral function simply reduces to $\delta(\epsilon-\epsilon_{\boldsymbol{k}})$, indicating that particles have a well-defined dispersion relation. Once again, $A_\epsilon(\boldsymbol{k})$ can be simply expressed as a function of the average Green's function:

$$\begin{aligned} A_\epsilon(\boldsymbol{k}) &= -2\overline{\langle\boldsymbol{k}|\Im\left[\frac{1}{\epsilon-\mathcal{H}\pm i0^+}\right]|\boldsymbol{k}\rangle} = -2\Im\left[\overline{G}^R(\boldsymbol{k},\epsilon)\right] \\ &= \frac{1}{\tau_\epsilon}\frac{1}{(\epsilon-\epsilon_{\boldsymbol{k}})^2+\frac{1}{4\tau_\epsilon^2}}. \end{aligned} \tag{1.60}$$

At the Born approximation, τ_ϵ does not have a strong dependence in the energy and the spectral function $A_\epsilon(\boldsymbol{k})$ – seen as a function of ϵ – is thus a Lorentzian of maximum 4τ, centered around $\epsilon_{\boldsymbol{k}}$, with a half-width at half-maximum equal to $1/2\tau$. In the weak disorder limit where $\tau \gg 1/\epsilon$, this function is strongly peaked around $\epsilon_{\boldsymbol{k}}$. As an example, we compare in Fig. (1.4) a spectral function extracted from numerical simulations with the corresponding Born prediction, corrected to take into account the small real part of the self-energy

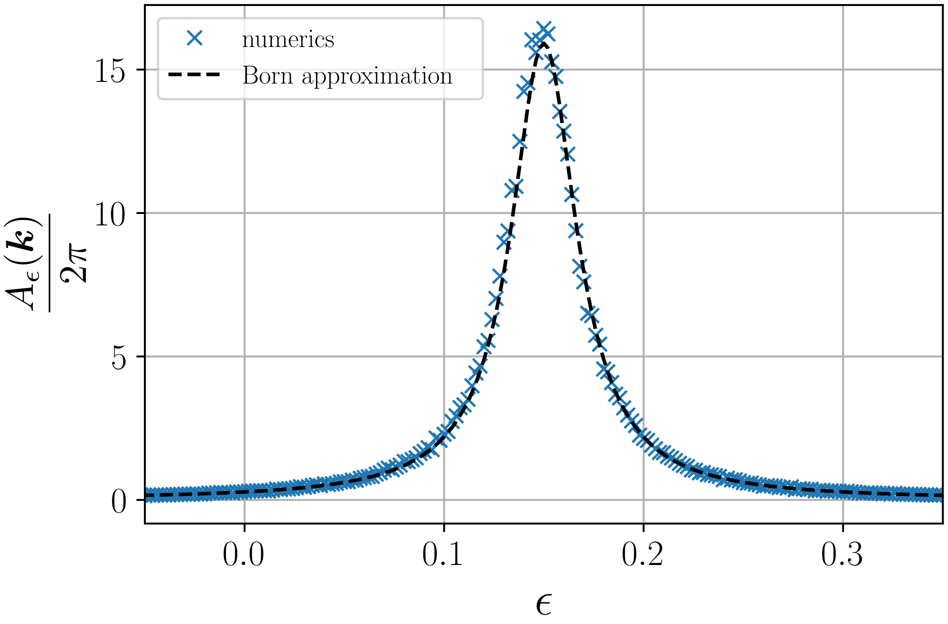

Figure 1.4 – Spectral function $A_\epsilon(\boldsymbol{k})$ as a function of energy, extracted from 2d numerical simulations. $A_\epsilon(\boldsymbol{k})$ is obtained by propagating an initial plane-wave $|\boldsymbol{k}\rangle$ with $k \simeq \pi/5$ in a Gaussian uncorrelated disorder of strength $\gamma = 0.04$. The size of the system is $L = 750$, with a discretization $\Delta x = \Delta y = 0.2$. The results are averaged over 128 realizations of the disorder. As expected, the spectral function is peaked around the disorder-free $\epsilon_{\boldsymbol{k}} \simeq 0.19$, with only a small shift due to the constant real part of the self-energy, that we neglected in the derivation of (1.60). The dashed line represents the Born prediction, whose maximum has been shifted to account for the real part of the self-energy.

that we neglected in (1.60). The spectral function is a central object for the physics of ultracold atoms in disorder, because it relates the momentum distribution $n_{\boldsymbol{k}}$, obtained by time-of-flight experiments to the energy distribution of the gas. Obtaining the precise energy distribution is crucial, for example in the search for the mobility edge E_c in the 3d Anderson localization transition, but also to study the out-of-equilibrium dynamics of interacting gases in the presence of disorder. However, the precise knowledge of the spectral function is a difficult task, especially in 2d and 3d and for low energies/momenta, as it requires a perfect knowledge of the self-energy, sometimes beyond the Born approximation. Ref. [188] reports the recently achieved direct measurement of spectral functions in 3d using state-dependent disorder potentials to selectively populate eigenstates around a precise energy.

Finally, recalling equation (1.53), we have the useful relation

$$\int \frac{\mathrm{d}\boldsymbol{k}''}{(2\pi)^d} A_\epsilon(\boldsymbol{k}) = -2 \int \frac{\mathrm{d}\boldsymbol{k}''}{(2\pi)^d} \Im \left[\overline{G}^R(\boldsymbol{k}'', \epsilon) \right] = 2\pi\nu_\epsilon. \tag{1.61}$$

1.6 Diffusion and coherent backscattering

In this section, we describe the theory of diffusion and coherent backscattering (or CBS) of a non-interacting ultracold gas of bosons launched with finite velocity in a disorder potential. To this end, we will compute analytically the time evolution of the average momentum distribution of the gas assuming weak disorder. As discussed in the introduction of this chapter, we specifically consider a quench protocol, where the gas is initially prepared in a plane-wave state $|\boldsymbol{k}_0\rangle$ and, at $t = 0$, the disorder potential V is instantaneously turned on. In doing so, we do not describe the effect of the small momentum spread of the initial state, inherent to real ultra-cold atom experiments [21]. This is justified since the momentum spread does not fundamentally change the picture of weak localization developed here, and only induces small corrections, which can be discussed a posteriori. Quench protocols naturally drive the gas out of equilibrium. As discussed below, in the absence of interactions, this dynamics is already non trivial: after a short transient regime of the order of a few mean free times, the multiple scattering regime settles and the gas reaches a time-independent diffusive state. The system also presents weakly localized modes, which manifest themselves as a time-dependent coherent backscattering peak in the momentum distribution. Without interactions, however, no real thermalization process takes place: the energy distribution of the particles remains constant in time since disorder scattering is elastic, and the gas can never be described by a Gibbs ensemble. The ingredient of particle interactions will be introduced in chapter 2.

1.6.1 Density kernel

In this section, we describe the establishment of classical particle diffusion associated with multiple scattering at weak disorder. This mechanism is naturally visible in the momentum distribution, $n_{\boldsymbol{k}}$. To this aim, we consider the evolution of a Bose gas of N particles in a box of volume $\mathcal{V}$, initially prepared as a plane-wave state $\phi(\boldsymbol{r}) \equiv \langle \boldsymbol{r}|\psi(t=0)\rangle = 1/\sqrt{\mathcal{V}}\exp(i\boldsymbol{k}_0.\boldsymbol{r})$, where $\rho_0 \equiv N/\mathcal{V}$ is the particle density. Since we are here dealing with single particle physics, for convenience, we will set $N = 1$ in the rest of this chapter. The Schrödinger equation

$$i\partial_t\psi(\boldsymbol{r},t) = \left[-\frac{\boldsymbol{\nabla}^2}{2m} + V(\boldsymbol{r})\right]\psi(\boldsymbol{r},t) \tag{1.62}$$

governs the evolution of the wavefunction $\psi(\boldsymbol{r},t)$. $V(\mathbf{r})$ is a Gaussian uncorrelated random potential, as described in the previous section.

The averaged momentum distribution of the gas at time t, $n_{\boldsymbol{k}}(t) \equiv \overline{|\psi(\boldsymbol{k},t)|^2}$, is normalized according to :

$$\int \frac{\mathrm{d}\boldsymbol{k}}{(2\pi)^d} n_{\boldsymbol{k}}(t) = 1, \tag{1.63}$$

The Fourier transform of Eq. (1.17) gives the expression of $\psi(\boldsymbol{k},t)$ and $\psi^*(\boldsymbol{k},t)$ at time $t > 0$, and for a given realization of the disorder, we have:

$$\psi(\boldsymbol{k},t) = \langle \boldsymbol{k}|\psi(t)\rangle = \int \frac{\mathrm{d}\epsilon}{2\pi} e^{-i\epsilon t} \int \frac{\mathrm{d}\boldsymbol{k}'}{(2\pi)^d} \langle \boldsymbol{k}|\hat{G}^R_\epsilon|\boldsymbol{k}'\rangle\, \phi(\boldsymbol{k}'), \tag{1.64}$$

and, using the definitions (1.21)

$$\psi^*(\boldsymbol{k},t) = \langle \psi(t)|\boldsymbol{k}\rangle = \int \frac{\mathrm{d}\epsilon}{2\pi} e^{i\epsilon t} \int \frac{\mathrm{d}\boldsymbol{k}'}{(2\pi)^d} \langle \boldsymbol{k}'|\hat{G}^A_\epsilon|\boldsymbol{k}\rangle\, \phi^*(\boldsymbol{k}'). \tag{1.65}$$

We then have for the momentum distribution :

$$\begin{aligned} n_{\boldsymbol{k}}(t) &= \overline{|\psi(\boldsymbol{k},t)|^2} \\ &= \int \frac{\mathrm{d}\epsilon_1\, \mathrm{d}\epsilon_2}{(2\pi)^2} e^{-i(\epsilon_1 - \epsilon 2)t} \int \frac{\mathrm{d}\boldsymbol{k}'\, \mathrm{d}\boldsymbol{k}''}{(2\pi)^{2d}} \overline{\langle \boldsymbol{k}|\hat{G}^R_\epsilon|\boldsymbol{k}'\rangle\, \langle \boldsymbol{k}''|\hat{G}^A_\epsilon|\boldsymbol{k}\rangle} \phi(\boldsymbol{k}')\phi^*(\boldsymbol{k}'') \\ &= \int \frac{\mathrm{d}\epsilon\, \mathrm{d}\omega}{(2\pi)^2} e^{-i\omega t} \mathcal{I}_{\epsilon,\omega}(\boldsymbol{k}). \end{aligned} \tag{1.66}$$

The last equality defines the density kernel $\mathcal{I}$ in terms of the energy-dependent, retarded and advanced Green's operators and of the initial state $|\phi\rangle$:

$$\mathcal{I}_{\epsilon,\omega}(\boldsymbol{k}) \equiv \int \frac{\mathrm{d}\boldsymbol{k}'}{(2\pi)^d} \frac{\mathrm{d}\boldsymbol{k}''}{(2\pi)^d} \overline{\langle \boldsymbol{k}|\hat{G}^R_{\epsilon+\omega/2}|\boldsymbol{k}'\rangle \langle \boldsymbol{k}''|\hat{G}^A_{\epsilon-\omega/2}|\boldsymbol{k}\rangle} \phi(\boldsymbol{k}')\phi^*(\boldsymbol{k}''), \tag{1.67}$$

with $\epsilon = (\epsilon_1 + \epsilon_2)/2$ and $\omega = \epsilon_1 - \epsilon_2$. In our specific case of an initial plane-wave, we have:

$$\phi(\boldsymbol{k}) = \frac{1}{\sqrt{\mathcal{V}}} \int \mathrm{d}\boldsymbol{r} e^{i(\boldsymbol{k}_0 - \boldsymbol{k}).\boldsymbol{r}} = \frac{(2\pi)^d}{\sqrt{\mathcal{V}}} \delta(\boldsymbol{k}_0 - \boldsymbol{k}). \tag{1.68}$$

$\mathcal{I}$ can be further simplified:

$$\mathcal{I}_{\epsilon,\omega}(\boldsymbol{k}) = \frac{1}{\mathcal{V}} \overline{\langle \boldsymbol{k} | \hat{G}^R_{\epsilon+\omega/2} | \boldsymbol{k}_0 \rangle \, \langle \boldsymbol{k}_0 | \hat{G}^A_{\epsilon-\omega/2} | \boldsymbol{k} \rangle}. \tag{1.69}$$

This kernel will be the central object of our diagrammatic expansion. Physically, it can be seen as the probability density to have particles with energy comprised between $\epsilon \pm \omega/2$ at point $\boldsymbol{k}$ in momentum space, starting from the initial state $|\boldsymbol{k}_0\rangle$. Mathematically, $\mathcal{I}$ is a complicated object a priori. Since it describes an average density, computing it exactly would require to take into account all possible interference between pairs of multiple scattering paths from the initial state k_0 to the final one k.

As mentioned in the introduction of this chapter, however, at weak disorder only two types of paths combinations need to be considered: direct paths where both amplitudes follow the same scattering sequence, and counter-propagating paths, where both paths go through the same sequence, but in reverse order. This leads to the simple decomposition:

$$\mathcal{I} = \mathcal{I}^D + \mathcal{I}^C, \tag{1.70}$$

where $\mathcal{I}^D$ is the contribution of the direct paths, and $\mathcal{I}^C$ the contribution of the counter-propagating paths.

1.6.2 Ladder diagrams

Diagrammatic expansion

To compute $\mathcal{I}^D$, we will once again need to perform a diagrammatic expansion in powers of the disorder. From the definition (1.69), it is obvious that, at the lowest order in disorder, $\mathcal{I}^D$ contains the term:

$$\begin{aligned} \mathcal{I}^{D\,(0)}_{\epsilon,\omega}(\boldsymbol{k}) &= \frac{1}{\mathcal{V}} \overline{\langle \boldsymbol{k} | \hat{G}^R_{\epsilon+\omega/2} | \boldsymbol{k}_0 \rangle} \; \overline{\langle \boldsymbol{k}_0 | \hat{G}^A_{\epsilon-\omega/2} | \boldsymbol{k} \rangle} \\ &= \overline{G}^R_{\epsilon+\omega/2}(\boldsymbol{k}) \, \overline{G}^A_{\epsilon-\omega/2}(\boldsymbol{k}) \times \frac{(2\pi)^2}{\mathcal{V}} \delta(\boldsymbol{k} - \boldsymbol{k}_0), \end{aligned} \tag{1.71}$$

where, in the second line, we have used that the operators $\overline{\hat{G}^{R/A}}$ are diagonal in momentum space. This term describes the ballistic propagation of a particle in an homogeneous effective medium of self-energy Σ (as represented by averages on Green's functions). In other words, it describes the contribution of particles that do not experience any scattering, for which the momentum is conserved as indicated by the Dirac delta-function.

The next contribution describes particles undergoing a single scattering event in the effective medium. This process is decomposed into three steps, where the particle first propagates ballistically towards a given point in configuration space, then is elastically scattered from the momentum state $\boldsymbol{k}_0$ to another $\boldsymbol{k}'$, and finally propagates towards point $\boldsymbol{k}$. To take into account all the possibilities of such a scenario, we integrate over the intermediate momenta $\boldsymbol{k}'$:

$$\begin{aligned}\mathcal{I}^{D\,(1)}_{\epsilon,\omega}(\boldsymbol{k}) &= \left[\int \frac{\mathrm{d}\boldsymbol{k}'}{(2\pi)^d}\mathcal{I}^{D\,(0)}_{\epsilon,\omega}(\boldsymbol{k}')\overline{V(\boldsymbol{k}')V(\boldsymbol{k}')}\right]\overline{G}^R_{\epsilon+\omega/2}(\boldsymbol{k})\,\overline{G}^A_{\epsilon-\omega/2}(\boldsymbol{k})\\ &= \frac{\gamma}{\mathcal{V}}\,\overline{G}^R_{\epsilon+\omega/2}(\boldsymbol{k}_0)\,\overline{G}^A_{\epsilon-\omega/2}(\boldsymbol{k}_0)\overline{G}^R_{\epsilon+\omega/2}(\boldsymbol{k})\,\overline{G}^A_{\epsilon-\omega/2}(\boldsymbol{k}) \qquad (1.72)\end{aligned}$$

where, in the last equality, we used the definition of the spatial correlation function of the disorder (1.48).

The structure of $\mathcal{I}^{D\,(0)}$ and $\mathcal{I}^{D\,(1)}$ suggests that there is a way to systematically write down any term of the expansion, so to be able to perform the infinite sum $\sum_n \mathcal{I}^{(n)}$, similarly to what we did to compute the average Green's function in Sec. 1.5.2. This procedure is usually done diagrammatically. Using our representation convention for the Green's function (Fig. 1.2) and for the correlation function $\mathcal{C}$ (Fig. 1.3), we represent in the first line of Fig. 1.5 the terms (1.71) and (1.72). Thanks to this representation, the next terms of the expansion are deduced easily, by building diagrams with the same structure, but with more impurity lines. This procedure yields the series of so-called "ladder" diagrams [125]. The series of ladder diagrams is generated iteratively as described in the second line of Fig.1.5. The corresponding equation reads:

$$\begin{aligned}\mathcal{I}^{D}_{\epsilon,\omega}(\boldsymbol{k}) \;&=\; \overline{G}^R_{\epsilon+\omega/2}(\boldsymbol{k})\overline{G}^A_{\epsilon-\omega/2}(\boldsymbol{k}) \times \frac{(2\pi)^d}{\mathcal{V}}\delta(\boldsymbol{k}-\boldsymbol{k}_0)\\ &\quad + \gamma\,\overline{G}^R_{\epsilon+\omega/2}(\boldsymbol{k})\overline{G}^A_{\epsilon-\omega/2}(\boldsymbol{k})\int \frac{\mathrm{d}^2\boldsymbol{k}'}{(2\pi)^d}\mathcal{I}^{D}_{\epsilon,\omega}(\boldsymbol{k}'). \qquad (1.73)\end{aligned}$$

This iterative equation is called the Bethe-Salpeter equation for the ladder diagrams [189].

Solving the Bethe-Salpeter equation

We can now solve equation (1.73) for $\mathcal{I}^D$. First, we integrate it over $\boldsymbol{k}$. This yields the following closed equation for the quantity $\mathcal{I}^D_{\epsilon,\omega} \equiv \int \frac{\mathrm{d}\boldsymbol{k}'}{(2\pi)^d}\mathcal{I}^D_{\epsilon,\omega}(\boldsymbol{k})$:

$$\mathcal{I}^D_{\epsilon,\omega} \;=\; \frac{1}{\mathcal{V}}\overline{G}^R_{\epsilon+\omega/2}(\boldsymbol{k}_0)\overline{G}^A_{\epsilon-\omega/2}(\boldsymbol{k}_0) + \gamma\,\mathcal{I}^D_{\epsilon,\omega}\int \frac{\mathrm{d}\boldsymbol{k}}{(2\pi)^d}\,\overline{G}^R_{\epsilon+\omega/2}(\boldsymbol{k})\overline{G}^A_{\epsilon-\omega/2}(\boldsymbol{k}), \qquad (1.74)$$

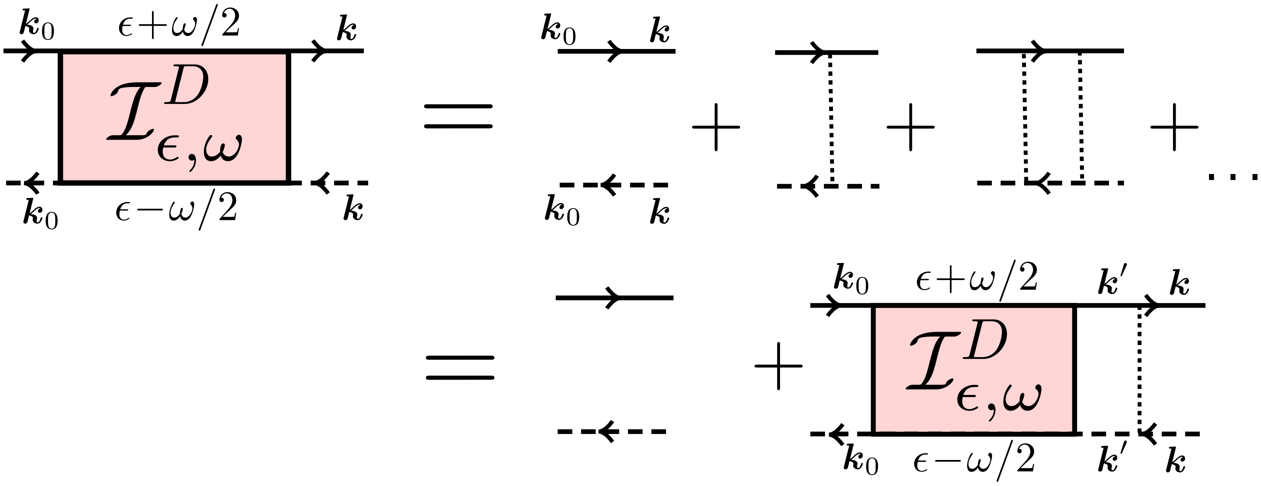

Figure 1.5 – Diagrammatic representation of the Bethe-Salpeter equation for ladder diagrams, Eq. (1.73). Upper solid lines with arrows refer to $\langle \boldsymbol{k}|G^R_{\epsilon+\omega/2}|\boldsymbol{k}_0\rangle$, and lower dashed lines to $\langle \boldsymbol{k}_0|G^A_{\epsilon-\omega/2}|\boldsymbol{k}\rangle$. We recall that for solid (dashed) lines, arrows coincide with the (opposite of the) direction of propagation. Dotted vertical lines symbolize the correlation function of the disorder.

and we obtain :

$$\mathcal{I}^D_{\epsilon,\omega} = \frac{1}{\mathcal{V}} \frac{\overline{G}^R_{\epsilon+\omega/2}(\boldsymbol{k}_0)\overline{G}^A_{\epsilon-\omega/2}(\boldsymbol{k}_0)}{1-\gamma \int \frac{\mathrm{d}\boldsymbol{k}}{(2\pi)^d}\, \overline{G}^R_{\epsilon+\omega/2}(\boldsymbol{k})\overline{G}^A_{\epsilon-\omega/2}(\boldsymbol{k})}. \tag{1.75}$$

The integral in the denominator is easily computed using expression (1.36) and yields [125]

$$\int \frac{\mathrm{d}\boldsymbol{k}}{(2\pi)^d}\, \overline{G}^R_{\epsilon+\omega/2}(\boldsymbol{k})\overline{G}^A_{\epsilon-\omega/2}(\boldsymbol{k}) = \frac{2\pi\tau_\epsilon\nu_\epsilon}{1-i\omega\tau_\epsilon}. \tag{1.76}$$

Inserting (1.76) into (1.75) and using the definition (1.54), we are left with

$$\mathcal{I}^D_{\epsilon,\omega} = \frac{1}{\mathcal{V}}\overline{G}^R_{\epsilon+\omega/2}(\boldsymbol{k}_0)\overline{G}^A_{\epsilon-\omega/2}(\boldsymbol{k}_0)\left(1+\frac{i}{\omega\tau_\epsilon}\right). \tag{1.77}$$

Equation (1.77) can, in turn, be inserted into the Bethe-Salpeter equation (1.73) to obtain:

$$\begin{aligned}\mathcal{I}^D_{\epsilon,\omega}(\boldsymbol{k}) &= \frac{1}{\mathcal{V}}\overline{G}^R_{\epsilon+\omega/2}(\boldsymbol{k})\overline{G}^A_{\epsilon-\omega/2}(\boldsymbol{k}) \\ &\times \left[(2\pi)^2\,\delta(\boldsymbol{k}-\boldsymbol{k}_0) + \gamma\, \overline{G}^R_{\epsilon+\omega/2}(\boldsymbol{k}_0)\overline{G}^A_{\epsilon-\omega/2}(\boldsymbol{k}_0)\left(1+\frac{i}{\omega\tau_\epsilon}\right)\right].\end{aligned} \tag{1.78}$$

Momentum-space distribution: ladder contribution

We can finally compute the ladder contribution to the average momentum distribution $n_{\boldsymbol{k}}^D$. Substituting our result (1.78) into the definition (1.66) yields[5]:

$$n_{\boldsymbol{k}}^D(t) = \frac{(2\pi)^2}{\mathcal{V}} \int \frac{\mathrm{d}\epsilon\,\mathrm{d}\omega}{(2\pi)^2} e^{-i\omega t}\, \overline{G}^R_{\epsilon+\omega/2}(\boldsymbol{k}) \overline{G}^A_{\epsilon-\omega/2}(\boldsymbol{k}) \delta(\boldsymbol{k}-\boldsymbol{k}_0)$$
$$+ \frac{\gamma}{\mathcal{V}} \int \frac{\mathrm{d}\epsilon\,\mathrm{d}\omega}{(2\pi)^2} e^{-i\omega t}\, \overline{G}^R_{\epsilon+\omega/2}(\boldsymbol{k}) \overline{G}^A_{\epsilon-\omega/2}(\boldsymbol{k}) \overline{G}^R_{\epsilon+\omega/2}(\boldsymbol{k}_0) \overline{G}^A_{\epsilon-\omega/2}(\boldsymbol{k}_0) \left(1 + \frac{i}{\omega \tau_\epsilon}\right). \tag{1.79}$$

At long time $t \gg \tau_\epsilon$, the complex exponentials from equation (1.79) will be highly oscillating functions of ω, and the integrals are dominated by the stationary phase $\omega \to 0$: the ω dependence of the arguments of the Green's function can be dropped. We are left with:

$$n_{\boldsymbol{k}}^D(t \gg \tau_\epsilon) = \frac{(2\pi)^2}{\mathcal{V}} \int \frac{\mathrm{d}\epsilon\,\mathrm{d}\omega}{(2\pi)^2} e^{-i\omega t}\, \overline{G}^R_{\epsilon}(\boldsymbol{k}) \overline{G}^A_{\epsilon}(\boldsymbol{k}) \delta(\boldsymbol{k}-\boldsymbol{k}_0)$$
$$+ \frac{i\gamma}{\mathcal{V}} \int \frac{\mathrm{d}\epsilon\,\mathrm{d}\omega}{(2\pi)^2} \frac{e^{-i\omega t}}{\omega \tau_\epsilon}\, \overline{G}^R_{\epsilon}(\boldsymbol{k}) \overline{G}^A_{\epsilon}(\boldsymbol{k}) \overline{G}^R_{\epsilon}(\boldsymbol{k}_0) \overline{G}^A_{\epsilon}(\boldsymbol{k}_0). \tag{1.80}$$

The integration over ω yields $\delta(t)$ for the first term, which can thus be neglected at finite time. In the second term, we get $-i$. The previous expression becomes:

$$n_{\boldsymbol{k}}^D(t \gg \tau) = \frac{\gamma}{\mathcal{V}\tau} \int \frac{\mathrm{d}\epsilon}{2\pi} \overline{G}^R_{\epsilon}(\boldsymbol{k}) \overline{G}^A_{\epsilon}(\boldsymbol{k}) \overline{G}^R_{\epsilon}(\boldsymbol{k}_0) \overline{G}^A_{\epsilon}(\boldsymbol{k}_0). \tag{1.81}$$

Using the simple relation $\overline{G}^R_{\epsilon}(\boldsymbol{k}) \overline{G}^A_{\epsilon}(\boldsymbol{k}) = -2\tau \Im \left[\overline{G}^R_{\epsilon}(\boldsymbol{k})\right]$, and the definition (1.60) of the spectral function, this equation can be recast as:

$$n_{\boldsymbol{k}}^D(t \gg \tau) = \frac{1}{2\pi\mathcal{V}} \int \frac{\mathrm{d}\epsilon}{2\pi} \frac{A_\epsilon(\boldsymbol{k}) A_\epsilon(\boldsymbol{k}_0)}{\nu_\epsilon}, \tag{1.82}$$

where we used that $2\pi\gamma\tau_\epsilon = \nu_\epsilon$, see Eq. (1.54). Equation (1.82) has a rather intuitive structure: the rightmost spectral function is interpreted as the probability density for a plane-wave of wavevector $\boldsymbol{k}_0$ to have energy ϵ in the random potential, while the other one gives the probability density for the wave with energy ϵ to have a momentum $\boldsymbol{k}$. It is clear that after integrating over the "intermediate" energies, the expression leads to the average density at point $\boldsymbol{k}$.

---

[5] The last term of this expression is not well-defined as it is written. In fact here, the notation $\int \frac{\mathrm{d}\omega}{2\pi} \frac{e^{-i\omega t}}{\omega}$ should be understood as $\int \frac{\mathrm{d}\omega}{2\pi} \frac{e^{-i\omega t}}{\omega + i0^+} \equiv \lim_{\eta\to 0} \int \frac{\mathrm{d}\omega}{2\pi} \frac{e^{-i\omega t}}{\omega + i\eta}$, following Feynman's prescription for the causality of quantum propagators.

Lastly, we introduce a quantity that will turn out to have a crucial role in the interacting case, the energy distribution of the gas f_ϵ[6]

$$f_\epsilon = \frac{A_\epsilon(\boldsymbol{k}_0)}{2\pi\nu_\epsilon}, \tag{1.83}$$

which is normalized according to

$$\int \mathrm{d}\epsilon \nu_\epsilon f_\epsilon = 1. \tag{1.84}$$

Equation (1.82) can in turn be rewritten as:

$$n^D_{\boldsymbol{k}}(t \gg \tau) = \frac{1}{2\pi\mathcal{V}} \int \frac{\mathrm{d}\epsilon}{2\pi} A_\epsilon(\boldsymbol{k}) f_\epsilon. \tag{1.85}$$

This equation shows that the diffusive part of the momentum distribution is essentially given by the energy distribution of the Bose gas in the disorder, as already discussed at the end of Sec. 1.5.3. Since multiple scattering is elastic, this energy distribution does not change in time. We will see in the next chapter that this is no longer true in the presence of interactions.

Diffusive ring

Using equation (1.85) and the expression of the spectral function (1.60), we can derive explicitly the shape of the average momentum distribution at long times :

$$n^D_{\boldsymbol{k}}(t \gg \tau) = \frac{1}{2\pi\tau\nu_{\epsilon_0}\mathcal{V}} \, \frac{1}{(\epsilon_{\boldsymbol{k}} - \epsilon_{\boldsymbol{k}_0})^2 + \frac{1}{\tau^2}}. \tag{1.86}$$

Equation (1.86) is an isotropic function of $\boldsymbol{k}$, centered at $|\boldsymbol{k}| = k_0$, which corresponds to the diffusive ring in Fig. 3.4 [169] and in the experimental results of Fig. 1.1. Its maximum is

$$n^D_{|\boldsymbol{k}|=k_0}(t \gg \tau) = n_{max} = \frac{\tau}{\pi\nu_{\epsilon_0}\mathcal{V}}. \tag{1.87}$$

The transverse shape of the ring is a Lorentzian of half-width at half-maximum $2m/(\tau^2 k_0)$, which is essentially the width of the energy distribution f_ϵ. The fact that $n^D_{\boldsymbol{k}}$ has an isotropic shape at long times was of course expected. Indeed, after a few τ, most of the particles have experienced multiple scattering in the disorder, and the memory of the initial condition, i.e. the direction of $\boldsymbol{k}_0$, is lost.

---

[6] Strictly speaking, according to the normalization condition (1.84), the product $\nu_\epsilon f_\epsilon$ is the energy distribution of the gas, while f_ϵ should be called the occupation number. Nevertheless, in this manuscript, we refer to f_ϵ as the energy distribution, because this name carries a more intuitive way of understanding the physics at play.

Full time evolution

Equation (1.86) has been obtained in the regime of long times $t \gg \tau$, where low scattering orders can be neglected. While an exact calculation of the diffusive contributions at any time is a difficult task in general (see, for instance [190] where this problem was addressed for a speckle potential), for the particular model of uncorrelated disorder we have found that the Bethe-Salpeter equation can be exactly solved. After performing the integrals over ϵ and ω, the first term of equation (1.79) simply becomes:

$$\frac{(2\pi)^d}{\mathcal{V}}\theta(t)e^{-t/\tau}\delta(\boldsymbol{k}-\boldsymbol{k}_0), \tag{1.88}$$

which describes the decay of the initial delta peak at $\boldsymbol{k} = \boldsymbol{k}_0$ (i.e. the initial plane-wave in momentum space), as particles get scattered and their momentum is randomized. For the second term, we find the more complicated expression

$$\frac{2\tau\gamma}{\mathcal{V}}\left[\frac{\tau}{1+\Delta_{\epsilon_{\boldsymbol{k}}}^2\tau^2} - \frac{\Delta_{\epsilon_{\boldsymbol{k}}}\tau\cos(\Delta_{\epsilon_{\boldsymbol{k}}}t)+\sin(\Delta_{\epsilon_{\boldsymbol{k}}}t)}{\Delta_{\epsilon_{\boldsymbol{k}}}(1+\Delta_{\epsilon_{\boldsymbol{k}}}^2\tau^2)}e^{-t/\tau}\right], \tag{1.89}$$

with $\Delta_{\epsilon_{\boldsymbol{k}}} = \epsilon_{\boldsymbol{k}} - \epsilon_{\boldsymbol{k}_0}$. One can check that in the limit of long times $t \gg \tau$, $n_{\boldsymbol{k}}(t)$ indeed reduces to (1.86). Inserting Eq. (1.89) in Eq. (1.79), we find that the height of the ring has the following time evolution:

$$n^D_{|\boldsymbol{k}|=k_0}(t) = \frac{(2\pi)^d}{\mathcal{V}}\theta(t)e^{-t/\tau}\delta(\boldsymbol{k}-\boldsymbol{k}_0) + n_{max}\left[1-e^{-t/\tau}\left(1+\frac{t}{\tau}\right)\right]. \tag{1.90}$$

As opposed to the case of a correlated potential [190], visible for instance in the experimental results of Fig. (1.1), where a correlated speckle was used, the ring grows isotropically in time for an uncorrelated potential. This is of course expected because single scattering over a δ-correlated potential is perfectly isotropic, thanks to the infinitely small size of the potential fluctuations.

1.6.3 Crossed diagrams and coherent backscattering

Let us now focus on the contribution of counter-propagating multiple scattering paths to the density kernel, $\mathcal{I}^C$. As we did to compute $\mathcal{I}^D$, we evaluate $\mathcal{I}^C$ by resumming the contribution of each scattering order.

Diagrammatic expansion

The diagrammatic expansion of $\mathcal{I}^C$ is redily obtained from the one of $\mathcal{I}^D$. Indeed, reversing the direction of propagation of one of the amplitudes in a diffusive sequence in principle gives the result. However, one should be careful: the first two diagrams of the expansion for $\mathcal{I}^D$,

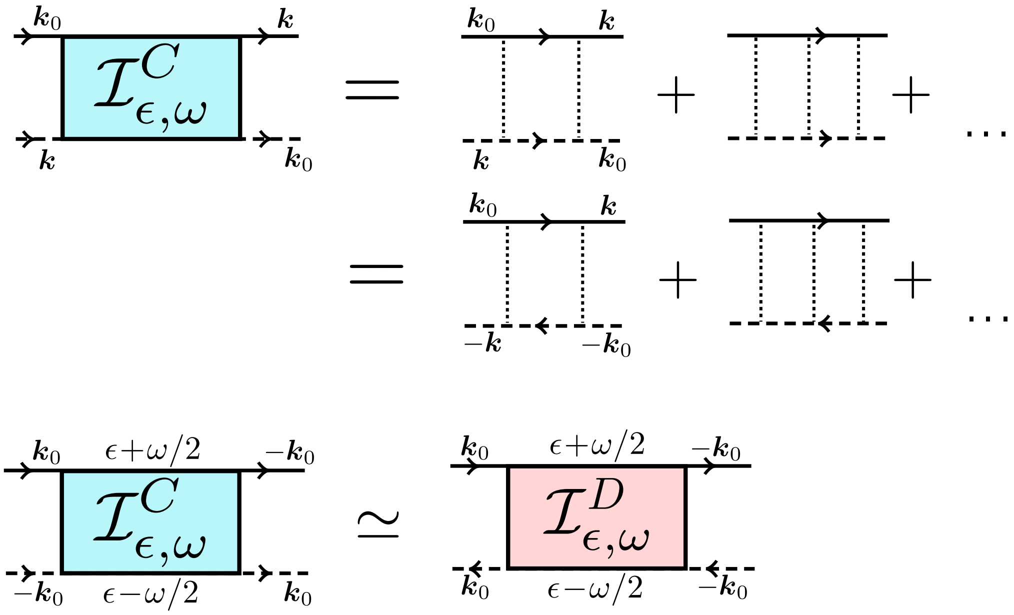

Figure 1.6 – Diagrammatic representation of the Bethe-Salpeter equation for crossed diagrams, Eq. (1.73). These diagrams describe the interference between time-reversed paths, responsible for coherent backscattering. The second equality follows from time-reversal invariance. The last line illustrates the fact that, in the long-time limit $t \gg \tau$ where low scattering orders have a negligible weight, the series of ladder and crossed diagrams coincide.

that we derived explicitly in (1.71) and (1.72), turn out to coincide with their time-reversed counterpart (this can be seen by exchanging the $\boldsymbol{k}$ and $\boldsymbol{k}_0$ arguments for $\overline{G}^A$ for example). We therefore must omit them to avoid 'counting' them twice. With this precaution in mind, reversing one of the arrows on all the higher order diagrams of Fig. 1.5 yields the full 'crossed' series of $\mathcal{I}_C$. The result is depicted diagrammatically in Fig. 1.6. As compared to the case of the ladder diagrams, however, the structure of the density kernel (represented by a blue box in the figures), which has its ingoing and outgoing momenta in a "crossed" configuration, does not allow for a direct resummation of the series, as we did previously to obtain the Bethe-Salpeter equation.

To circumvent this issue, we use that our system is time-reversal invariant, which is justified since no source of decoherence of absorption is present in this model. This property is symbolized by the formal relation:

$$\overline{G}^{R/A}(\boldsymbol{k},t) = \overline{G}^{A/R}(-\boldsymbol{k},t). \tag{1.91}$$

Time-reversal invariance thus allows us to reverse the direction of propagation of one of the amplitudes in the diagrams in the first line of Fig. 1.6, while changing the sign of its ingoing and outgoing momenta. The resulting diagrams are depicted in the second line of the figure.

We then perform the following change of variables: $\{\mathbf{K} = (\boldsymbol{k} - \boldsymbol{k}_0)/2 = -\mathbf{K}';\ \mathbf{Q} = \boldsymbol{k} + \boldsymbol{k}_0\}$. After this procedure, the resulting density kernel, which we will call $\tilde{\mathcal{I}}^C(\boldsymbol{K}, \boldsymbol{K}', \boldsymbol{Q})$, has a form similar to the kernel $\mathcal{I}^D(\boldsymbol{k})$. Assuming that the transfer momentum $\boldsymbol{Q}$ is small compared to $\boldsymbol{K}$ (an hypothesis that will be verified a posteriori), we can rewrite the multiple-scattering series for $\tilde{\mathcal{I}}^C$ under an iterative form to obtain the Bethe-Salpeter equation for the crossed diagrams (see the last line in Fig. 1.6):

$$\begin{aligned} \tilde{\mathcal{I}}^C_{\epsilon,\omega}(\boldsymbol{K}, \boldsymbol{K}', \boldsymbol{Q}) &= \frac{\gamma^2}{\mathcal{V}}\, \overline{G}^R_{\epsilon_+}(\boldsymbol{K}_+)\overline{G}^A_{\epsilon_-}(\boldsymbol{K}_-) \\ &\times\ \overline{G}^R_{\epsilon_+}(\boldsymbol{K}'_+)\overline{G}^A_{\epsilon_-}(\boldsymbol{K}'_-) \int \frac{\mathrm{d}^2\boldsymbol{K}''}{(2\pi)^2} \overline{G}^R_{\epsilon_+}(\boldsymbol{K}''_+)\overline{G}^A_{\epsilon_-}(\boldsymbol{K}''_-) \\ &+ \gamma\ \overline{G}^R_{\epsilon_+}(\boldsymbol{K}'_-)\overline{G}^A_{\epsilon_-}(\boldsymbol{K}'_-) \int \frac{\mathrm{d}^2\boldsymbol{K}''}{(2\pi)^2} \tilde{\mathcal{I}}^C_{\epsilon,\omega}(\boldsymbol{K}, \boldsymbol{K}'', \boldsymbol{Q}), \end{aligned} \tag{1.92}$$

where we introduced $\boldsymbol{K}_\pm \equiv \boldsymbol{K} \pm \boldsymbol{Q}/2$ and $\epsilon_\pm \equiv \epsilon \pm \omega/2$ to lighten the notations. To simplify this expression, we can perform the first integral in the right-hand side, which yields, in the weak disorder limit [125],

$$\int \frac{\mathrm{d}\boldsymbol{K}''}{(2\pi)^d} \overline{G}^R_{\epsilon+\omega/2}(\boldsymbol{K}''+\boldsymbol{Q}/2)\overline{G}^A_{\epsilon-\omega/2}(\boldsymbol{K}''-\boldsymbol{Q}/2) = \frac{2\pi\tau_\epsilon\nu_\epsilon}{1 - i\omega\tau_\epsilon + D_\epsilon \boldsymbol{Q}^2\tau_\epsilon}, \tag{1.93}$$

where $D^{(d)}_\epsilon = k_\epsilon \ell_\epsilon/(md)$ is the diffusion coefficient for a wave at energy ϵ in dimension d. Hence, using the definition $1/\tau = 2\pi\gamma\nu_\epsilon$, we find

$$\begin{aligned} \tilde{\mathcal{I}}^C_{\epsilon,\omega}(\boldsymbol{K}, \boldsymbol{K}', \boldsymbol{Q}) &= \gamma\, \overline{G}^R_{\epsilon_+}(\boldsymbol{K}'_+)\overline{G}^A_{\epsilon_-}(\boldsymbol{K}'_-) \\ &\times \left[\frac{1}{\mathcal{V}} \frac{\overline{G}^R_{\epsilon_+}(\boldsymbol{K}_+)\overline{G}^A_{\epsilon_-}(\boldsymbol{K}_-)}{1 - i\omega\tau_\epsilon + D_\epsilon \boldsymbol{Q}^2\tau_\epsilon} + \int \frac{\mathrm{d}\boldsymbol{K}''}{(2\pi)^d} \tilde{\mathcal{I}}^C_{\epsilon,\omega}(\boldsymbol{K}, \boldsymbol{K}'', \boldsymbol{Q}) \right]. \end{aligned} \tag{1.94}$$

Solving the Bethe-Salpeter equation for crossed diagrams

To solve equation (1.94), we proceed as for the ladder diagrams, the essential difference being the presence of the transfer momentum $\boldsymbol{Q}$. We first integrate over $\boldsymbol{K}'$ and use again Eq. (1.93) to obtain an expression for $\tilde{\mathcal{I}}^C_{\epsilon,\omega}(\boldsymbol{K}, \boldsymbol{Q})$:

$$\begin{aligned} \tilde{\mathcal{I}}^C_{\epsilon,\omega}(\boldsymbol{K}, \boldsymbol{Q}) = \frac{1}{\mathcal{V}} &\overline{G}^R_{\epsilon+\omega/2}(\boldsymbol{K}+\boldsymbol{Q}/2)\overline{G}^A_{\epsilon-\omega/2}(\boldsymbol{K}-\boldsymbol{Q}/2) \\ &\times \left[\frac{1}{(1 - i\omega\tau_\epsilon + D\boldsymbol{Q}^2\tau_\epsilon)(-i\omega\tau_\epsilon + D\boldsymbol{Q}^2\tau_\epsilon)} \right]. \end{aligned} \tag{1.95}$$

Substituting (1.95) into (1.94) yields, for the crossed density kernel:

$$\begin{aligned}\tilde{\mathcal{I}}^{C}_{\epsilon,\omega}(\boldsymbol{K},\boldsymbol{K}',\boldsymbol{Q}) &= \frac{\gamma}{\mathcal{V}}\overline{G}^{R}_{\epsilon_+}(\boldsymbol{K}'_+)\overline{G}^{A}_{\epsilon_-}(\boldsymbol{K}'_-)\overline{G}^{R}_{\epsilon_+}(\boldsymbol{K}_+)\overline{G}^{A}_{\epsilon_-}(\boldsymbol{K}_-) \\ &\quad\times\left[\frac{1}{-i\omega\tau_\epsilon + D_\epsilon \boldsymbol{Q}^2\tau_\epsilon}\right]. \end{aligned} \tag{1.96}$$

Coming back to the original momentum variables, we finally obtain:

$$\tilde{\mathcal{I}}^{C}_{\epsilon,\omega}(\boldsymbol{k}) = \frac{\gamma}{\mathcal{V}}\overline{G}^{R}_{\epsilon_+}(\boldsymbol{k})\overline{G}^{A}_{\epsilon_-}(\boldsymbol{k})\overline{G}^{R}_{\epsilon_+}(\boldsymbol{k}_0)\overline{G}^{A}_{\epsilon_-}(\boldsymbol{k}_0)\left[\frac{1}{-i\omega\tau_\epsilon + D_\epsilon(\boldsymbol{k}+\boldsymbol{k}_0)^2\tau_\epsilon}\right]. \tag{1.97}$$

Except for the term proportional to $(\boldsymbol{k}+\boldsymbol{k}_0)^2$ in the denominator of the right-hand side, we recover exactly the same form as the third term of the ladder density kernel (1.78) (which describes the long time limit). At this stage, we can already infer the well-known result :

$$\mathcal{I}^{C}_{\epsilon,\omega}(-\boldsymbol{k}_0) = \mathcal{I}^{D}_{\epsilon,\omega}(-\boldsymbol{k}_0) \tag{1.98}$$

at long times ($\omega\tau \ll 1$). This indicates that, as a consequence of the interference between time-reversed paths, the magnitude of the momentum distribution is exactly doubled at backscattering.

Momentum space distribution: Crossed contribution

We finally compute the ladder contribution to the average momentum distribution $n^{C}_{\boldsymbol{k}}$. At long time, it only differs from the diffusive contribution by the denominator factor $D_\epsilon(\boldsymbol{k}+\boldsymbol{k}_0)^2\tau_\epsilon$:

$$\begin{aligned} n^{C}_{\boldsymbol{k}}(t) = \frac{\gamma}{\mathcal{V}}\int\frac{\mathrm{d}\epsilon\,\mathrm{d}\omega}{(2\pi)^2}e^{-i\omega t}\,&\overline{G}^{R}_{\epsilon+\omega/2}(\boldsymbol{k})\overline{G}^{A}_{\epsilon-\omega/2}(\boldsymbol{k}) \\ \times\ &\overline{G}^{R}_{\epsilon+\omega/2}(\boldsymbol{k}_0)\overline{G}^{A}_{\epsilon-\omega/2}(\boldsymbol{k}_0)\left[\frac{1}{-i\omega\tau_\epsilon + D_\epsilon(\boldsymbol{k}+\boldsymbol{k}_0)^2\tau_\epsilon}\right]. \end{aligned} \tag{1.99}$$

At long times $t \gg \tau_\epsilon$, we can again omit the ω dependence of the Green's functions to obtain, after performing the Fourier transform over ω

$$n^{C}_{\boldsymbol{k}}(t\gg\tau) = \frac{1}{(2\pi)^2\mathcal{V}}\int\mathrm{d}\epsilon A_\epsilon(\boldsymbol{k})f_\epsilon\,e^{-D_\epsilon(\boldsymbol{k}+\boldsymbol{k}_0)^2 t} = n^{D}_{\boldsymbol{k}}(t\gg\tau)e^{-D_\epsilon(\boldsymbol{k}+\boldsymbol{k}_0)^2 t}. \tag{1.100}$$

We see that the crossed contribution consists of a peak of height n_{max} centered at the exact backscattering direction $-\boldsymbol{k}_0$, and whose half-width at half-maximum evolves in time as $1/\sqrt{Dt}$, as experimentally measured in [21]. This peak is called the Coherent Backscattering (CBS) effect, and features a doubling of the probability for the atoms to be backcattered as compared to the classical diffusive picture. It constitutes a direct manifestation of weak localization in the momentum distribution of a non-interacting Bose gas subjected to a disorder potential.

Full time evolution

While Eq. (1.100) holds for long time only, the full time evolution of the CBS peak maximum for a δ-correlated potential can also be derived by performing the integral in (1.99) at $\boldsymbol{k} = -\boldsymbol{k}_0$, without taking the $\omega \to 0$ limit. The exact result is :

$$n^C_{\boldsymbol{k}}(t) = n_{max}\left[1 - e^{-t/\tau}\left(1 + \frac{t}{\tau} + \frac{t^2}{2\tau^2}\right)\right]. \tag{1.101}$$

Note that, as expected, the CBS and diffusive amplitudes coincide at long time, but not at short time $t \sim \tau$ where low scattering orders – described by the terms within square brackets – come into play. The short-time behavior of the CBS peak height has an extra term, compared to Eq. (1.90), which is due to the absence of the low scattering order in the series of crossed diagrams. Both contribution have a different short-time behavior which should be visible in numerical simulations.

Conclusion

In this chapter, we have introduced the basic concepts and equations which will be used in the next chapters. We have constructed a microscopic diagrammatic theory describing the temporal evolution of a non-interacting (single particle) gas in the presence of a weak disorder. We have shown how to compute basic quantities such as the density of states, the spectral function, the scattering mean free time and mean free path from the statistical properties of the disorder, in the weak disorder regime where the Born approximation is valid. We have studied how the momentum distribution of a gas initially launched with a finite velocity evolves with time. In the long-time limit, the momentum distribution tends to a stationary non-thermal isotropic distribution. In addition, a peak develops around the exact backscattering direction, whose intensity is equal to the background, and whose width decreases like $1/\sqrt{t}$.

Chapter 2

Kinetic theory for non-equilibrium, weakly localized bosons

Introduction

In the previous chapter, we have described the temporal evolution of a non-interacting Bose gas in a spatially disordered potential. Following this scenario, from now on we include the ingredient of particle interactions, focusing on the case of a dilute Bose gas. Precisely, we consider the out-of-equilibrium dynamics of a Bose gas following a simultaneous "quantum quench" of both a disorder potential and interactions. In contrast with the rather simple non-interacting dynamics exposed in chapter 1, in the presence of interactions the system experiences a more or less fast thermalization process that eventually drives it to an ergodic equilibrium state. This problem falls in line with a recent, intense research activity in the field of non-equilibrium quantum gases [74, 89, 99, 191–193]. In this context, a phenomenon that has attracted considerable attention is many-body localization. Originally, many-body localization was identified as a finite temperature phase transition between a conducting, thermal phase, and a "many-body localized" insulating phase for interacting electrons in a disordered metal [110, 111]. Later on, the concept of many-body localization has been identified as a seemingly very fundamental phenomenon of ergodicity breaking, through which an isolated, many-body disordered system cannot thermalize to a conventional Gibbs ensemble due to the disorder [106–109]. Many-body localization has, since then, been observed in various experiments [113–116], but still raises a number of open questions [109]. Our ambition, in this chapter and the subsequent ones, will be rather to focus on the limit of *weak* interactions and disorder, where the system remains essentially ergodic but, nevertheless, a nontrivial interplay between weak localization and interactions occurs. For this purpose, we will come back to the theoretical description of the momentum distribution presented in the previous chapter, but we will now include interactions within the diagrammatic transport theory. This chapter will present the core of the theory, and, as such, is rather technical.

Specifically, here we construct the weak localization diagrammatic theory in the presence of interactions. This will lead us to generalized Bethe-Salpether equations for both diffusive and weakly localized modes, from which we will derive simple kinetic equations for the diffusive ring and the coherent backscattering (CBS) peak introduced in the previous chapter. The practical consequences of these equations and the comparison with ab initio numerical simulations based on the Gross-Pitaevskii equation (GPE) will be addressed in the next chapter.

2.0.1 Weak localization and interactions in electronic systems

Before addressing the non-equilibrium bosonic problem, it is useful to first recall some known elements about the question of weak localization in interacting systems. Historically, this problem was first considered in the context of weakly disordered conductors, where the impact of the Coulomb interaction between electrons on the conductivity is twofold:

- Due to interactions, electrons are not only sensitive to the disorder potential, but also to the fluctuations of the electronic density. In the multiple scattering regime, the diffusive electronic motion induced by the disorder tends to reinforce the effects of interactions compared to the ballistic regime. This leads to a reduction of the conductivity, which turns out to be of the order of the weak localization correction [194, 195]. This effect, called the Altshuler-Aronov correction [196–198], is a purely incoherent effect. It can be distinguished from the weak localization correction by applying a magnetic field that destroys the latter in a controlled fashion [199, 200].
- In a metal, the Coulomb interaction between two conduction electrons is efficiently screened by the presence of the other electrons. This allows for a description of conduction electrons as independent quasi-particles with a finite lifetime ('Fermi liquid'). This finite lifetime is closely related the time τ_ϕ during which the particles maintain their phase coherence. As a consequence, the counter-propagating multiple scattering sequences of length larger than $L_\phi = v_F \tau_\phi$ (with v_F the velocity at the Fermi level) will not interfere, and the weak localization correction is reduced compared to the non-interacting case. This equivalence between the quasi-particle lifetime and the phase coherence time has also been proven experimentally, for example in 1d, where the temperature dependence of τ_ϕ has been measured in metals with few magnetic impurities [201, 202]. As we will see in this chapter, a similar effect occurs for CBS of nonequilibrium bosons.

2.0.2 Interactions and coherent backscattering

In the context of coherent backscattering, the first seminal works addressing the role of "interactions" appeared in the context of nonlinear optics, precisely in disordered media displaying a Kerr nonlinearity (i.e., a refractive index depending on the wave intensity) [203–205], or in atomic vapors where the nonlinear behavior stems from the internal atomic structure [205–208]. Later on, this problem was extended to the propagation of atom lasers through disordered junctions, a configuration described by a stationary Gross-Pitaevskii equation fully similar to the nonlinear wave equation in optics [205, 209–212]. In all these works, it was shown that interactions have dramatic effects of the CBS: For strong enough repulsive interactions for instance, they lead to an inversion of the CBS peak. This inversion was also recently shown to be robust in the many-body regime [213]. The impact of interactions on the *out-of-equilibrium* dynamics of weakly disordered Bose gases, on the other hand, has been addressed more recently. In [169, 214, 215] for instance, the temporal spreading of wave-packets was described by a generalized diffusion equation self-consistently renormalized by the mean-field nonlinear potential of the Gross-Pitaevskii equation. Later on, this approach was complemented by a kinetic description of inelastic particle collisions [172, 216]. In all these works, however, all weak localization effects were neglected, the dynamics being assumed purely diffusive in the absence of interactions. It is precisely the goal of the present chapter to fill this gap. To this end, we will consider the same physical configuration as in the previous chapter, namely the temporal evolution of a disordered Bose gas initially prepared as a plane-wave state in momentum space, with the addition of an interaction quench at $t = 0$. To keep the things simple and to connect with the non-interacting regime, we will restrict ourselves to a dilute Bose gas and thus construct our interacting quantum transport theory starting from the disordered Gross-Pitaevskii equation.

2.1 Mean-field description of Bose gases in disorder

In this section, we give an elementary derivation of the Gross-Pitaevskii equation that governs the evolution of a dilute Bose gas in a disorder potential. This equation describes atom-atom interactions by means of a classical, mean-field approximation.

2.1.1 Many-body Hamiltonian

We consider a quantum gas of N identical bosons of mass m, evolving from $t = 0$ onward under the simultaneous presence of interactions and an external (trapping, disorder...) potential V. Interactions can be modeled by a two-body Van der Waals interaction potential U, and the dynamics of the gas is encoded in the many-body Hamiltonian

$$\mathcal{H} = \int \mathrm{d}\boldsymbol{r}\hat{\psi}^\dagger(\boldsymbol{r},t)\left[-\frac{\hbar^2\Delta}{2m}+V(\boldsymbol{r})\right]\hat{\psi}(\boldsymbol{r},t)+\frac{1}{2}\int \mathrm{d}\boldsymbol{r}\mathrm{d}\boldsymbol{r}'\,\hat{\psi}^\dagger(\boldsymbol{r},t)\hat{\psi}^\dagger(\boldsymbol{r}',t)U(\boldsymbol{r}-\boldsymbol{r}')\hat{\psi}(\boldsymbol{r},t)\hat{\psi}(\boldsymbol{r}',t), \tag{2.1}$$

written in second quantization. The bosonic field operator $\hat{\psi}$ satisfies the commutation relations

$$\begin{aligned}\left[\hat{\psi}(\boldsymbol{r},t)\hat{\psi}^\dagger(\boldsymbol{r}',t)\right] &= \delta(\boldsymbol{r}-\boldsymbol{r}'),\\ \left[\hat{\psi}(\boldsymbol{r},t)\hat{\psi}(\boldsymbol{r}',t)\right] &= \left[\hat{\psi}^\dagger(\boldsymbol{r},t)\hat{\psi}^\dagger(\boldsymbol{r}',t)\right] = 0.\end{aligned} \tag{2.2}$$

2.1.2 Effective two-body interactions in a dilute ultracold gas

At low enough temperature, the physics of the system is dominated by low energies. In this regime, the interaction between atoms can be described in terms of *s-wave* scattering processes, whose properties are encoded in a single characteristic length, the s-wave scattering length a [217]. Provided that the typical density ρ_0 of the gas is low enough, the average inter-atomic distance is much larger than the s-wave scattering length $|a| \ll \rho_0^{-1/d}$, and the precise structure of the interaction potential is not resolved. Thus, it can be replaced by any scattering potential that yields the same scattering length a. The simplest choice is to take the contact pseudo-potential [218]

$$U(\boldsymbol{r}) = g\delta(\boldsymbol{r}), \tag{2.3}$$

where g is a dimension-dependent function of the scattering length a, which measures the strength of the effective interaction. Substituting (2.3) into (2.1) yields

$$\mathcal{H} = \int \mathrm{d}\boldsymbol{r}\, \hat{\psi}^\dagger(\boldsymbol{r},t)\left[-\frac{\hbar^2\Delta}{2m}+V(\boldsymbol{r})\right]\hat{\psi}(\boldsymbol{r},t) + \frac{g}{2}\int \mathrm{d}\boldsymbol{r}\, \hat{\psi}^\dagger(\boldsymbol{r},t)\hat{\psi}^\dagger(\boldsymbol{r},t)\hat{\psi}(\boldsymbol{r},t)\hat{\psi}(\boldsymbol{r},t). \tag{2.4}$$

In the Heisenberg picture, the time-evolution of the field operator is given by

$$i\hbar\partial_t\hat{\psi}(\boldsymbol{r},t) = \left[\hat{\psi}(\boldsymbol{r},t),\mathcal{H}\right] \tag{2.5}$$

which yields, using the bosonic commutation relations (2.2),

$$i\hbar\partial_t\hat{\psi}(\boldsymbol{r},t) = \left[-\frac{\hbar^2\Delta}{2m}+V(\boldsymbol{r})+g\hat{\psi}^\dagger(\boldsymbol{r},t)\hat{\psi}(\boldsymbol{r},t)\right]\hat{\psi}(\boldsymbol{r},t). \tag{2.6}$$

2.1.3 Bogoliubov approximation

Let us now assume that the Bose gas is initially prepared in a 3d trapping potential, so that it typically forms a Bose-Einstein condensate (BEC) at low temperature. The ground state (or condensate mode) is much more populated than the excited modes. This justifies a decomposition of the field operator as

$$\hat{\psi}(\boldsymbol{r},t) = \phi_0(\boldsymbol{r},t)\hat{a}_0 + \delta\hat{\psi}(\boldsymbol{r},t), \tag{2.7}$$

where $\hat{a}_0$ and ϕ_0 are, respectively, the annihilation operator and the wavefunction of the condensate mode. At low temperature, the contribution of non-condensed modes $\delta\hat{\psi}(\boldsymbol{r},t)$ is typically a small perturbation of the total field operator and can be neglected. We are left with the approximate expression $\phi_0(\boldsymbol{r},t)\hat{a}_0$ for the field operator. The condensate mode being macroscopically populated, i.e, $n_0 = \hat{a}_0^\dagger\hat{a}_0 \simeq N$ with N very large, we can follow Bogoliubov's prescription [219, 220] and replace the annihilation operator $\hat{a}_0$ by the corresponding c-number $\sqrt{N}$. The field operator is now proportional to the classical field ϕ_0, which means that we adopt a classical description of the collective motion of the atoms in the condensate, neglecting the influence of the thermal cloud formed by excited atoms. For consistency with the normalization to unity of the density in subsequent chapters, we will call $\psi(\boldsymbol{r},t) \equiv \phi_0(\boldsymbol{r},t)$ the wavefunction of the condensate, such that

$$\hat{\psi}(\boldsymbol{r},t) \simeq \sqrt{N}\psi(\boldsymbol{r},t), \tag{2.8}$$

and

$$\int \mathrm{d}\boldsymbol{r}|\psi(\boldsymbol{r},t)|^2 = 1. \tag{2.9}$$

Substituting this equation into (2.6) yields the Gross-Pitaevskii equation for the time-evolution of ψ:

$$i\hbar\partial_t\psi(\boldsymbol{r},t) = \left[-\frac{\hbar^2\Delta^2}{2m} + V(\boldsymbol{r}) + gN|\psi(\boldsymbol{r},t)|^2\right]\psi(\boldsymbol{r},t). \tag{2.10}$$

This equation corresponds to a mean-field description of the Bose-Einstein condensate, in the sense that we have reduced the many-body problem to a one-body problem, where the nonlinear term $gN|\psi(\boldsymbol{r},t)|^2$ represents the effective potential felt by a particle at point $\boldsymbol{r}$ as the result of its interaction with all the other particles. Note that by setting the normalization of the density (2.9) – which imposes particle conservation – to unity, we technically describe the evolution of a single particle with a nonlinearity of strength $g \times N$, rather than N particles interacting with interaction strength g. However, it follows from the structure of the Gross-Pitaevskii equation that these two problems are strictly equivalent.

In this section, we have given a somewhat simplistic derivation of the Gross-Piteavskii equation. It can be derived more rigorously [221], and has proven to be a very successful tool for the interpretation of experimental results involving weakly interacting bosons [219]. Despite being a very simplified version of the many-body problem, it is still difficult to obtain analytical results within this mean-field approximation, in particular in an out-of-equilibrium context. In this chapter, we nevertheless manage to exploit it to construct an effective quantum transport theory for a simple statistical observable (the average momentum distribution) in the weak-disorder regime. Numerical implementations of the Gross-Pitaevskii equation are, on the other hand, relatively easy, and may offer valuable insight. In our 2d geometry, quasi-exact[1] simulations can be performed up to a relatively long times at a reasonable cost. Their implementation is described in section 3.1.4.

2.2 Short-time Momentum space dynamics

In this section, we construct the nonlinear version of the quantum transport theory of chapter 1. We recall that we are interested in the out-of-equilibrium dynamics of a 2d Bose gas expanding in a disorder potential, initially prepared in a plane wave state $|\boldsymbol{k}_0\rangle$, in the presence of weak interactions encoded in the nonlinear term of Eq. (2.10). Generally speaking, in this chapter we consider a regime where the interactions are small enough so that their effect slowly builds upon the diffusive description of multiple scattering. For simplicity, in the following we consider a Gaussian, uncorrelated disorder potential V satisfying

$$\overline{V(\boldsymbol{r})} = 0 \quad \text{and} \quad \overline{V(\boldsymbol{r})V(\boldsymbol{r}')} = \gamma\delta(\boldsymbol{r}-\boldsymbol{r}'). \tag{2.11}$$

In the rest of this chapter, we again set $\hbar = 1$ to lighten the notations.

2.2.1 Average momentum distribution

The plane wave state $\phi(\boldsymbol{r}) = e^{i\boldsymbol{k}_0\cdot\boldsymbol{r}}/\sqrt{\mathcal{V}} = \langle\boldsymbol{r}|\boldsymbol{k}_0\rangle$ being a stationary state of the Gross-Pitaevskii equation (2.10), the gas will display, on average, a uniform spatial density at all times. On the contrary, as seen in the previous chapter, the momentum distribution $n_{\boldsymbol{k}}$ exhibits a non-trivial time evolution. In chapter 1, see Eq. (1.66), we have shown that it could be expressed in terms of an average density kernel $\mathcal{I}_{\epsilon,\omega}$:

$$n_{\mathbf{k}}(t) = \overline{|\psi(\boldsymbol{k},t)|^2} = \int \frac{\mathrm{d}\epsilon\,\mathrm{d}\omega}{(2\pi)^2} e^{-i\omega t}\mathcal{I}_{\epsilon,\omega}(\boldsymbol{k}), \tag{2.12}$$

with, in the absence of interactions, the definition

$$\mathcal{I}_{\epsilon,\omega}(\boldsymbol{k}) = \overline{\langle\boldsymbol{k}|\hat{G}^R_{\epsilon+\omega/2}|\boldsymbol{k}_0\rangle\,\langle\boldsymbol{k}_0|\hat{G}^A_{\epsilon-\omega/2}|\boldsymbol{k}\rangle}. \tag{2.13}$$

Due to our choice for the condensate wavefunction (2.8), the number of particles N appears explicitly in the Gross-Pitaevskii equation (2.10), and the momentum distribution is normalized to unity:

$$\int \frac{\mathrm{d}^2\boldsymbol{k}}{(2\pi)^2} n_{\boldsymbol{k}}(t) = 1, \tag{2.14}$$

---

[1] In the sense that they are limited only by the available computer resources.

which imposes the conservation of the number of particles. We also recall some results of chapter 1 that will be useful for our computations. In the absence of interactions, the density kernel at weak disorder can be split into an incoherent (diffusive) and a coherent (CBS) contribution:

$$\mathcal{I}_{\epsilon,\omega}(\boldsymbol{k}) = \mathcal{I}^D_{\epsilon,\omega}(\boldsymbol{k}) + \mathcal{I}^C_{\epsilon,\omega}(\boldsymbol{k}), \tag{2.15}$$

with

$$\begin{aligned}\mathcal{I}^D_{\epsilon,\omega}(\boldsymbol{k}) &= \overline{G}^R_{\epsilon+\omega/2}(\boldsymbol{k})\overline{G}^A_{\epsilon-\omega/2}(\boldsymbol{k}) \\ &\times \left[(2\pi)^2\,\delta(\boldsymbol{k}-\boldsymbol{k}_0) + \gamma\,\overline{G}^R_{\epsilon+\omega/2}(\boldsymbol{k}_0)\overline{G}^A_{\epsilon-\omega/2}(\boldsymbol{k}_0)\left(1+\frac{i}{\omega\tau_\epsilon + i0^+}\right)\right]\end{aligned} \tag{2.16}$$

and

$$\mathcal{I}^C_{\epsilon,\omega}(\boldsymbol{k}) = \gamma\,\overline{G}^R_{\epsilon_+}(\boldsymbol{k})\overline{G}^A_{\epsilon_-}(\boldsymbol{k})\overline{G}^R_{\epsilon_+}(\boldsymbol{k}_0)\overline{G}^A_{\epsilon_-}(\boldsymbol{k}_0)\left[\frac{1}{-i\omega\tau_\epsilon + D_\epsilon(\boldsymbol{k}+\boldsymbol{k}_0)^2\tau_\epsilon}\right]. \tag{2.17}$$

The average Green function is given by Eq. (1.36) of the previous chapter, $\tau_\epsilon = (2\pi\gamma\nu_\epsilon)^{-1}$ is the mean free time and $D_\epsilon = \epsilon\tau/m$ is the diffusion coefficient. The energy dispersion of the particles being small for elastic scattering and at weak disorder, we can perform the on-shell approximation and replace the energy dependent quantities τ_ϵ, D_ϵ as well as the mean free path $\ell_\epsilon = k\tau_\epsilon$ by their value at the initial energy $\epsilon_0 = k_0^2/2m$. We thus omit the energy subscript for these quantities in the following.

2.2.2 Weak interactions

While developing an exact quantum transport theory accounting for both interactions and disorder is a formidable task, even at the level of the Gross-Pitaevskii equation (2.10), relatively simple results can be obtained when interactions are "weak" compared with the disorder. To quantify this limit, we first note that the interaction term in the disordered Gross-Pitaevskii equation can be seen as an additional, but nonlinear, random potential (see Fig.2.1), which causes the atoms to be scattered on the spatial density fluctuations. The main idea of this chapter is to treat this potential as a perturbation of the ladder and crossed scattering series. Physically, this amounts to assuming that scattering events on the nonlinear potential are rare compared to scattering events on the random potential. In terms of time scales, this condition reads $\tau_{\mathrm{NL}} \gg \tau$, where τ_{NL} is the particle interaction time. To estimate this quantity, we use the Fermi golden rule

$$\frac{1}{2\tau_{\mathrm{NL}}} = \pi\int\frac{\mathrm{d}^2\boldsymbol{k}'}{(2\pi)^2}\delta(\epsilon-\epsilon_{\boldsymbol{k}'})\tilde{\mathcal{C}}_{\mathrm{NL}}(\boldsymbol{k}-\boldsymbol{k}'), \tag{2.18}$$

where we introduced the power spectrum of the nonlinear potential,

$$\tilde{\mathcal{C}}_{\mathrm{NL}}(\boldsymbol{k}) \equiv \int d^2(\boldsymbol{r}-\boldsymbol{r}')(gN)^2\overline{|\psi(\boldsymbol{r},t)|^2|\psi(\boldsymbol{r}',t)|^2}e^{i\boldsymbol{k}(\boldsymbol{r}-\boldsymbol{r}')}. \tag{2.19}$$

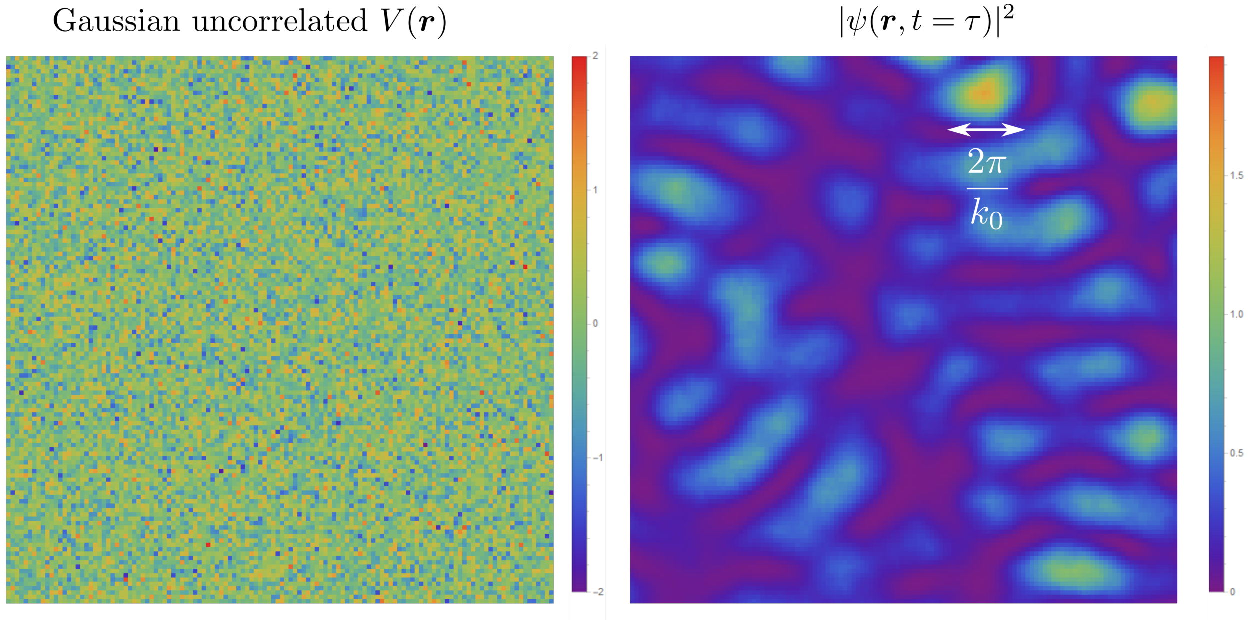

Figure 2.1 – Left: Visual example of a single realization of a numerical Gaussian uncorrelated disorder potential. Within the discretized space needed to perform numerical simulations (see chapter 3), the disorder displays no characteristic length scale. Right: Density of the gas, after letting the initial plane wave evolve in the uncorrelated potential during a mean free time time τ. The density forms a speckle potential, correlated over the De Broglie wavelength $\lambda_{\text{DB}} = 2\pi/k_0$, in accordance with Eq. (2.20). Parameters are chosen such that we are in the weak disorder limit $k_0\ell \gg 1$, and $g\rho_0$ is small enough so that interaction events are very rare compared to disorder scattering. We also observe that $V(\boldsymbol{r})$ and $|\psi(\boldsymbol{r}, t)|^2$ do not appear to be correlated with one another, in agreement with the result (2.44).

To leading approximation, the density-density correlator is not modified by interactions, and reads [125]

$$\overline{|\psi(\boldsymbol{r},t)|^2|\psi(\boldsymbol{r}',t)|^2} = \frac{1}{\mathcal{V}^2}\left[1 + J_0(k_0|\boldsymbol{r}-\boldsymbol{r}'|)e^{-|\boldsymbol{r}-\boldsymbol{r}'|/\ell}\right], \tag{2.20}$$

so that we define

$$\tau_{\mathrm{NL}} = \frac{\epsilon_0}{(g\rho_0)^2}. \tag{2.21}$$

By defining the mean free path for particle collisions as $\ell_{\mathrm{NL}} \equiv k_0\tau_{\mathrm{NL}}/m$, we then rewrite the criterion of rare particle collisions and weak disorder as

$$k_0\ell_{\mathrm{NL}} \gg k_0\ell \gg 1. \tag{2.22}$$

In the following, we will assume these conditions to be fulfilled. In this limit, the effect of interactions on the ladder and crossed diagrammatic series can be estimated perturbatively[2] by interrupting the multiple scattering sequences – generated by the iterating the Bethe-Salpeter equation – with interaction events. More precisely, the Bethe-Salpeter equation is modified by adding irreducible, elementary diagrams representing the possible interaction processes, at sufficiently low order in the interaction strength $g\rho_0$ to fullfill condition (2.22). A similar approach was previously used in [204, 205, 209, 210] to describe the stationary coherent backscattering effect of continuous waves in finite media, and in [169, 214, 215] to model the dynamics of interacting wave packets in the diffusive limit. The latter configuration was later extended for wave packets in the localization regime [119, 120], but by taking into account first-order corrections in g only, see Sec. 2.3.1, while neglecting second-order corrections responsible for thermalization. In the present scenario, we will see that the former are negligible while the latter control the evolution of the gas.

2.2.3 Born series

When $g \neq 0$, the notion of Green's function can strictly speaking no longer be utilized to express the intensity kernel, as we did in Eq. (2.13). Nevertheless, the definition (2.12) of $n_{\boldsymbol{k}}$ can still be written, by redefining the intensity kernel in terms of the wavefunction ψ:

$$\mathcal{I}_{\epsilon,\omega}(\boldsymbol{k}) \equiv \overline{\psi_{\epsilon+\omega/2}(\boldsymbol{k})\psi^*_{\epsilon-\omega/2}(\boldsymbol{k})}, \tag{2.23}$$

where

$$\psi_\epsilon(\boldsymbol{k}) \equiv \int \mathrm{d}^2\boldsymbol{r}\int_{-\infty}^{\infty}\mathrm{d}t\; e^{i\epsilon t}e^{-i\boldsymbol{k}\cdot\boldsymbol{r}}\psi(\boldsymbol{r},t). \tag{2.24}$$

---

[2] Our theory will be perturbative in the sense that elementary scattering and interaction processes of higher order in $k_0\ell$ and $g\rho_0$ are systematically neglected. However, at fixed order in these parameters, we take into account an arbitrary large number of sequences of such processes, in a non-perturbative way.

As a consequence, in the presence of interactions, the diagrammatic quantum transport theory is constructed from the Lippmann-Schwinger equation associated with the Gross-Pitaevskii equation (2.10):

$$\begin{aligned}\psi_\epsilon(\boldsymbol{k}) = \phi(\boldsymbol{k}) + G_0(\epsilon,\boldsymbol{k})\Bigg[\int \frac{\mathrm{d}^2\boldsymbol{k}'}{(2\pi)^2} V(\boldsymbol{k}')\psi_\epsilon(\boldsymbol{k}-\boldsymbol{k}') \\ +g\int\frac{d\epsilon_1}{2\pi}\frac{d\epsilon_2}{2\pi}\int\frac{\mathrm{d}^2\boldsymbol{k}_1}{(2\pi)^2}\frac{\mathrm{d}^2\boldsymbol{k}_2}{(2\pi)^2}\psi_{\epsilon_1}(\boldsymbol{k}_1)\psi^*_{\epsilon_2}(\boldsymbol{k}_2)\psi_{\epsilon-\epsilon_1+\epsilon_2}(\boldsymbol{k}-\boldsymbol{k}_1+\boldsymbol{k}_2)\Bigg],\end{aligned} \tag{2.25}$$

where $G_0(\epsilon,\boldsymbol{k}) = (\epsilon - \boldsymbol{k}^2/2m + i0^+)^{-1}$ is the free-space retarded Green's function (well-defined from Eq. (2.10) with $g=0$). Iteration of Eq. (2.25) leads to an expansion of ψ_ϵ in powers of V and g known as the Born series. In addition to the usual scattering processes on the random potential, this Born series also involves particle interactions, which can be thought of as scattering events on the nonlinear potential, as mentioned above. These two elementary processes are diagrammatically shown in Fig. 2.2, together with the conservation rules for energies and momenta. From the Born series for ψ_ϵ, one can construct a Bethe-Salpeter equation for the density kernel $\mathcal{I}_{\epsilon,\omega}(\boldsymbol{k})$. Indeed, by multiplying Eq. (2.25) – taken at energy $\epsilon+\omega/2$ – by $\psi^*_{\epsilon-\omega/2}$ and taking the disorder average, we arrive at:

$$\begin{aligned}\mathcal{I}_{\epsilon,\omega}(\boldsymbol{k}) = \phi(\boldsymbol{k})\psi^*_{\epsilon-\omega/2}(\boldsymbol{k}) + G_0^R(\epsilon+\omega/2,\boldsymbol{k})\Bigg[\int\frac{\mathrm{d}^2\boldsymbol{k}'}{(2\pi)^2}\overline{V(\boldsymbol{k}')\psi_{\epsilon+\omega/2}(\boldsymbol{k}-\boldsymbol{k}')\psi^*_{\epsilon-\omega/2}(\boldsymbol{k})} \\ +gN\int\frac{d\epsilon_1}{2\pi}\frac{d\epsilon_2}{2\pi}\int\frac{\mathrm{d}^2\boldsymbol{k}_1}{(2\pi)^2}\frac{\mathrm{d}^2\boldsymbol{k}_2}{(2\pi)^2}\overline{\psi_{\epsilon_1}(\boldsymbol{k}_1)\psi^*_{\epsilon_2}(\boldsymbol{k}_2)\psi_{\epsilon_3+\omega/2}(\boldsymbol{k}-\boldsymbol{k}_1+\boldsymbol{k}_2)\psi^*_{\epsilon-\omega/2}(\boldsymbol{k})}\Bigg],\end{aligned} \tag{2.26}$$

where we denoted $\epsilon_3 = \epsilon - \epsilon_1 + \epsilon_2$. We can then evaluate the disorder averages from this expression diagrammatically, by writing down all possible arrangements of amplitudes $\psi_\epsilon(\boldsymbol{k})$ and intensities $\mathcal{I}_{\epsilon,\omega}(\boldsymbol{k})$ that obey the rules of Fig. 2.2. In the next section, we will use this procedure to derive a Bethe-Salpeter equation for $\mathcal{I}_{\epsilon,\omega}(\boldsymbol{k})$ in the weakly interacting limit. In the regime where particle collisions are less frequent than collisions on the random potential – remember condition (2.22) – a splitting of $\mathcal{I}_{\epsilon,\omega}$ into a ladder $\mathcal{I}^D_{\epsilon,\omega}$ and a crossed contribution $\mathcal{I}^C_{\epsilon,\omega}$, can still be identified. The next two sections will be devoted to a derivation of kinetic equations for these components.

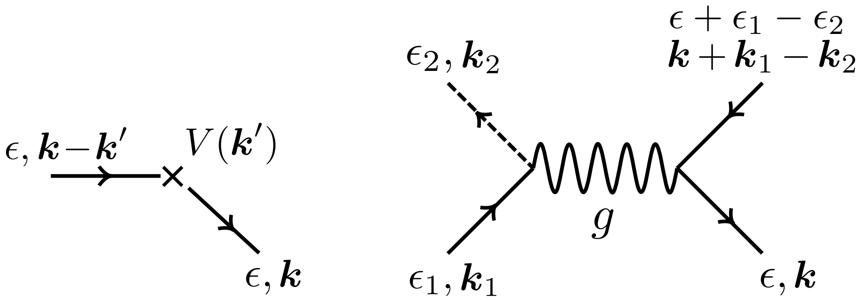

Figure 2.2 – The Born series obtained by iterating the Lippmann-Schwinger equation (2.25) generates terms built on scattering processes on the random potential V (left) and on the nonlinear potential $g|\psi|^2$ (right). The solid and dashed lines with arrows refer to the free-space, retarded and advanced Green's functions, respectively. The cross refers to the random potential V and the wavy line to the interaction parameter g. For each vertex, the lower-right line $(\epsilon, \boldsymbol{k})$ is the outgoing field, and integrations over ϵ_1, ϵ_2, $\boldsymbol{k}'$, $\boldsymbol{k}_1$ and $\boldsymbol{k}_2$ are understood.

2.3 Kinetic theory for diffusive atoms

Let us first focus on the construction of a Bethe-Salpeter equation for $\mathcal{I}^D_{\epsilon,\omega}$, i.e. for atoms that are purely diffusive in the non-interacting limit. The latter is obtained by adding corrective terms to the Bethe-Salpeter for $g = 0$, in which the ladder sequence can be interrupted by one or several particle interaction events. We first consider the corrections of first order in $g\rho_0$, which are known to dominate the dynamics in the stationary configurations of [204, 209, 210], and for the spreading of weakly interacting wave packets [169, 214, 215]. In our out-of-equilibrium quench scenario however, we will show that they turn out to have negligible influence on the dynamics, unlike second order corrections.

2.3.1 First order nonlinear corrections

To build the elementary diagrams that represent the first-order, iterative correction to the linear Bethe-Salpeter equation, we have to insert a single nonlinear interaction event between two disorder scattering events in a multiple scattering sequence for the density, represented by a ladder diagram $\mathcal{I}^D_{\epsilon,\omega}$. The interaction term $g|\psi|^2$ being itself proportional to the density, this interaction event has to be connected to another ladder diagram, which can be seen as an external "source" term.

Using the rules of Fig. 2.2 to position the incoming and outgoing momenta, as well as the energies, we obtain the diagram (a) represented in Fig. 2.3 (plus its complex conjugate, which has been omitted here for clarity). One can check that iterating this diagram indeed yields a multiple scattering sequence interrupted only by non-consecutive interaction events.

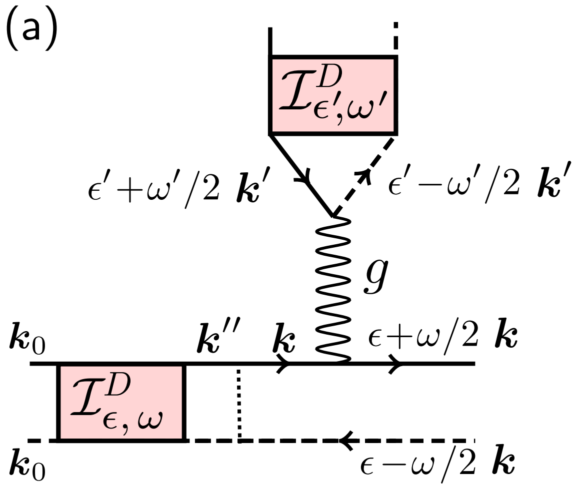

Figure 2.3 – First-order diagrammatic correction to the Bethe-Salpeter equation for $\mathcal{I}^D_{\epsilon,\omega}$, involving one interaction event. Red boxes refer to an incoming, ladder-type sequence $\mathcal{I}^D_{\epsilon,\omega}$, where, apart from particle interaction processes, the two paths propagate along the same sequence of scatterers in the same direction. The solid and dashed lines symbolize $\overline{G}^R_\epsilon$ and $\overline{G}^A_\epsilon$, respectively, the vertical dotted line the correlation function in Eq. (2.11), and the wavy lines a particle interaction event, see Fig. 2.2.

Computation of diagram 2.3(a)

To write down the contribution of diagram 2.3(a), one simply needs to compute the energies and momenta of every Green's function and intensity box, using the rules of Fig. 2.2. Integration over the incoming variables then yields

$$\mathcal{I}^{D\,(a)}_{\epsilon,\omega}(\boldsymbol{k})=2gN\gamma\int\frac{\mathrm{d}\epsilon'}{2\pi}\frac{\mathrm{d}\omega'}{2\pi}\frac{\mathrm{d}^2\boldsymbol{k}'}{(2\pi)^2}\frac{\mathrm{d}^2\boldsymbol{k}''}{(2\pi)^2}\Big[\overline{G}^R_{\epsilon+\omega/2-\omega'}(\boldsymbol{k})\overline{G}^R_{\epsilon+\omega/2}(\boldsymbol{k})\times\overline{G}^A_{\epsilon-\omega/2}(\boldsymbol{k})\mathcal{I}^D_{\epsilon',\omega'}(\boldsymbol{k}')\mathcal{I}^D_{\epsilon-\omega'/2,\omega-\omega'}(\boldsymbol{k}'')\Big], \tag{2.27}$$

where the factor 2 stems from the Wick decomposition of the average $\overline{\psi_{\epsilon_1}\psi^*_{\epsilon_2}\psi_{\epsilon-\epsilon_1+\epsilon_2}\psi^*_\epsilon}$ from Eq. (2.26), and the Fourier transform of the correlation function of the potential $\tilde{\mathcal{C}}(\boldsymbol{k})=\gamma$. It corresponds to the two different ways to pair incoming field amplitudes into ladder intensities connected to the nonlinear vertex. In other words, it takes into account the second possible interaction kernel obtained by exchanging subscripts 1 and 2 in Fig. 2.2. Using the definition (2.12) of $n_{\boldsymbol{k}}(t)$, and the normalization condition (2.14), we get

$$\int\frac{\mathrm{d}^2\boldsymbol{k}'}{(2\pi)^2}\int\frac{\mathrm{d}\epsilon'}{2\pi}\mathcal{I}^D_{\epsilon',\omega'}(\boldsymbol{k}')=\int\mathrm{d}t\,e^{i\omega' t}\int\frac{\mathrm{d}^2\boldsymbol{k}'}{(2\pi)^2}\overline{|\psi(\boldsymbol{k}',t)|^2}=\int\mathrm{d}t\,e^{i(\omega'+i0^+)t}=\frac{1}{-i\omega'+0^+}, \tag{2.28}$$

where the second equality follows from using the normalization condition (2.14), which ensures particle conservation. Eq. (2.27) becomes

$$\mathcal{I}^{D\,(a)}_{\epsilon,\omega}(\boldsymbol{k})=2gN\gamma\int\frac{\mathrm{d}\omega'}{2\pi}\frac{\mathrm{d}^2\boldsymbol{k}''}{(2\pi)^2}\frac{\left[\overline{G}^R_{\epsilon+\omega/2-\omega'}(\boldsymbol{k})\overline{G}^R_{\epsilon+\omega/2}(\boldsymbol{k})\overline{G}^A_{\epsilon-\omega/2}(\boldsymbol{k})\mathcal{I}^D_{\epsilon-\omega'/2,\omega-\omega'}(\boldsymbol{k}'')\right]}{-i\omega'+0^+}. \tag{2.29}$$

We recall that (see Eq. (1.36))

$$\overline{G}^R_\epsilon(\boldsymbol{k}) = \frac{1}{\epsilon-\epsilon_{\boldsymbol{k}}-\Sigma^R}, \tag{2.30}$$

with $\Sigma''^R < 0$ (we recall our notation for the real and imaginary parts of the self-energy: $\Sigma = \Sigma' + i\Sigma''$). We saw in the previous chapter that Σ'' is independent of k for an uncorrelated potential. Here it is also implicitly evaluated on-shell, i.e., at energy ϵ_0. Therefore $\overline{G}^R_{\epsilon+\omega/2-\omega'}(\boldsymbol{k})$ has a pole in the upper part of the complex plane with respect to the integration over ω'. Using expression (2.16), the same can be said of $\int \frac{\mathrm{d}^2\boldsymbol{k}''}{(2\pi)^2}\mathcal{I}_{\epsilon-\omega'/2,\omega-\omega'}(\boldsymbol{k}'')$. The integral over ω' is then easily computed using the residue theorem for the only pole in the lower part of the complex plane, $\omega' = -i0^+$. This yields, after taking the limit to 0:

$$\mathcal{I}^{D\,(a)}_{\epsilon,\omega}(\boldsymbol{k})=2g\rho_0\gamma[\overline{G}^R_{\epsilon+\omega/2}(\boldsymbol{k})]^2\overline{G}^A_{\epsilon-\omega/2}(\boldsymbol{k})\int\frac{\mathrm{d}^2\boldsymbol{k}''}{(2\pi)^2}\mathcal{I}^D_{\epsilon,\omega}(\boldsymbol{k}''). \tag{2.31}$$

Energy shift

From Eq. (2.31), we can show that the contribution of the diagram 2.3(a) boils down to a constant energy shift $-2g\rho_0$ of $\overline{G}^R_\epsilon$ in the linear Bethe-Salpeter equation that we recall here (see derivation in chapter 1):

$$\mathcal{I}^D_{\epsilon,\omega}(\boldsymbol{k}) \;=\; \overline{G}^R_{\epsilon+\omega/2}(\boldsymbol{k})\overline{G}^A_{\epsilon-\omega/2}(\boldsymbol{k})\times(2\pi)^2\delta(\boldsymbol{k}-\boldsymbol{k}_0)+\gamma\,\overline{G}^R_{\epsilon+\omega/2}(\boldsymbol{k})\overline{G}^A_{\epsilon-\omega/2}(\boldsymbol{k})\int\frac{\mathrm{d}^2\boldsymbol{k}'}{(2\pi)^2}\mathcal{I}^D_{\epsilon,\omega}(\boldsymbol{k}'). \tag{2.32}$$

To see this, we first perform the substitution $\epsilon \to \epsilon - 2g\rho_0$ in the second term in the right-hand side of Eq. (2.32). This is equivalent to assuming that after the first disorder scattering event, all retarded average Green's functions have their energy shifted. The first term is left untouched because it corresponds to the ballistic or "coherent" mode, which has experienced no disorder scattering, and thus no interaction event (since condition (2.22) is fulfilled) :

$$\mathcal{I}^D_{\epsilon,\omega}(\boldsymbol{k}) \;=\; \overline{G}^R_{\epsilon+\omega/2}(\boldsymbol{k})\overline{G}^A_{\epsilon-\omega/2}(\boldsymbol{k})\times(2\pi)^2\delta(\boldsymbol{k}-\boldsymbol{k}_0)+\gamma\,\overline{G}^R_{\epsilon+\omega/2-2g\rho_0}(\boldsymbol{k})\overline{G}^A_{\epsilon-\omega/2}(\boldsymbol{k})\int\frac{\mathrm{d}^2\boldsymbol{k}'}{(2\pi)^2}\mathcal{I}^D_{\epsilon,\omega}(\boldsymbol{k}'). \tag{2.33}$$

Then, using the definition (2.30) of the average retarded Green's function, one has the following expansion for small g:

$$\overline{G}^R_{\epsilon-2g\rho_0}(\boldsymbol{k}) \simeq \overline{G}^R_{\epsilon}(\boldsymbol{k}) + 2g\rho_0[\overline{G}^R_{\epsilon}(\boldsymbol{k})]^2. \tag{2.34}$$

Substituting Eq (2.34) into Eq. (2.33) we get

$$\begin{aligned}\mathcal{I}^D_{\epsilon,\omega}(\boldsymbol{k}) &= \overline{G}^R_{\epsilon+\omega/2}(\boldsymbol{k})\overline{G}^A_{\epsilon-\omega/2}(\boldsymbol{k}) \times (2\pi)^2\delta(\boldsymbol{k}-\boldsymbol{k}_0) + \gamma\,\overline{G}^R_{\epsilon+\omega/2}(\boldsymbol{k})\overline{G}^A_{\epsilon-\omega/2}(\boldsymbol{k}) \int \frac{\mathrm{d}^2\boldsymbol{k}'}{(2\pi)^2}\mathcal{I}^D_{\epsilon,\omega}(\boldsymbol{k}') \\ &\quad + 2g\rho_0\gamma[\overline{G}^R_{\epsilon+\omega/2}(\boldsymbol{k})]^2\overline{G}^A_{\epsilon-\omega/2}(\boldsymbol{k}) \int \frac{\mathrm{d}^2\boldsymbol{k}''}{(2\pi)^2}\mathcal{I}_{\epsilon,\omega}(\boldsymbol{k}''). \end{aligned} \tag{2.35}$$

The right-hand side of Eq. (2.32) is modified by an extra term which is exactly equal to $\mathcal{I}^{D\,(a)}_{\epsilon,\omega}(\boldsymbol{k})$ from Eq. (2.31). We conclude that adding diagram 2.3(a) in the linear Bethe-Salpeter equation is equivalent to shifting the average retarded Green's functions energy by $-2g\rho_0$. The same conclusion holds for the complex conjugate of diagram 2.3(a), with the energy shift affecting the advanced Green's function. Due to condition (2.22), this shift is small compared to the characteristic energies of the system and, as a consequence, first-order nonlinear corrections to the Bethe-Salpeter equation do not quantitatively affect the diffusive dynamics. Note, in passing, that this result is in stark contrast with the scenario where one follows the spreading of a wave packet in position space. In this case, diagrams of the type of Fig. 2.3(a) were shown to significantly modify the wave-packet density distribution [169, 214, 215]. The difference lies in the behavior of the mean density $\overline{|\psi(\boldsymbol{r},t)|^2}$, which explicitly depends on time and space for an initial wave packet, whereas it always remains uniform and time independent for an initial plane wave.

2.3.2 Modification of the self-energy

As discussed in the previous section, leading-order nonlinear corrections to the Bethe-Salpeter equation for the diffusive intensity boil down to a constant energy shift of the Green's functions. In turn, this shift can alternatively be described in terms of a correction, linear in g, to the real part of the self-energy. As stated in the beginning of Sec. 2.2.3, the concept of Green's function – and thus, of self-energy – is not rigorously defined when $g \neq 0$. However, hinted by the conclusion of the last (sub)section, we can derive equivalent objects from the Born series (2.25) by complete analogy with the linear case. As we will see, this approach is valid at least within our assumptions (2.22). The expansion of $\Sigma(\epsilon,\boldsymbol{k})$ obtained in this way is displayed in Fig. 2.4.

Born approximation

The first diagram of Fig. 2.4 is the usual Born approximation for the disorder potential,

$$\Sigma(\boldsymbol{k},\epsilon) = \int \frac{\mathrm{d}\boldsymbol{k}''}{(2\pi)^d} G_0(\boldsymbol{k}'',\epsilon)\tilde{\mathcal{C}}(\boldsymbol{k}''-\boldsymbol{k}). \tag{2.36}$$

The imaginary part of Eq. (2.36) defines the scattering mean free time τ, as discussed in chapter 1. As we will see later when computing the energy distributions of the gas, the average energy of bosons in the disorder potential is also shifted, due to the real part of the self-energy.

First order nonlinear correction

The second self-energy diagram is the nonlinear correction corresponding to the density diagram 2.3(a). It is purely real, simply given by :

$$\Sigma^{(1)}(\epsilon,\boldsymbol{k}) = 2gN \int \frac{\mathrm{d}\epsilon'\omega'}{(2\pi)^2}\frac{\mathrm{d}^2\boldsymbol{k}'}{(2\pi)^2}\mathcal{I}^D_{\epsilon',\omega'}(\boldsymbol{k}') = 2g\rho_0, \tag{2.37}$$

and indeed describes a constant shift of the Green's function energy by $-2g\rho_0$. The value of this shift can be qualitatively explained as follows. At very short times $t \ll \tau$, no scattering has occured and the gas resembles the initial plane wave. Thus the average interaction energy, given by [222]

$$\epsilon_{\text{int}} = \frac{gN}{2}\int \mathrm{d}\boldsymbol{r}\overline{|\psi(\boldsymbol{r},t)|^4}, \tag{2.38}$$

is equal to $g\rho_0/2$, as $\overline{|\psi(\boldsymbol{r},t)|}^4 = \overline{|\psi(\boldsymbol{r},t)|^2}^2 \sim 1/\mathcal{V}^2$. After a few τ, the density $|\psi(\boldsymbol{r},t)|^2$ becomes itself a spatially distributed random variable (see Fig. 2.1), and we have $\overline{|\psi(\boldsymbol{r},t)|}^4 = 2\overline{|\psi(\boldsymbol{r},t)|^2}^2 \sim 2/\mathcal{V}^2$. This result is called the Rayleigh law for weak disorder. Consequently, after a few mean free times, the value of ϵ_{int} is doubled to $g\rho_0$. In terms of self-energy, which contains the interaction energy for two particles, this corresponds to a shift of $2g\rho_0$.

Screening effect

At first order in g, another type of self-energy diagram comes into play. The latter follows from the observation that the two random potentials $V(\boldsymbol{r})$ and $g|\psi(\boldsymbol{r},t)|^2$ in the Gross-Pitaevskii equation (2.10) may be *correlated*. By iterating the Born series (2.25), it is clear that terms proportional to the hybrid correlation term $\overline{|\psi(\boldsymbol{r},t)|^2 V(\boldsymbol{r}')}$ will arise, and should thus included in the self-energy. This defines a second version of Eq. (2.36),

$$\Sigma^{(2)}(\boldsymbol{k},\epsilon) = \int \frac{\mathrm{d}\boldsymbol{k}''}{(2\pi)^d} G_0(\boldsymbol{k}'',\epsilon)\,\tilde{\mathcal{C}}^{(2)}(\boldsymbol{k}''-\boldsymbol{k}), \tag{2.39}$$

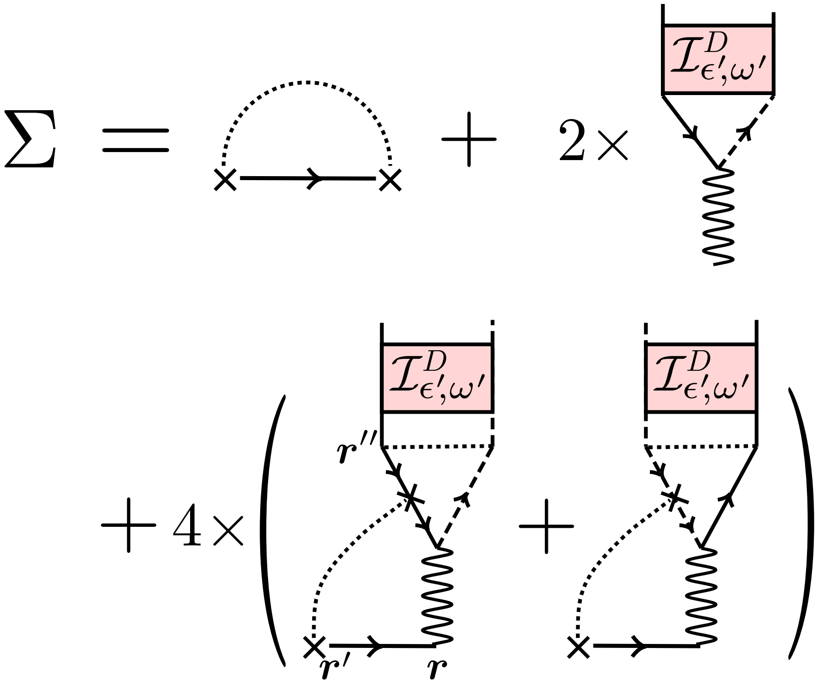

Figure 2.4 – Leading-order contributions to an expansion of the self-energy when $g \neq 0$. Symbols have the same meaning as in Fig. 2.3.

with the power spectrum

$$\tilde{\mathcal{C}}^{(2)}(\boldsymbol{k}) \equiv 4\int d^2(\boldsymbol{r}-\boldsymbol{r}')\, g\, \overline{|\psi(\boldsymbol{r},t)|^2 V(\boldsymbol{r}')}\, e^{i\boldsymbol{k}(\boldsymbol{r}-\boldsymbol{r}')}. \tag{2.40}$$

In the factor 4 added, one factor 2 again stems from the two possibilities to pair the incoming fields into ladder intensities [same factor as in Eq. (2.27)], and another factor 2 counts the other combination $\overline{|\psi(\boldsymbol{r}',t)|^2 V(\boldsymbol{r})}$. The self-energy diagrams corresponding to Eq. (2.39) are shown in the lower part of Fig. 2.4.

The self-energy $\Sigma^{(2)}$ corresponds to a screening effect where fluctuations of the random potential are smoothed by the nonlinearity, and is well known in the Thomas-Fermi regime of strong interactions [223]. The hybrid correlator is conveniently expressed in position space as follows:

$$\begin{aligned}\overline{|\psi(\boldsymbol{r},t)|^2 V(\boldsymbol{r}')} = \gamma^2 \int \mathrm{d}^2\boldsymbol{r}'' \int \frac{\mathrm{d}\epsilon'}{2\pi}\frac{\mathrm{d}\omega'}{2\pi} e^{-i\omega' t} \mathcal{I}_{\epsilon',\omega'}(\boldsymbol{r}'')& \\ \times \left[G_0^*(\boldsymbol{r}''-\boldsymbol{r},)G_0(\boldsymbol{r}''-\boldsymbol{r}',\epsilon')G_0(\boldsymbol{r}'-\boldsymbol{r},\epsilon') + \text{c.c.}\right].& \end{aligned} \tag{2.41}$$

This simplifies to:

$$\overline{|\psi(\boldsymbol{r},t)|^2 V(\boldsymbol{r}')} = \frac{i\gamma\rho_0}{2\pi\nu_{\epsilon_0}}[G_0(\boldsymbol{r}-\boldsymbol{r}',\epsilon_0)^2 - G_0^*(\boldsymbol{r}-\boldsymbol{r}',\epsilon_0)^2], \tag{2.42}$$

where we invoked particle conservation [see Eq. (2.28)] and used that the energy remains peaked around $\epsilon \simeq \epsilon_0 \equiv \boldsymbol{k}_0^2/2m$ at short time. The self energy (2.39) can then be rewritten as

$$\Sigma^{(2)}(\boldsymbol{k},\epsilon) \simeq \frac{4g\rho_0\gamma i}{2\pi\nu_{\epsilon_0}} \int \mathrm{d}^2\boldsymbol{r}\, e^{-i\boldsymbol{k}\cdot\boldsymbol{r}} G_0(\boldsymbol{r},\epsilon) \times [G_0(\boldsymbol{r},\epsilon_0)^2 - G_0^*(\boldsymbol{r},\epsilon_0)^2]. \tag{2.43}$$

Evaluating the integral on-shell, i.e. for $\epsilon = \epsilon_0$ and $\boldsymbol{k} = \boldsymbol{k}_0$, we obtain the following estimate for the imaginary part of $\Sigma^{(2)}$:

$$\Sigma''^{(2)}(\boldsymbol{k}_0,\epsilon_0) \sim \frac{g\rho_0}{k_0\ell} \ll g\rho_0. \tag{2.44}$$

In the weak-disorder regime considered throughout this chapter, this contribution to the self energy is thus negligible. This is clearly visible in the example depicted in Fig. 2.1, where the disorder potential and the density display no spatial correlations with each other, indicating that $\overline{|\psi(\boldsymbol{r},t)|^2 V(\boldsymbol{r}')}$ is very small. A similar decay with $k_0\ell$ is also expected for the real part of $\Sigma^{(2)}$, though its precise form requires a regularization beyond the Born approximation, as for $\Sigma^{(0)}$.

2.3.3 Summary

We have derived the first-order nonlinear corrections to the Bethe-Salpeter equation for the diffusive component of the gas. The most important correction is a small and constant energy shift of the average Green's functions, which has no effect on the dynamics of the gas. In addition to this shift, there also exist first-order nonlinear corrections shifting the imaginary part of $\Sigma(\epsilon,\boldsymbol{k})$. These corrections stem from correlations between the disorder and nonlinear potentials in the Gross-Pitaevskii equation (2.10), but turn out to be very small in the weak-disorder limit. From now on, we will thus neglect these self-energy corrections, and always evaluate average Green's functions simply using Eq. (2.30), with $\Sigma(\epsilon,\boldsymbol{k}) \simeq -i/2\tau$.

2.3.4 Second-order corrections

We now examine interaction corrections to the ladder Bethe-Salpeter equation (2.32) that are of second order in g. Since each interaction vertex g is connected to four field amplitudes (see Fig. 2.2), these corrections involve six incoming field amplitudes, i.e they are proportional to the third power of the density. Due to the condition (2.22), we also know that at least one disorder scattering event occurs before every interaction event, similarly to the leading-order corrections. Since the disorder scattering events are described by ladder diagrams (for weak disorder), we group the six incoming arrows into three incoming ladder sequences $\mathcal{I}^D_{\epsilon_i,\omega_i}$, each of them originating from different disorder scattering events. Analyzing all possible non-trivial ways (i.e. those which do not reduce to a mere energy shift) of connecting the incoming arrows to the g vertices, we arrive at the diagrams shown in Fig. 2.5.

Expression of the Bethe-Salpeter equation

To write down the expression for the diagrams of Fig. 2.5, one just needs to compute the energies and momenta for all Green's functions using the rules of Fig. 2.2. The corresponding Bethe-Salpeter equation reads:

$$\begin{aligned}
\mathcal{I}^D_{\epsilon,\omega}(\boldsymbol{k}) = \overline{G}^R_{\epsilon+\omega/2}(\boldsymbol{k})\overline{G}^A_{\epsilon-\omega/2}(\boldsymbol{k}) \Bigg[& (2\pi)^2\delta(\boldsymbol{k}-\boldsymbol{k}_0) + \gamma \int \frac{\mathrm{d}^2\boldsymbol{k}'}{(2\pi)^2}\mathcal{I}^D_{\epsilon,\omega}(\boldsymbol{k}') \\
&+ (g\rho_0\gamma)^2 \times \Big[\prod_{i=1,2}\int \frac{\mathrm{d}\epsilon_i \mathrm{d}\omega_i}{(2\pi)^4}\frac{\mathrm{d}^2\boldsymbol{k}_i\mathrm{d}^2\boldsymbol{k}'_i}{(2\pi)^8}\mathcal{I}^D_{\epsilon_i,\omega_i}(\boldsymbol{k}'_i)\overline{G}^R_{\epsilon_i+\omega_i/2}(\boldsymbol{k}_i)\overline{G}^A_{\epsilon_i-\omega_i/2}(\boldsymbol{k}_i)\Big] \\
&\times \Bigg\{ 2\gamma\overline{G}^R_{\epsilon_3+\Omega_1/2}(\boldsymbol{k}_3)\overline{G}^A_{\epsilon_3-\Omega_1/2}(\boldsymbol{k}_3)\int\frac{\mathrm{d}^2\boldsymbol{k}'_3}{(2\pi)^2}\mathcal{I}^D_{\epsilon_3,\Omega_1}(\boldsymbol{k}'_3) \\
&+ \gamma\Big(4\overline{G}^R_{\epsilon_4+\Omega_1/2}(\boldsymbol{k}_4) + 2\overline{G}^A_{\epsilon_3-\Omega_1/2}(\boldsymbol{k}_3)\Big)\overline{G}^R_{\epsilon+\Omega_2}(\boldsymbol{k})\int\frac{\mathrm{d}^2\boldsymbol{k}'}{(2\pi)^2}\mathcal{I}^D_{\epsilon_5,\Omega_1}(\boldsymbol{k}') \\
&+ \gamma\Big(4\overline{G}^A_{\epsilon_4-\Omega_1/2}(\boldsymbol{k}_4) + 2\overline{G}^R_{\epsilon_3+\Omega_1/2}(\boldsymbol{k}_3)\Big)\overline{G}^A_{\epsilon-\Omega_2}(\boldsymbol{k})\int\frac{\mathrm{d}^2\boldsymbol{k}'}{(2\pi)^2}\mathcal{I}^D_{\epsilon_6,\Omega_1}(\boldsymbol{k}')\Bigg\}\Bigg],
\end{aligned} \tag{2.45}$$

where we defined $\epsilon_3 = \epsilon_1 + \epsilon_2 - \epsilon$, $\epsilon_4 = \epsilon + \epsilon_1 - \epsilon_2$, $\epsilon_5 = \epsilon - (\omega_1 + \omega_2)/2$, $\epsilon_6 = \epsilon + (\omega_1 + \omega_2)/2$, $\Omega_1 = \omega - \omega_1 - \omega_2$, $\Omega_2 = \omega/2 - \omega_1 - \omega_2$ for energies, and $\boldsymbol{k}_3 = \boldsymbol{k}_1 + \boldsymbol{k}_2 - \boldsymbol{k}$, $\boldsymbol{k}_4 = \boldsymbol{k} + \boldsymbol{k}_1 - \boldsymbol{k}_2$ for momenta.

Kinetic equation for diffusive modes

Let us start by defining the quantities $f_\epsilon(t)$ and $f^C_\epsilon(t)$:

$$f_\epsilon(t) \equiv \frac{1}{2\pi\nu_\epsilon}\int\frac{\mathrm{d}^2\boldsymbol{k}}{(2\pi)^2}\int_{-\infty}^{\infty}\frac{\mathrm{d}\omega}{2\pi}e^{-i\omega t}\mathcal{I}^D_{\epsilon,\omega}(\boldsymbol{k}). \tag{2.46}$$

$$f^C_\epsilon(t) \equiv \frac{1}{2\pi\nu_\epsilon}\int\frac{\mathrm{d}^2\boldsymbol{k}}{(2\pi)^2}\int_{-\infty}^{\infty}\frac{\mathrm{d}\omega}{2\pi}e^{-i\omega t}\mathcal{I}^C_{\epsilon,\omega}(\boldsymbol{k}). \tag{2.47}$$

$$\tag{2.48}$$

The normalization condition (2.14), and the decomposition (2.15) of the intensity kernel imply that the sum $f_\epsilon(t) + f^C_\epsilon(t)$ is normalized according to

$$\int \mathrm{d}\epsilon\nu_\epsilon\left[f_\epsilon(t) + f^C_\epsilon(t)\right] = 1, \tag{2.49}$$

which imposes the conservation of the number of particles. This condition naturally identifies the product $\nu_\epsilon f_\epsilon(t)$ (respectively $\nu_\epsilon f^C_\epsilon(t)$) as the energy distribution of the diffusive (coherent) component of the gas, and f_ϵ (f^C_ϵ) as the corresponding occupation numbers.

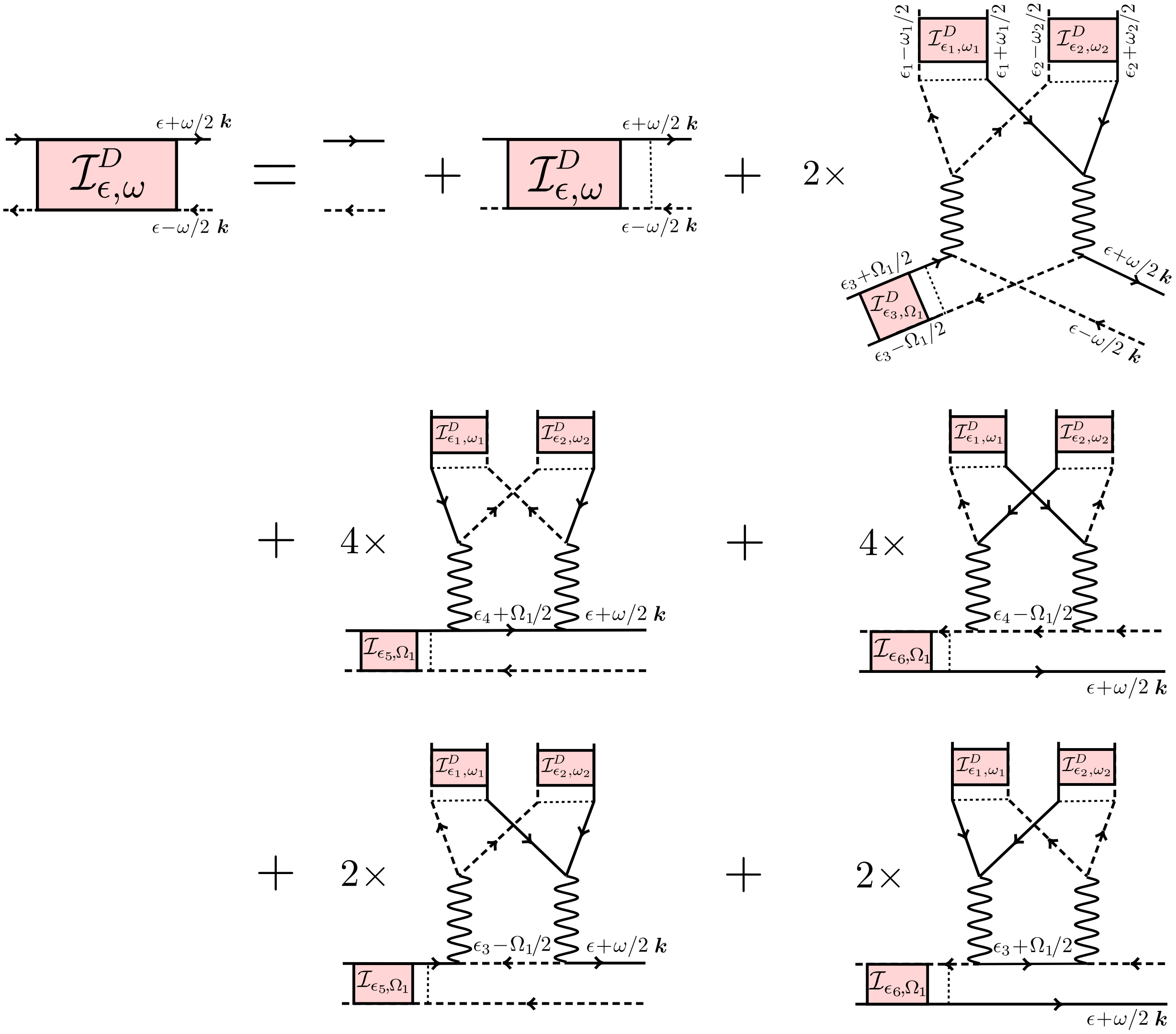

Figure 2.5 – Diagrammatic representation of the Bethe-Salpeter equation for the diffusive contribution to the momentum distribution, $\mathcal{I}^D_{\epsilon,\omega}(\boldsymbol{k})$, taking into account second-order interaction corrections (following our conclusions from Section 2.3.1, first-order interaction diagrams are discarded). Symbols have the same meaning as in Fig. 2.3. The numerical prefactors account for the possible combinations of propagation lines connecting to the vertex g.

From Eq. (2.45) we can derive a closed kinetic equation for the occupation number of the diffusive atoms $f_\epsilon(t)$ in the limit $t \gg \tau$. To obtain it, we proceed as follows. First, we integrate the Bethe-Salpeter equation (2.45) over $\boldsymbol{k}$. The limit $t \gg \tau$ is equivalent to $\omega\tau, \omega_i\tau \ll 1$ ($i = 1, 2$) in the integrands, so we simply omit the ω, ω_i dependence of the Green's functions. This leads to a closed equation for the quantity:

$$\mathcal{I}_{\epsilon,\omega} \equiv \int \frac{\mathrm{d}^2\boldsymbol{k}}{(2\pi)^2} \mathcal{I}_{\epsilon,\omega}(\boldsymbol{k}). \tag{2.50}$$

In the limit $\omega\tau \ll 1$, we also simplify the second and third terms in the right-hand side of Eq. (2.45), using that

$$\gamma \int \frac{\mathrm{d}^2\boldsymbol{k}}{(2\pi)^2} \overline{G}^R_{\epsilon+\omega/2}(\boldsymbol{k}) \overline{G}^A_{\epsilon-\omega/2}(\boldsymbol{k}) \simeq 1 + i\omega\tau. \tag{2.51}$$

Within the same limit, we also set all ω, ω_1 and ω_2 to zero in the frequency arguments of the Green's functions, and in the energy arguments of the intensities (so that $\epsilon_5 = \epsilon_6 = \epsilon$). At this stage, we are left with:

$$\begin{aligned}
\mathcal{I}^D_{\epsilon,\omega} = {} & \overline{G}^R_\epsilon(\boldsymbol{k}_0)\overline{G}^A_\epsilon(\boldsymbol{k}_0) + (1 + i\omega\tau)\mathcal{I}^D_{\epsilon,\omega} \\
& + (g\rho_0\gamma)^2 \int \frac{\mathrm{d}^2\boldsymbol{k}}{(2\pi)^2} \overline{G}^R_\epsilon(\boldsymbol{k})\overline{G}^A_\epsilon(\boldsymbol{k}) \times \left[\prod_{i=1,2} \int \frac{\mathrm{d}\epsilon_i \mathrm{d}\omega_i}{(2\pi)^4} \frac{\mathrm{d}^2\boldsymbol{k}_i}{(2\pi)^4} \overline{G}^R_{\epsilon_i}(\boldsymbol{k}_i)\overline{G}^A_{\epsilon_i}(\boldsymbol{k}_i)\mathcal{I}^D_{\epsilon_i,\omega_i}\right] \\
& \times \Bigg\{ 2\gamma\, \overline{G}^R_{\epsilon_3}(\boldsymbol{k}_3)\overline{G}^A_{\epsilon_3}(\boldsymbol{k}_3)\mathcal{I}^D_{\epsilon_3,\Omega_1} \\
& \qquad + 4\gamma\Big(\overline{G}^R_{\epsilon_4}(\boldsymbol{k}_4)\overline{G}^R_\epsilon(\boldsymbol{k}) + \overline{G}^A_{\epsilon_4}(\boldsymbol{k}_4)\overline{G}^A_\epsilon(\boldsymbol{k})\Big)\mathcal{I}^D_{\epsilon,\Omega_1} \\
& \qquad + 2\gamma\left(\overline{G}^A_{\epsilon_3}(\boldsymbol{k}_3)\overline{G}^R_\epsilon(\boldsymbol{k}) + \overline{G}^R_{\epsilon_3}(\boldsymbol{k}_3)\overline{G}^A_\epsilon(\boldsymbol{k})\right)\mathcal{I}^D_{\epsilon,\Omega_1} \Bigg\}.
\end{aligned} \tag{2.52}$$

To perform the remaining integrals over $\boldsymbol{k}$, $\boldsymbol{k}_1$ and $\boldsymbol{k}_2$, we use several times the following identities:

$$\begin{aligned}
\overline{G}^R_\epsilon(\boldsymbol{k})\overline{G}^A_\epsilon(\boldsymbol{k}) &= i\tau\left(\overline{G}^R_\epsilon(\boldsymbol{k}) - \overline{G}^A_\epsilon(\boldsymbol{k})\right) \\
&= \frac{i}{2\pi\nu_\epsilon\gamma}\int \mathrm{d}^2\boldsymbol{r} e^{-i\boldsymbol{k}\cdot\boldsymbol{r}} \left\{\overline{G}^R_\epsilon(\boldsymbol{r}) - \overline{G}^A_\epsilon(\boldsymbol{r})\right\},
\end{aligned} \tag{2.53}$$

where the second equality stems from the definition of τ, and we have used the relation

$$\int \frac{\mathrm{d}^2\boldsymbol{k}}{(2\pi)^2} \overline{G}^R_\epsilon(\boldsymbol{k})\overline{G}^A_\epsilon(\boldsymbol{k}) e^{i\boldsymbol{k}\boldsymbol{r}} = \int \mathrm{d}^2\boldsymbol{r}' \overline{G}^R_\epsilon(\boldsymbol{r}')\overline{G}^A_\epsilon(\boldsymbol{r} - \boldsymbol{r}'). \tag{2.54}$$

We also systematically neglect products of the type $\overline{G}^R_\epsilon(\boldsymbol{r})\overline{G}^R_\epsilon(\boldsymbol{r})$ and $\overline{G}^A_\epsilon(\boldsymbol{r})\overline{G}^A_\epsilon(\boldsymbol{r})$, which give contributions smaller by a factor $1/(k_0\ell) \ll 1$. Eq. (2.52) becomes:

$$\begin{aligned}
-i\omega\mathcal{I}^D_{\epsilon,\omega} = {} & i\left[\overline{G}^R_\epsilon(\boldsymbol{k}_0) - \overline{G}^A_\epsilon(\boldsymbol{k}_0)\right] \\
& + \frac{(g\rho_0)^2}{(2\pi)^3}\prod_{i=1,2}\int\frac{\mathrm{d}\epsilon_i\mathrm{d}\omega_i}{(2\pi)^2}\frac{\mathcal{I}^D_{\epsilon_i,\omega_i}}{\nu_{\epsilon_i}}\int\mathrm{d}^2\boldsymbol{r}[\overline{G}^R_{\epsilon_1}(\boldsymbol{r}) - \overline{G}^A_{\epsilon_1}(\boldsymbol{r})][\overline{G}^R_{\epsilon_2}(\boldsymbol{r}) - \overline{G}^A_{\epsilon_2}(\boldsymbol{r})][\overline{G}^R_{\epsilon}(\boldsymbol{r}) - \overline{G}^A_{\epsilon}(\boldsymbol{r})] \\
& \times\left\{2\frac{\mathcal{I}^D_{\epsilon_1+\epsilon_2-\epsilon,\omega-\omega_1-\omega_2}}{\nu_{\epsilon_1+\epsilon_2-\epsilon}}[\overline{G}^R_{\epsilon_1+\epsilon_2-\epsilon}(\boldsymbol{r}) - \overline{G}^A_{\epsilon_1+\epsilon_2-\epsilon}(\boldsymbol{r})]\right. \\
& \qquad + 2\frac{\mathcal{I}^D_{\epsilon,\omega-\omega_1-\omega_2}}{\nu_{\epsilon}}[\overline{G}^R_{\epsilon_1+\epsilon_2-\epsilon}(\boldsymbol{r}) - \overline{G}^A_{\epsilon_1+\epsilon_2-\epsilon}(\boldsymbol{r})] \\
& \qquad\qquad \left. - 4\frac{\mathcal{I}^D_{\epsilon,\omega-\omega_1-\omega_2}}{\nu_{\epsilon}}[\overline{G}^R_{\epsilon+\epsilon_1-\epsilon_2}(\boldsymbol{r}) - \overline{G}^A_{\epsilon+\epsilon_1-\epsilon_2}(\boldsymbol{r})]\right\}.
\end{aligned} \tag{2.55}$$

We then Fourier transform with respect to ω and use the definition of the occupation number $f_\epsilon(t)$:

$$f_\epsilon(t) \equiv \frac{1}{2\pi\nu_\epsilon}\int\frac{\mathrm{d}\omega}{2\pi}e^{-i\omega t}\mathcal{I}_{\epsilon,\omega}. \tag{2.56}$$

This finally yields

$$\partial_t f_\epsilon = \delta(t)\frac{A_\epsilon(\boldsymbol{k}_0)}{\nu_\epsilon} + \int_{\epsilon_1,\epsilon_2,\epsilon_3\geq 0}\mathrm{d}\epsilon_1\mathrm{d}\epsilon_2\; W(\epsilon,\epsilon_1,\epsilon_2)\Big[(f_\epsilon + f_{\epsilon_3})f_{\epsilon_1}f_{\epsilon_2} - f_\epsilon f_{\epsilon_3}(f_{\epsilon_1} + f_{\epsilon_2})\Big], \tag{2.57}$$

with the following expression for the kernel W:

$$W(\epsilon,\epsilon_1,\epsilon_2) = \frac{(g\rho_0)^2}{4\pi^3\nu_\epsilon}\int\mathrm{d}^2\boldsymbol{r}\,[\overline{G}^R_\epsilon(\boldsymbol{r}) - \overline{G}^A_\epsilon(\boldsymbol{r})][\overline{G}^R_{\epsilon_1}(\boldsymbol{r}) - \overline{G}^A_{\epsilon_1}(\boldsymbol{r})] \times [\overline{G}^R_{\epsilon_2}(\boldsymbol{r}) - \overline{G}^A_{\epsilon_2}(\boldsymbol{r})][\overline{G}^R_{\epsilon_3}(\boldsymbol{r}) - \overline{G}^A_{\epsilon_3}(\boldsymbol{r})], \tag{2.58}$$

where we denoted $\epsilon_3 \equiv \epsilon_1 + \epsilon_2 - \epsilon$. The integration range of ϵ_1 and ϵ_2 covers all energies allowed by the densities of states ν_{ϵ_1}, ν_{ϵ_2} and $\nu_{\epsilon_1+\epsilon_2-\epsilon}$ contained in the definition of the occupation numbers. At weak disorder, the density of states coincides, at leading order, with the free-space one, which imposes ϵ_1, ϵ_2, $\epsilon_3 \geq 0$. Equation (2.57) constitutes a kinetic equation for the occupation number $f_\epsilon(t)$, whose dynamics is governed by the collision kernel (2.58). The kinetic equation should be complemented by an initial condition, which is here provided by the "coherent mode", i.e. the first term in the right-hand side of Eq. (2.45). The latter gives:

$$f_\epsilon(t = 0^+) = \frac{A_\epsilon(\boldsymbol{k}_0)}{2\pi\nu_\epsilon} \equiv f^{(0)}_\epsilon, \tag{2.59}$$

which is nothing but the occupation number for $g = 0$ that we introduced in chapter 1. The fact that the non-interacting value of f_ϵ plays the role of the initial condition for the interacting problem is due to our assumption that particle collisions are less frequent than scattering events on the disorder, Eq. (2.22). Indeed, in this regime the diffusive ring first establishes, and only then do interactions come into play.

Multiplying equation (2.57) by ν_ϵ, and integrating over ϵ, we obtain

$$\partial_t \left[\int \mathrm{d}\epsilon \nu_\epsilon f_\epsilon(t) \right] = 0, \tag{2.60}$$

as the triple integral in the right-hand side is equal to its opposite by permutations of the energy arguments. This implies that the normalization of the product $\nu_\epsilon f_\epsilon$ is conserved over time:

$$\int \mathrm{d}\epsilon \nu_\epsilon f_\epsilon(t) = \int \mathrm{d}\epsilon \frac{A_\epsilon(\boldsymbol{k}_0)}{2\pi} = 1. \tag{2.61}$$

As expected, no dissipation is associated with the out-of-equilibrium evolution of diffusive modes in our isolated system. The kinetic equation (2.57) indicates that, in the presence of interactions, the diffusives modes undergo a thermalization process, during which energies are redistributed over time by the interactions. As will be discussed in detail in chapter 5, this process ultimately drives the system towards a thermal equilibrium state that can be described by a Gibbs ensemble, as prescribed by statistical mechanics.

Notice that Eqs. (2.57) and (2.58) coincide with the standard Boltzmann kinetic equation for Bose gases in the limit of large occupation numbers, where the gas is described by a classical field [224]. The sole effect of disorder on the dynamics appears in the collision Kernel W, where disorder-averaged Green's functions appear instead of free-space ones. As we show below, however, at weak disorder the final expression of W is in turn independent of any disorder parameter (in particular, the diffusion coefficient or the scattering mean free path do not appear). For weakly interacting diffusive bosons, disorder thus only manifests itself through the spectral function, involved both in the initial condition $f_\epsilon(0)$ and in Eq. (2.63) that connects the energy distribution to the momentum distribution. This situation would of course change drastically at stronger disorder or in the localization regime, where W would take a different expression. See, for example, an analysis of the 1d case in [121]. Equation (2.57) has been used, in particular in [172], to qualitatively discuss the possible emergence of a Bose condensate at very long time, but without microscopic justification. We note that the kinetic equation (2.57) has also been derived in [216] by means of a classical field theory in the presence of disorder.

Interaction kernel

Let us now examine in detail the interaction kernel (2.58). By performing the integration over $\boldsymbol{r}$, we obtain [216, 225]:

$$W(\epsilon;\epsilon_1,\epsilon_2) = \frac{m^3(g\rho_0)^2}{2\pi^4\nu_\epsilon}\frac{K\left(\frac{2\sqrt[4]{\epsilon\epsilon_1\epsilon_2\epsilon_3}}{\sqrt{\epsilon_1\epsilon_2}+\sqrt{\epsilon\epsilon_3}}\right)}{\sqrt{\epsilon_1\epsilon_2}+\sqrt{\epsilon\epsilon_3}}, \tag{2.62}$$

where $\epsilon_3 \equiv \epsilon_1 + \epsilon_2 - \epsilon$, and K is the complete elliptic integral of the first kind.

Momentum distribution

We obtain the diffusive contribution to the momentum distribution for $g \neq 0$ by integrating Eq. (2.45) over ϵ and taking the Fourier transform with respect to ω. At leading order in the interaction strength, the term proportional to g^2 in the right-hand side can be neglected, such that, in the hydrodynamic regime $\omega\tau \ll 1$, we have:

$$n_{\boldsymbol{k}}^D = \int_{-\infty}^{\infty} \mathrm{d}\epsilon\, A_\epsilon(\boldsymbol{k}) f_\epsilon(t). \tag{2.63}$$

This formula quite naturally generalizes the non-interacting case, for which $f_\epsilon(t)$ reduces to $f_\epsilon^{(0)}$. In the presence of interactions, the distribution $f_\epsilon(t)$ is no longer constant in time, which leads to an evolution of the diffusive background. Note that the normalization of the diffusive part of the momentum distribution, $\int \mathrm{d}^2\boldsymbol{k}/(2\pi)^2 n_{\boldsymbol{k}}^D = 1$ directly follows from the normalization of the energy distribution (2.61), very much like in the non-interacting limit [125].

In summary, in this section, we have derived a kinetic equation for the occupation number of the diffusive component of the Bose gas, starting from microscopic considerations. We have also shown that within our limits defined by condition (2.22), the collision kernel W is independent of the disorder. It is important to note that this result is different from the case of electrons in low-temperature disordered conductors, where the diffusive motion strengthens the effect of interactions [125, 194, 226].

2.4 Kinetic theory for coherent backscattering

We now move on to the construction of a Bethe-Salpeter equation for $\mathcal{I}^C_{\epsilon,\omega}$, i.e. for the atoms that contribute to the CBS peak in the non-interacting limit. As for the diffusive background, it is obtained by adding corrective terms to the Bethe-Salpeter for $g = 0$, in which the crossed sequence can be interrupted by one or several particle interaction events. As for diffusive atoms, we first show that the first-order corrections are again negligible, while second-order ones dominate the dynamics of coherent backscattering.

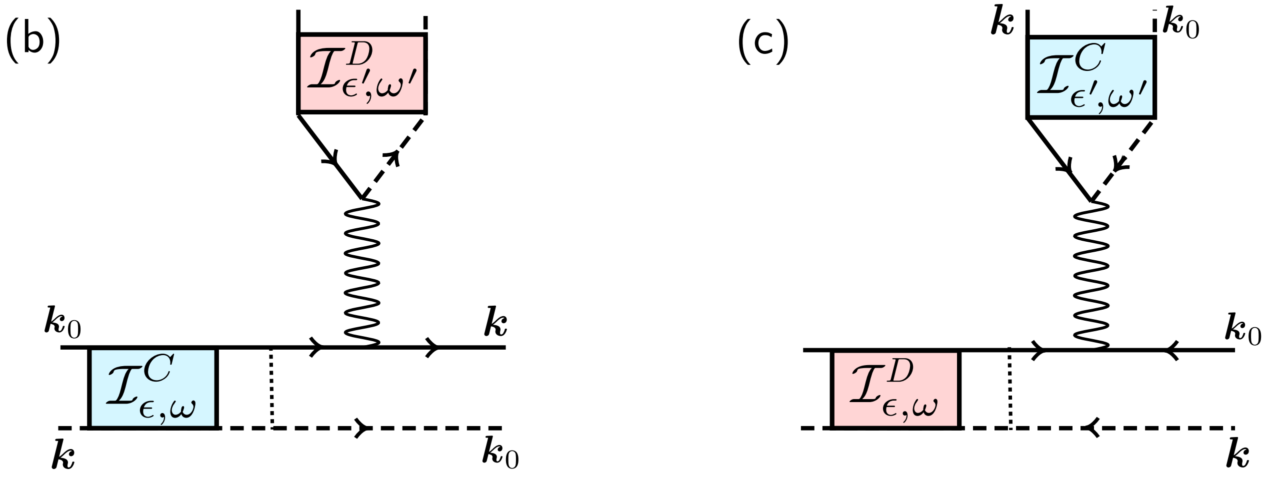

Figure 2.6 – First-order diagrammatic correction to the Bethe-Salpeter equation for $\mathcal{I}^C_{\epsilon,\omega}$, involving one interaction event. Red boxes refer to an incoming, ladder-type sequence $\mathcal{I}^D_{\epsilon,\omega}$, where, apart from particle interaction processes, the two paths propagate along the same sequence of scatterers in the same direction. Blue boxes refer to time-reversed scattering sequences as in chapter 1. The solid and dashed lines symbolize $\overline{G}^R_\epsilon$ and $\overline{G}^A_\epsilon$, respectively, the vertical dotted line the correlation function in Eq. (2.11), and the wavy lines a particle interaction event, see Fig. 2.2.

2.4.1 First-order nonlinear corrections

As for the diffusive background, we first address the first-order nonlinear corrections to the linear Bethe-Salpeter equation. Using the same reasoning as in section 2.3.1, we have to insert a single interaction event in a multiple scattering sequence that includes time-reversed intensity diagrams $\mathcal{I}^C_{\epsilon,\omega}$, either as the main sequence or as the 'source'. Again following the rules from Fig. 2.2 for energy and momenta, we end up with the two diagrams depicted in Fig. 2.6, as well as their complex conjugates. A third diagram that would involve two time-reversed density $\mathcal{I}^C_{\epsilon,\omega}$ cannot exist because there would be no way to position energies and momenta according to the rules of Fig. 2.2.

Computation of diagram 2.6(b)

To compute diagram 2.6(b), we proceed as was done in the non-interacting case to derive the Bethe-Salpeter equation for the coherent component: invoking time-reversal invariance, we can reverse one arrow connected to the counter propagating intensity $\mathcal{I}^C_{\epsilon,\omega}(\boldsymbol{k})$, and change its $\boldsymbol{k}$ arguments to the opposite direction. We then perform the change of variables $\{\boldsymbol{K} = (\boldsymbol{k}-\boldsymbol{k}_0)/2 = -\boldsymbol{K}'; \boldsymbol{Q} = \boldsymbol{k}+\boldsymbol{k}_0\}$. After these transformations, diagram 2.6(b) – depicted in Fig. 2.7(b) – has the same iterative structure as its incoherent counterpart 2.3(a). We can then integrate over the outgoing momenta of the resulting quantity $\tilde{\mathcal{I}}^C_{\epsilon,\omega}(\boldsymbol{K},\boldsymbol{K}'',\boldsymbol{Q})$, to obtain:

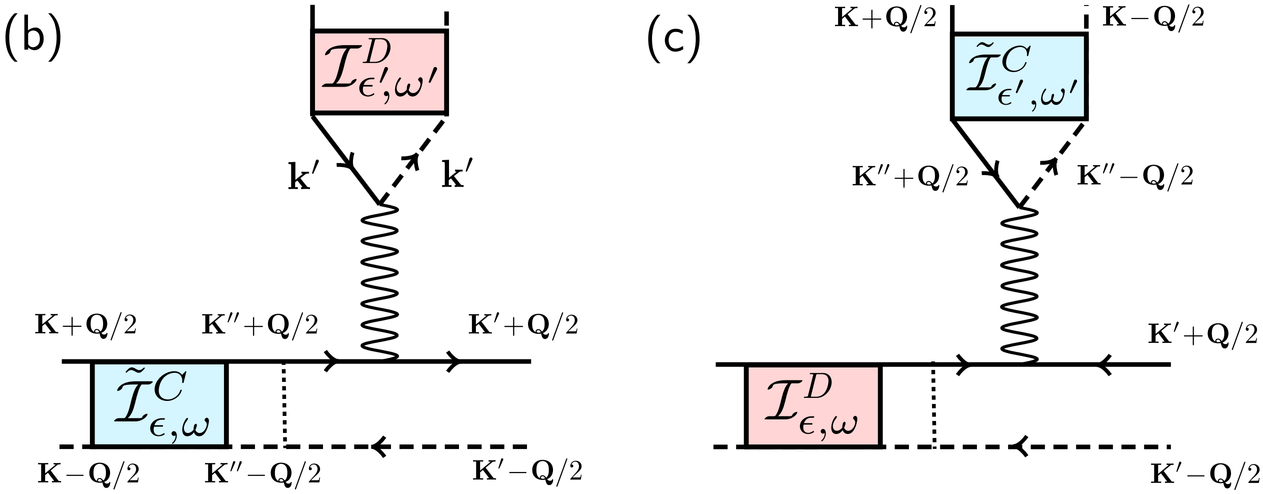

Figure 2.7 – First-order diagrams for the quantities $\tilde{\mathcal{I}}^{C\,(b)}_{\epsilon,\omega}(\boldsymbol{K},\boldsymbol{K}',\boldsymbol{Q})$ and $\tilde{\mathcal{I}}^{C\,(c)}_{\epsilon,\omega}(\boldsymbol{K},\boldsymbol{K}',\boldsymbol{Q})$, obtained from diagrams 2.6(b) and (c) by reversing the advanced Green's functions (and its $\boldsymbol{k}$-arguments), and performing the change of variables $\{\boldsymbol{K}=(\boldsymbol{k}-\boldsymbol{k}_0)/2=-\boldsymbol{K}',\boldsymbol{Q}=\boldsymbol{k}+\boldsymbol{k}_0\}$. Thanks to time-reversal invariance, they are equal to their corresponding diagram in Fig. 2.6: $\mathcal{I}^{C\,(b)}_{\epsilon,\omega}(\boldsymbol{k})\equiv\tilde{\mathcal{I}}^{C\,(b)}_{\epsilon,\omega}(\boldsymbol{K},\boldsymbol{K}',\boldsymbol{Q})$. In this form, it has a correct iterative structure, and can be added to the linear Bethe-Salpeter equation for the coherent component.

$$\begin{aligned}\mathcal{I}^{C\,(b)}_{\epsilon,\omega}(\boldsymbol{k}) &\equiv \tilde{\mathcal{I}}^{C\,(b)}_{\epsilon,\omega}(\boldsymbol{K},\boldsymbol{K}',\boldsymbol{Q})\\ &= 2g\rho_0\gamma\int\frac{\mathrm{d}\epsilon'}{2\pi}\frac{\mathrm{d}\omega'}{2\pi}\frac{\mathrm{d}^2\boldsymbol{k}'}{(2\pi)^2}\frac{\mathrm{d}^2\boldsymbol{K}''}{(2\pi)^2}\Big[\overline{G}^R_{\epsilon+\omega/2-\omega'}(\boldsymbol{K}'+\boldsymbol{Q}/2)\overline{G}^R_{\epsilon+\omega/2}(\boldsymbol{K}'+\boldsymbol{Q}/2)\\ &\qquad\times\overline{G}^A_{\epsilon-\omega/2}(\boldsymbol{K}-\boldsymbol{Q}/2)\mathcal{I}^D_{\epsilon',\omega'}(\boldsymbol{k}')\tilde{\mathcal{I}}^C_{\epsilon-\omega'/2,\omega-\omega'}(\boldsymbol{K},\boldsymbol{K}'',\boldsymbol{Q})\Big],\end{aligned} \tag{2.64}$$

where we have used that $\overline{G}^{(R/A)}_{\epsilon}(-\boldsymbol{k})=\overline{G}^{(R/A)}_{\epsilon}(\boldsymbol{k})$.

The rest of the calculation is very similar to what we did for diagram 2.3(a): we use identity (2.28) and compute the integral over ω' using the residue theorem on the only pole situated in the lower half-plane of the complex space, $\omega'=-i0^+$. We are left with :

$$\tilde{\mathcal{I}}^{C\,(b)}_{\epsilon,\omega}(\boldsymbol{K},\boldsymbol{K}',\boldsymbol{Q})=2g\rho_0\gamma\Big[\overline{G}^R_{\epsilon+\omega/2}(\boldsymbol{K}'+\boldsymbol{Q}/2)\Big]^2\overline{G}^A_{\epsilon-\omega/2}(\boldsymbol{K}-\boldsymbol{Q}/2)\int\frac{\mathrm{d}^2\boldsymbol{K}''}{(2\pi)^2}\tilde{\mathcal{I}}^C_{\epsilon,\omega}(\boldsymbol{K},\boldsymbol{K}'',\boldsymbol{Q}), \tag{2.65}$$

which is equivalent to :

$$\mathcal{I}^{C\,(b)}_{\epsilon,\omega}(\boldsymbol{k})=2g\rho_0\gamma\Big[\overline{G}^R_{\epsilon+\omega/2}(\boldsymbol{k})\Big]^2\overline{G}^A_{\epsilon-\omega/2}(\boldsymbol{k}_0)\int\frac{\mathrm{d}^2\boldsymbol{K}''}{(2\pi)^2}\tilde{\mathcal{I}}^C_{\epsilon,\omega}(\boldsymbol{k}-\boldsymbol{k}_0,\boldsymbol{K}'',\boldsymbol{k}+\boldsymbol{k}_0), \tag{2.66}$$

By proceeding exactly as in the last section, one can show that this diagram and its complex conjugate only amount to a constant shift $-2g\rho_0$ of the Green's functions energies in the linear Bethe-Salpeter equation for $\mathcal{I}^C_{\epsilon,\omega}(\boldsymbol{k})$, Eq. (1.94), derived in chapter 1. The conclusion is the same: since the spatial density is uniform, the energy shift has no impact on the dynamics. We will neglect the contribution of these diagrams in what follows.

Computation of diagram 2.6(c)

To compute diagram 2.6(c), we again start by reversing one of the counterpropagating Green's function, and performing the same change of variables as in the previous section. These transformations yield the equivalent diagram for $\tilde{\mathcal{I}}^{C\,(c)}_{\epsilon,\omega}(\boldsymbol{K},\boldsymbol{K}',\boldsymbol{Q})$, depicted in Fig. 2.7. Thanks to time-reversal invariance, the two diagrams are equal. Diagram 2.7(c) reads :

$$\begin{aligned}\tilde{\mathcal{I}}^{C\,(c)}_{\epsilon,\omega}(\boldsymbol{K},\boldsymbol{K}',\boldsymbol{Q}) = 2g\rho_0\gamma\int \frac{\mathrm{d}\epsilon'}{2\pi}\frac{\mathrm{d}\omega'}{2\pi}\frac{\mathrm{d}^2\boldsymbol{k}'}{(2\pi)^2}\frac{\mathrm{d}^2\boldsymbol{K}''}{(2\pi)^2}&\Big[\overline{G}^R_{\epsilon+\omega/2-\omega'}(\boldsymbol{K}'+\boldsymbol{Q}/2)\overline{G}^R_{\epsilon+\omega/2}(\boldsymbol{K}'+\boldsymbol{Q}/2)\\ &\times\overline{G}^A_{\epsilon-\omega/2}(\boldsymbol{K}'-\boldsymbol{Q}/2)\tilde{\mathcal{I}}^C_{\epsilon',\omega'}(\boldsymbol{K},\boldsymbol{K}'',\boldsymbol{Q})\mathcal{I}^D_{\epsilon-\omega'/2,\omega-\omega'}(\boldsymbol{k}')\Big].\end{aligned} \tag{2.67}$$

This time, we cannot use Eq. (2.28) to simplify Eq. (2.67). Instead, we use the expression (2.17) for $\mathcal{I}^C$ to perform the integration over ϵ' and $\boldsymbol{K}''$:

$$\begin{aligned}\int\frac{\mathrm{d}\epsilon'}{2\pi}\frac{\mathrm{d}^2\boldsymbol{K}''}{(2\pi)^2}\tilde{\mathcal{I}}^C_{\epsilon',\omega'}(\boldsymbol{K},\boldsymbol{K}'',\boldsymbol{Q}) &= \int\frac{\mathrm{d}\epsilon'}{2\pi}\frac{\overline{G}^R_{\epsilon'+\omega'/2}(\boldsymbol{K}+\boldsymbol{Q}/2)\overline{G}^A_{\epsilon'-\omega'/2}(\boldsymbol{K}-\boldsymbol{Q}/2)}{DQ^2\tau-i\omega'\tau}\\ &= \frac{1}{DQ^2-i\omega'},\end{aligned} \tag{2.68}$$

where we recall that $D=\epsilon_0\tau/m$ is the diffusion coefficient, taken on the energy shell. Here the second equality is only valid in the diffusive limit of long times $\omega'\tau\ll 1$ and over large distances $Q\ell\ll 1$. Using expression (2.16) for $\mathcal{I}^D$ in this limit, we also compute:

$$\int\frac{\mathrm{d}^2\boldsymbol{k}'}{(2\pi)^2}\mathcal{I}^D_{\epsilon-\omega'/2,\omega-\omega'}(\boldsymbol{k}') = \frac{\overline{G}^R_{\epsilon+\omega/2-\omega'}(\boldsymbol{k}_0)\overline{G}^A_{\epsilon-\omega/2}(\boldsymbol{k}_0)}{-i(\omega-\omega')+0^+}. \tag{2.69}$$

Substituting (2.68) and (2.69) into (2.67) yields:

$$\begin{aligned}\tilde{\mathcal{I}}^{C\,(c)}_{\epsilon,\omega}(\boldsymbol{K},\boldsymbol{K}',\boldsymbol{Q}) = 2g\rho_0\gamma\int\frac{\mathrm{d}\omega'}{2\pi}\frac{1}{(DQ^2-i\omega')(i\omega'-i\omega+0^+)}&\Big[\overline{G}^R_{\epsilon+\omega/2-\omega'}(\boldsymbol{K}'+\boldsymbol{Q}/2)\\ \times\overline{G}^R_{\epsilon+\omega/2}(\boldsymbol{K}'+\boldsymbol{Q}/2)\overline{G}^A_{\epsilon-\omega/2}(\boldsymbol{K}'-\boldsymbol{Q}/2)&\overline{G}^R_{\epsilon+\omega/2-\omega'}(\boldsymbol{k}_0)\overline{G}^A_{\epsilon-\omega/2}(\boldsymbol{k}_0)\Big].\end{aligned} \tag{2.70}$$

One can check that this expression has only one pole in the lower complex half-plane with respect to the integration over ω'. The residue theorem applied to this pole, $\omega'=-iDQ^2$, gives:

$$\tilde{\mathcal{I}}^{C\,(c)}_{\epsilon,\omega}(\boldsymbol{K},\boldsymbol{K}',\boldsymbol{Q}) = 2g\rho_0\gamma\frac{1}{(DQ^2 - i\omega + 0^+)}\Big[\overline{G}^R_{\epsilon+\omega/2+iDQ^2}(\boldsymbol{K}'+\boldsymbol{Q}/2) \tag{2.71}$$
$$\times\overline{G}^R_{\epsilon+\omega/2}(\boldsymbol{K}'+\boldsymbol{Q}/2)\overline{G}^A_{\epsilon-\omega/2}(\boldsymbol{K}'-\boldsymbol{Q}/2)\overline{G}^R_{\epsilon+\omega/2+iDQ^2}(\boldsymbol{k}_0)\overline{G}^A_{\epsilon-\omega/2}(\boldsymbol{k}_0)\Big]\,.$$

Finally, we get for diagram 2.6(c), in the diffusive limit :

$$\mathcal{I}^{C\,(c)}_{\epsilon,\omega}(\boldsymbol{k}) = 2g\rho_0\gamma\frac{\Big[\overline{G}^R_{\epsilon+\omega/2+iD(\boldsymbol{k}+\boldsymbol{k}_0)^2}(\boldsymbol{k}_0)\Big]^2\,\overline{G}^R_{\epsilon+\omega/2}(\boldsymbol{k}_0)\overline{G}^A_{\epsilon-\omega/2}(\boldsymbol{k})\overline{G}^A_{\epsilon-\omega/2}(\boldsymbol{k}_0)}{D(\boldsymbol{k}+\boldsymbol{k}_0)^2 - i\omega + 0^+}. \tag{2.72}$$

When $\boldsymbol{k} = -\boldsymbol{k}_0$, i.e. in the backscattering direction, it is straightforward to see that all three diagrams 2.3(a), 2.6(b) and (c) are equal. In this case, the contribution of diagram 2.6(c) can be recast as an additional shift of $-2g\rho_0$ of the Green's functions energy, which has no effect on the dynamics, and is negligible within our limit (2.22). On the other hand, for any $\boldsymbol{k} \neq -\boldsymbol{k}_0$, this expression is of order $1/k_0\ell$ because of the diffusion coefficient $D \propto k_0\ell$ in the denominator. It can therefore be safely neglected in the weak disorder limit $k_0\ell \gg 1$.

At this stage, an important comment is in order. In the stationary scenario considered in [204, 205, 209], it was shown that specific concatenations of the diagram 2.6(c) were leading to a dephasing between the reversed amplitudes, which could even change the sign of the coherent backscattering peak. We just showed, however, that, in the present dynamical setup, these combinations have a negligible weight. To get a more intuitive approach of this phenomenon, we show in a more visual fashion in Fig. 2.8 one example of interference sequence between time-reversed paths built from diagram 2.6(c). The peculiarity of this sequence is that both the direct (solid) path and its time-reversed (dashed) partner are involved in the particle interaction process. If the direct path undergoes the interaction process at a certain time t_{coll}, and thus the time-reversed path at time $t - t_{\text{coll}}$, the temporal locality of the interactions imposes that $t_{\text{coll}} = t - t_{\text{coll}}$, i.e. that $t_{\text{coll}} = t/2$. In other words, the interaction event must occur at a very specific time (more precisely, within a time window of width $1/k_0\ell$, centered around $t/2$). Within such a short time window, and given the condition (2.22), it is highly improbable that two (or more) collisions occur. Any concatenation of diagrams 2.6(c) can thus be safely neglected here. Note the similarities of this reasoning with the experimental protocol of Ref. [22], where a dephasing pulse applied to a system of 2d ultracold atoms in disorder at a specific time t lead to a destruction (for $t \neq T/2$, where T is the average time needed for the atoms to go trough the crossed scattering sequence) and a revival (for $t = T/2$) of the CBS peak.

In summary, in this section, we have demonstrated that all leading-order corrections in g to the Bethe-Salpeter equation for the coherent component are either negligible or have no impact on the dynamics: an examination of the second order diagrams is again required.

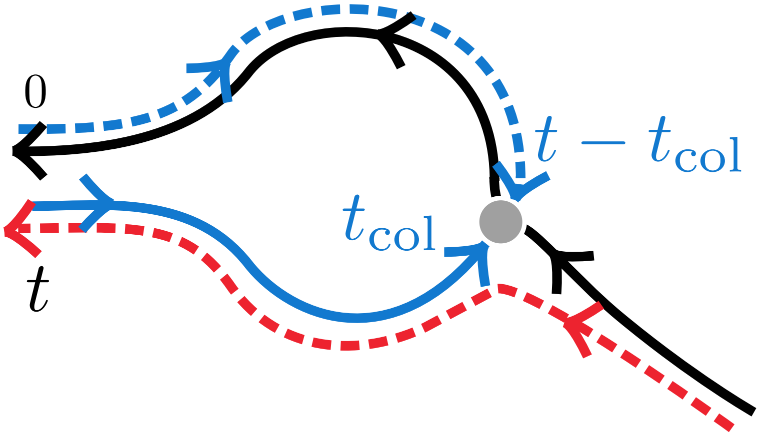

Figure 2.8 – Example of interference sequence generated by the diagram in Fig. 2.6(c) (for a better visualization, we momentarily change the definition of arrows, which here always indicate the direction of propagation. black (resp. red) arrows represent retarded (resp. advanced) Green's functions). Blue arrows represent the hypothetical path followed by two amplitudes starting at opposite sides of the sequence at $t = 0$, if they were to meet at a specific point in space to interact (here represented by the grey circle). The direct path, starting at $t = 0$, undergoes a particle interaction event at t_{col}, and the time reversed-path at $t - t_{\mathrm{col}}$. The interaction being local in time, we must have $t_{\mathrm{col}} = t/2$. The interaction event must occur within a very narrow time window, of the order of $1/k_0\ell$. Within such a short window, it is highly improbable that several interaction events can occur (remember that we chose g small to have rare interaction events). As a consequence, any concatenation of this diagram is negligible, of order $1/k_0\ell$.

2.4.2 Second-order corrections

We now examine all the second-order corrections to the Bethe-Salpeter equation for the coherent component. To write down all possible diagrams, one good method is to start from the diffusive diagrams of Fig. 2.5, and try to replace one (or more) diffusive intensities $\mathcal{I}^D$ with counterpropagating intensities $\mathcal{I}^C$, by reversing one of the outgoing arrows. One then just needs to check if the new diagrams respect the rules of Fig. 2.2.

Negligible diagrams

We have found 13 topologically different second-order diagrams that can be built from combinations of $\mathcal{I}^D$ and $\mathcal{I}^C$. However, as explained in the caption of Fig. 2.8 – and proven in the specific case of diag. 2.6(c) –, any concatenation of a diagram where two counterpropagating amplitudes participate in the same interaction event is expected to be of order $1/k_0\ell$ at long enough times, and thus negligible in the weak-disorder limit. We can therefore safely neglect the second order diagrams for which it is the case.

For example, the interference counterpart of the upper-right diagram in Fig. 2.5 contains two counterpropagating amplitudes that participate in the same interaction event, and is thus negligible at long time. To give another intuitive example for this argument, we show in Fig. 2.9 an interference sequence that would correspond to the upper-right diagram in Fig. 2.5 in which an amplitude is time-reversed. It is a second-order example of the mechanism of Fig. 2.8: here, again, because the two interaction processes involve both the direct and the reversed paths, they must occur almost simultaneously, at $t_{\text{col}} \simeq t/2$, which is extremely improbable given the rarity of particle collisions that we assume. This type of diagram is thus negligible.

Expression of the Bethe-Salpeter equation

All non-negligible second-order corrections to be added to the linear Bethe-Salpeter equation for time-reversed sequences are shown in Fig. 2.10. Note that, as compared to the diffusive corrections in Fig. 2.5, there are only four different topologies, and not five. These topologies are the same as those of the four last diffusive diagrams in Fig. 2.5. Consequently, the Bethe-Salpeter equation for $\mathcal{I}^C_{\epsilon,\omega}$ is similar to Eq. (2.45): after using the time-reversal invariance and a change of variables for the momenta as we already did several times in Sec. 2.4.1, we essentially recover the same equation as for the diffusive case, except for the missing diagram :

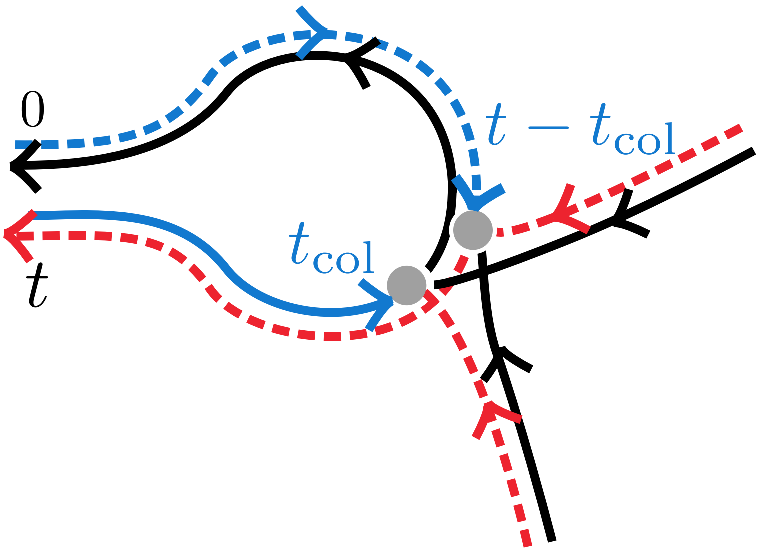

Figure 2.9 – Example of interference sequence between time-reversed paths involving two collisions (for a better visualization we momentarily change the definition of arrows, which here always indicate the direction of propagation). Black (resp. red) arrows represent retarded (resp. advanced) Green's functions. As for the diagram of Fig. 2.8, the interaction processes involve both the direct and the reversed paths. This imposes them to occur almost simultaneously, at $t_{\mathrm{col}} \simeq t/2$, which is very unlikely. This diagram is therefore negligible.

$$
\begin{aligned}
\mathcal{I}^C_{\epsilon,\omega}(\boldsymbol{k}) = \tilde{\mathcal{I}}^C_{\epsilon,\omega}(\boldsymbol{K},\boldsymbol{K}',\boldsymbol{Q}) = \overline{G}^R_{\epsilon+\omega/2}(\boldsymbol{K}'+\boldsymbol{Q}/2)\overline{G}^A_{\epsilon-\omega/2}(\boldsymbol{K}'-\boldsymbol{Q}/2)\Bigg[\ (2\pi)^2\delta(\boldsymbol{K}-\boldsymbol{K}') \\
+\gamma\int\frac{\mathrm{d}^2\boldsymbol{K}''}{(2\pi)^2}\tilde{\mathcal{I}}^C_{\epsilon,\omega}(\boldsymbol{K},\boldsymbol{K}'',\boldsymbol{Q}) + (g\rho_0\gamma)^2\Big[\prod_{i=1,2}\int\frac{\mathrm{d}\epsilon_i\mathrm{d}\omega_i}{(2\pi)^4}\frac{\mathrm{d}^2\boldsymbol{k}_i\mathrm{d}^2\boldsymbol{k}'_i}{(2\pi)^8}\mathcal{I}^D_{\epsilon_i,\omega_i}(\boldsymbol{k}'_i)\overline{G}^R_{\epsilon_i+\omega_i/2}(\boldsymbol{k}_i)\overline{G}^A_{\epsilon_i-\omega_i/2}(\boldsymbol{k}_i)\Big] \\
\times\Bigg\{\gamma\Big(4\overline{G}^R_{\epsilon_4+\Omega_1/2}(\boldsymbol{K}_4+) + 2\overline{G}^A_{\epsilon_3-\Omega_1/2}(\boldsymbol{K}_3+)\Big)\overline{G}^R_{\epsilon+\Omega_2}(\boldsymbol{K}'+\boldsymbol{Q}/2)\int\frac{\mathrm{d}^2\boldsymbol{K}''}{(2\pi)^2}\tilde{\mathcal{I}}^C_{\epsilon_5,\Omega_1}(\boldsymbol{K},\boldsymbol{K}'',\boldsymbol{Q}) \\
+\gamma\Big(4\overline{G}^A_{\epsilon_4-\Omega_1/2}(\boldsymbol{K}_4-) + 2\overline{G}^R_{\epsilon_3+\Omega_1/2}(\boldsymbol{K}_3-)\Big)\overline{G}^A_{\epsilon-\Omega_2}(\boldsymbol{K}'-\boldsymbol{Q}/2)\int\frac{\mathrm{d}^2\boldsymbol{K}''}{(2\pi)^2}\tilde{\mathcal{I}}^C_{\epsilon_6,\Omega_1}(\boldsymbol{K},\boldsymbol{K}'',\boldsymbol{Q})\Bigg\}\Bigg],
\end{aligned}
\tag{2.73}
$$

where we defined $\epsilon_3 = \epsilon_1 + \epsilon_2 - \epsilon$, $\epsilon_4 = \epsilon + \epsilon_1 - \epsilon_2$, $\epsilon_5 = \epsilon - (\omega_1+\omega_2)/2$, $\epsilon_6 = \epsilon + (\omega_1+\omega_2)/2$, $\Omega_1 = \omega - \omega_1 - \omega_2$, $\Omega_2 = \omega/2 - \omega_1 - \omega_2$ for energies, and $\boldsymbol{K}_3(\pm) = \boldsymbol{k}_1 + \boldsymbol{k}_2 - \boldsymbol{K}' \mp \boldsymbol{Q}/2$, $\boldsymbol{K}_4(\pm) = \boldsymbol{K}' \pm \boldsymbol{Q}/2 + \boldsymbol{k}_1 - \boldsymbol{k}_2$ for momenta. We recall that the change of variables used after reversing one of the trajectories is : $\{\boldsymbol{K} = (\boldsymbol{k}_0 - \boldsymbol{k})/2 = -\boldsymbol{K}'; \boldsymbol{Q} = \boldsymbol{k}_0 + \boldsymbol{k}\}$.

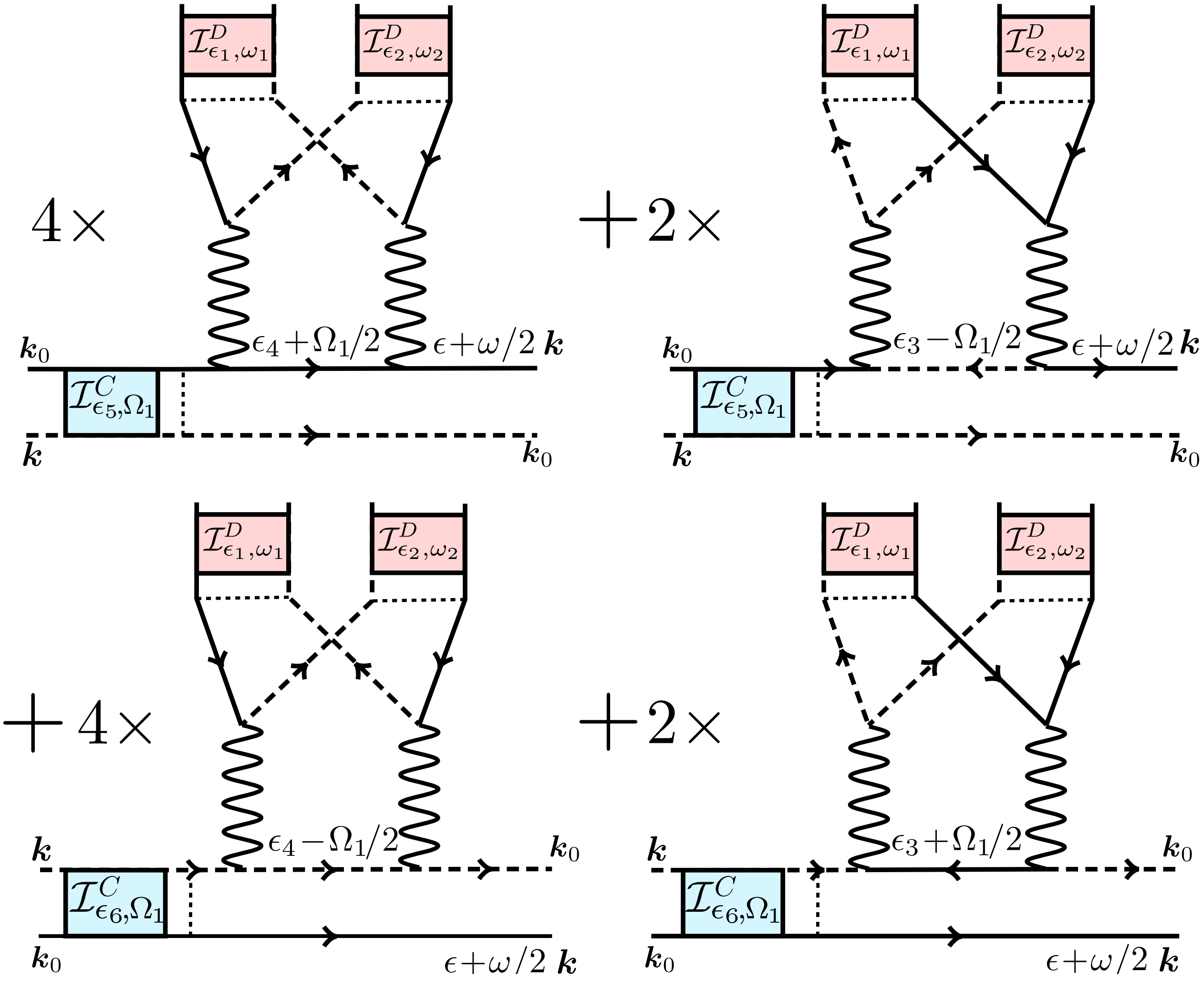

Figure 2.10 – Second-order corrections to the Bethe-Salpeter equation for the CBS contribution to the momentum distribution, $\mathcal{I}^C_{\epsilon,\omega}(\boldsymbol{k})$. Symbols have the same meaning as in Fig. 2.6. Recall that the two wave paths involved in the blue boxes propagate in opposite directions (the incoming and outgoing momenta $\boldsymbol{k}_0$ and $\boldsymbol{k}$ are explicitly indicated for clarity). The numerical prefactors account for the possible combinations of propagation lines connecting to the vertex g.

.

2.4.3 Kinetic equation for the CBS modes

The derivation of the collision integral follows the exact same steps as in Sec. 2.3.4 in the diffusive case. For this reason and for clarity, we do not rewrite the whole calculation explicitly in this section.

Collision integral

By closely following the derivation of Sec. 2.3.4, one can easily see that the missing diagram, i.e. the missing term in Eq. (2.73) compared to the diffusive case, is the one responsible for the term $\propto f_{\epsilon_1+\epsilon_2-\epsilon} f_{\epsilon_1} f_{\epsilon_2}$ in Eq. (2.57). Because of this missing term, the factor $f^C_\epsilon(t)$ present in each of the other terms of the collision integral can be factored out. Precisely, following the exact same steps as before, we obtain, for the "coherent" occupation number f^C_ϵ defined in (2.47), the kinetic equation

$$\partial_t f^C_\epsilon = f^C_\epsilon \int_{\epsilon_1,\epsilon_2,\epsilon_3\geq 0} \mathrm{d}\epsilon_1 \mathrm{d}\epsilon_2 \, W(\epsilon,\epsilon_1,\epsilon_2) \Big[f_{\epsilon_1} f_{\epsilon_2} - f_{\epsilon_3}(f_{\epsilon_1} + f_{\epsilon_2}) \Big], \tag{2.74}$$

where $\epsilon_3 \equiv \epsilon_1 + \epsilon_2 - \epsilon$, and the kernel W is still given by Eqs. (2.62). The initial condition is again set by the non-interacting limit, $f^C_\epsilon(t=0) = f^{(0)}_\epsilon$.

CBS peak amplitude

As in the diffusive case, we integrate the iterative equation for $\mathcal{I}^C$ over the energy ϵ, and take its Fourier transform with respect to ω. In the long-time limit, and neglecting terms of higher order in g, we infer the momentum-space amplitude of the coherent backscattering peak:

$$\overline{|\psi^C(-\boldsymbol{k}_0, t)|^2} = \int_{-\infty}^{\infty} \mathrm{d}\epsilon \, A_\epsilon(\boldsymbol{k}_0) f^C_\epsilon(t). \tag{2.75}$$

At this stage, we already expect the asymmetry between the kinetic equations for f^C_ϵ and f_ϵ to induce different dynamical evolutions of the CBS peak and diffusive background. Furthermore, due to the missing term (which has a positive sign), the norm of the coherent distribution decreases as a function of time, whereas it is conserved in the diffusive case. As will be described in chapter 3, this in turn leads to a decay of the CBS peak (relative to the diffusive ring) at long time[3].

---

[3] As is well known, adding CBS to the diffusive contribution leads to a breakdown of global normalization when $g=0$. This is also the case when $g \neq 0$, as seen from the fact that $\int \mathrm{d}\epsilon \, \nu_\epsilon f^C_\epsilon(t) \neq 0$. Restoring such a normalization requires a fine account of weak localization corrections [125, 227], which is beyond the scope of this manuscript.

Conclusion

In this chapter, we have constructed a microscopic diagrammatic theory describing the out-of-equilibrium evolution of a weakly interacting disordered Bose gas in momentum space. Assuming weak disorder and rare particle collisions, we have extended the linear, non-interacting diagrammatic theory of the previous chapter to derive coupled kinetic equations for the two main physical processes at work in this regime, particle diffusion and coherent backscattering. Our approach has revealed a noticeable asymmetry in the kinetic equations for these two contributions. As will be seen in the next chapter, this asymmetry is in turn responsible for a decay of the CBS peak contrast. We will also confirm this phenomenon with ab initio numerical simulations for the disordered Gross-Pitaevskii equation.

Chapter 3

Coherent backscattering and diffusion in 2d interacting Bose gases: kinetic theory vs. numerics

Introduction

In this chapter, we detail the predictions of the kinetic theory developed in chapter 2 for the out-of-equilibrium dynamics of a Bose gas in two dimensions, focusing on the regime of short times. We also compare these predictions to ab initio Gross-Pitaevskii simulations. In the first part of the chapter, we describe our numerical implementation of these simulations, which rely on separate treatments of the disorder and the nonlinearity. Our numerical code gives access to the full time-evolution of the condensate wavefunction (and thus, to all dynamical observables), starting from any initial state in an arbitrary random potential. In the second part, we present an in-depth numerical study of the short-time evolution of the momentum distribution, and confront it with the predictions of the kinetic equations derived in chapter 2. Obtaining an analytical solution at all times for the kinetic equations is a difficult problem, so we start by solving the latter numerically and find a good qualitative agreement with the ab initio simulations. We then develop semi-analytical approximations of the kinetic equations at short times, which yield an estimation of the time scales associated with the dynamics of both the diffusive ring and the coherent backscattering (CBS) peak, again in good agreement with the simulations. In particular, we provide theoretical predictions for the temporal decay of the contrast of the CBS peak, which measures how sensitive to interactions are the diffusive and the weakly localized modes of the gas. Finally, we also show that the simulated momentum distribution is accurately matched by the kinetic theory over relatively long times, during which interactions slowly turn the diffusive ring into a thermal state. In this chapter, we set $\hbar = 1$ and $m = 1$ for convenience.

3.1 Numerical implementation of the 2d Gross-Pitaevskii equation

In this section, we describe our numerical implementation of the Gross-Pitaevskii equation for interacting cold atoms in a disorder potential:

$$i\partial_t \psi(\boldsymbol{r},t) = \left[-\frac{\Delta^2}{2} + V(\boldsymbol{r}) + g|\psi(\boldsymbol{r},t)|^2\right]\psi(\boldsymbol{r},t) = \mathcal{H}\psi(\boldsymbol{r},t), \tag{3.1}$$

where ψ is the condensate wavefunction, V is the disorder potential and g is the interaction strength.

3.1.1 Discretization of space and time

To propagate numerically a given initial condition $\psi(\boldsymbol{r}, t = 0)$ with equation (3.1), we start by discretizing the space on a regular grid of size $\mathcal{V} = L_x \times L_y$ with lattice spacing a. We also define an reference length scale L_0, from which all the length scales of the original problem will be expressed. The amount of discretization of the system is controlled by the ratio L_0/a, which represents the number of numerical points per unit of physical length. Our theoretical results from the previous chapters being derived in continuous space, we ideally want to compare them with simulations in the continuous limit $L_0/a \to \infty$. In practice, it is sufficient to choose a discretization fine enough so that all the relevant length scales of the system are well resolved. Throughout the manuscript, when discussing simulation results, we express momenta in units of $1/L_0$, length in L_0, times in L_0^2, and energies in $1/L_0^2$. The disorder amplitude γ is also expressed in $1/L_0^2$. When the discretization a is not specified, it is implicitly assumed equal to 1.

The space being of finite size, we also impose periodic boundary conditions, in order to minimize boundary effects. Still, L_x and L_y must be chosen large enough, typically much larger than the mean free path ℓ. We denote the value of the discrete wavefunction on site (i, j) at time t by $\psi_{i,j}(t)$. In discretized space, the Laplacian in equation (3.1) is replaced by its discrete version:

$$\Delta\psi_{i,j}(t) = \frac{\psi_{i+1,j}(t) + \psi_{i-1,j}(t) + \psi_{i,j+1}(t) + \psi_{i,j-1}(t) - 4\psi_{i,j}(t)}{a^2}, \tag{3.2}$$

and the full Gross-Pitaevskii equation reads

$$i\partial_t\psi_{i,j}(t) = -\frac{\Delta\psi_{i,j}(t)}{2} + V_{i,j}\psi_{i,j}(t) + g|\psi_{i,j}(t)|^2\psi_{i,j}(t), \tag{3.3}$$

where $V_{i,j}$ is the value of the random potential on site (i, j). For $V = 0$ and $g = 0$, one recovers the stationary plane wave solutions of the free Hamiltonian by solving $\mathcal{H}\psi_{i,j} = \epsilon\psi_{i,j}$

$$\psi_{i,j} = \frac{1}{\sqrt{\mathcal{V}}} e^{i(k_x ia + k_y ja)} \qquad \left(k_x = \frac{n\pi}{L_x}, k_y = \frac{m\pi}{L_y} \quad n, m \in \mathbb{Z} \right) \tag{3.4}$$

with the corresponding periodic dispersion relation

$$\epsilon(k_x, k_y) = \frac{2 - \cos(k_x a) - \cos(k_y a)}{a^2} \simeq \frac{k_x^2 + k_y^2}{2} \quad \text{if} \quad (k_x, k_y) \ll 1. \tag{3.5}$$

Accessible energies are thus comprised between 0 and $4/a^2$, and all integrations over momenta should be done over the first Brillouin zone $-\pi/a \leq k_{x/y} < -\pi/a$. Note that in the non-interacting case $g = 0$, this problem is directly mapped onto the 2d version of the Anderson problem with the hopping term $t = -1/2a^2$ by shifting the energies (3.5) by the constant term $2/a^2$ [126]. This discretization of space provides a simple representation of the physical system, with the considerable advantage that the application of the discrete disorder Hamiltonian to $\psi_{i,j}$

$$\mathcal{H}_0 \psi_{i,j} \equiv \mathcal{H}_{(g=0)} \psi_{i,j} = -\frac{\Delta \psi_{i,j}}{2} + V_{i,j} \psi_{i,j} \tag{3.6}$$

is a sparse matrix in configuration space, where the disorder is diagonal ($\langle i', j' | V | i, j \rangle = V_{i,j} \delta_{i,i'} \delta_{j,j'}$) and the Laplacian (3.2) only involves neighboring sites. Any computation involving products of this matrix is thus performed efficiently. In return, the dispersion relation and the density of states (see Fig. 3.3) are modified, so that a comparison of numerical results with real experiments requires a very small discretization step a, which is computationally demanding. We could also discretize the Laplacian over more points (for example by taking into account the second neighbors), which reduces discretization effects on the dispersion relation but also reduces the sparsity of the Hamiltonian, implying larger computation times. In this thesis however, the physical phenomena we are interested in are in essence not sensitive to a change of the dispersion relation or the density of states, so we make the choice of efficiency by using (3.2) and a spatial step only small enough to resolve the characteristic length scales of the problems.

3.1.2 Generation of a random potential

Generating an uncorrelated potential on a spatial grid does not represent a challenge: one simply needs to pick a value following the desired distribution for each lattice site. In this manuscript, we mostly use a Gaussian uncorrelated potential, whose discrete spatial correlations read

$$\overline{V_{\boldsymbol{r}} V_{\boldsymbol{r}'}} = \gamma \delta_{\boldsymbol{r},\boldsymbol{r}'} / a^2, \tag{3.7}$$

where δ is the *Kronecker* delta. Note that in practice, due to the discretization, the uncorrelated potential is effectively correlated over the lattice spacing a. However, since we perform simulations using correlated potentials in chapter 4, we describe their implementation here. In cold atom experiments where optical speckle potentials are the most common, the disorder potential is modeled by the intensity in the far-field reflection (or transmission) on a thin plate displaying a certain amount of disorder (see e.g [21, 228]). To impose a certain spatial correlation on the final potential, one generally puts a mask on top of the plate, which imprints its own Fourier transform on top of the far-field intensity, serving as a spatial correlation function. For example, the application of a Gaussian mask on the plate will result in a Gaussian correlation function proportional to $\exp(-\boldsymbol{r}^2/2\sigma^2)$, where the correlation length σ depends on the distance between the plate and the observation plane, the wavelength of the laser and the size of the mask [7, 8, 175]. Numerically, we proceed in analogy with this protocol: after generating an uncorrelated disorder with given distribution, we compute the convolution of this grid with the desired correlation function (the Fourier transform of our "mask"). This convolution is done simply in Fourier space, where it reduces to a simple multiplication. Taking the modulus square of the convolution then produces the desired disorder potential. A visual example of the results is displayed on Fig. 3.1. Note that when the disorder potential is correlated, we choose the correlation length σ as the reference length scale for the system.

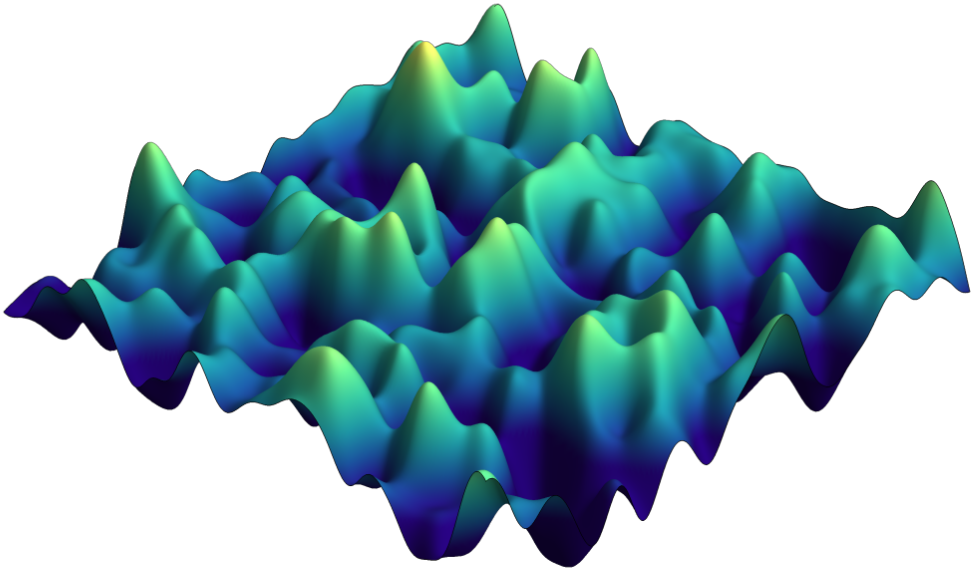

Figure 3.1 – Visual representation of a numerically generated disorder potential, with a Gaussian on-site distribution and Gaussian spatial correlation. The presented sample has dimensions $25\sigma \times 25\sigma$, where σ is the correlation length. The spatial discretization step a is chosen small enough compared to σ to have a smooth 3d plot.

3.1.3 Propagation in the non-interacting case

After generating the disorder potential, we want to perform the temporal evolution of a given initial state $|\psi(t=0)\rangle$ with equation (3.1). We start with the non-interacting case $g=0$. The formal solution to the Schrödinger equation is written

$$|\psi(t)\rangle = \hat{U}(t)\,|\psi(t=0)\rangle = e^{-i\mathcal{H}_0 t}\,|\psi(t=0)\rangle\,. \tag{3.8}$$

where $\hat{U}(t)$ is known as the evolution operator of the system. The knowledge of $\hat{U}$ at all times is sufficient to derive the whole time-evolution. Thus we need to find a representation for the exponential which allows for an efficient numerical approximation. A direct diagonalization of the Hamiltonian is of course excluded because of the large dimension of the Hilbert space. For this kind of problem, one usually relies on iterative methods, in which the wavefunction is evaluated at successive intervals of time δt. The simplest approach is a so-called split-step algorithm: the evolution of the wave function over a time period δt is performed by splitting the evolution operator into the product of the kinetic part and the disorder part

$$\exp(-i\mathcal{H}_0\delta t) \simeq \exp(+i\Delta/2\delta t)\exp(-iV\delta t). \tag{3.9}$$

The disorder and kinetic parts are then computed and applied to the wave function respectively in configuration and momentum space, where they are diagonal. Switching from one space to the other is conveniently done by performing a fast Fourier transform. In practice, we have found that such a method is rather slow when the discretization step a is not very small, which is our case here. Likewise, explicit numerical methods of solving partial differential equation such as the simple Euler or Runge-Kutta methods are known to be rather inefficient for long-time propagation, as they require a small time step δt to guarantee numerical stability [229]. Implicit methods, like the Crank-Nicholson algorithm [230], generally display better numerical stability, in theory allowing the use of a larger δt, but require to solve large linear systems of equations, which remains computationally demanding. Moreover, the precision of this algorithm in only of the order of $\mathcal{O}(\delta t^2)$, which still imposes a rather small discretization of time for reasonably accurate results. Both of these problems can be tackled by performing an expansion of the evolution operator in Chebychev polynomials of the Hamiltonian, as described in [231–234]. As we will see, the method is particularly adapted to our case, where a is not required to be very small, hence the spectrum of the Hamiltonian typically extends over a small energy range $\sim [0, 4/a^2]$. In these conditions, the algorithm, described in detail in the rest of this subsection, proves to be rather fast, and is essentially exact, the error being exponentially small with the number of terms kept in the Chebychev expansion, and thus scaling like $\exp(-\alpha/\delta t)$, with α a fixed number, as explained in section 3.1.3.

Chebychev polynomials

Chebychev polynomials are a family of polynomials $(T_n)_{n\in\mathbb{N}}$ which are usually defined iteratively by the sequence [235]:

$$\begin{cases} T_{n+1}(x) = 2xT_n(x) - T_{n-1}(x), \\ T_0(x) = 1,\, T_1(x) = x. \end{cases} \tag{3.10}$$

The Chebychev polynomial T_n is of degree n and can be expressed as $T_n(x) = \cos\left(n \arccos(x)\right)$. An interesting property of these polynomials is that they form an orthogonal basis of the set of piecewise smooth and continuous functions over a normed vector space. Their orthogonality relation reads

$$\int_{-1}^{1} \mathrm{d}x \frac{T_n(x)T_m(x)}{\sqrt{1-x^2}} = \frac{\pi}{2}\delta_{n,m}(2-\delta_{n,0}). \tag{3.11}$$

As a consequence, any function f suitably defined over the vector space can be expanded into a Chebychev series

$$f(x) = \sum_{n=0}^{+\infty} c_n T_n(x), \tag{3.12}$$

whose convergence is assured for $|x| < 1$.

Expansion of the evolution operator over Chebyshev polynomials

The Chebyshev series (3.12) converges only for $|x| < 1$, so it cannot be directly used to expand the evolution operator $e^{-i\mathcal{H}_0 t}$, because the spectrum of the Hamiltonian $\mathcal{H}_0$ is unknown, due to the presence of the disorder potential, which can display rare events of large magnitude. To overcome this obstacle, we rescale the energy spectrum by performing the following transformation:

$$\begin{aligned} \mathcal{H}_0' &= \frac{\mathcal{H}_0 - E_1}{E_2} \\ E_1 &= \frac{\epsilon_{\text{max}} + \epsilon_{\text{min}}}{2} \\ E_2 &= \frac{\epsilon_{\text{max}} - \epsilon_{\text{min}}}{2} \end{aligned} \tag{3.13}$$

where ϵ_{max} and ϵ_{min} are the bounds of the energy spectrum. The new Hamiltonian $\mathcal{H}_0'$ has all its eigenvalues in $[-1, 1]$, and the evolution operator reads

$$\hat{U}(t) = \mathrm{e}^{-i\mathcal{H}_0 t} = e^{-iE_1 t} e^{-iE_2 \mathcal{H}_0' t}. \tag{3.14}$$

The quantity $e^{-iE_2\mathcal{H}_0't}$ can then be decomposed over the basis of Chebychev polynomials as

$$e^{-iE_2\mathcal{H}_0't} = \sum_{n=0}^{+\infty} c_n T_n(\mathcal{H}_0'), \tag{3.15}$$

and the value of the coefficients c_n follow directly from the orthogonality relation (3.11):

$$\begin{aligned} c_0 &= \frac{2}{\pi}\int_{-1}^{1} \mathrm{d}x \frac{\mathrm{e}^{-iE_2xt}}{\sqrt{1-x^2}} = 2J_0(E_2t) \\ c_n &= \frac{1}{\pi}\int_{-1}^{1} \mathrm{d}x \frac{T_n(x)\mathrm{e}^{-iE_2xt}}{\sqrt{1-x^2}} = (-i)^n J_n(E_2t), \end{aligned} \tag{3.16}$$

where $J_n(x)$ is the n^{th} order Bessel function of the first kind. In the numerical implementation, we never explicitly form the operator of Eq. (3.15), but rather work with the object

$$e^{-iE_2\mathcal{H}_0't}\left|\psi(t=0)\right\rangle = \sum_{n=0}^{+\infty} c_n T_n(\mathcal{H}_0')\left|\psi(t=0)\right\rangle. \tag{3.17}$$

The $T_n(\mathcal{H}_0')\left|\psi(t=0)\right\rangle$ are then computed from the recurrence relation

$$T_{n+1}(\mathcal{H}_0')\left|\psi(t=0)\right\rangle = 2\mathcal{H}_0'[T_n(\mathcal{H}_0')\left|\psi(t=0)\right\rangle] - T_{n-1}(\mathcal{H}_0')\left|\psi(t=0)\right\rangle, \tag{3.18}$$

where the most computationally demanding operation $2\mathcal{H}_0'[T_n(\mathcal{H}_0')\left|\psi(t=0)\right\rangle]$ is optimized by using the fact that $\mathcal{H}_0'$ is sparse. In fact, at this stage, the computation of the sum in (3.17) is even further optimized by the use of the so-called "Clenshaw" trick [236]. This method allows for minimal memory usage, by performing an efficient reordering of the sum in powers of $\mathcal{H}_0'$.

Choice of the truncation order

In practice, we have to truncate the full series at a certain order. This is where the decomposition over Chebychev polynomials proves very effective: as it turns out, for large n, the first order Bessel function J_n decays exponentially with n [225]. Consequently, provided the truncation of the series is at large enough order, the finite sum yields a quasi-exact approximation of the evolution operator. More precisely, the Bessel function $J_n(E_2t)$ being exponentially small when $n \gg E_2t$ [225], the truncation of the series at order $n_{\max}$ allows for a precise estimation of the evolution operator up to a time $t \simeq n_{\max}/E_2$. The iterative computation of the Chebyschev polynomials being numerically stable up to very large orders, there is a priori no need to split the time evolution into small steps $t = m\delta t$: using (3.18) to compute m times the sum (3.17) up to order $N = \delta t E_2$ is equivalent to computing it once up to order $N' = tE_2 = mN$. We will see, however, that the treatment of the nonlinearity at $g \neq 0$ requires to use small time steps δt, in which case the former solution is used.

Estimation of the bounds of the spectrum

A precise estimation of ϵ_{min} and ϵ_{max} for a given realization of the disorder is important for the efficiency of the procedure: the larger the value of their difference E_2, the higher is the order n_{max} at which we need to evaluate the series. Absolute bounds for the spectrum of $\mathcal{H}$ can be naively estimated by taking the lowest and largest possible values for both the kinetic and the disorder potential energy:

$$\begin{aligned}\epsilon^{\text{abs}}_{\text{min}} &= V_{\text{min}}\\ \epsilon^{\text{abs}}_{\text{max}} &= \frac{4}{a^2} + V_{\text{max}}.\end{aligned} \tag{3.19}$$

However, a simple minimization procedure yields more precise bounds for the spectrum of the Hamiltonian: for an arbitrary state $|\phi\rangle$ which is not orthogonal to the eigenstate of $\mathcal{H}$ with the lowest (resp. highest) eigenvalue, we have

$$\left|(\mathcal{H} - \epsilon^{\text{abs}}_{\text{min}})^n \, |\phi\rangle\right|^2 \overset{n\to\infty}{\sim} \left(\epsilon_{\text{max}} - \epsilon^{\text{abs}}_{\text{min}}\right)^{2n}, \tag{3.20}$$

$$\left|(\mathcal{H} - \epsilon^{\text{abs}}_{\text{max}})^n \, |\phi\rangle\right|^2 \overset{n\to\infty}{\sim} \left(\epsilon_{\text{min}} - \epsilon^{\text{abs}}_{\text{max}}\right)^{2n}, \tag{3.21}$$

In practice, to evaluate ϵ_{max} (resp. ϵ_{min}), we choose for $|\psi\rangle$ an eigenstate of the free Hamiltonian with the highest (resp. lowest) possible energy, i.e the plane wave $|\boldsymbol{k}\rangle$ with $\boldsymbol{k} = (\pi/a, \pi/a)$ (resp. $\boldsymbol{k} = 0$), and we stop to apply the operator in the left hand side when the ratio between two consecutive values is roughly constant, yielding

$$\left(\epsilon_{\text{max}} - \epsilon^{\text{abs}}_{\text{min}}\right)^2 \overset{n\to\infty}{\sim} \frac{\left|(\mathcal{H} - \epsilon^{\text{abs}}_{\text{min}})^{n+1} \, |\phi\rangle\right|^2}{|(\mathcal{H} - \epsilon^{\text{abs}}_{\text{min}})^n \, |\phi\rangle \, |^2}, \tag{3.22}$$

$$\left(\epsilon_{\text{min}} - \epsilon^{\text{abs}}_{\text{max}}\right)^2 \overset{n\to\infty}{\sim} \frac{\left|(\mathcal{H} - \epsilon^{\text{abs}}_{\text{max}})^{n+1} \, |\phi\rangle\right|^2}{|(\mathcal{H} - \epsilon^{\text{abs}}_{\text{max}})^n \, |\phi\rangle \, |^2}. \tag{3.23}$$

To stay on the safe side, the computed value of ϵ_{max} (resp. ϵ_{min}) is increased (resp. decreased) by a few percents, as any eigenvalue of the Hamiltonian outside of the spectrum bounds estimation leads to a dramatic exponential divergence of the series (3.15).

3.1.4 Numerical integration of the full Gross-Pitaevskii equation

In the previous subsection 3.1.3, we described our numerical technique for the implementation of the disordered part of the Gross-Pitaevskii equation. In this subsection, we add the nonlinearity, and consider the full equation (3.3) with $g \neq 0$. The time-dependence of the nonlinear term seems to invalidate our previous approach. However, if g remains small enough to be considered as a small perturbation of the Hamiltonian, the effect of interactions can be added on top of the Chebychev expansion. Indeed, we show in this section that one can separate the linear and nonlinear parts of the evolution operator evaluated at a small enough time step δt. For $g \neq 0$, the formal solution of the Gross-Pitaevskii equation can be written

$$|\psi(\delta t)\rangle = \hat{U}(\delta t)\,|\psi(0)\rangle = \mathcal{T}\exp\left(-i\int_0^{\delta t}\mathrm{d}t'\,\left[\mathcal{H}_0(t') + g|\psi(\boldsymbol{r},t')|^2\right]\right)|\psi(0)\rangle\,, \tag{3.24}$$

where $\mathcal{T}$ denotes the time ordering operator. Inserting the Taylor expansion of the nonlinear term at short times:

$$g|\psi(\boldsymbol{r},\delta t)|^2 = g|\psi(\boldsymbol{r},0)|^2 + \delta t\, g\partial_t|\psi(\boldsymbol{r},t)|^2|_{t=0} + \mathcal{O}(\delta t^2) \tag{3.25}$$

into Eq. (3.24), we obtain

$$\begin{aligned}|\psi(\delta t)\rangle &= \mathcal{T}\exp\left(-i\int_0^{\delta t}\mathrm{d}t'\,\left[\mathcal{H}_{g=0} + g|\psi(\boldsymbol{r},0)|^2 + t'\,g\partial_t|\psi(\boldsymbol{r},t)|^2|_{t=0} + \mathcal{O}(t'^2)\right]\right)|\psi(0)\rangle\\ &= \mathcal{T}\exp\left(-i\delta t\left[\mathcal{H}(t=0)\right] - i\frac{\delta t^2}{2}\,g\partial_t|\psi(\boldsymbol{r},t)|^2|_{t=0} + \mathcal{O}(\delta t^3)\right)|\psi(0)\rangle\,. \end{aligned}\tag{3.26}$$

Noticing that all the nested commutators of the two operators involved are at least of order $\mathcal{O}(\delta t^3)$, we can split the exponential using the well-known Baker–Campbell–Hausdorff formula:

$$|\psi(\delta t)\rangle = \exp\left(-i\frac{\delta t^2}{2}\,g\partial_t|\psi(\boldsymbol{r},t)|^2|_{t=0}\right)\exp\left(-i\delta t\left[\mathcal{H}(t=0)\right]\right)|\psi(0)\rangle + \mathcal{O}(\delta t^3), \tag{3.27}$$

and further simplify the rightmost exponential term with the symmetrized Trotter formula:

$$\begin{aligned}\exp\left(-i\delta t\left[\mathcal{H}(t=0)\right]\right) &= \exp\left(-i\delta t\left[\mathcal{H}_{g=0} + g|\psi(\boldsymbol{r},0)|^2\right]\right)\\ &= \exp\left(-i\frac{\delta t}{2}g|\psi(\boldsymbol{r},0)|^2\right)\exp\left(-i\delta t\mathcal{H}_{g=0}\right)\exp\left(-i\frac{\delta t}{2}g|\psi(\boldsymbol{r},0)|^2\right) + \mathcal{O}(\delta t^3).\end{aligned}\tag{3.28}$$

Using again the Taylor expansion (3.25), we arrive at

$$|\psi(\delta t)\rangle = \exp\left(-i\frac{\delta t}{2}g|\psi(\boldsymbol{r},\delta t)|^2\right)\exp\left(-i\delta t\mathcal{H}_{g=0}\right)\exp\left(-i\frac{\delta t}{2}g|\psi(\boldsymbol{r},0)|^2\right)|\psi(0)\rangle + \mathcal{O}(\delta t^3). \tag{3.29}$$

Under this form, we can compute the evolution operator $\hat{U}(\delta t)$ with small error over a time step δt, set by the validity of the Taylor expansion of the linear term. The exponential in the center is evaluated with the Chebychev expansion described in the last paragraph, and the nonlinear term in the leftmost exponential is computed at each time step by the application of the two rightmost exponentials:

$$|\psi(\boldsymbol{r}, \delta t)|^2 = \left| \langle \boldsymbol{r}| \exp\left(-i\delta t \mathcal{H}_{g=0}\right) \exp\left(-i\frac{\delta t}{2} g|\psi(\boldsymbol{r}, 0)|^2\right) |\psi(0)\rangle \right|^2 . \tag{3.30}$$

In the range of parameters used in this manuscript, the condition on the time step δt from the nonlinear propagation is the main restriction for performing simulations at very long times, or for very large values of $g\rho_0$. When the time step is chosen too large, the norm of the simulated density exhibits large deviations from its expected value after a certain evolution time. When it is very small, the computation time increases dramatically. We have not precisely benchmarked the optimal value of δt for a given set of input parameters. However, in practice, we have found that keeping the non-linear phase $g\rho_0\delta t \sim 10^{-3}$ guarantees that the norm of the numerically computed density is within 1% of its exact value for the system sizes and times we consider, at least for weak disorder strengths.

This numerical implementation of the GPE is rather rudimentary, and is only computationally efficient when the interaction strength is the smallest energy scale in the problem. While this is typically the case when we study the effect of interactions on the CBS peak and the diffusive ring, in the next chapters we will be studying regimes where interactions becomes comparable, even larger than the disorder strength and the kinetic energy. In this case we are forced to choose low values of δt, which considerably increases simulation times. A lot of more refined, and thus more efficient numerical implementations of the GPE exist in the litterature [237], for instance in the context of superfluid turbulence where the apparition of non-linear vortices is taken into account [238, 239]. In the following however, we chose to stick with this suboptimal implementation, because of its availability, avoiding development times that are non-negligible on the time scale of a PhD. Despite this, our numerical scheme allows to compute the full time-resolved propagation of an initial state with the GPE (3.1) in a quasi-exact manner, in the sense that precision is only limited by computational resources. From the knowledge of the wavefunction $|\psi(t)\rangle$, we can then compute the dynamical evolution of all the relevant observables of the system. The efficiency of the algorithm is such that for the numerical results presented in this thesis, simulation times rarely exceeds one day.

3.1.5 Simulated spectral functions and density of states

In what follows, we make extensive use of simulated spectral functions $A_\epsilon(\boldsymbol{k})$ and density of states ν_ϵ. To obtain the spectral function from simulated data, we follow the method from

[240]. Starting from the definition

$$A_\epsilon(\boldsymbol{k}) \equiv 2\pi\overline{\langle \boldsymbol{k}|\delta(\epsilon-\mathcal{H})|\boldsymbol{k}\rangle}, \tag{3.31}$$

we use the positive-time representation of the Dirac delta function to obtain:

$$A_\epsilon(\boldsymbol{k}) = 2\Im\frac{1}{\epsilon-\mathcal{H}-i0^+} = 2\Re\int_0^{+\infty} \mathrm{d}\epsilon\ e^{i\epsilon t}\ \overline{\langle \boldsymbol{k}|e^{-i\mathcal{H}t}|\boldsymbol{k}\rangle}. \tag{3.32}$$

The integral in the left hand side is the positive-time Fourier transform of the autocorrelation function $A(t) = \overline{\langle\psi(t=0)|\psi(t)\rangle}$, starting with an initial plane wave $|\boldsymbol{k}\rangle$. To obtain it numerically, we thus simply compute the overlap between the state $|\psi(t)\rangle$ and the initial plane wave state. The final time T of the propagation gives the energy resolution of the spectral function $\Delta_\epsilon = 1/T$. Examples of simulated spectral functions for a wide range of $\boldsymbol{k}$ values are displayed in Fig. 3.2. Note, in particular, that the Lorentzian expression

$$A_\epsilon(\boldsymbol{k}) = \frac{1}{\tau_\epsilon}\frac{1}{(\epsilon-\epsilon_{\boldsymbol{k}})^2+\frac{1}{4\tau_\epsilon^2}} \tag{3.33}$$

for $A_\epsilon(\boldsymbol{k})$, derived in the Born approximation, is indeed valid for values of $\boldsymbol{k}$ that fulfill the weak disorder condition $k\ell \gg 1$. We recall that for a 2d Gaussian uncorrelated disorder potential (see Sec. 1.5.3 of chapter 1), .

$$\tau_\epsilon \equiv \tau = 1/\gamma \quad \text{and} \quad \ell_k = k\tau \simeq \ell_{k_0}, \tag{3.34}$$

where the last equality is the on-shell approximation of the scattering mean free path, which stems from the low dispersion of the momenta around the initial value k_0, due to elastic scattering. At lower momentum values, the disorder is felt more strongly by the atoms, and their spectral functions extends towards negative energies, indicating that they may be trapped in shallow potential wells. At larger momentum, the modification of the density of states (see Fig. 3.3) due to the discretization is more important, and the width of the numerical spectral function is no longer given by Eq. (3.34).

The density of states per unit volume is obtained in a similar manner by propagating a point-like initial state $|\boldsymbol{r}\rangle$ with any $\boldsymbol{r}$:

$$\nu_\epsilon = \frac{1}{\mathcal{V}}\int \mathrm{d}\boldsymbol{r}\overline{\langle \boldsymbol{r}|\delta(\epsilon-\mathcal{H})|\boldsymbol{r}\rangle} = \overline{\langle \boldsymbol{r}|\delta(\epsilon-\mathcal{H})|\boldsymbol{r}\rangle} = \frac{1}{\pi}\Re\int_0^{+\infty} \mathrm{d}\epsilon\ e^{i\epsilon t}\ \overline{\langle \boldsymbol{r}|e^{-i\mathcal{H}t}|\boldsymbol{r}\rangle}, \tag{3.35}$$

where, in the second equality, we have used that the local density of states is uniform after taking the disorder average, restoring translationnal invariance. Examples of simulated density of states are displayed in Fig. 3.3, where the combined effects of disorder and discretization are highlighted.

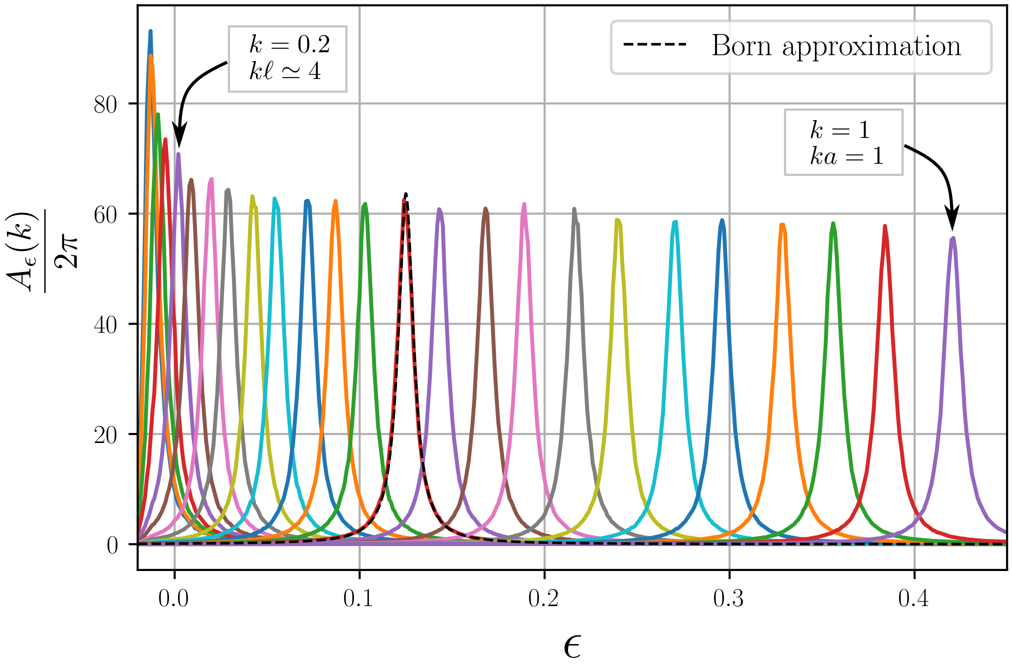

Figure 3.2 – Simulated spectral functions for the Gaussian uncorrelated disorder at fixed $\gamma = 0.01$, for various values of $|\boldsymbol{k}|$, ranging from 0 to 1, with a step $\delta k = 0.04$. The system size is set to 500×500, with spatial discretization $a = 1$, and the results are averaged over 960 realizations of the disorder. The dashed line is the Born prediction of the Lorentzian shape (3.31), for $k = 0.5$. To account for the small effect of the real part of the self-energy (i.e. the deviation of the maximum of the spectral function from the kinetic energy $\epsilon_k = 0.125$), its maximum is slightly shifted to match the maximum of the simulated spectral function. In the central region of the figure, the spectral functions all have the same approximately width $1/\tau = 0.01$ and height $2\tau/\pi \simeq 62.8$, because τ in Eq. (3.33) is independent of the energy (see text). In the left part of the figure, the spectral functions start to deviate from a Lorentzian form around $k \simeq 0.2$, i.e. $k\ell \simeq 4$, since the Born approximation ceases to be valid. In the right side of the figure, the spectral function still has a Lorentzian shape, but τ is no longer given by Eq. (3.34). This is due to the discretization – ka becomes non-negligible – which modifies the density of states (see Fig. 3.3) and the dispersion relation (see Eq. (3.5)).

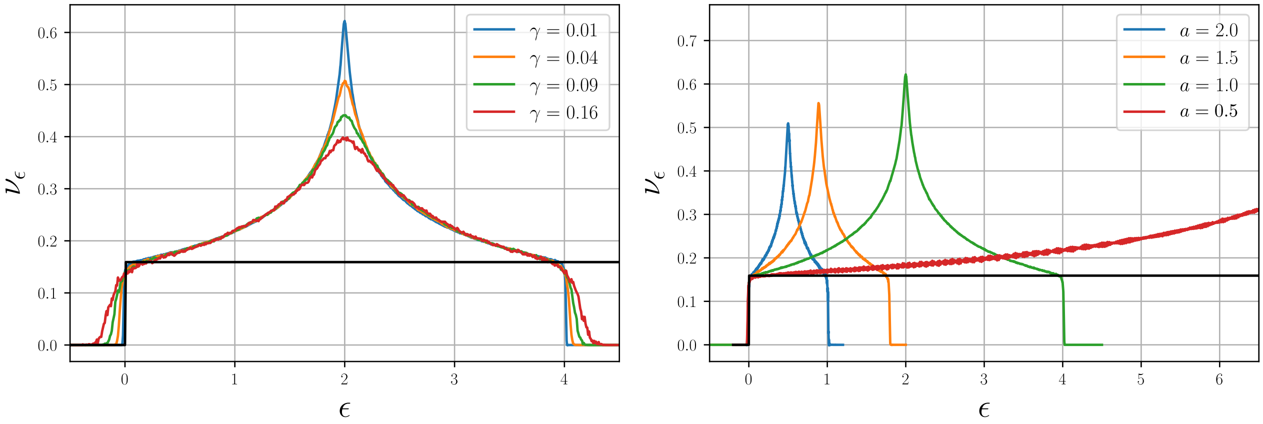

Figure 3.3 – Left: Density of states (DoS) per unit volume at fixed discretization $a = 1$ and for various values of the disorder strength. The system size is set to 500×500, and the results are averaged over 9600 realizations of the disorder. The free (continuous) density of states, $\nu_\epsilon^{(0)} = \theta(\epsilon)/2\pi$ is displayed in black for comparison. The peak in the center in the famous Van Hove singularity for the DoS of a discretized system [241]. Disorder tends to extend the DoS towards negative energies, and further increase the deviation from the free-space continuous value. In 2d, these corrections are of order $(k\ell)^{-1}$ [125] (where $k = \sqrt{2\epsilon}$) and we thus neglect them in first approximation. Right: Simulated DoS at fixed $\gamma = 0.01$ and for various values of the discretization a. This plot displays the dependence in $4/a^2$ of the maximum energy, suggested by the discrete dispersion relation (3.5). More importantly, we see that the discrete DoS is a reasonable approximation of the free DoS for energies $\epsilon \ll 1/(2a^2)$, which corresponds to the condition $ka \ll 1$ to recover the continuous dispersion relation (see Eq. (3.5)). This condition is necessary to compare our simulation results with continuous-space theories.

3.2 CBS and diffusive ring in the presence of interactions: numerics versus kinetic theory

Armed with the numerical scheme described in section 3.1, we can simulate the temporal evolution of the wavefunction $\psi(\boldsymbol{r}, t)$ for a given realization of the disorder, and deduce from it the observables we are interested in. The disorder average is then obtained by repeating the numerical experiment with different realizations of V. In this section, we use the simulations to unveil the effects of interactions on the diffusive ring and the CBS peak. We compare our results with the predictions of the kinetic equations derived in chapter 2. To this aim, we first recall the two coupled kinetic equations for the energy distributions f_ϵ and f_ϵ^C, respectively associated to the diffusive and CBS modes (see sections 2.3 and 2.4):

$$\partial_t f_\epsilon = \int_{\epsilon_1,\epsilon_2,\epsilon_3 \geq 0} \mathrm{d}\epsilon_1 \mathrm{d}\epsilon_2 \, W(\epsilon, \epsilon_1, \epsilon_2) \Big[(f_\epsilon + f_{\epsilon_1+\epsilon_2-\epsilon}) f_{\epsilon_1} f_{\epsilon_2} - f_\epsilon f_{\epsilon_1+\epsilon_2-\epsilon} (f_{\epsilon_1} + f_{\epsilon_2}) \Big] \tag{3.36}$$

$$\partial_t f_\epsilon^C = f_\epsilon^C \int_{\epsilon_1,\epsilon_2,\epsilon_3 \geq 0} \mathrm{d}\epsilon_1 \mathrm{d}\epsilon_2 \, W(\epsilon, \epsilon_1, \epsilon_2) \Big[f_{\epsilon_1} f_{\epsilon_2} - f_{\epsilon_1+\epsilon_2-\epsilon} (f_{\epsilon_1} + f_{\epsilon_2}) \Big], \tag{3.37}$$

where $\epsilon_3 = \epsilon_1 + \epsilon_2 - \epsilon$, and W is the interaction kernel, expressed is 2d as

$$W(\epsilon, \epsilon_1, \epsilon_2) = \frac{m^3 (g\rho_0)^2}{2\pi^4 \nu_\epsilon} \frac{K\left(\frac{2\sqrt[4]{\epsilon\epsilon_1\epsilon_2\epsilon_3}}{\sqrt{\epsilon_1\epsilon_2} + \sqrt{\epsilon\epsilon_3}} \right)}{\sqrt{\epsilon_1\epsilon_2} + \sqrt{\epsilon\epsilon_3}}. \tag{3.38}$$

Both equations are complemented with the initial condition

$$f_\epsilon(t=0) = f_\epsilon^C(t=0) = \frac{A_\epsilon(\boldsymbol{k}_0)}{2\pi\nu_\epsilon} \equiv f_\epsilon^{(0)}, \tag{3.39}$$

with $A_\epsilon(\boldsymbol{k}_0)$ being the spectral function evaluated at the momentum $\boldsymbol{k}_0$ of the initial plane wave. We finally recall that these equations hold in a regime where interactions are typically much smaller than the fluctuations of the disorder potential, with particle interactions occurring at the scale

$$\tau_{\mathrm{NL}} = \epsilon_0/(g\rho_0)^2 \gg \tau, \tag{3.40}$$

3.2.1 Density plots of the momentum distribution

We first show in Fig. 3.4 3d plots of the simulated momentum density $n_{\boldsymbol{k}}(t) = \overline{\psi^*(\boldsymbol{k}, t)\psi(\boldsymbol{k}, t)}$ at different times, obtained from direct numerical simulations of the Gross-Pitaevskii equation in the absence of interactions. The plots reveal the short-time dynamical picture predicted in chapter 1: starting from the initial plane wave (a δ peak at $\boldsymbol{k}_0$), we observe the formation of the diffusive ring and of the CBS peak around the backscattering direction. At intermediate times $t \leq \tau$, the ring grows isotropically, and after a few τ, the initial plane-wave mode has completely decayed. The CBS peak emerges on the same time scale, and eventually reaches twice the height of the ring, a consequence of the time-reversal invariance of the system, which imposes $n^D_{-\boldsymbol{k}_0} = n^C_{-\boldsymbol{k}_0}$ (see Eq. (1.100) of chapter 1). The system has then reached a quasi-stationary state, except for the visible narrowing of the CBS peak width with increasing time. We showed in section 1.6.3 that the width of the peak evolves as $1/\sqrt{Dt}$, with D the diffusion coefficient.

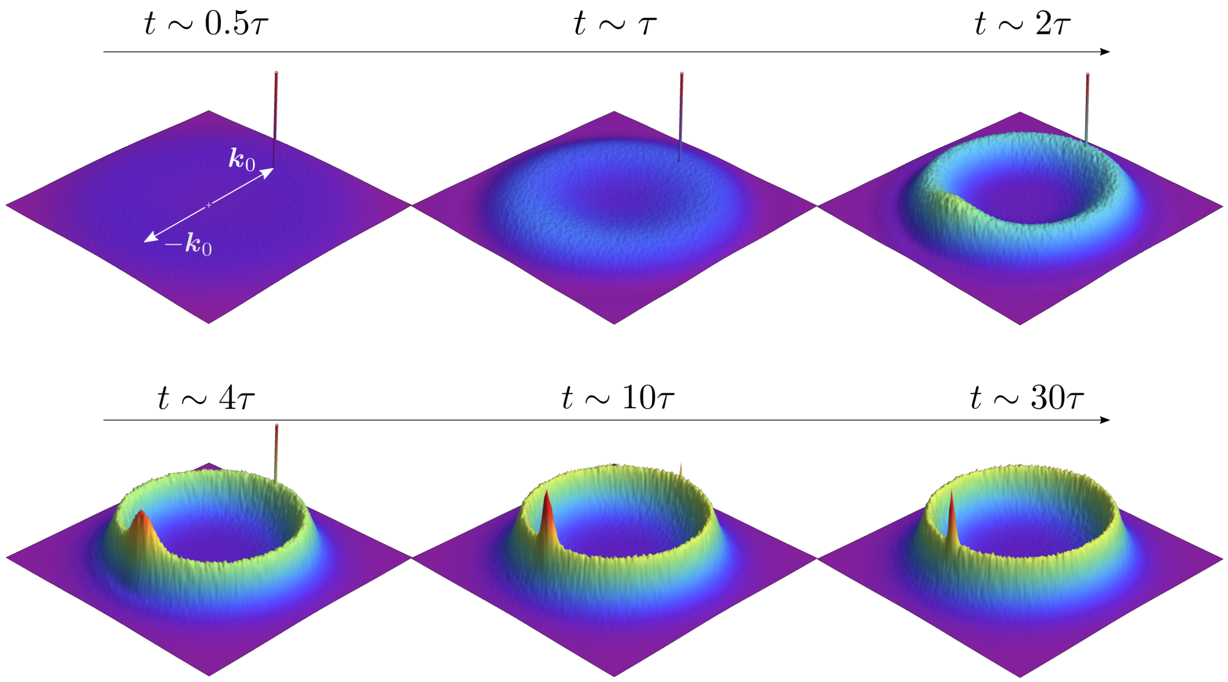

Figure 3.4 – Momentum distributions obtained from 2d simulations at different times for a disorder strength $\gamma = 0.01$ (mean scattering time $\tau = 100$ in the Born approximation (3.34)) and an initial momentum $k_0 \simeq \pi/12$ (corresponding to $k_0\ell \sim 6.85$), averaged over 2048 realizations of a Gaussian uncorrelated disorder. To obtain a good resolution in momentum space, we have to set a large system size 1200×1200. At $t = 0$, the initial plane wave is a delta peak at $\boldsymbol{k} = \boldsymbol{k}_0$ in momentum space. It then decays exponentially and the diffusive ring grows isotropically, as predicted by equation (1.89). The CBS peak, around the backscattering direction, starts growing after a few τ, and gets narrower with time, as suggested by (1.100).

We then display in Fig. 3.5 the temporal evolution of the momentum distribution in the presence of interactions with the same parameters. The value of g is chosen such that $\tau_{\text{NL}} \gg \tau$, the regime of validity of our kinetic equations. Due to this separation of time scales, the short-time picture $t < \tau_{\text{NL}}$ is similar to the non-interacting case. As t reaches τ_{NL}, however, a destruction of the CBS peak and a broadening of the diffusive ring are noticeable. After a few τ_{NL}, the CBS peak has completely vanished, in accordance with the asymmetric nature of the kinetic equations for diffusive and weakly localized modes discussed in section

2.4.3 of chapter 2. Eventually, the diffusive ring is also washed out and the momentum distribution becomes smooth and centered around zero. This phenomenon, to which we will come back later on, marks the onset of thermalization of the Bose gas.

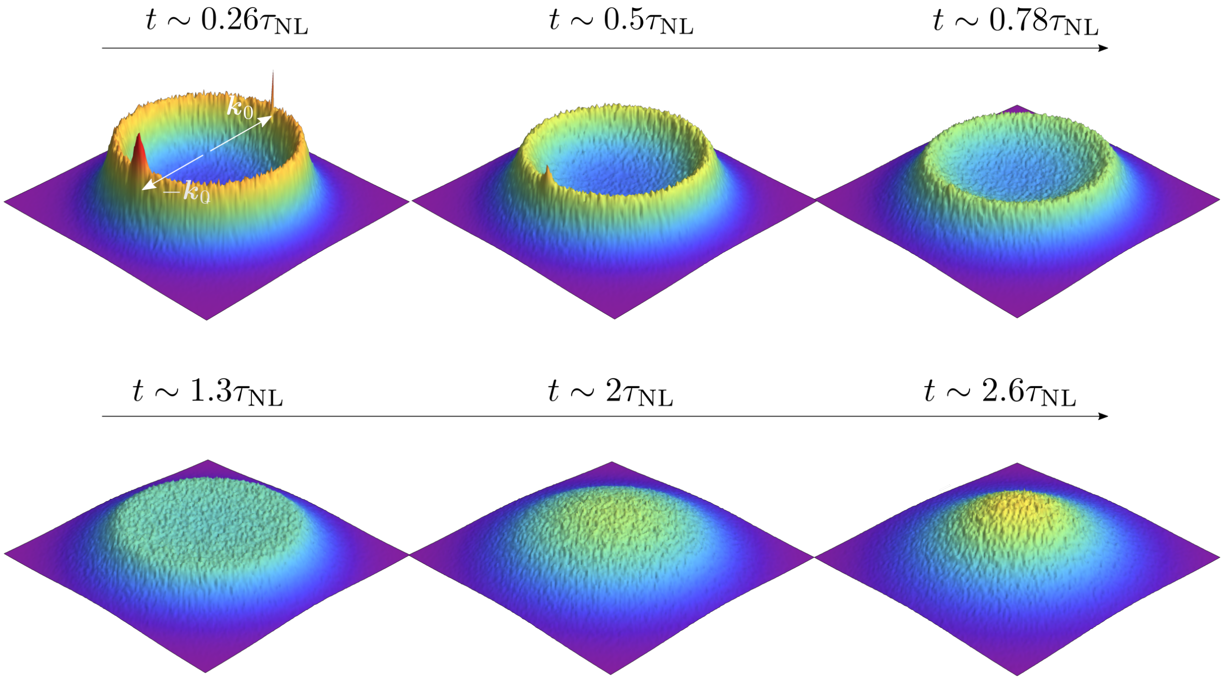

Figure 3.5 – Density plots of the momentum distribution obtained from 2d simulations at different times with the same parameters as Fig. 3.4, but with $g\rho_0 = 0.003 \neq 0$, such that $\tau_{\mathrm{NL}} \simeq 3807 \simeq 38\tau$. The plots at $t \sim 0.26\tau_{\mathrm{NL}}$ and $0.78\tau_{\mathrm{NL}}$ are taken at the same time than the last two plots of Fig. 3.4. The destruction of the CBS peak appears clearly, as well as the broadening and the collapse of the diffusive ring towards small momenta. Notice that, with these parameters, the CBS peak contrast never reaches 1, which would be the case if the time scales τ and τ_{NL} were more separated.

3.2.2 Numerical solution of the kinetic equations

We now wish to compare the ab initio results to our kinetic theory. Finding an exact analytical solution for the kinetic equations (3.36) and (3.37) is difficult in general, so we need to solve them numerically. As first-order differential equations, they are easily handled by any differential equation solver (we used "solve_ivp" from the python library Scipy [242]), provided that one can compute the collision integral on the right hand side at each time t. To do this, it should be first noted that the energy integrals in the right hand side of Eqs. (3.36) and (3.37) run over all energies allowed by the density of states. At the level of the Born approximation where the kernel W is derived, only positive energies are included, because we neglected corrections of order $(k_0\ell)^{-1}$ that extend the density of states towards negative energies (see Fig. 3.3). We thus compare the kinetic equations with simulations in the weak disorder regime $k_0\ell \gg 1$ and use the free density of states $\nu_\epsilon^{(0)} = \theta(\epsilon)/2\pi$. We also choose our simulation parameters to have $k_0 a \ll 1$, so that $\nu_\epsilon^{(0)}$ is a good approximation of the discrete density of states (see Fig. 3.3). In order to be consistent with our approximations, we also use the expression (3.33) of the spectral function in the Born approximation for the initial condition $f_\epsilon(t=0)$. Just like the density of states, this expression is only valid at intermediate momenta and energies (see Fig. 3.2). Consequently, our solutions of the kinetic equations are not accurate at low k and low energies ϵ. At relatively short time, however, we focus on the evolution of $n_{\boldsymbol{k}}$ around $|\boldsymbol{k}| = k_0$, so this description is sufficient. The free density of states imposes the integration domain $\mathcal{D} = \{(\epsilon_1, \epsilon_2) | \, \epsilon_1 > 0, \, \epsilon_2 > 0, \, \epsilon_1 + \epsilon_2 - \epsilon > 0\}$. The main difficulty in the implementation of the kinetic equations is the interaction kernel (3.38), which presents a wide range of (integrable) singularities over the integration domain $\mathcal{D}$. Indeed, as shown in Fig. 3.6, the interaction kernel diverges on the two lines $\epsilon_1 = \epsilon$ and $\epsilon_2 = \epsilon$. The divergence is logarithmic, symmetric around ϵ:

$$W(\epsilon, \epsilon_1, \epsilon_2) \overset{\epsilon_{1,2}\to\epsilon}{\sim} -\ln\left|\epsilon_{1,2} - \epsilon\right| . \tag{3.41}$$

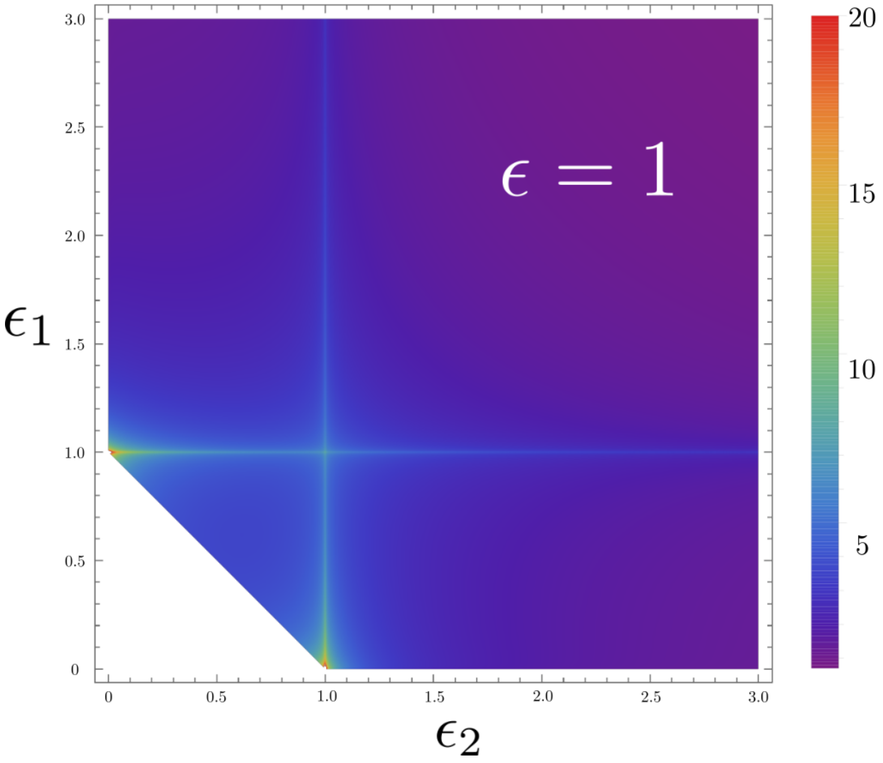

Figure 3.6 – Density plot of the kernel $W(\epsilon = 1, \epsilon_1, \epsilon_2)$ over the domain definition of the collision integrals, $\mathcal{D}$. The two visible lines $\epsilon = \epsilon_1$ and $\epsilon = \epsilon_2$ are the logarithmic divergences (3.41) of the kernel.

These divergences make the numerical integration of the kernel a priori difficult. However, in the case of the kinetic equation for the diffusive modes, the part of the integrand involving the energy distributions vanishes linearly as $\epsilon_{1,2} \to \epsilon$, thus canceling the singularities. In a numerical integration scheme, one can thus simply put the values of the integrand to 0 in this region, to avoid any errors stemming from the evaluation of W at a singular point. This strategy, on the other hand, cannot be used for the kinetic equation (3.37), for which the integrand stays finite on the singular lines. We have found, however, that by computing the integral with a high density of points around the singular lines, we obtain an approximation that does not depend on the discretization of the energy grid. This numerical scheme is once more quasi-exact, and numerical errors are well controlled. The only approximation is the Born approximation, which sets the validity of the expressions for the density of states, the spectral functions and the collision kernel W. When studying the decay of the CBS, we will see that this method reproduces the behavior of numerical simulations within a reasonable error. We show in Fig. 3.7 the temporal evolution of f_ϵ and f_ϵ^C obtained with this numerical scheme.

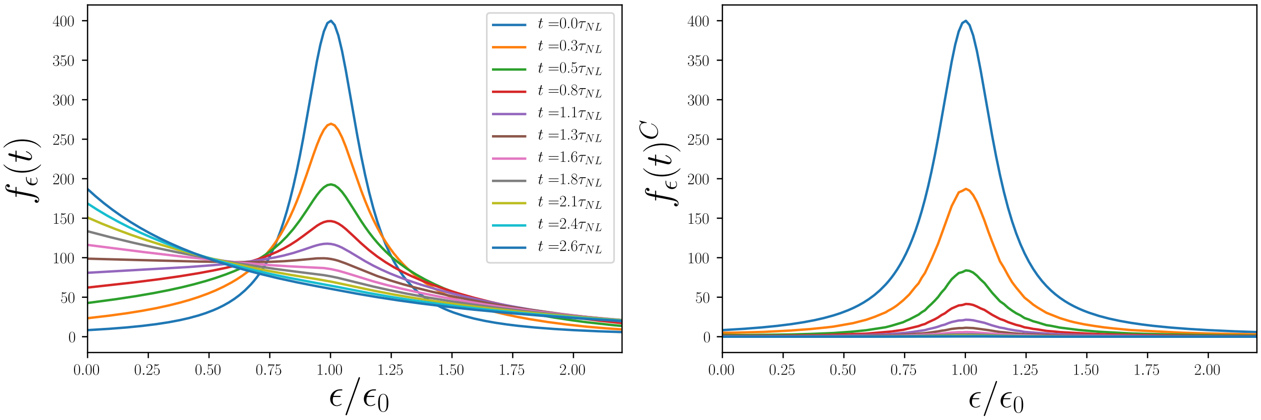

Figure 3.7 – Numerically computed solutions of the kinetic equations at different times. The parameters used are the same as in Fig 3.5. The initial condition is derived from the expression of $A_\epsilon(\boldsymbol{k})$ in the Born approximation, and the free density of states $\nu_\epsilon^{(0)} = \theta(\epsilon)/2\pi$. The asymmetry between the two collision integrals is well illustrated by these solutions, with the leftmost one conserving its norm, and the rightmost quickly vanishing.

3.2.3 Short-time decay of the height of the ring and CBS

Let us first recall the expressions of the heights of the ring and the CBS peak as a function of the energy distributions from chapter 2 :

$$n^D_{|k|=k_0}(t) = \int_{-\infty}^{\infty} \mathrm{d}\epsilon\, A_\epsilon(k) f_\epsilon(t) \times \left[1 - e^{-t/\tau}\left(1 + \frac{t}{\tau}\right)\right] \tag{3.42}$$

$$n^C_{-\boldsymbol{k}_0}(t) = \int_{-\infty}^{\infty} \mathrm{d}\epsilon\, A_\epsilon(-\boldsymbol{k}_0) f^C_\epsilon(t) \times \left[1 - e^{-t/\tau}\left(1 + \frac{t}{\tau} + \frac{t^2}{2\tau^2}\right)\right] . \tag{3.43}$$

To describe the times $t \leq \tau$, we have here multiplied the right-hand side of both equations by the same short-time corrections as in the linear case that we derived in sections 1.6.2 and 1.6.3. This is a very good approximation in the regime $\tau_{\mathrm{NL}} \gg \tau$ considered here (the effect of interactions is negligible at the scale of τ, as discussed in section 2.3.2 of chapter 2). In Fig. 3.8, we show fits of the Gross-Pitaevskii simulation results to Eqs. (3.42) and (3.43), with f_ϵ and f^C_ϵ computed from the kinetic equations (3.36) and (3.37) and using $g\rho_0$ as a fit parameter. The spectral functions and density of states used in the computation of $n_{\boldsymbol{k}}(t)$ and for the initial state $f^{(0)}_\epsilon$ of the kinetic equations are the theoretical expressions at the Born approximation. As seen in Fig. 3.8, the agreement between the kinetic theory and the Gross-Pitaevskii simulations is excellent at all times. We note, however, that, for the ring height, the fitted values of $g\rho_0$ differ by $\sim 10\%$ compared to those chosen in numerical simulations, and for the CBS height by $\sim 30\%$. One possible reason for this difference is the numerical uncertainties in the resolution of the collision integrals described in the last paragraph. This discrepancy could also stem from higher-order interaction contributions that renormalize the interaction strength g and are not taken into account in the present work.[1]

3.2.4 Estimation of the decay rates

An important information one may extract from the time-dependent evolutions in Fig. 3.8 are the characteristic time scales τ_{ring} and τ_{CBS} governing the decay of the diffusive ring and of the CBS peak height. In this section, we evaluate them with the help of the kinetic equations.

Diffusive ring

At short time $t \ll \tau_{\mathrm{NL}}$, an approximate solution of the kinetic equation (3.36) for the diffusive modes can be found. In this regime, all the relevant energy scales remain close to the initial plane wave energy $\epsilon_0 = k_0^2/2m$, so that we can perform an expansion of the energy distribution f_ϵ around this value,

---

[1] Note that this analysis was done long before the work presented in subsection 3.2.5, in which we present a precise fit of the transverse shape of the ring at longer times, without any fit parameter. In that section, we use simulated spectral functions $A_\epsilon(\boldsymbol{k})$, and introduce an energy shift that sets their maximum at the kinetic energy $\epsilon_{\boldsymbol{k}}$, taking into account the real part of the self energy. The results from this subsection and the next one would most probably gain in accuracy from this trick.

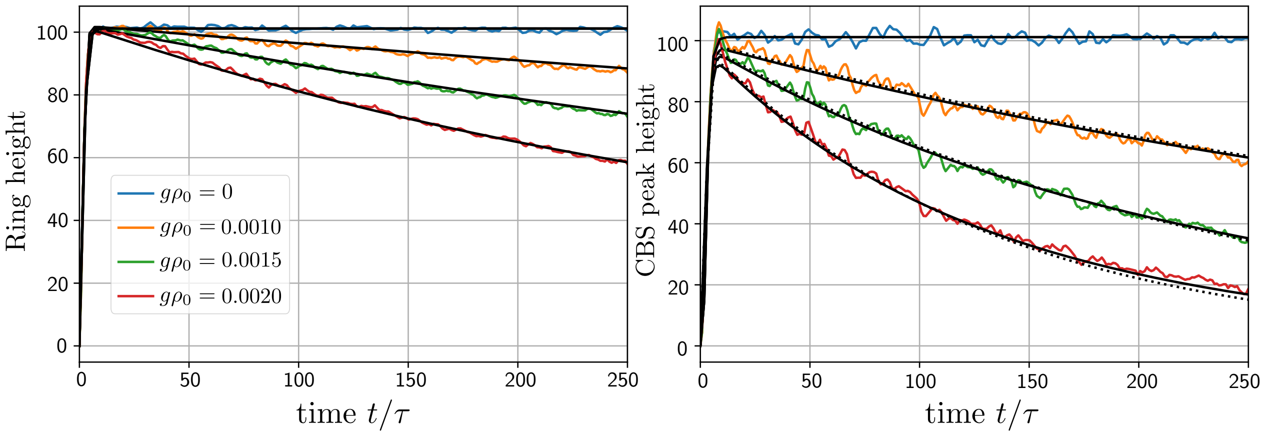

Figure 3.8 – Heights of the diffusive ring and of the CBS peak versus time for increasing values of $g\rho_0$ from top to bottom. Colored curves are the Gross-Pitaevskii simulation data and solid black curves are solutions of the kinetic equations, using the interaction strength $g\rho_0$ as a fit parameter. Numerical data for the ring are obtained by computing the maximum value of $n_{\boldsymbol{k}}(t)$ along the direction perpendicular to $\boldsymbol{k}_0$, where no CBS is present. Data for the CBS peak are obtained by subtracting the momentum distribution rotated by 90° from $n_{\boldsymbol{k}}(t)$. Dotted curves are the approximate formula (3.57). Here $k_0 = \pi/5$, $\gamma \simeq 0.0182$, which corresponds to $k_0\ell \sim 21.7$. Data are averaged over 16000 realizations. $\tau_{\text{NL}} \sim \epsilon_0/(g\rho_0)^2$ varies from around 200000 to 50000, while $\tau \sim 500$.

$$f_\epsilon(t) \simeq f_{\epsilon_0}(t) + (\epsilon-\epsilon_0)\partial_\epsilon f_\epsilon(t)\big|_{\epsilon=\epsilon_0} + \frac{(\epsilon-\epsilon_0)^2}{2}\,\partial_\epsilon^2 f_\epsilon(t)\big|_{\epsilon=\epsilon_0}\,. \tag{3.44}$$

Noting that the energy distribution $f_\epsilon(t)$ is maximal around ϵ_0, we can set $\partial_\epsilon f_\epsilon(t)\big|_{\epsilon=\epsilon_0}$ to 0 in the previous equation. Inserting this expansion into the kinetic equation then yields, at the lowest order:

$$\partial_t f_{\epsilon_0}(t) = -\int_{\epsilon_1,\epsilon_2,\epsilon_1+\epsilon_2-\epsilon\geq 0} \mathrm{d}\epsilon_1\mathrm{d}\epsilon_2\; W(\epsilon_0,\epsilon_1,\epsilon_2)(\epsilon_0-\epsilon_1)(\epsilon_0-\epsilon_2)f_{\epsilon_0}^2(t)\;\partial_\epsilon^2 f_\epsilon(t)\big|_{\epsilon=\epsilon_0}\,. \tag{3.45}$$

At the short times considered here, the initial energy distribution has not been dramatically affected, and we can make the approximation $f_{\epsilon_0}^2(t) \simeq f_{\epsilon_0}^2(t=0)$ in the right-hand side of equation (3.45). Moreover, since all energies are close to ϵ_0, and the initial spectral function is very peaked for weak disorder, we can regularize the integral[2] by substituting $f_{\epsilon_0}^2(t=0)$ with the product $f_{\epsilon_1}(t=0)f_{\epsilon_2}(t=0)$. We obtain that the energy distribution obeys a diffusion equation in the energy domain:

$$\partial_t f_\epsilon(t) \simeq -D_{\epsilon_0}\partial_\epsilon^2 f_\epsilon(t) \qquad \text{for} \quad \epsilon \sim \epsilon_0, \tag{3.46}$$

---

[2] Which is otherwise divergent, since $W(\epsilon,\epsilon_1,\epsilon_2) \overset{\epsilon_{1,2}\to\infty}{\sim} 1/\sqrt{\epsilon_{1/2}}$. This divergence at infinity is expected, since we directly replace the energy distributions by their truncated Taylor expansion under the integral sign.

with

$$D_{\epsilon_0} \simeq \int_{\epsilon_1,\epsilon_2,\epsilon_1+\epsilon_2-\epsilon\geq 0} \mathrm{d}\epsilon_1 \mathrm{d}\epsilon_2 \, W(\epsilon_0,\epsilon_1,\epsilon_2)(\epsilon_0-\epsilon_1)(\epsilon_0-\epsilon_2)A_{\epsilon_1}(\boldsymbol{k}_0)A_{\epsilon_2}(\boldsymbol{k}_0). \tag{3.47}$$

The general solution of equation (3.46) is

$$f_\epsilon(t) \simeq \int_{-\infty}^{+\infty} \mathrm{d}\epsilon' \frac{f^{(0)}_{\epsilon'}}{\sqrt{4\pi D_{\epsilon_0} t}} \exp\left[-\frac{(\epsilon-\epsilon')^2}{4D_{\epsilon_0}t}\right], \tag{3.48}$$

which, in turn, yields for the momentum distribution, at $t > \tau$:

$$n^D_{\boldsymbol{k}} = \int_{-\infty}^{+\infty} \mathrm{d}\epsilon \mathrm{d}\epsilon' \, \frac{A_\epsilon(\boldsymbol{k})A_{\epsilon'}(\boldsymbol{k}_0)}{\nu_\epsilon\sqrt{4\pi D_{\epsilon_0} t}} \exp\left[-\frac{(\epsilon-\epsilon')^2}{4D_{\epsilon_0}t}\right]. \tag{3.49}$$

After performing the integral over ϵ, using the expression (3.33) for the spectral function, we finally get

$$n^D_{\boldsymbol{k}} = \frac{1}{\pi\nu_{\epsilon_0}\tau\sqrt{4\pi D_{\epsilon_0}t}} \int_{-\infty}^{+\infty} \mathrm{d}u \frac{1}{(\epsilon_{\boldsymbol{k}}-\epsilon_0+u)^2+\frac{1}{\tau^2}} \exp\left[-\frac{u^2}{4D_{\epsilon_0}t}\right], \tag{3.50}$$

where we changed the variable $\epsilon' \to u = \epsilon' - \epsilon_0$. In the non-interacting limit where $D_{\epsilon_0} \to 0$, the integral is dominated by small values of u. At the lowest order for instance, one obviously recovers the expression for the Lorentzian shape of the ring, Eq. (1.86):

$$n^{D\,(g=0)}_{\boldsymbol{k}}(t) = \frac{1}{\pi\nu_{\epsilon_0}\tau}\frac{1}{(\epsilon_{\boldsymbol{k}}-\epsilon_0)^2+\frac{1}{\tau^2}}. \tag{3.51}$$

For a time t such that $2D_{\epsilon_0}t \ll 1/\tau^2$, equation (3.49) can be expanded as

$$\begin{aligned} n^D_{\boldsymbol{k}} &\simeq \frac{1}{\pi\tau\nu_{\epsilon_0}}\left[\frac{1}{(\epsilon_{\boldsymbol{k}}-\epsilon_0)^2+\frac{1}{\tau^2}} - \frac{2D_{\epsilon_0}t}{\tau^2}\frac{1}{\left((\epsilon_{\boldsymbol{k}}-\epsilon_0)^2+\frac{1}{\tau^2}\right)^3}\right] \\ &= n^{D\,(g=0)}_{\boldsymbol{k}}\left[1-\frac{2D_{\epsilon_0}t}{\tau^2}\frac{1}{\left((\epsilon_{\boldsymbol{k}}-\epsilon_0)^2+\frac{1}{\tau^2}\right)^2}\right]. \end{aligned} \tag{3.52}$$

In particular, the height of the ring $n^D_{\boldsymbol{k}_0}$ decays at short times over a characteristic time $\tau_{\text{ring}} = 1/2D_{\epsilon_0}\tau^2$ according to

$$n^D_{\boldsymbol{k}_0} = n^{D\,(g=0)}_{\boldsymbol{k}_0}\left(1-\frac{t}{\tau_{\text{ring}}}\right). \tag{3.53}$$

Using the definition (3.47) of the diffusion coefficient, we obtain that

$$\frac{1}{\tau_{\mathrm{ring}}} = C_1 \frac{(g\rho_0)^2}{\epsilon_0} = \frac{C_1}{\tau_{\mathrm{NL}}}, \tag{3.54}$$

where C_1 is a numerical constant, which can be evaluated numerically using Eq. (3.47), and a priori only depends of γ and k_0. We obtain the simple result that the decay rate τ_{ring} scales with the particle interaction time τ_{NL}. We also see that the condition $2D_{\epsilon_0} t \ll 1/\tau^2$ effectively reduces to $t \ll \tau_{\mathrm{NL}}$, as we assumed at the beginning of this section. Note that, in this short-time regime, the ring maintains its approximate Lorentzian form, and its Half-Width at Half-Maximum (HWHM) $\Delta k(t)$ consequently increases according to

$$\Delta k(t) \sim (1 + Ct/\tau_{\mathrm{NL}})/\ell. \tag{3.55}$$

Eq. (3.53) suggests that the short-time behavior of $n^D_{\boldsymbol{k}_0}$ can be approximated by an exponential decay

$$n^D_{\boldsymbol{k}_0}(t) \simeq \frac{\tau}{\pi \nu_{\epsilon_0}} e^{-t/\tau_{\mathrm{ring}}} \times \left[1 - e^{-t/\tau}\left(1 + \frac{t}{\tau}\right)\right]. \tag{3.56}$$

Coherent backscattering peak

In the case of the CBS peak, an approximate expression for the temporal decay can be inferred from the kinetic equation (3.37). Indeed, since the time dependence of the diffusive background, encoded in the distribution $f_\epsilon(t)$ in the right-hand side of the equation is rather slow, in first approximation f_ϵ decays exponentially, which suggests the simple form

$$n^C_{-\boldsymbol{k}_0}(t) \simeq \frac{\tau}{\pi \nu_{\epsilon_0}} e^{-t/\tau_{\mathrm{CBS}}} \times \left[1 - e^{-t/\tau}\left(1 + \frac{t}{\tau} + \frac{t^2}{2\tau^2}\right)\right]. \tag{3.57}$$

To estimate the decay rate τ_{CBS}, we simply perform a short-time expansion of the solution $f^C(t)$:

$$f^C_\epsilon(t) \simeq f^{(0)}_\epsilon - \partial_t f^C_\epsilon(t)\Big|_{t=0} t + \mathcal{O}(t^2). \tag{3.58}$$

Substituting this expansion into the expression of the momentum distribution in the backscattering direction $n^C_{-\boldsymbol{k}_0}(t)$, we arrive at

$$n^C_{-\boldsymbol{k}_0}(t) \simeq \frac{\tau}{\pi \nu_{\epsilon_0}} \left(1 - \frac{t}{\tau_{\mathrm{CBS}}} + \mathcal{O}(t^2)\right) \times \left[1 - e^{-t/\tau}\left(1 + \frac{t}{\tau} + \frac{t^2}{2\tau^2}\right)\right] \tag{3.59}$$

where we defined

$$\tau_{\mathrm{CBS}}^{-1} \equiv \frac{\pi\nu_{\epsilon_0}}{\tau} \int \mathrm{d}\epsilon\, A_\epsilon(\boldsymbol{k}_0)\, \partial_t f_\epsilon^C(t)\Big|_{t=0} t. \tag{3.60}$$

By substituting the Taylor expansion for $f_\epsilon^C(t)$ in the CBS kinetic equation (3.37), we obtain a numerical estimation of $\partial_t f_\epsilon^C(t)\big|_{t=0}$, which yields:

$$\frac{1}{\tau_{\mathrm{CBS}}} = C_2 \frac{(g\rho_0)^2}{\epsilon_0} = \frac{C_2}{\tau_{\mathrm{NL}}}, \tag{3.61}$$

where C_2 is a numerical constant, which can be evaluated numerically using Eqs. (3.60) and (3.37). C_2 a priori only depends on γ and k_0, like C_1. Using a numerical estimation of C_2, we plot Eq. (3.57) in dashed lines over the simulation results in the right graph of Fig. 3.8. The agreement is remarkably good, which confirms the quasi-exponential decay of the CBS peak. The data in Fig. 3.8 makes it possible to extract the numerical values of C_1 and C_2. We find $C_1 \approx 2.27$ and $C_2 \approx 7.17$. Estimating the values of these parameters from the kinetic theory using Eqs. (3.47), (3.37) and (3.60) is a delicate task, and we obtained only rough estimates which are slightly larger by few tens of percent.

The characteristic times governing the decay of the diffusive background and CBS peak, Eqs. (3.54) and (3.61), respectively, are therefore both proportional to the particle interaction time τ_{NL} (3.40), previously defined in chapter 2 using the Fermi golden rule. While this is quite a natural result, it should be noted that we find $C_2 \simeq 3C_1$, and thus the decay time for CBS is approximately three times shorter than the decay time for the diffusive background. In other words, the CBS peak is way more sensitive to interactions, as clearly seen in Fig. 3.8.

Contrast of the coherent backscattering peak

To confirm these semi-analytical results, we also compare the theoretical predictions (3.54) and (3.61) to the decay rates extracted from the Gross-Pitaevskii numerical simulations. For this purpose, we compute numerically the CBS maximum and diffusive amplitude versus time for several values of the disorder strength γ. We then extract the slope of these curves within a narrow time window following the curve maxima (located near $t = 15\tau$ in Fig. 3.8). The results are shown in Fig. 3.9 as a function of the disorder parameter $k_0\ell$ (lower points are obtained from the decay of the diffusive ring and upper points from the decay of the CBS peak). The theoretical predictions (3.54) and (3.61) are shown on the same graph, and they match very well the simulations. These results show, remarkably, the independence of the collision time – i.e. of the coefficients C_1 and C_2 – on the disorder strength. This can be understood: in the weak disorder regime, the spectral function $A_\epsilon(\boldsymbol{k})$ and the distribution f_ϵ are narrow Lorentzian functions, which facilitates the evaluation of Eqs. (3.47), (3.37) and (3.60). It then turns out that C_1 and C_2 should not depend on γ, in agreement with the results shown in Fig. 3.9. By computing numerically the slopes for several values of g, we have also verified the $(g\rho_0)^2$ dependence of $(\tau_{\mathrm{ring}})^{-1}$ and $(\tau_{\mathrm{CBS}})^{-1}$.

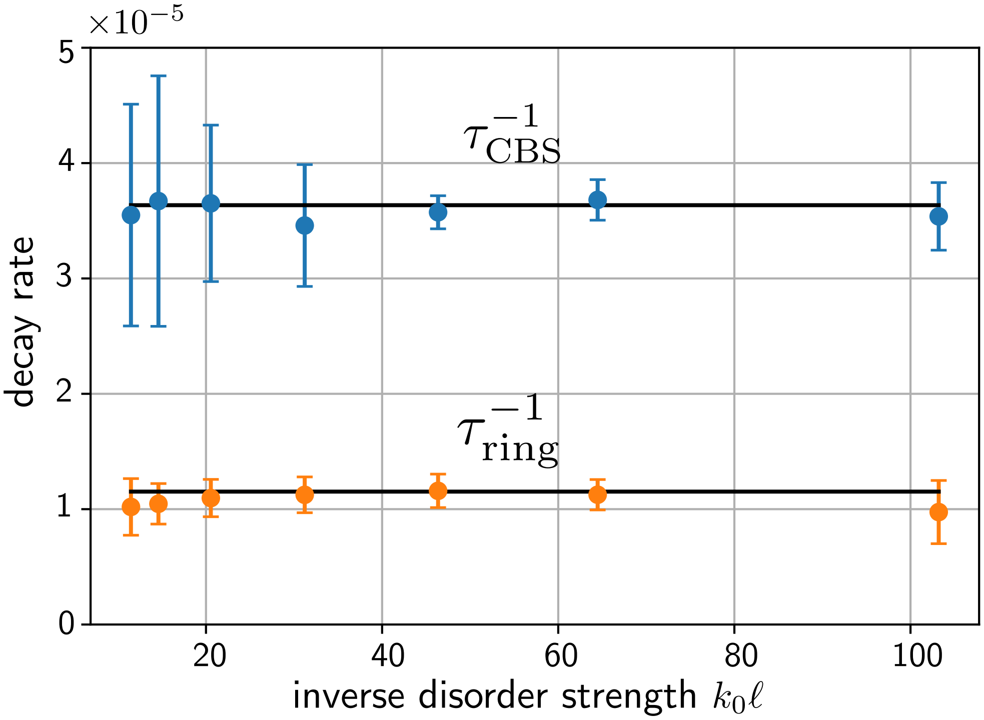

Figure 3.9 – Decay rates $\tau_{\mathrm{ring}}^{-1}$ and τ_{CBS}^{-1} for the diffusive background (lower orange dots) and CBS (upper blue dots) amplitudes, at fixed $g\rho_0 = 0.001$. Dots are obtained from our numerical simulations, by computing the slope of the simulation curves in Fig. 3.8 for several values of γ (error bars originate from the fitting of the slopes by a straight line). From right to left: $\gamma = 0.0036, 0.0056, 0.0081, 0.0121, 0.0182, 0.0256, 0.0324, 0.0506$. Data are displayed as a function of the dimensionless disorder parameter $k_0\ell$.

In summary, we have shown that the decay rates for the diffusive ring and the CBS are universal, as they do not depend on the disorder strength γ, provided that $k_0\ell \gg 1$. We have also provided estimations of τ_{ring} and τ_{CBS} in a quasi-exact way, confirmed by the simulations in Fig. 3.9. As a consequence of Eqs. (3.56) and (3.57), the contrast of the CBS peak decays exponentially as

$$\frac{n^C_{-\boldsymbol{k}_0}}{n^D_{-\boldsymbol{k}_0}} \simeq \exp\left(-\frac{t}{\tau_\phi}\right), \tag{3.62}$$

with a relaxation rate

$$\frac{1}{\tau_\phi} \equiv \frac{1}{\tau_{\mathrm{CBS}}} - \frac{1}{\tau_{\mathrm{ring}}} \simeq \frac{5(g\rho_0)^2}{\epsilon_0}, \tag{3.63}$$

again controlled by the particle collision time τ_{NL}. With this result, we establish an interesting connection with condensed-matter electronic systems, for which the effect of electron-electron interactions on the weak localization correction in a disordered conductor can be explained by the finite electronic coherence time τ_ϕ. Note, however, that, for electrons in low-dimensional conductors, the decay of weak localization with the particle interaction time has been derived analytically, and is not strictly exponential: in 2d geometries, it is rather of the form $\exp(-t/(\tau_{\text{in}} \ln t))$ (τ_{in} being the electronic equivalent of our τ_{NL}) [243]. Whether or not similar logarithmic corrections are present in our case remains an interesting open problem.

3.2.5 Thermalization of the diffusive ring

Using our numerical solution of the kinetic equation for the diffusive mode (3.36), we can also compare the prediction of the kinetic approach for the transverse shape of the ring with the Gross-Pitaevskii simulations, from short time to the regime $t \geq \tau_{\text{NL}}$, where the thermalization process completely smoothens the momentum distribution (see the last pictures in Fig. 3.5). We have seen in subsection 3.1.5 that the theoretical expressions for the density of states and the spectral functions at the Born approximation fail at low energies and momenta, as $k\ell$ becomes smaller (see Figs. 3.2 and 3.3). In this region, obtaining a precise analytical expression of the spectral functions beyond the Born approximation is a very hard problem [240, 244]. In an effort to take these discrepancies into account, to achieve a good precision for the transverse shape of the ring at all k (and not just for $k \sim k_0$ as in the previous subsection), we wish to solve the kinetic equation (3.36) using a numerically simulated density of states, and a numerically simulated spectral function for the initial condition $f_\epsilon^{(0)}$. However, we are again confronted to the fact that our kernel W is computed in the Born approximation, and is not strictly speaking valid at low energies (and not defined for negative energies). To address this difficulty, we proceed as follows. We first compute numerical spectral functions $A_\epsilon(k)$ for different values of k, and shift them in energy to set the maximum at the kinetic energy ϵ_k. This approximation is roughly equivalent to neglecting the real part of the self-energy. We then compute the corresponding density of states by integrating these shifted spectral functions over $\boldsymbol{k}$ (see Eq. (1.61) in chapter 1). The kinetic equation (3.36) is solved for $f_\epsilon(t)$ using this density of states, and taking for the initial condition the (shifted) simulated spectral function $A_\epsilon(\boldsymbol{k}_0)$. Finally, the momentum distribution is computed from equation (3.42) at different k, once again using the simulated spectral functions. The results are displayed in Fig. 3.10 and agree well with the simulated momentum distribution up to $t \sim 2\tau_{\text{NL}}$, except at very low values of the momentum. At these values, our semi-analytical procedure fails to describe important corrections to the Born approximation (see, e.g., the significative change in the shape of the spectral functions in Fig. 3.2).

Of course, the kinetic equation (3.36) accurately describes the momentum density at intermediate momenta (around $k = k_0$) at all times. However, as can be seen in Fig. 3.10, at times $t \gg \tau_{\text{NL}}$, thermalization shifts the momentum distribution towards low momenta that

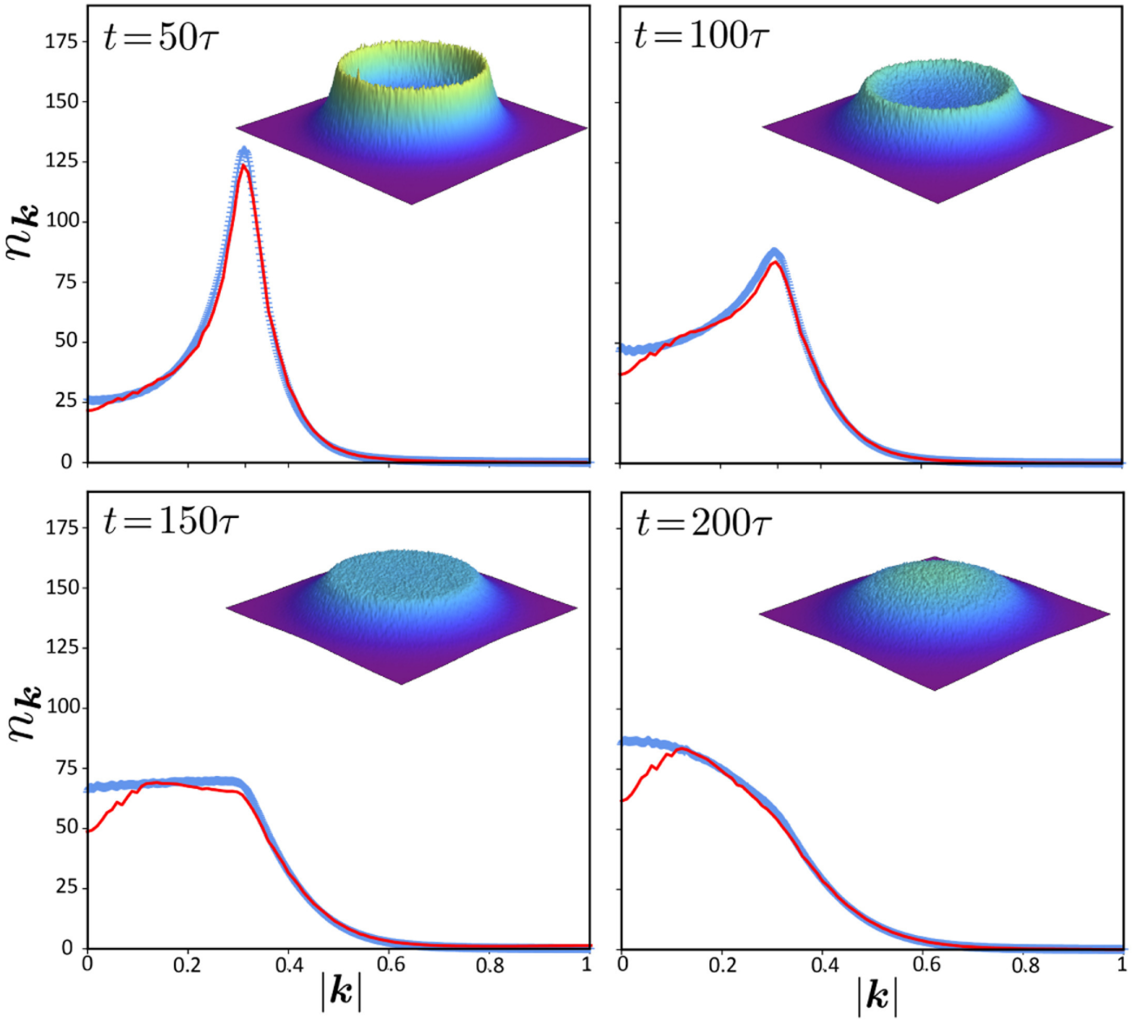

Figure 3.10 – Radial cuts of the momentum distribution $n_{\boldsymbol{k}}(t)$ at four increasing times. The insets show the corresponding density plots in the (k_x, k_y) plane. Chosen parameters are $k_0 \simeq \pi/10$ and $\gamma = 0.01$, corresponding to a mean free time $\tau = 100$, and the interaction energy is set to $g\rho_0 = 0.002$. Note that these parameters are very similar to the ones of Figs. 3.4 and 3.5. The distributions involve an angular average and are further averaged over 1680 disorder realizations. Solid red curves are solutions of the theoretical kinetic equations 3.36 and 3.37, computed using simulated spectral functions, as described in the main text.

cannot be described by the Born approximation. Moreover, in this long-time regime, the diminishing width of the momentum distribution requires a fine discretization in momentum space, and thus simulations of very large systems over long times. These two constraints set a computational limit to the numerical study of the momentum space dynamics of our system. In the last chapter of this thesis, devoted to the long-time thermalization process of the system, we will circumvent this issue by monitoring the dynamics of the system through the time-resolved coherence function of the gas, g_1, which is the Fourier transform of the momentum distribution $n_{\boldsymbol{k}}$.

Conclusion

In this chapter, we have compared the predictions of the kinetic theory of chapter 2 with ab initio simulations of the disordered Gross-Pitaevskii equation, in the limit of weak disorder and rare particle collisions. By numerically solving the kinetic equations, we have shown that the energy distributions for the diffusive and coherent components of the gas have different temporal evolutions. In terms of the momentum distribution, these evolutions consist of a broadening of the diffusive ring and a destruction of the CBS peak. These two effects are indeed observed in our simulations, and quantitatively compare with the results of the kinetic theory, thus validating the approach developed in chapter 2. To describe more precisely the short-time dynamics, we have also introduced an approximate semi-analytical description of both effects, from which we obtained a good estimation of the effective decay rates τ_{ring}^{-1} and τ_{CBS}^{-1} resulting from the asymmetry between the two kinetic equations. In particular, we have found that the contrast of the CBS peak is well captured by an exponentially decay with a characteristic time $\tau_\phi \sim \epsilon_0/5(g\rho_0)^2$. This time scale can be interpreted as an effective dephasing mechanism for the counter-propagating amplitudes responsible for CBS. To some extent, this effect is similar to what happens for weak localization, due to electron-electron interactions, in disordered conductors, usually presented as a decoherence process [245–247]. Finally, at longer times, we have seen that the broadening of the diffusive ring eventually leaves room to a complete smoothing of the momentum distribution, hinting the beginning of a thermalization process. In this long-time regime, the momentum distribution shifts towards low momenta, where the effects of disorder are stronger, which complicates both theoretical and numerical approaches. We leave the study of the long-time thermalization for the final chapter of this thesis. In the next chapter, we will still focus on the short-time dynamics of the gas in the opposite regime of interactions stronger than the disorder, where multiple scattering becomes negligible and the gas displays an interesting prethermal behavior.

Chapter 4

Prethermalization in disorder

Introduction

In the previous chapters, our main focus was the effect of weak particle interactions on the diffusion and weak localization phenomena in a disordered Bose gas. To study them, we have looked at the short-time dynamical evolution of the momentum distribution of the gas, in a completely out-of-equilibrium scenario induced by a quench in both disorder and interactions. Until now, however, we have restricted ourselves to the regime where the disorder is typically larger than interactions. Within this limit, we have described both numerically and theoretically the destruction of the coherent backscattering peak due to particle interactions. On a longer time scale controlled by the particle interaction time τ_{NL}, the diffusive motion of the atoms is also impacted, and the momentum distribution slowly acquires a smooth isotropic shape centered around $\boldsymbol{k} = 0$. We have interpreted this phenomenon as the establishment of thermalization, a slow relaxation process that eventually drives isolated interacting systems towards a state of thermal equilibrium, for which the value of macroscopic quantities are time independent, as prescribed by statistical mechanics [69–71]. This thermalization process will be the topic of our final chapter.

In the present chapter, we again explore the interplay between disorder and interactions in a far from equilibrium Bose gas, but this time in the regime where interactions, albeit weak, are typically stronger than the disorder. This intermediate limit between the homogeneous case and the strongly disordered case remains poorly explored, especially in dimensions larger than one. When interactions are strong enough, disorder scattering is expected to vanish, and this regime should display a physics closer to the one of the homogeneous gas. To emphasize the differences with the physics addressed in the previous chapter, we will first look at the structural changes in the momentum distribution as interactions are increased. We will then see that the relevant dynamics is revealed more naturally by the spatial coherence function g_1 of the gas. Using a hydrodynamic approach, we will derive the short time-evolution of g_1 and compare it to the spatial coherence function in the multiple scattering regime. As interactions are increased, one naively expects that the system thermalizes on a shorter time scale. On the contrary, however, we will show that the system quickly reaches a specific non-thermal state, from which it departs very slowly, before eventually undergoing full thermalization. In this metastable state, the gas displays a light-cone spreading of its spatial correlation, within which the fluctuations exhibit properties resembling those of a true thermal equilibrium, including a certain degree of universality. We interpret this phenomenon as a form of prethermalization, an exotic relaxation process usually displayed by systems slightly perturbed from integrability, and here occuring as a consequence of disorder. In the following, we again set $\hbar = 1$.

4.1 Effect of interactions on the momentum distribution

To get a first insight on the dynamics of the system for strong interactions, we compute numerically the time-resolved momentum distributions for increasing interaction strengths, starting from the nearly linear regime discussed in chapters 1 and 2. Note that for a reason that will become apparent later (see 4.3.2), the numerical simulations in this chapter are performed using a correlated disorder potential $V(\boldsymbol{r})$, namely a blue-detuned speckle [7, 228, 248], with a mean value $\overline{V(\boldsymbol{r})} = 0$ and a Gaussian correlation function

$$\overline{V(\boldsymbol{r})V(\boldsymbol{r}')} = V_0^2 \exp\left(-\frac{|\boldsymbol{r}-\boldsymbol{r}'|^2}{2\sigma^2}\right), \tag{4.1}$$

where σ denotes the correlation length of the disorder.

In the multiple scattering regime, the hierarchy of energy scales is typically $\epsilon_0 > V_0 > g\rho_0$, where $\epsilon_0 = k_0^2/2m$. The time evolution of the momentum distribution observed numerically in this regime is shown in column a of Fig. 4.1. The results are qualitatively similar to what was found in the previous chapters, incidentally showing that at time $t > \tau$ the general shape of the momentum distribution is not affected by the fact that the disorder is correlated. We then compute the momentum distributions at very similar times, but now progressively increasing the interaction strength. In the intermediate regime where $\epsilon_0 > g\rho_0 > V_0$, displayed in Fig. 4.1b, particle interactions scramble the distribution before the diffusive ring is fully formed, and the onset of thermalization is visible at much shorter times. As interactions become larger than the kinetic energy, $g\rho_0 > V_0, \epsilon_0$ (Figs. 4.1 c and d), we observe the emergence of interference rings that span the whole momentum distribution, suggesting that the condensate field ψ acquires a long-range spatial phase coherence. In this regime, disorder scattering is in fact negligible, and interactions make the gas behave more and more like a fluid [220, 249].

These qualitative observations suggest that the first-order spatial correlation function of the Bose gas plays a particular role in the regime of stronger interactions:

$$g_1(\boldsymbol{r},t) \equiv \mathcal{V}\overline{\psi^*(0,t)\psi(\boldsymbol{r},t)} = \int \frac{d^2\boldsymbol{k}}{(2\pi)^2} n_{\boldsymbol{k}}(t) e^{i\boldsymbol{k}\cdot\boldsymbol{r}}, \tag{4.2}$$

where we recall that the overbar refers to the disorder average. As is well known, the spatial decay of g_1 provides a measure of the spatial coherence of the Bose gas. For example, the g_1 correlation of a thermal gas usually decays exponentially in space, while for a Bose-Einstein condensate, g_1 saturates at large r. From the numerical point of view, looking at g_1 instead of n_k has a specific advantage: its long range spatial decay can be extrapolated from its behavior over relatively small distances, which does not require simulations over large systems. On the other hand, the momentum distribution n_k is typically concentrated around the low k values, and its study requires a fine discretization of the momentum space, implying large systems sizes.

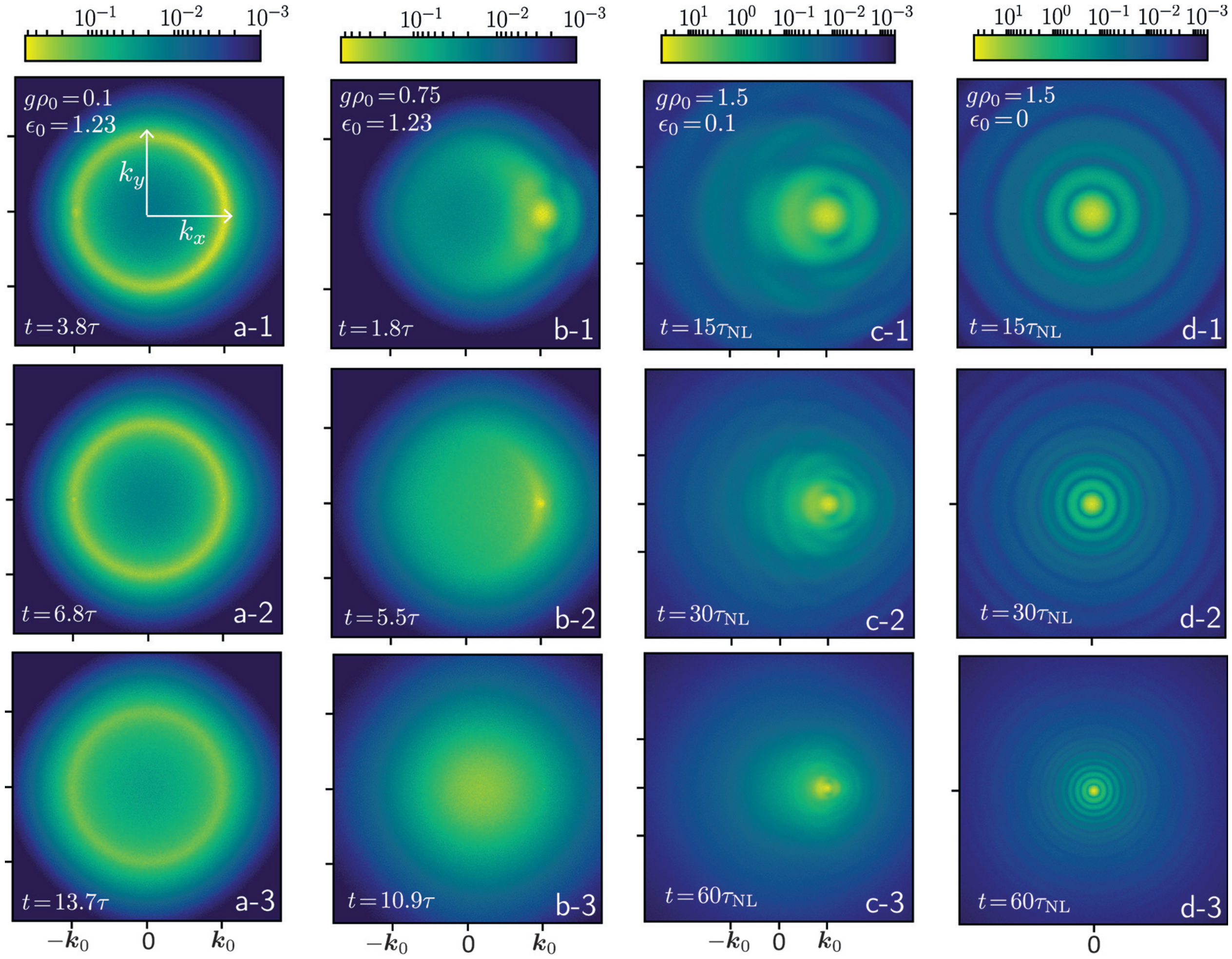

Figure 4.1 – Momentum distribution $n_{\boldsymbol{k}}(t)$ of an interacting Bose gas launched with momentum $\boldsymbol{k}_0$ in a 2d random potential. Rows correspond to three successive times, given either in units of the scattering mean free time τ or of the nonlinear time $\tau_{\mathrm{NL}} \sim \epsilon_0/(g\rho_0)^2$. For all plots, the disorder amplitude is set to $V_0 = 0.4$. (a) $\epsilon_0 > V_0 > g\rho_0$: particles experience multiple scattering on the random potential (with here $k_0\ell = 18.0$). This gives rise to the incoherent diffusive ring in momentum space, and the CBS peak. As time increases, CBS vanishes and the distribution slowly thermalizes due to particle interactions. (b) $\epsilon_0 > g\rho_0 > V_0$: increased interactions compete with disorder and thermalize the distribution before the elastic ring is fully formed. (c) $g\rho_0 > \epsilon_0 > V_0$: interactions are larger than the kinetic energy, so that the gas starts to behave like a fluid. The initial small disorder-induced field fluctuations are coherently enhanced and yield an interference ring pattern in momentum space. (d) $g\rho_0 > V_0 > \epsilon_0 = 0$: same regime as in column (c) but for a gas initially at rest. The interference pattern is more visible as kinetic energy vanishes.

4.2 Spatial coherence in the multiple scattering regime

To have a benchmark for the coherent properties of the interacting Bose gas, we first consider the spatial coherence expected in the multiple scattering regime. We obtain the coherence function g_1 from the average momentum distribution derived in chapter 2, using Eq. (4.2).

4.2.1 Non-interacting case

In the non-interacting case, we recall that the long-time momentum distribution for the diffusive modes is described, in the Born approximation, by an isotropic Lorentzian shape after a few τ (see Eq. (1.86) of chapter 1):

$$n_{\boldsymbol{k}}(g=0) = \frac{1}{\pi\nu\tau}\frac{1}{(\epsilon_k - \epsilon_0)^2 + 1/\tau^2}, \tag{4.3}$$

for a Gaussian uncorrelated potential. The result is of course the same for a correlated potential, the finite correlation simply boiling down to a change of the scattering mean free time τ. The latter is set by the imaginary part of the self-energy $\Sigma = \Sigma' + i\Sigma''$:

$$\frac{1}{\tau} \equiv -2\Sigma'' = 2\pi\int\frac{\mathrm{d}\boldsymbol{k}''}{(2\pi)^d}\tilde{\mathcal{C}}(\boldsymbol{k}''-\boldsymbol{k})\delta(\epsilon-\epsilon_{\boldsymbol{k}''}), \tag{4.4}$$

where $\tilde{\mathcal{C}}$ is the Fourier transform of the disorder correlation function, i.e. the power spectrum of the disorder. For a potential with Gaussian correlation (4.1), we find

$$\tilde{\mathcal{C}}(\boldsymbol{k}) = 2\pi V_0^2\sigma^2\exp\left(-\frac{1}{2}k^2\sigma^2\right), \tag{4.5}$$

which leads to the following expression for τ:

$$\frac{1}{\tau} = 2\pi V_0^2\sigma^2 e^{-k_0^2\sigma^2} I_0(k_0^2\sigma^2). \tag{4.6}$$

Here I_0 denotes the modified Bessel function of the first kind. Using Eq. (4.3), we find the coherence function:

$$g_1(\boldsymbol{r},t) = J_0(k_0 r)\exp(-r/\ell) \qquad (g=0), \tag{4.7}$$

with $r \equiv |\boldsymbol{r}|$, J_0 the Bessel function of the first kind and $\ell = (k_0/m)\tau$ is the mean free path. Note that this expression is essentially the first-order correlation function of the 2d matter-wave speckle pattern formed by the particles scattered in the random potential [250]. It shows that the coherence length of the Bose gas is rather short in the multiple-scattering regime[1], of the order of the de Broglie wavelength $2\pi/k_0$. We show in Fig. 4.3 (in black) the g_1 function computed numerically for $g = 0$, together with the above theoretical formula.

---

[1] In the multiple scattering regime and for correlated disorder, the g_1 function has a small imaginary part at very short times $t \leq \tau$, as the momentum distribution is not yet fully isotropic. Here, we focus on a regime $t \gg \tau$, where this imaginary part can be neglected.

4.2.2 Broadening of the diffusive ring

For small but nonzero g, interactions lead to a decay and a broadening of the diffusive ring, both controlled by the nonlinear time $\tau_{\rm NL} = \epsilon_0/(g\rho_0)^2$. We have found in chapter 2 that the time evolution of the energy distribution $f_\epsilon(t)$ is described by a Boltzmann-like kinetic equation in this regime. While $f_\epsilon(t)$ ultimately becomes thermal when $t \gg \tau_{\rm NL}$ [172], as long as $t < \tau_{\rm NL}$ the scattering ring remains well resolved (as in Figs. 4.1a-1-3) and we have seen that the time evolution of $f_\epsilon(t)$ is approximately captured by a diffusion process in the energy domain:

$$f_\epsilon(t) \simeq \int d\epsilon' \frac{f^{(0)}_{\epsilon'}}{\sqrt{4\pi D_{\epsilon_0} t}} \exp\left[-\frac{(\epsilon-\epsilon')^2}{4D_{\epsilon_0}t}\right], \tag{4.8}$$

with a diffusion coefficient in energy space such that $2D_{\epsilon_0}\tau_{\rm NL} \sim 1/\tau^2$. Eq. (4.8) yields, for the momentum distribution,

$$n^D_{\boldsymbol{k}} = n^{D\,(g=0)}_{\boldsymbol{k}} \left[1 - C_1 \frac{t}{\tau_{\rm NL}} \frac{1}{(\epsilon_{\boldsymbol{k}}-\epsilon_0)^2 + 1/\tau^2}\right], \tag{4.9}$$

where C_1 is a numerical constant, which we estimated to be of the order of 2 using numerical simulations, see chapter 3. According to Eq. (4.9), at short time, the ring maintains its approximate Lorentzian form, and its Half-Width at Half-Maximum (HWHM) $\Delta k(t)$ consequently increases linearly in time:

$$\Delta k(t) \sim (1 + Ct/\tau_{\rm NL})/\ell. \tag{4.10}$$

This broadening is illustrated in Fig. 4.2, which shows radial cuts of the scattering ring, obtained by numerically solving the disordered Gross-Pitaevskii equation at successive times[2]. As long as $t < \tau_{\rm NL}$, we find that width extracted from these cuts indeed grows linearly in time.

The Fourier transform of Eq. (4.9) yields

$$g_1(\boldsymbol{r}, t) \simeq J_0(k_0 r) \exp\left[-\Delta k(t) r\right]. \tag{4.11}$$

The short-time evolution of the coherence function is therefore controlled by the width of the diffusive ring. As shown in Fig. 4.3, Eq. (4.11) describes very well the numerical results for g_1 at $g \neq 0$. Here the main effect of interactions is to smoothen the matter-wave speckle,

---

[2] The attentive reader will notice that the measured value of the constant C_1 differs from the measured value of 2.27 from chapter 3 by a factor 3. In fact, the independence of this constant on the strength of disorder and interactions heavily relies on the separation of the time scales τ and $\tau_{\rm NL}$, because we assumed that the ring is fully formed before it relaxes due to interactions. In the previous chapter, we checked that independence for ratios $\tau_{\rm NL}$ ranging from ~ 700 to $\sim 10^5$. Here, we choose $\tau_{\rm NL} \sim 17\tau$, so that it is natural to expect some discrepancies. While this choice is made essentially because simulations with a correlated disorder are more computationally demanding (due to a much thinner discretization required), it provides the interesting result that the linear time evolution of the width is remarkably robust as τ approaches $\tau_{\rm NL}$.

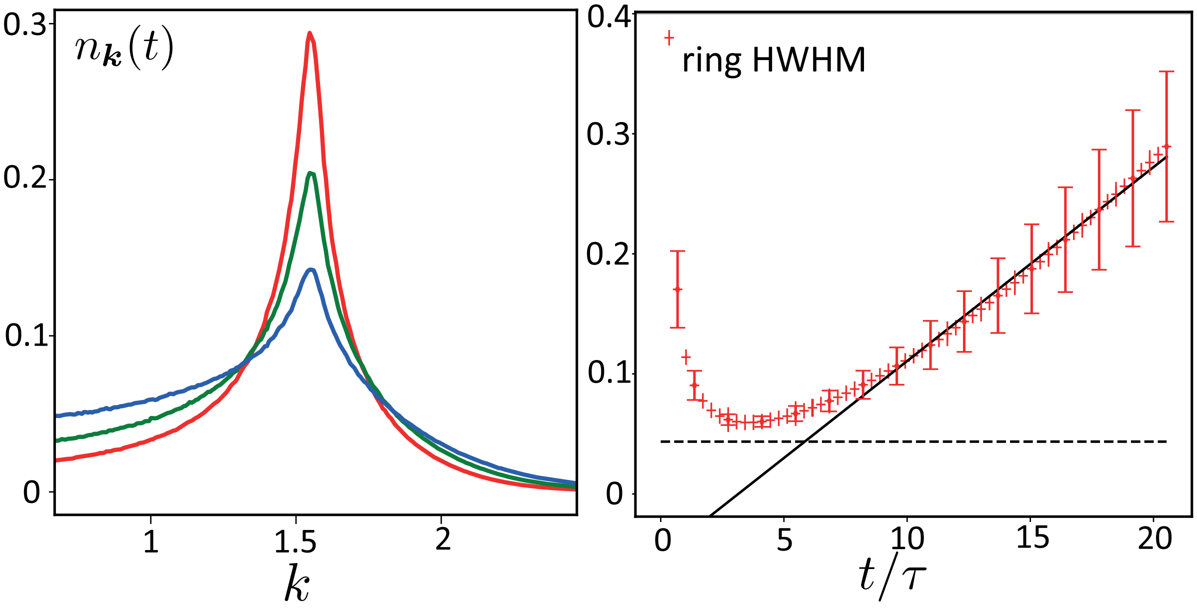

Figure 4.2 – Left: radial cuts of the scattering ring, computed numerically at times $t = 10.9\tau$, 15.1τ and 19.8τ from top to bottom (numerical data points have been joined for clarity). Each cut involves an angular average of the momentum distribution. Right: HWHM of the ring, obtained by fitting the radial cuts with a Lorentzian profile in a k-window of width 0.8 centered on k_0 (red symbols). Error bars are deduced from the χ^2 goodness of the fits. The solid line is a linear fit $\Delta k_{\mathrm{fit}}(t) = 1/\ell[1 + 6.38(t - 5.84\tau)/\tau_{\mathrm{NL}}]$, which confirms the linear evolution of $\Delta k(t)$. The dashed line shows the $g = 0$ result, $\Delta k = 1/\ell$. Here $g\rho_0 = 0.07$, $V_0 = 0.2$, $k_0 = 1.57$, $k_0\ell = 36$. The chosen system size is $L = 200\pi$, and the discretization is such that there are 7.5 points per correlation length. Results are averaged over 4800 realizations. With these parameters, $\tau = 14.6$ and $\tau_{\mathrm{NL}} \simeq 251.5$.

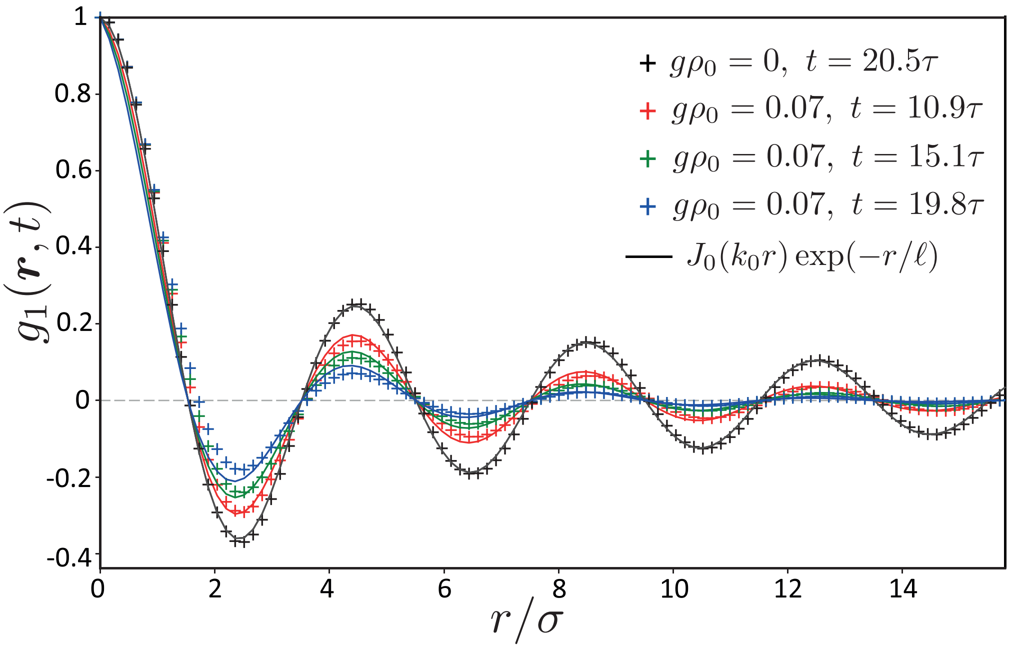

Figure 4.3 – Radial cuts of the coherence function $g_1(\boldsymbol{r}, t)$ of the Bose gas in the multiple scattering regime. Parameters are the same as in Fig. 4.2, such that $\tau = 14.6$ and $\tau_{\mathrm{NL}} \simeq 251.5$. The cuts also involve an angular average of g_1. For $g = 0$ (outer black symbols, numerics, and solid black curve, theory) the function is independent of time after a few τ and exhibits oscillations at the scale $2\pi/k_0$. In the presence of interactions, these oscillations are smoothed. Colored solid curves for $g \neq 0$ are the theoretical prediction, Eq. (4.11), in which we take the expression $\Delta k(t) = \Delta k_{\mathrm{fit}}(t)$ given in the caption of Fig. 4.2.

without significantly affecting the coherence of the gas. This picture would of course change at long time $t \gg \tau_{\mathrm{NL}}$, where the momentum distribution starts to significantly deviate from Eq. (4.3) and approaches a thermal law [172]. This limit will be extensively discussed in chapter 5.

4.3 Coherence function in the hydrodynamic regime

We now address the opposite regime where $g\rho_0 \gg V_0 \gg \epsilon_0$. In this limit, and according to the discussion in Sec. 4.1, the dynamics is dominated by the interactions, while disorder plays the role of a small perturbation. In the context of homogeneous 3d condensates, at equilibrium and at low enough temperatures, the condensate mode in macroscopically occupied and the quantum and thermal fluctuations induce a negligible depletion of the condensates into the other modes. This allows for a good approximation of the total field operator by the complex wavefunction of the condensate [220, 222, 251] (see the reasoning used for our elementary derivation of the GPE in chapter 2). The wavefunction of the condensate is thus usually written as $\psi = \psi_0 + \delta\psi$, with ψ_0 the condensate wave function and $\delta\psi$ describing the fluctuations. In lower dimensions and in particular in 2d, however, a macroscopic condensate structure is prohibited by the Mermin-Wagner theorem [252], so that this complex representation is a priori not valid. In fact, in this case, the phase of the wave function tends to fluctuate more than in 3d. This imposes to describe the gas using a density-phase repretation [253–257] :

$$\Psi(\boldsymbol{r}, t) = \sqrt{\rho(\boldsymbol{r}, t)} \exp[i\theta(\boldsymbol{r}, t)], \tag{4.12}$$

where both the density ρ and the phase θ fluctuate. As compared to the usual situation of a Bose gas subjected to quantum or thermal fluctuations though, in our case ρ and θ fluctuate purely due to the presence of the random potential.

4.3.1 Hydrodynamic description

Substituting Eq. (4.12) into the GPE and separating the real and imaginary parts leads to the coupled equations

$$\frac{\partial\rho}{\partial t} = -\frac{1}{m}\nabla(\rho\nabla\theta) \tag{4.13}$$

$$\frac{\partial\theta}{\partial t} = \frac{1}{2m}\frac{\nabla^2\sqrt{\rho}}{\sqrt{\rho}} - \frac{1}{2m}(\nabla\theta)^2 - V(\boldsymbol{r}) - g\rho, \tag{4.14}$$

complemented with the initial conditions $\rho(\boldsymbol{r}, t = 0) = \rho_0$ and $\theta(\boldsymbol{r}, t = 0) = \boldsymbol{k}_0 \cdot \boldsymbol{r}$. Aside from the disorder potential $V(\boldsymbol{r})$, Eqs. (4.13) and (4.14) are respectively the continuity and the Euler equation for a fluid with density $\rho(\boldsymbol{r}, t)$ and velocity $\nabla\theta(\boldsymbol{r}, t)$. As expected, we end up with the out-of-equilibrium formulation of the hydrodynamic description of the gas, in which the density is the modulus square of ψ, while the velocity of the fluid is given by the gradient of the phase, $\nabla\theta(\boldsymbol{r}, t)$. This description, originally employed by Bogoliubov to explain describe the superfluid behavior of Helium-4, was subsequently adapted to the superfluidity of cold atomic Bose gases [220, 222, 253].

Density and phase fluctuations

As the gas evolves in time, the density $\rho(\boldsymbol{r}, t)$ and the phase $\theta(\boldsymbol{r}, t)$ fluctuate due to the presence of the disorder potential. The typical fluctuations of the disorder being very small compared to the typical interaction energy, we make use of perturbation theory. The hydrodynamic description proves useful in this respect: we directly write the density in the form $\rho(\boldsymbol{r}, t) = \rho_0 + \delta\rho(\boldsymbol{r}, t)$, where $\delta\rho(\boldsymbol{r}, t)$ is a small density fluctuation, and make no assumption on the phase fluctuations, which may be strong in this regime [256]. However, Eq. (4.13), which can be rewritten as

$$\frac{\partial\delta\rho}{\partial t} = -\frac{1}{m}\nabla\delta\rho\cdot\nabla\theta - \frac{1}{m}(\rho_0 + \delta\rho)(\nabla^2\theta), \tag{4.15}$$

imposes that the fluctuations of the *gradient* of the phase $\delta\nabla\theta$ are necessarily of the same order than $\delta\rho$. Without disorder first, $\delta\rho(\boldsymbol{r},t)=0$ and, substituting Eq. (4.12) into (4.14), we find the unperturbed solution

$$\psi^{(0)}(\boldsymbol{r},t)=\sqrt{\rho_0}\,e^{i\boldsymbol{k}_0\cdot\boldsymbol{r}-\left(\frac{k_0^2}{2m}+g\rho_0\right)t}. \tag{4.16}$$

Thus, for small disorder, it is convenient to write the phase as $\theta(\boldsymbol{r},t)=\boldsymbol{k}_0\cdot\boldsymbol{r}-(k_0^2/2m+g\rho_0)t+\delta\theta(\boldsymbol{r},t)$, and linearize Eqs. (4.13) and (4.14) around the homogeneous solution $\psi^{(0)}$ with respect to the small parameters $\delta\rho$ and $\nabla\delta\theta$. This leads to the Bogoliubov-De Gennes (BdG) equations [258]

$$\frac{\partial\delta\rho}{\partial t}=-(\boldsymbol{v}\cdot\nabla)\delta\rho-\frac{\rho_0}{m}\nabla^2\delta\theta \tag{4.17}$$
$$\frac{\partial\delta\theta}{\partial t}=-(\boldsymbol{v}\cdot\nabla)\delta\theta+\frac{1}{4m\rho_0}\nabla^2\delta\rho-V(\boldsymbol{r})-g\delta\rho, \tag{4.18}$$

where $\boldsymbol{v}=\boldsymbol{k}_0/m$. They are complemented with the initial conditions $\delta\rho(\boldsymbol{r},t)=0=\delta\theta(\boldsymbol{r},t)$ (the initial state being a pure plane wave). Eqs. (4.17) and (4.18) can be conveniently recast under the usual form of the BdG equations

$$i\frac{\partial\boldsymbol{\phi}(\boldsymbol{r},t)}{\partial t}=\mathcal{L}\boldsymbol{\phi}(\boldsymbol{r},t)+2\sqrt{\rho_0}V(\boldsymbol{r})\begin{bmatrix}0\\1\end{bmatrix} \tag{4.19}$$

with

$$\boldsymbol{\phi}(\boldsymbol{r},t)\equiv\begin{bmatrix}\delta\rho(\boldsymbol{r},t)/\sqrt{\rho_0}\\ 2i\sqrt{\rho_0}\,\delta\theta(\boldsymbol{r},t)\end{bmatrix}\quad\text{and}\quad\mathcal{L}=\begin{bmatrix}-i(\boldsymbol{v}\cdot\nabla) & -\frac{1}{2m}\nabla^2\\ -\frac{1}{2m}\nabla^2+2g\rho_0 & -i(\boldsymbol{v}\cdot\nabla)\end{bmatrix}. \tag{4.20}$$

This linear system is easily solved in Fourier space. Denoting by $\tilde{\boldsymbol{\phi}}(\boldsymbol{k},t)$ the Fourier transform of $\boldsymbol{\phi}(\boldsymbol{r},t)$ using the initial conditions for $\delta\rho$ and $\delta\theta$, we obtain

$$\tilde{\boldsymbol{\phi}}(\boldsymbol{k},t)=-2i\sqrt{\rho_0}\tilde{V}(\boldsymbol{k})\int_0^t \mathrm{d}t'e^{i\tilde{\mathcal{L}}(\boldsymbol{k})\times(t'-t)}\begin{bmatrix}0\\1\end{bmatrix}, \tag{4.21}$$

where

$$\tilde{\mathcal{L}}(\boldsymbol{k})=\begin{bmatrix}\boldsymbol{v}\cdot\boldsymbol{k} & -\frac{k^2}{2m}\\ -\frac{k^2}{2m}+2g\rho_0 & \boldsymbol{v}\cdot\boldsymbol{k}\end{bmatrix}. \tag{4.22}$$

$\tilde{\mathcal{L}}(\boldsymbol{k})$ can be readily diagonalized, with eigenvalues $\lambda_\pm=\pm\omega_{\boldsymbol{k}}+\boldsymbol{v}\cdot\boldsymbol{k}$, where $\omega_{\boldsymbol{k}}=\sqrt{\epsilon_{\boldsymbol{k}}(\epsilon_{\boldsymbol{k}}+2g\rho_0)}$ is the well-known Bogoliubov spectrum, and we recall that $\epsilon_k=\boldsymbol{k}^2/2m$. In fact, we performed here a time-dependent Bogoliubov transformation: we showed that the dynamics of the interacting system can be mapped onto the equivalent problem of a gas of non-interacting quasi-particles with the dispersion relation $\omega_k + \boldsymbol{v}\cdot\boldsymbol{k}$. At low momenta $k \ll k_c$, where

$$k_c \equiv \sqrt{mg\rho_0}, \tag{4.23}$$

the elementary excitations of the system are phonons, characterized by a linear dispersion relation $E(\boldsymbol{k}) = c_s k + \boldsymbol{v}\cdot\boldsymbol{k}$, where $c_s = \sqrt{g\rho_0/m}$ is the associated sound velocity. This part of the spectrum is responsible for the superfluid properties of Bose gases at equilibrium [220]. At high momenta, $k \gg k_c$, we recover the free-particle behavior as $\omega_{\boldsymbol{k}} \sim \epsilon_{\boldsymbol{k}}$.

Substituting the diagonal form of $\tilde{\mathcal{L}}(\boldsymbol{k})$ into the general solution (4.21), and performing the integral over t', we find

$$\tilde{\boldsymbol{\phi}}(\boldsymbol{k},t) = \sqrt{\rho_0}\tilde{V}(\boldsymbol{k}) \begin{bmatrix} \frac{\epsilon_{\boldsymbol{k}}}{\omega_{\boldsymbol{k}}}\left(F(\boldsymbol{k},t) + F^*(-\boldsymbol{k},t)\right) \\ F(\boldsymbol{k},t) - F^*(-\boldsymbol{k},t) \end{bmatrix} \quad \text{with} \quad F(\boldsymbol{k}) = \frac{1-e^{i(\omega_{\boldsymbol{k}}-\boldsymbol{v}\cdot\boldsymbol{k})\,t}}{\omega_{\boldsymbol{k}}-\boldsymbol{v}\cdot\boldsymbol{k}}. \tag{4.24}$$

Inverting the change of variables we made in equation (4.20), we finally obtain, for the density and phase fluctuations

$$\delta\rho(\boldsymbol{r},t) = \rho_0 \int \frac{d^2\boldsymbol{k}}{(2\pi)^2}\tilde{V}(\boldsymbol{k})\frac{\epsilon_{\boldsymbol{k}}}{\omega_{\boldsymbol{k}}}\left[F(\boldsymbol{k},t) + F^*(-\boldsymbol{k},t)\right]e^{i\boldsymbol{k}\cdot\boldsymbol{r}}, \tag{4.25}$$

$$\delta\theta(\boldsymbol{r},t) = \frac{1}{2i}\int \frac{d^2\boldsymbol{k}}{(2\pi)^2}\tilde{V}(\boldsymbol{k})\left[F(\boldsymbol{k},t) - F^*(-\boldsymbol{k},t)\right]e^{i\boldsymbol{k}\cdot\boldsymbol{r}}. \tag{4.26}$$

For the sake of simplicity, we will now restrict ourselves to the case where the atomic cloud is initially at rest, $\boldsymbol{k}_0 = 0$, corresponding to Fig. 4.1d-1-3. The effect of an initial velocity of the atomic cloud will be discussed later, in section 4.3.3. Here, we are not interested in the drag force induced by a superfluid flow around an obstacle, as is frequently encountered in the literature [259–262], but rather in the evolution of the spatial coherence. In this limiting case, $F(\boldsymbol{k})$=$(1-e^{i\omega_{\boldsymbol{k}}t})/\omega_{\boldsymbol{k}}$, and Eqs. (4.25) and (4.26) reduce to

$$\delta\rho(\boldsymbol{r},t) = 2\rho_0 \int \frac{d^2\boldsymbol{k}}{(2\pi)^2}\tilde{V}(\boldsymbol{k})\frac{1-\cos(\omega_{\boldsymbol{k}}\,t)}{\epsilon_{\boldsymbol{k}}+2g\rho_0}e^{i\boldsymbol{k}\cdot\boldsymbol{r}}, \tag{4.27}$$

$$\delta\theta(\boldsymbol{r},t) = \int \frac{d^2\boldsymbol{k}}{(2\pi)^2}\tilde{V}(\boldsymbol{k})\frac{\sin(\omega_{\boldsymbol{k}}\,t)}{\omega_{\boldsymbol{k}}}e^{i\boldsymbol{k}\cdot\boldsymbol{r}}. \tag{4.28}$$

Eq. (4.27) confirms a posteriori the assumption that the density fluctuations remain small at weak enough disorder. Indeed, one can verify that the quantity $\sqrt{\overline{\delta\rho^2}}/\rho_0$, which measures the amplitude of the disorder fluctuations, is always small as long as $V_0/g\rho_0 \ll 1$. Additionally, one can show that the spatial extension of the amplitude of the density fluctuations is controlled by the characteristic length

$$\xi \equiv 1/k_c = \frac{1}{\sqrt{mg\rho_0}}, \tag{4.29}$$

called the healing length, which represents the size of the typical variations of the wavefunction. Phase fluctuations, on the other hand, can a priori be arbitrarily large.

Coherence function

Using the expressions for the density and phase fluctuations, Eqs. (4.27) and (4.28), we can now derive the coherence function. To this aim, we start from the definition (4.2), which in the density-phase formalism reads

$$g_1(\boldsymbol{r},t) \equiv \mathcal{V}\overline{\sqrt{\rho(0,t)\rho(\boldsymbol{r},t)}e^{i\Delta\theta(\boldsymbol{r},t)}} \tag{4.30}$$

where $\Delta\theta(\boldsymbol{r},t) \equiv \delta\theta(\boldsymbol{r},t) - \delta\theta(0,t)$. Substituting $\rho(\boldsymbol{r},t) = \rho_0 + \delta\rho(\boldsymbol{r},t)$ into this expression, and expanding to the second order in $\delta\rho$, we obtain

$$g_1(\boldsymbol{r},t) = \mathcal{V}\rho_0\left(\overline{e^{i\Delta\theta}} + \frac{1}{2\rho_0}\overline{(\delta\rho+\delta\rho')e^{i\Delta\theta}} - \frac{1}{8\rho_0^2}\overline{(\delta\rho^2+\delta\rho'^2-2\delta\rho\delta\rho')e^{i\Delta\theta}}\right), \tag{4.31}$$

where we use the notations $\delta\rho(0,t) = \delta\rho$ and $\delta\rho(\boldsymbol{r},t) = \delta\rho'$ for clarity. To simplify the averages, we replace the exponentials by their (infinite) Taylor series, and use the Wick theorem to decompose terms of the type $\overline{(\delta\rho)^n(\Delta\theta)^l}$ into sums of second order averages $\overline{\delta\rho\Delta\theta}$, $\overline{\delta\rho^2}$ and $\overline{\Delta\theta^2}$. This procedure yields the simple identities [256]:

$$\begin{aligned}
&\overline{e^{i\Delta\theta}} = e^{-\overline{\Delta\theta^2}/2}\\
&\overline{\delta\rho\, e^{i\Delta\theta}} = e^{-\overline{\Delta\theta^2}/2}\left(i\overline{\delta\rho\Delta\theta}\right)\\
&\overline{\delta\rho^2\, e^{i\Delta\theta}} = e^{-\overline{\Delta\theta^2}/2}\left(\overline{\delta\rho^2} - \overline{\delta\rho\Delta\theta}^2\right)\\
&\overline{\delta\rho\delta\rho'\, e^{i\Delta\theta}} = e^{-\overline{\Delta\theta^2}/2}\left(\overline{\delta\rho\delta\rho'} - \overline{\delta\rho\Delta\theta}\,.\,\overline{\delta\rho'\Delta\theta}\right).
\end{aligned} \tag{4.32}$$

Eq. (4.31) becomes:

$$\begin{aligned}
g_1(\boldsymbol{r},t) = \mathcal{V}\rho_0\Bigg(1 &+ \frac{i}{2\rho_0}\left(\overline{\delta\rho\Delta\theta} + \overline{\delta\rho'\Delta\theta}\right)\\
&-\frac{1}{8\rho_0^2}\left[\overline{\delta\rho^2} + \overline{\delta\rho'^2} - 2\overline{\delta\rho\delta\rho'} - (\overline{\delta\rho\Delta\theta} - \overline{\delta\rho'\Delta\theta})^2\right]\Bigg)\, e^{-\overline{\Delta\theta^2}/2}.
\end{aligned} \tag{4.33}$$

This equation can be further simplified by using Eqs. (4.25) and (4.26). Indeed, noticing that

$$\overline{\tilde{V}(\boldsymbol{k})\tilde{V}(\boldsymbol{k}')} = (2\pi)^2\tilde{C}(\boldsymbol{k})\delta(\boldsymbol{k}+\boldsymbol{k}'), \tag{4.34}$$

where we recall that $\tilde{C}(\boldsymbol{k}) = \int d\boldsymbol{r} e^{i\boldsymbol{k}\cdot\boldsymbol{r}}\overline{V(0)V(\boldsymbol{r})} = 2\pi V_0^2\sigma^2 e^{-k^2\sigma^2/2}$ is the disorder power spectrum, we see that

$$\overline{\delta\rho\Delta\theta} = -\overline{\delta\rho'\Delta\theta} = -2\int\frac{d^2\boldsymbol{k}}{(2\pi)^2}\tilde{C}(\boldsymbol{k})\left[\frac{1-\cos(\omega_{\boldsymbol{k}}t)}{\epsilon_{\boldsymbol{k}}+2g\rho_0}\right]\left[\frac{\sin(\omega_{\boldsymbol{k}}t)}{\omega_{\boldsymbol{k}}}\right]\left[1-e^{-i\boldsymbol{k}\cdot\boldsymbol{r}}\right]. \tag{4.35}$$

We also neglect the term $(\overline{\delta\rho\Delta\theta}-\overline{\delta\rho'\Delta\theta})^2$, which is of second order in the small parameter $V_0/g\rho_0$. All in all, we find for the coherence function of the gas:

$$g_1(\boldsymbol{r},t)=\mathcal{V}\rho_0\exp\left\{-\frac{1}{8\rho_0^2}\overline{\big[\delta\rho(\boldsymbol{r},t)-\delta\rho(0,t)\big]^2}-\frac{1}{2}\overline{\big[\delta\theta(\boldsymbol{r},t)-\delta\theta(0,t)\big]^2}\right\} \tag{4.36}$$

Again using the explicit expression of the density and phase fluctuations, Eqs. (4.25) and (4.26), we have

$$\overline{\big[\delta\rho(\boldsymbol{r},t)-\delta\rho(0,t)\big]^2}=8\rho_0^2\int\frac{d^2\boldsymbol{k}}{(2\pi)^2}\tilde{C}(\boldsymbol{k})\left[\frac{1-\cos(\omega_{\boldsymbol{k}}\,t)}{\epsilon_{\boldsymbol{k}}+2g\rho_0}\right]^2\big(1-\cos(\boldsymbol{k}\cdot\boldsymbol{r})\big)\,, \tag{4.37}$$

$$\overline{\big[\delta\theta(\boldsymbol{r},t)-\delta\theta(0,t)\big]^2}=2\int\frac{d^2\boldsymbol{k}}{(2\pi)^2}\tilde{C}(\boldsymbol{k})\left[\frac{\sin(\omega_{\boldsymbol{k}}\,t)}{\omega_{\boldsymbol{k}}}\right]^2\big(1-\cos(\boldsymbol{k}\cdot\boldsymbol{r})\big)\,, \tag{4.38}$$

which yields the final expression for g_1:

$$g_1(\boldsymbol{r},t)=\rho_0\exp\left\{-\int\frac{d^2\boldsymbol{k}}{(2\pi)^2}\tilde{C}(\boldsymbol{k})\left(\left[\frac{1-\cos(\omega_k t)}{\epsilon_k+2g\rho_0}\right]^2+\left[\frac{\sin(\omega_k t)}{\omega_k}\right]^2\right)(1-\cos(\boldsymbol{k}\cdot\boldsymbol{r}))\right\}. \tag{4.39}$$

4.3.2 Structure of the coherence function

To interpret physically the structure of Eq. (4.39), we start by performing the angular integral, which leads to

$$g_1(\boldsymbol{r},t)=\rho_0\exp\left\{-V_0^2\sigma^2\int_0^{+\infty}\mathrm{d}k\,k\,e^{-k^2\sigma^2/2}\left(\left[\frac{1-\cos(\omega_k t)}{\epsilon_k+2g\rho_0}\right]^2+\left[\frac{\sin(\omega_k t)}{\omega_k}\right]^2\right)\big[1-J_0(kr)\big]\right\}. \tag{4.40}$$

We then use the change of variables $k\to k/\xi$ to recast this equation under the form:

$$\begin{aligned}g_1(\boldsymbol{r},t)=\rho_0\exp\Bigg\{&-\frac{1}{4}\frac{V_0^2}{(g\rho_0)^2}\frac{\sigma^2}{\xi^2}\int_0^{+\infty}\mathrm{d}k k\,e^{-\frac{k^2}{2}\frac{\sigma^2}{\xi^2}}\\&\times\left(\left[\frac{1-\cos(\tilde{\omega}_k\frac{2c_st}{\xi})}{\tilde{\epsilon}_k+1}\right]^2+\left[\frac{\sin(\tilde{\omega}_k\frac{2c_st}{\xi})}{\tilde{\omega}_k}\right]^2\right)\big[1-J_0(kr/\xi)\big]\Bigg\}\,,\end{aligned} \tag{4.41}$$

where $\tilde{\omega}_k=\sqrt{\tilde{\epsilon}_k(\tilde{\epsilon}_k+1)}$ and $\tilde{\epsilon}_k=k^2/4$. Under this form, the physical content of Eq. (4.39) becomes more apparent as we know discuss. First of all, we notice that the decay of the coherence function is controlled by the parameter

$$\left(\frac{V_0\sigma}{g\rho_0\xi}\right)^2. \tag{4.42}$$

The ratio $V_0/g\rho_0$ being the small parameter of our perturbation theory, this result a priori indicates a slow spatial decay of coherence in the regime considered. As it turns out, however, the decay can be made stronger by tuning the ratio between the correlation length σ and the healing length ξ. This result has a rather intuitive physical origin: if the typical size of the disorder potential hills (and wells) σ is much smaller than the healing length, then the initial density fluctuations it produces will be quickly "smoothed" by the interaction potential, and a large spatial coherence is established. On the other hand, if the typical spatial extent of the initial fluctuations is larger than ξ, the smoothing effect of interactions will take longer to settle in.

Influence of disorder correlations

The ratio σ/ξ also appears in the Gaussian exponential in Eq. (4.41), which effectively selects the momenta that participate in the integral. Physically, this can be understood as follow: a disorder with correlation length σ will typically produce partial waves of momentum $k \sim k_\sigma = 1/\sigma$. Thus, when $\sigma/\xi \gg 1$, we have $k_\sigma \ll k_c = 1/\xi$. k_c being the momentum value that separates the linear, phononic part of the Bogoliubov spectrum from the quadratic part, the choice of this ratio decides which type of excitations plays a role in the dynamics of the system. This is the reason why we originally chose to use a correlated disorder potential in this chapter: the effect of interactions being encoded in the low energy part of the spectrum, we wanted to leave us the possibility to give more weight to the low-lying energy excitations of the system. However, as we will see in the next section where the integral is computed explicitly, the general behavior of the coherence function remains smooth as we turn from a correlated to an uncorrelated potential, the ratio σ/ξ only modifying the overall amplitude of g_1. This is due to the fact that the prefactor (4.42) remains well-defined in the limit of uncorrelated disorder where $\sigma \to 0$, $V_0 \to \infty$ with the product $V_0^2\sigma^2$ constant, corresponding to $\overline{V(\boldsymbol{r})V(\boldsymbol{r}')} = \gamma\delta(\boldsymbol{r}-\boldsymbol{r}')$ with $\gamma \equiv V_0^2\sigma^2$.

Dynamical spreading of correlations

Under the form (4.41), we see that the spatial extent of g_1 is characterized by two characteristic lengths, the healing length ξ and the dynamic length scale

$$r_c(t) \equiv 2c_s t. \tag{4.43}$$

The ratio of these two lengths, $r_c(t)/\xi = 2g\rho_0 t$, suggests that the short-time dynamics of the gas is governed by the characteristic time $\tau_g \equiv 1/g\rho_0$.

At very short times $t \leq \tau_g$, we typically have $r_c(t) \leq \xi$, and the trigonometric functions in the integrand can be expanded, yielding:

$$g_1(\boldsymbol{r},t) = \rho_0 \exp\left\{-t^2 V_0^2 \frac{\sigma^2}{\xi^2}\int_0^{+\infty} \mathrm{d}k k\, e^{-\frac{k^2}{2}\frac{\sigma^2}{\xi^2}}\left[1 - J_0(kr/\xi)\right]\right\}$$
$$= \rho_0 \exp\left\{-t^2 V_0^2 \left[1 - e^{-\frac{r^2}{2\sigma^2}}\right]\right\}. \tag{4.44}$$

g_1 thus first quickly decays at the scale of of the correlation length σ, after which it is constant over the whole space, and very close to its initial constant value 1, as $tV_0 \geq V_0/g\rho_0 \ll 1$. At such short times, the effect of interactions is not yet visible, and the coherence function strongly resembles that of the initial plane wave.

At longer times $t \gg \tau_g$, the two length scales ξ and $r_c(t)$ are well separated, and we distinguish two main limits:

- $r \ll r_c(t)$. In general, the integral is dominated by values of k such that the argument of the Bessel function is large, $k \gg \xi/r$, up to an upper limit imposed by the Gaussian exponential. In this case, this condition translates into $k \gg \xi/r \gg \xi/r_c(t)$. Consequently, the arguments of the sine and cosine functions are typically very large, which leads to very fast oscillations as k increases. Thus, we can in first approximation replace them by their average value over one period $\langle(1-\cos(x))^2\rangle = 3/2$ and $\langle\sin^2(x)\rangle = 1/2$. We obtain a time-independent expression of the coherence function:

$$g_1(\boldsymbol{r},t) \simeq \rho_0 \exp\left\{-8\frac{V_0^2}{(g\rho_0)^2}\frac{\sigma^2}{\xi^2}\int_0^{+\infty} \mathrm{d}k\, \frac{(k^2+1)}{k(k^2+4)^2}\, e^{-\frac{k^2}{2}\frac{\sigma^2}{\xi^2}}\left[1 - J_0(kr/\xi)\right]\right\}. \tag{4.45}$$

When $r \ll \xi$, the argument of the Bessel function is close to 0 and g_1 can be approximated by a Gaussian :

$$g_1(\boldsymbol{r},t) \simeq \rho_0 \exp\left\{-\alpha \frac{r^2}{\xi^2}\,\mathcal{H}_1\left(\frac{\sigma^2}{\xi^2}\right)\right\}, \tag{4.46}$$

where

$$\alpha = \frac{1}{2}\frac{V_0^2}{g\rho_0^2}\frac{\sigma^2}{\xi^2}, \tag{4.47}$$

and $\mathcal{H}_1$ is the function defined by

$$\mathcal{H}_1(x) = \frac{(4+6x)e^{2x}\,E_1(2x) - 3}{2} \quad \text{with} \quad E_1(x) = \int_x^{+\infty} \mathrm{d}t\frac{e^{-t}}{t}. \tag{4.48}$$

In the opposite limit $r \gg \xi$, we split the integral at the intermediate value ξ/r. The integral involving the low values of k is negligible, and, in the other, we can simply neglect the Bessel function, which has large argument. We find that g_1 decays algebraically:

$$g_1(\boldsymbol{r},t) \simeq \rho_0 \left[\mathcal{H}_2\left(\frac{\sigma^2}{\xi^2}\right) \frac{\xi}{r} \right]^{\alpha}, \tag{4.49}$$

with the same α as in Eq. (4.45), and

$$\mathcal{H}_2(x) = \sqrt{x}\, \exp\left\{ \frac{(1+6x)e^{2x}\, E_1(2x) - 3 - \gamma_{\mathrm{em}}}{2} \right\}, \tag{4.50}$$

where $\gamma_{\mathrm{em}} \simeq 0.577$ is the Euler-Mascheroni constant.

- $r \gg r_c(t)$. In this case, the argument of the Bessel function is always very large, and we can neglect it. Similarly to the previous case, we split the integral at $k = \xi / r_c(t)$, and show that the term corresponding to large k values dominates. We find that the coherence function does not depend on r within this limit:

  $$g_1(\boldsymbol{r},t) = \rho_0 \exp\left\{ -\frac{1}{4} \frac{V_0^2}{(g\rho_0)^2} \frac{\sigma^2}{\xi^2} \int_0^{+\infty} \mathrm{d}k k\, e^{-\frac{k^2}{2}\frac{\sigma^2}{\xi^2}} \left(\left[\frac{1 - \cos(\tilde{\omega}_k \frac{2c_s t}{\xi})}{\tilde{\epsilon_k} + 1} \right]^2 + \left[\frac{\sin(\tilde{\omega}_k \frac{2c_s t}{\xi})}{\tilde{\omega}_k} \right]^2 \right) \right\}. \tag{4.51}$$

  Furthermore, if we assume that $r_c(t) \gg \xi$ (which is always the case at long enough times), we can again replace the sine and cosine by their averages, and we find

  $$g_1(\boldsymbol{r},t) \simeq \rho_0 \left[\frac{\mathcal{H}_2\left(\frac{\sigma^2}{\xi^2}\right)}{2} \frac{\xi}{r_c(t)} \right]^{\alpha}. \tag{4.52}$$

  In the region of large r, the coherence function thus displays a plateau that decays algebraically in time, with the same exponent as for the spatial algebraic decay at intermediate r.

Our analysis of Eq. (4.41) shows that for a weak disorder such that $V_0 \ll g\rho_0$, the 2d coherence function displays algebraically decaying correlations that spread in a light-cone fashion, with velocity $2c_s$. A similar 2d algebraic scaling was found in [263], in a configuration where the fluctuations were however encoded in the initial state and not in a disorder potential.

This behavior has also been predicted in other quench-like configurations more commonly encountered in the literature [75, 89, 101, 105, 264, 265]. In these works however, the initial fluctuations are of quantum or thermal origin. Here, we have shown that this behavior can be induced by another source of fluctuations, the disorder potential, which can be easily varied experimentally.

Outside of the light cone, g_1 has a constant value over the whole space, which is reminiscent of the perfect coherence of the initial plane wave. This time-dependent plateau decays algebraically in time.

These results are obviously in strong contrast with the multiple scattering regime, where the Bose gas displays a very low spatial coherence (compare with Eq. (4.11)). Although we are here in an out-of-equilibrium context, notice that the algebraic part of g_1 is very similar to the one of a 2d quasi-condensate *at thermal equilibrium*, which exhibits algebraic quasi-long range order [266], as opposed to the true long-range order of a BEC in 3d condensate (for which $g_1(\boldsymbol{r}) = 1$) [220, 222]. The presence of this coherent structure is also usually associated with superfluid properties of a fraction of the gas, as observed below the BKT phase transition [60, 260, 267, 268]. Due to these analogies, the decay of g_1 here observed in a non-equilibrium context is known as prethermalization (see also the discussion of section 4.3.4).

Comparison with simulations

Within the linearization approach that led us to Eq. (4.41), the disorder fluctuations are described in terms of independent Bogoliubov quasi-particles, which reduce to phonons at low-energy. Using advanced quantum field theories that go beyond the Bogoliubov description, the effect of collisions between these phonons can be taken into account, as was done for example in 1d in [269]. In this work, it was shown that phonon-phonon interactions slowly change the momentum distribution of the particles, and make the system slowly depart from the algebraic regime described here by Eq. (4.49) . While the effect of these collisions remains small at short time, it was found in [263] that even at short time it is necessary to take them into account in order to achieve a quantitative agreement with numerical simulations for g_1. We account for this change by adding a phenomenological, fitting parameter $\beta(t)/k$ in the second line of Eq. (4.41), which becomes $(\beta(t)/k+[(1-\cos(E_kt))/(\epsilon_k+2g\rho_0)]^2+[\sin(E_kt)/E_k]^2)$. The factor $1/k$ is here introduced somewhat arbitrarily to reduce the weight of phonon collisions at short scale. We have verified that an alternative fitting option, independent of k, also allows us to reproduce the numerical results [263], albeit less accurately at short scale. A comparison between Eq. (4.36), modified according to this procedure, and the exact simulations for g_1, is shown in Fig. 4.4 (parameters are here the same as those in Figs. 4.1d). The agreement is every good, except for the small spatial variations of g_1 in the vicinity of the light-cone boundary, which are not present in the simulation results. One reason might be a smoothing of these variations due to particle collisions.

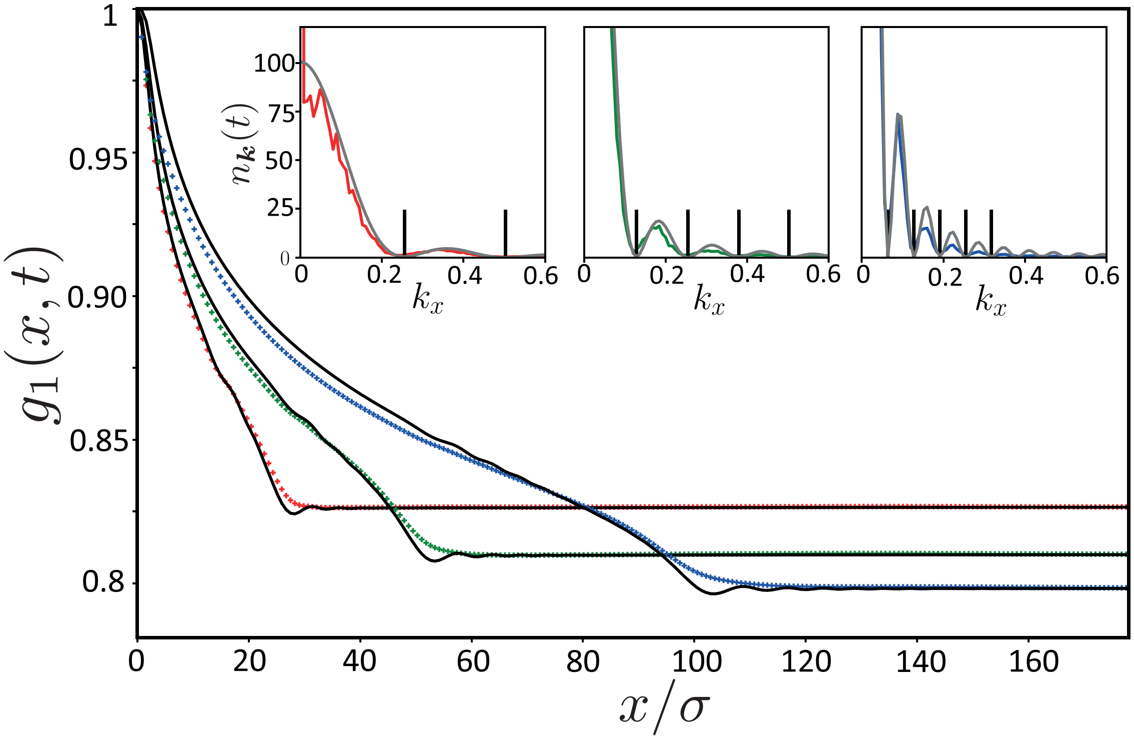

Figure 4.4 – Cut along x of the coherence function $g_1(\boldsymbol{r},t)$ in the regime $V_0 \ll g\rho_0$. Symbols show the numerical results obtained at times $t = 15\tau_{\rm NL}$, $30\tau_{\rm NL}$ and $60\tau_{\rm NL}$ from bottom to top. Solid curves are the theoretical prediction, Eq. (4.36), including a phenomenological $\beta(t)/k$ correction accounting for phonon collisions, as discussed in the main text. Fit values are $\beta(15\tau_{\rm NL}) = -0.0055$, $\beta(30\tau_{\rm NL}) = -0.094$ and $\beta(60\tau_{\rm NL}) = -0.152$. Insets show cuts along k_x of the numerical momentum distributions at the same times (corresponding to Figs. 4.1d-1-3), together with the theory, Eq. (4.53). Here $g\rho_0 = 1.5$, $V_0 = 0.4$, $k_0 = 0$, and the chosen system size is $L = 250\pi\sigma$. With these parameters, $\tau_{\rm NL} = 0.67$ and $\sigma/\xi = 1.22$.

Momentum distribution

When $V_0/g\rho_0 \ll 1$, one can expand the exponential in Eq. (4.41), so that the momentum distribution $n_{\boldsymbol{k}}(t)$ at $\boldsymbol{k} \neq 0$ is in first approximation given by the simple law

$$n_{\boldsymbol{k}}(t) \simeq \rho_0 B(\boldsymbol{k}) \left(\left[\frac{1-\cos(\omega_k t)}{\epsilon_k + 2g\rho_0} \right]^2 + \left[\frac{\sin(\omega_k t)}{\omega_k} \right]^2 \right). \tag{4.53}$$

Such a profile consists of concentric rings whose minima are located at positions $k_n = (\sqrt{2}/\xi)\{-1 + [1 + (\pi n/g\rho_0 t)^2]^{1/2}\}^{1/2}$, where n is a non-zero positive integer. These rings are well visible in the distributions of Figs. 4.1d-1-3. Physically, they originate from both the interference bteween phonons, which are propagating with a phase $\pm\omega_k t$, yieding, interference pattern $\sim \cos(2\omega_k t)$, and between the phonons and the mean field (which has a constant phase), which yield the interference pattern $\sim \cos(\omega_k t)$. The spacing $\sim \pi/(c_s t)$ between the rings decreases in time, signaling that the interfering particles are further and further apart as time grows. Eq. (4.53) is displayed in the inset of Fig. 4.4, together with cuts along k_x of the distributions in Figs. 4.1d-1-3 extracted from simulations. The agreement is again very good, in particular for the positions of the minima, indicated by vertical lines.

4.3.3 Initial finite velocity

An interesting question is the impact on the previous results of taking finite values for the initial momentum k_0 of the plane wave. Starting back from Eqs. (4.25) and (4.26), we can derive the g_1 function for a finite initial momentum $k_0 < k_c$ (see Eq. (4.23))

$$\begin{aligned} g_1(\boldsymbol{r}, t, \phi) &= \rho_0 \exp\left\{ -\alpha \frac{\sigma^2}{\xi^2} \int_0^{+\infty} \mathrm{d}k \, e^{-\frac{k^2}{2}\frac{\sigma^2}{\xi^2}} \frac{\mathcal{I}_M(k, r, \phi)}{k} - i\boldsymbol{k}_0 \cdot \boldsymbol{r} \right\}, \\ \mathcal{I}_M(k, r, \phi) &= \frac{1}{\pi} \int_0^{\pi} \frac{1 - 3M^2 \cos^2\theta}{(1 - M^2\cos^2\theta)^2} \left[1 - \cos\left[k\frac{r}{\xi} \cos(\theta + \phi) \right] \right], \end{aligned} \tag{4.54}$$

where $M = \frac{v}{c_s}$ is the Mach number associated with the flow of the fluid, and ϕ is the angle between the initial $\boldsymbol{k}_0$ and the axis along which we look at g_1. At low Mach numbers $M < 1$, $\mathcal{I}_M$ becomes independent of ϕ, and we can compute Eq. (4.54). Along the direction perpendicular to k_0, the g_1 function at $r \ll r_c(t)$ is algebraic with the same α (4.47) as before:

$$g_1(\boldsymbol{r}, t) \simeq \rho_0 \left[e^{\gamma_{\mathrm{em}}/2} \frac{\sigma^2}{\xi^2} \frac{\xi}{r} \right]^{\alpha}. \tag{4.55}$$

This result is illustrated in Fig. 4.5. It is important to note, however, that in the direction along $\boldsymbol{k}_0$, g_1 is modified by the extra phase term $i\boldsymbol{k}_0 \cdot \boldsymbol{r}$, and generally has an anisotropic shape. This means that the coherence function retains a certain memory of this initial condition over

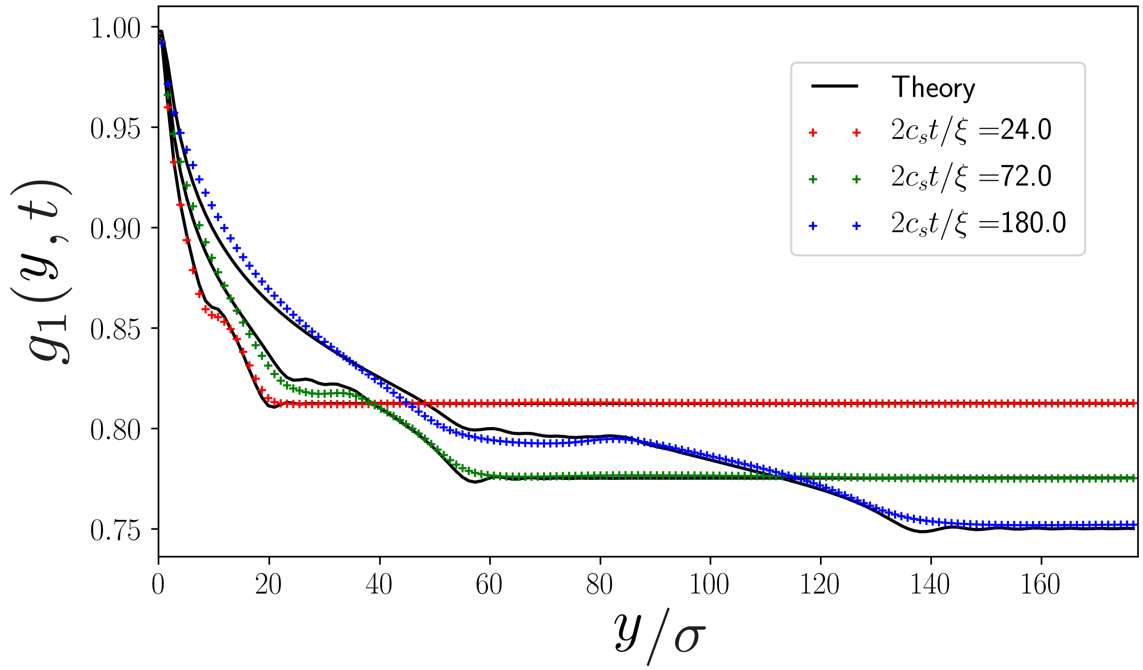

Figure 4.5 – Cut along y (perpendicular to the direction of $\boldsymbol{k}_0$) of the coherence function $g_1(\boldsymbol{r}, t)$ in the superfluid regime for finite $k_0 \simeq 0.2683$. Symbols show the numerical results obtained at successive times with the same parameters as in Fig. 4.4. Solid curves are the theoretical prediction, Eq. (4.54), including a phenomenological $\beta(t)/k$ correction accounting for phonon collisions, as described in the caption of Fig. 4.4. In this regime, the algebraic decay of g_1 at low x and the light-cone spreading are still present, the only different with the case of the gas initially at rest $k_0 = 0$ being the spatial modulation in the shape of a "step", preceding the edge of the light cone.

a relatively long time, even after the plateau reaches the edge of the system. Furthermore, when $M > 1$, our calculations present some unexplained divergences, indicating a drastic change in the behavior of g_1, which we also observed numerically.

4.3.4 Discussion

We have mentioned in the introduction of the thesis that when an integrable system is slightly perturbed from integrability, its evolution exhibits a two-stage exotic dynamics characterized by well separated time scales [99], with first a fast evolution into a quasi-thermal state, and later a relaxation toward full thermalization. The first "prethermalization process" has recently been generalized to a number of physical systems, both quantum or classical, at high and low energy [80, 98, 101, 104]. While a global picture of prethermalization is still lacking, a certain number of characteristics of the phenomenon are commonly accepted and observed, such as a clear separation of time scales, the slow loss of memory of the initial conditions, the emergence of a certain degree of universality during the long metastable evolution, and structural similarities between the quasi-stationary state and the final thermal state [270].

In this chapter, we have considered a weakly interacting quenched Bose gas with a very weak disorder. In the limit of vanishing disorder, the initial plane wave being a stationary state of the Gross-Pitaevskii equation, the gas is in a state of metastable (and non-thermal) equilibrium. The addition of a small disorder brings the system away from this equilibrium. In this sense, we are in a situation of near-integrability, where one could expect the onset of prethermalization. This view of our quench scenario sheds a new light to the results of this chapter. Indeed, we observe that the system first relaxes quickly (on a time scale $\tau_g \sim 1/g\rho_0$), showing correlations which spread in a light-cone fashion, towards a state which algebraic spatial coherence. A very similar behavior was for instance observed in a series of experiments using 1d quantum gases on a microchip [105, 271, 272]. In these works, a quench was realized by suddenly splitting the cloud in half generates quantum noise, and the phase correlation between the two halves of the gas spread linearly in time during the dynamical evolution, see Fig. 4.6. Just like in our system, in these experiments, once the light cone reaches the edges of the system, $r_c(t) = L$, i.e. at time $t = L/2c_s$, the plateau vanishes[3] and the g_1 function is purely exponential (here in 1d, but purely algebraic in 2d), as if the gas was in thermal equilibrium.

Forgetting for a moment the effect of the weak disorder potential, we could thus define an effective temperature T_{eff} for the gas as a function of the initial quench parameters $V_0, g\rho_0, \sigma$,

---

[3] This does not mean, however, that the memory of the initial condition is lost, as the decay of g_1 is still dependent on initial parameters. For example, the algebraic exponent (4.47) depends on the correlation of the disorder, which shapes the initial density fluctuations. Likewise, as we have seen in subsection 4.3.3, for a gas launched with an initial velocity k_0 the coherence function still heavily depends on k_0.

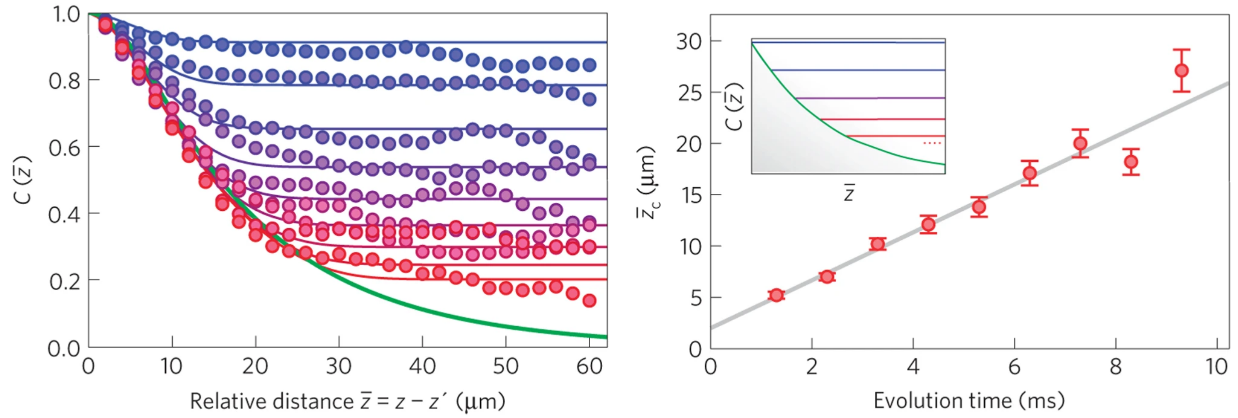

Figure 4.6 – Left : Experimental phase correlation functions between two atomic clouds at a relative distance $\bar{z}$, resulting from the split of an initially trapped Bose gas in 1d. The bottom (green) line is the theoretical correlation function of the prethermalized state. Right : Position of the crossover distance between the zone where correlations decay, and the zone retaining the initial long-range order of the gas before the splitting as a function of evolution time t. The linear behavior reveals the light-cone spreading of correlations. Adapted from [272].

using the relation between the algebraic decay coefficient of a homogeneous superfluid at equilibrium and the thermal de Broglie wavelength λ_T [273], as well as our expression of α under Eq. (4.46). We will see however in the next chapter that the true equilibrium temperature of the gas, whose relation to the initial parameters is fully determined by the conservation of energy and number of particles, is larger than T_{eff}. The description of our prethermal state using a single effective temperature, however, is a bit at odds with the usual picture of prethermalization for near-integrable quantum systems, where the transient state is described by a generalized Gibbs ensemble (GGE) (i.e. by several effective "temperatures", each associated with the relaxation of a conserved quantity) [73, 89, 102]. Indeed, in the GGE description, several Lagrange multipliers are usually necessary to fully describe the system. In our case, this number reduces to 1, probably because our system has few conserved quantities. This was also observed in [105], where it was explained by the reduced number of conserved quantities caused by the particular quench protocol.

Note, finally, that the algebraic exponent α of Eq. (4.47) is independent of the precise shape of the disorder spectrum $\tilde{C}(\boldsymbol{k})$. In fact, the whole equation only depends on the small set of parameters $\{\xi, \sigma, g\rho_0, V_0\}$ and is thus, to a large extent, universal. This hint at universality is reinforced by the discussion following Eq. (4.47), in which we have shown that the dynamical picture developed here would not change for an uncorrelated disorder potential.

4.4 Conclusion

In this chapter, we have described theoretically the short-time dynamics of a 2d Bose gas, in the limit where the interactions are stronger than the disorder, in contrast with the previous chapters. We have seen that the main differences between the two regimes could be described in term of spatial coherence. The latter is of very short range in the multiple scattering regime, while it becomes long range when interactions are stronger. In the latter case, the disorder essentially induces small density fluctuations, which are coherently enhanced by the interacting potential during the time evolution. The spatial correlation of these fluctuations decays algebraically over a region that spreads linearly in time, at twice the speed of sound. This intermediate state is quickly reached by the system, and presents a certain degree of universality, and strong similarities with a thermal state. This can be understood as a prethermalization process, stemming from the weak breaking of integrability by the disorder potential. In the next and final chapter, we will extend our study to much longer times, through simulations that eventually demonstrate the establishment of full thermalization. This will be the occasion to quantify the associated time scales in the difference regimes we have considered. We will also precisely describe some features of the 2d equilibrium phase diagram, at finite temperature, which is to our knowledge not fully established yet.

Chapter 5

Thermal equilibrium of 2d weakly interacting disordered Bose gases following a quench

Introduction

In this chapter, we present and discuss simulation results on the properties of a quenched 2d disordered Bose gas as it approaches thermal equilibrium at long time. We again restrict ourselves to the regime of weak interactions, and describe the dynamics of the gas on the basis of the disordered Gross-Pitaesvkii equation. We will see that this choice of a classical approach compels us to discretize space in order to observe thermalization, in contrast to the previous chapters, where we always considered space to be continuous. In this context, we find that the thermalization process is associated with the dynamical formation of a Berezinskii-Kosterlitz-Thouless (BKT) transition [55, 56, 274] for the 2D Bose gas [62, 273]. By varying the initial properties of the latter, as well as the disorder and interaction strengths, we use our simulations to establish the global phase diagram of the disordered gas at thermal equilibrium. In particular, we investigate the effects of disorder on the superfluid-to-normal BKT transition. The access to the full time evolution of the gas, monitored via the coherence function g_1, allows us to put in perspective the equilibrium phase diagram with the preceding out-of-equilibrium dynamics. Although they are obtained within a classical field description, we do not expect our results to differ from the corresponding many-body description at weak interactions. In this chapter, we set for simplicity $\hbar = 1$ and $k_B = 1$.

5.1 Thermalization of a disordered Bose gas

We start by recalling the Bolztmann-like kinetic equation governing the time-evolution of the diffusive modes in a weakly interacting Bose disordered gas in two dimensions, which has been derived in chapter 2:

$$\partial_t f_\epsilon = \int_{\epsilon_1,\epsilon_2,\epsilon_3\geq 0} \mathrm{d}\epsilon_1 \mathrm{d}\epsilon_2 \, W(\epsilon,\epsilon_1,\epsilon_2)\Big[(f_\epsilon + f_{\epsilon_3})f_{\epsilon_1}f_{\epsilon_2} - f_\epsilon f_{\epsilon_3}(f_{\epsilon_1} + f_{\epsilon_2})\Big], \tag{5.1}$$

where $\epsilon_3 = \epsilon_1 + \epsilon_2 - \epsilon$, and $f_\epsilon(t)$ is the occupation number[1] of the diffusive modes at time t. A simple analysis [70] yields the stationary solutions of this equation, which cancel its right-hand side. These solutions are candidates for the occupation number at thermal equilibrium, and are of the form

$$f_\epsilon = \frac{T}{\epsilon - \mu} \tag{5.2}$$

where T and μ are two constants. This distribution, known as the Rayleigh-Jeans distribution, in fact coincides with the low-energy limit of the famous Bose-Einstein distribution

$$f_\epsilon = \left[\exp\left(\frac{\epsilon-\mu}{T}\right) - 1\right]^{-1}, \tag{5.3}$$

where T and μ are referred to as respectively the temperature and chemical potential of the gas at equilibrium. This formula is a direct consequence of the indistinguishability of quantum particles. Our classical description being essentially valid in a regime of high degeneracy, it is natural that it describes the low energies of the gas, i.e., $\epsilon \ll T - \mu$. The Rayleigh-Jeans distribution (5.2) was originally introduced to describe the spectrum of the black-body radiation (i.e. the radiation spectrum of an assembly of photons), where it can be computed from classical electrodynamics [275, 276]. In this context, it describes very well the low-energies of the black-body spectrum, but yields unphysical ultraviolet divergence, a phenomenon known as the ultraviolet catastrophe. These issues were corrected by an empirical law, later explained by Planck in 1900 by introducing the quantization of the energy levels [277]. Using this assumption, he derived the law that bears his name, which is the analogue of Eq. (5.3) for an assembly of photons, and correctly describes the high-energy limit of the spectrum.

---

[1] In all previous chapters, we intentionally referred to this quantity as the energy distribution of the gas, for the sake of simplicity. The true definition of energy distribution of the gas is, however, the product $\nu_\epsilon f_\epsilon(t)$, indeed normalized to 1, where ν_ϵ is the density of states per unit volume. In the previous chapters, where we considered continuous systems, the DoS was always approximated by its constant value in homogeneous systems, $\nu_\epsilon^{(0)} = m/2\pi$, so that identifying $f_\epsilon(t)$ with the energy distribution was harmless. In this chapter, we will consider a discrete system, where the previous approximation of the DoS is not true. Moreover, in the context of equilibrium physics the denomination "occupation number" is widely used, so we will comply to this convention in this chapter.

5.1.1 Temperature and chemical potential

In Eq. (5.2), the temperature and chemical potential are the canonical thermodynamic variables associated respectively with the conservation of total energy E and the conservation of the number of particles N. For our quenched 2d Bose gas, these two conservation laws fully determine T and μ as functions of the initial condition and quench parameters, $(g\rho, V_0, k_0)$. They are linked by the conservation laws

$$N = \int_{\mu}^{+\infty} \mathrm{d}\epsilon\, \nu_\epsilon \frac{T}{\epsilon - \mu}, \tag{5.4}$$

$$E = \frac{k_0^2}{2m} + g\rho_0 + \overline{V} = \int_{\mu}^{+\infty} \mathrm{d}\epsilon\, \nu_\epsilon \epsilon \frac{T}{\epsilon - \mu}, \tag{5.5}$$

where ν_ϵ is the disorder-average density of states per unit volume. Note that for Eqs. (5.4) and (5.5) to be defined at all energies, the chemical potential μ must be smaller than the ground state energy of the system. This is where the disordered and homogeneous case differ: in the presence of a Gaussian disorder for instance, one can always find energy states of arbitrarily low (negative) energy, such that the energy integrals in Eqs. (3) and (4) strictly speaking range from $-\infty$ to $+\infty$. Such states form the so-called Lifshitz tail of the average density of states [278]. They, however, are extremely rare. For this reason, in the following we will consider for simplicity that the energy spectrum is bounded from below by a certain energy $-\delta\epsilon_{\text{disorder}}$, below which the average density of states is negligibly small, as illustrated in the plot in Fig. 5.1. While we do not know the precise value of the lower bound $-\delta\epsilon_{\text{disorder}}$, we can accurately replace it by the chemical potential μ, which is necessary smaller by definition of the occupation number, and therefore yields the same result (this what is done in Eqs. (5.4) and (5.5)). In what follows, we use a Gaussian, uncorrelated disorder potential, with $\overline{V} = 0$ and $\overline{V(\boldsymbol{r})V(\boldsymbol{r}')} = \gamma\delta_{\boldsymbol{r},\boldsymbol{r}'}/a^2$.

For a given initial number of particles N and total energy E, if there exists T and μ that verify both Eqs. (5.4) and (5.5), then the system will indeed evolve towards a equilibrium thermal state, well-described by the Rayleigh-Jeans distribution (5.2).

5.1.2 Ultraviolet catastrophe

Both energy integrals in (5.5) and (5.4) diverge at high energy. These divergences, which correspond exactly to the ultraviolet catastrophe of the black-body radiation spectrum, indicate that, within a classical approach, the gas can, strictly speaking, never thermalize in the continuous limit. To circumvent this issue, in this chapter, we abandon the idea of describing the continuous system as faithfully as possible, and consider a discretized version of the problem, for which the atoms are in a lattice with elementary spatial step a. In simulations,

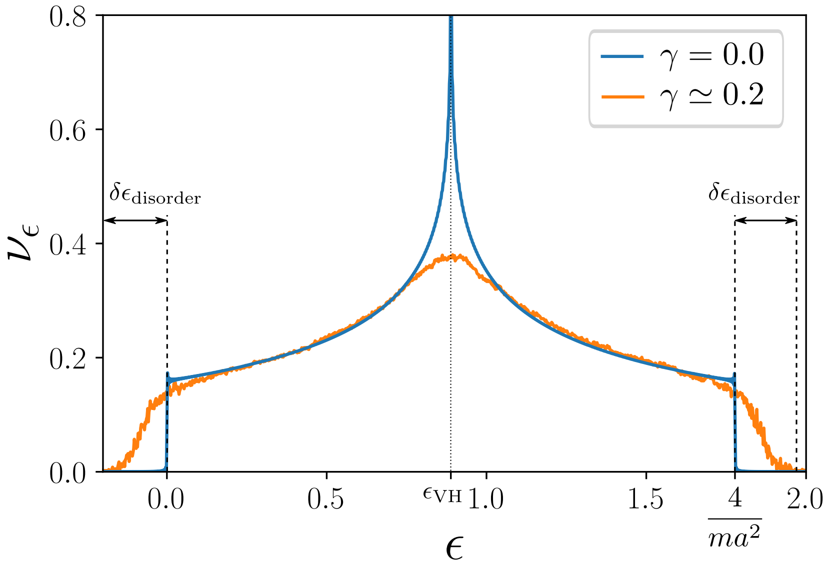

Figure 5.1 – Simulated density of states per unit volume of a 2D Bose gas in a lattice of step a, at small (orange curve) and vanishing (blue curve) disorder. The system size is $L = 800$ and the lattice spacing is $a = 1.5$. For the disordered case, we use a Gaussian, uncorrelated random potential $V(\boldsymbol{r})$ such that $\overline{V(\boldsymbol{r})} = 0$ and $\overline{V(\boldsymbol{r})V(\boldsymbol{r'})} = \gamma\delta_{\boldsymbol{r},\boldsymbol{r'}}/a^2$, and the density of states is averaged over 11520 disorder realizations. For $\gamma \neq 0$, the density of states is approximately bounded within the energy range $[\delta\epsilon_{\text{disorder}}, \frac{4}{ma^2} + \delta\epsilon_{\text{disorder}}]$.

we are thus released from the constraint to choose a discretization step a much smaller than the characteristic length scales of the physical system, as was previously the case. Within this description, the energy spectrum is bounded from above by $\epsilon_{\max} = 4/ma^2 + \delta\epsilon_{\text{disorder}}$ (see Fig. 5.1, and the discretization of the GPE in Chapter 3), and no divergence is present anymore.

5.1.3 Emergence of a quasicondensate at low energy

Using the simulated density of states at finite disorder from Fig. 5.1, we can solve the implicit equation (5.5) for E and μ (the temperature being a multiplicative factor in both conservation laws, we can initially simply set it to 1 for this analysis). The results are displayed in Fig. 5.2. We see that:

- If the energy E injected in the system is above a certain threshold $E = E^*$ (which depends on the disorder strength γ), we can always find a pair (E, μ) that satisfies the energy conservation law with $\mu < 0$, indicating that the system indeed thermalizes towards the corresponding Rayleigh-Jeans distribution. The temperature T is then determined from the other conservation rule (5.4). This regime corresponds to the normal side of the BKT superfluid-to-normal transition.
- The second energy threshold, situated at the central energy of the density of states, is

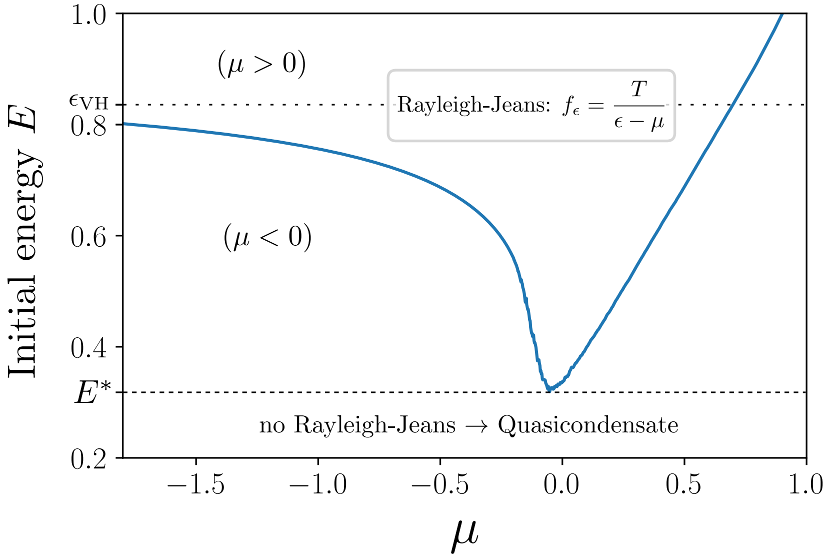

Figure 5.2 – Couples of solutions (E, μ) of the equation (5.5) for the conservation of energy, using the simulated density of states from Fig. 5.1 at $\gamma \simeq 0.2$. Below a certain energy E^* injected into the system (in our case mostly controlled by initial kinetic energy, and thus the value of k_0), the Rayleigh-Jeans distribution yields no solution for the conservation of energy. Above E^*, a solution exists, so that the gas lies in a normal thermal phase describes. The threshold $\epsilon_{\rm VH}$ refers to the energy around which the density of states is symmetric, as a result of the discretization of the system (see text).

an irrelevant consequence of the symmetric behavior of the average density of states around this value (see Fig. 5.1). Due to this symmetry, the situation is the same as in the intermediate energy range, but with a positive μ. Indeed, Eq. (5.5) is left unchanged by the change of variables $\epsilon' = 4/m\Delta_r^2 - \epsilon$, with the effective chemical potential $\mu' = 4/m\Delta_r^2 - \mu > 0$.

- For initial energies below E^*, there is no value of μ that satisfies the conservation of energy: the thermal equilibrium cannot be described by the Rayleigh-Jeans distribution. This result signals a breakdown of Eqs. (5.4)-(5.5) due to an accumulation of particles in the low-energy states of the gas, featuring the formation of a quasi-condensate.

Since we do not know the full expression of the atomic occupation number owing to the presence of the quasi-condensate at low energy, especially in the presence of disorder, we cannot derive the equilibrium temperature and chemical potential from the initial parameters using the conservation laws as in the normal regime. In the next section, devoted to the construction of the long-time equilibrium phase diagram, we will thus determine them with an alternative numerical method.

5.2 Full time evolution of the coherence function

To grasp an intuitive picture of the dynamics of the gas, from the initial quench, in both disorder and interactions, to its final thermal equilibrium, we show in the left plots of Figs. 5.3 and 5.4 snapshots of the coherence function g_1 of the gas at successive times, respectively for $V_0 < g\rho_0$ and $V_0 > g\rho_0$[2]. Aside from the stronger discretization of space, the former corresponds exactly to the regime described in chapter 4, while the latter is the multiple scattering regime of chapters 1 and 2. As previously done in chapter 4, we define a characteristic time scale for the short-time dynamics of the gas when interactions effects dominate:

$$\tau_g \equiv 1/g\rho_0. \tag{5.6}$$

5.2.1 Interactions larger than disorder

The left plot of Fig. 5.3 shows cuts along x of the isotropic g_1 coherence function in the case where the initial interaction energy $g\rho_0$ is much larger than the disorder strength V_0. At short times, the light-cone spreading of density correlations is visible. Notice, however, that as compared to chapter 4 here disorder is uncorrelated. We see that the coherence function decays algebraically at all times. The right plot shows the long-time evolution of the algebraic exponent $\alpha(t)$. It indicates that during a relatively long pre-thermal regime, $\alpha(t)$ decreases very slowly, until it eventually saturates at long time. This saturation is the hallmark of a full thermalization of the quenched Bose gas. The algebraic decay of g_1, here observed at long time, indicates that, for the initial parameters chosen $(k_0, g\rho_0, \gamma)$, the Bose gas reaching thermal equilibrium behaves as a *quasi-condensate*, i.e. it displays a quasi long-range order. This behavior, as we will see below, is also associated with a finite superfluid fraction.

Note that due to the periodic boundary conditions, the coherence function computed at long times is affected by the superposition of spurious coherent waves that have reached the edge of the system and constructively interfere with themselves. This numerical artifact leads to large variations of the coherence near the edge of the system. To reduce this effect, the plots of the coherence function are averaged over simulations results using different system sizes, which averages out the stray interference. The error bars in the right plot of Fig. 5.3 correspond to the standard deviation of the slopes obtained with this procedure. It also proves that the shape of our simulated g_1 functions is globally independent of the system size at all times.

---

[2] To be consistent with the notation for the strength of the correlated potential used in chapter 4 (see section 4.3.2, we define here $V_0 = \sqrt{\gamma/a}$.

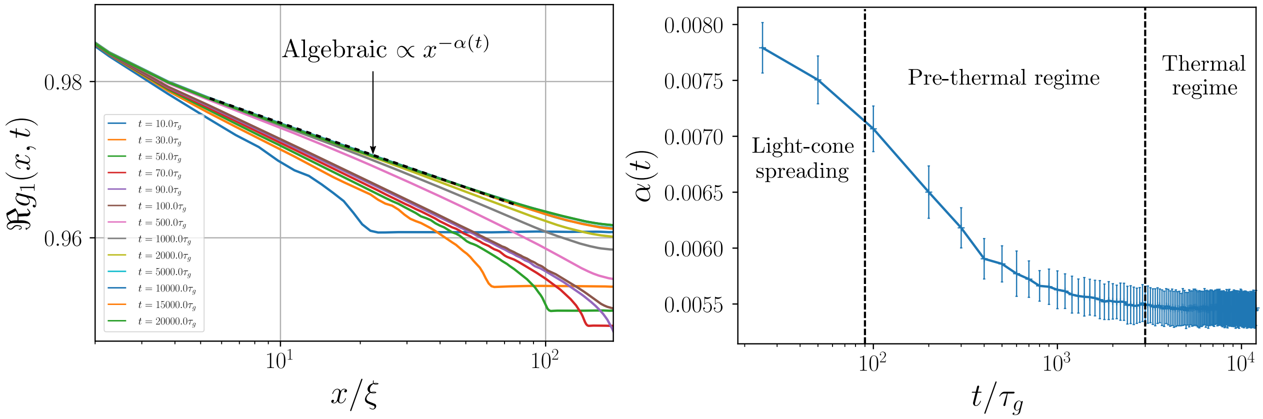

Figure 5.3 – Left: Full time evolution of the g_1 function obtained with the initial quench parameters $k_0 = 0$, $\gamma \simeq 0.2$ and $g\rho_0 = 1.0$. Here, $V_0 = \sqrt{\gamma} > g\rho_0$ and we are thus close to the prethermal regime of chapter 4. The results are averaged over system sizes from $L = 340$ to $L = 400$, by steps of 5, to avoid unwanted noise near $x = L$, caused by the boundary conditions (see main text). Right: algebraic exponent $\alpha(t)$, extracted from the slope of the g_1 function in log-log plot for the same parameters, starting at the first time where the fit by an algebraic law is conclusive. The error bars indicate the standard deviation of the measured value of $\alpha(t)$ over the set of different system sizes.

5.2.2 Disorder larger than interactions

In the left panel of Fig. 5.4, we plot the time evolution of g_1 in the opposite regime where disorder effects dominate the dynamics, $V_0 > g\rho_0$, and for a finite value of k_0. We observe at short times the speckle correlation where $g_1 \propto J_0(k_0 r)\exp(-r/\ell)$, and at long times an exponential decay of g_1. The latter corresponds to the normal-fluid phase discussed in the previous section, associated with a relatively high temperature. This long-time behavior could have been expected because the energy of the system is in this case much higher due to the finiteness of k_0. The right plot of Fig. 5.4 shows the time evolution of the exponential decay length. We observe that thermalization is much faster in this case. This is due to the absence of a prethermal regime, which is expected because the system is very far from integrability when disorder is stronger. As in the previous section, the plot is also averaged over simulations results using several system sizes. The error bars in the right plot of Fig. 5.4 show that the exponential decay length is roughly insensitive to the system size.

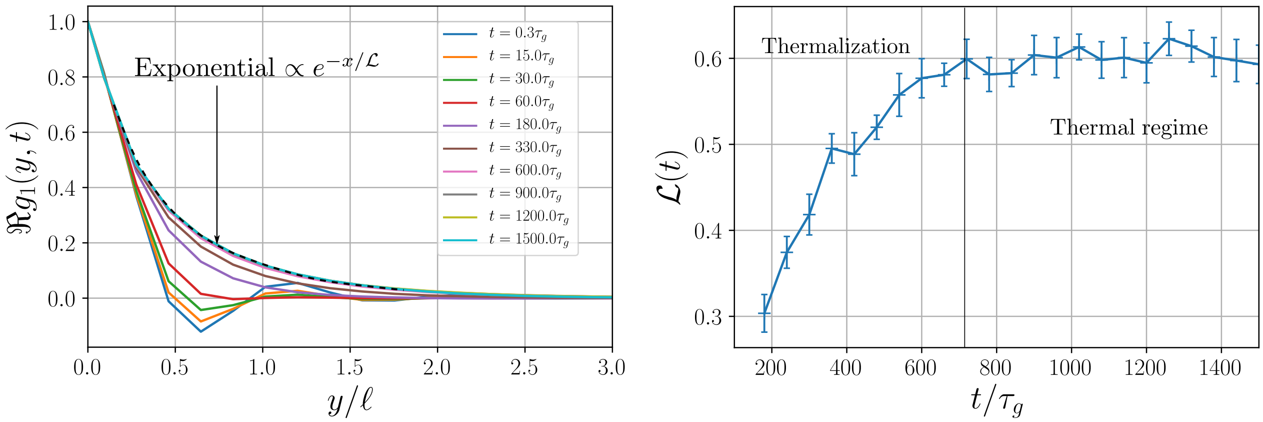

Figure 5.4 – Left: Full time evolution of the g_1 function obtained with the initial quench parameters $k_0 = 0.75$, $\gamma \simeq 0.2$ and $g\rho_0 = 0.003$, thus in the multiple scattering regime of chapters 1 and 2. The results are again averaged over system sizes starting at $L = 350$ up to $L = 400$, by steps of 5. Right: exponential decay length $\mathcal{L}(t)$, extracted from the g_1 functions at different times, in a log-plot for the same parameters, starting at the first time where the fit by an exponential law is conclusive. The error bars indicate the standard deviation of the measured value of $\mathcal{L}(t)$ over the set of different system sizes.

5.3 Equilibrium phase diagram of the 2d disordered Bose gas

In this section, we numerically establish the temperature-disorder equilibrium phase diagram of our 2d disordered Bose gas by analyzing the long-time thermal state reached by the system for various initial quench parameters. We assume that thermal equilibrium is reached when the simulated g_1 function becomes independent of time in a chosen spatial window. A more precise criterion will be given in Section 5.3.3, where we provide an estimation of the thermalization time over the phase diagram.

5.3.1 Determination of T and μ

To place data points on the phase diagram, we need to know the values of the temperature T and the chemical potential μ of the thermal equilibrium reached for every given set of initial quench parameters $(V_0, g\rho_0, k_0)$. As explained in the introduction, in general we cannot simply infer these values from the conservation laws (5.4) and (5.5), due to the presence of a quasi-condensate for a certain set of initial conditions. Instead, for each set of parameters, we compute the time evolution of both $g_1(\boldsymbol{r}, t)$ and the energy distribution $f_\epsilon(t)\nu_\epsilon$. While a direct numerical computation of the occupation number $f_\epsilon(t)$ is complicated, the energy distribution can be obtained by a rather simple numerical procedure: we start by propagating the initial plane wave $|\boldsymbol{k}_0\rangle$ using the numerical scheme of chapter 3, up to the desired measurement

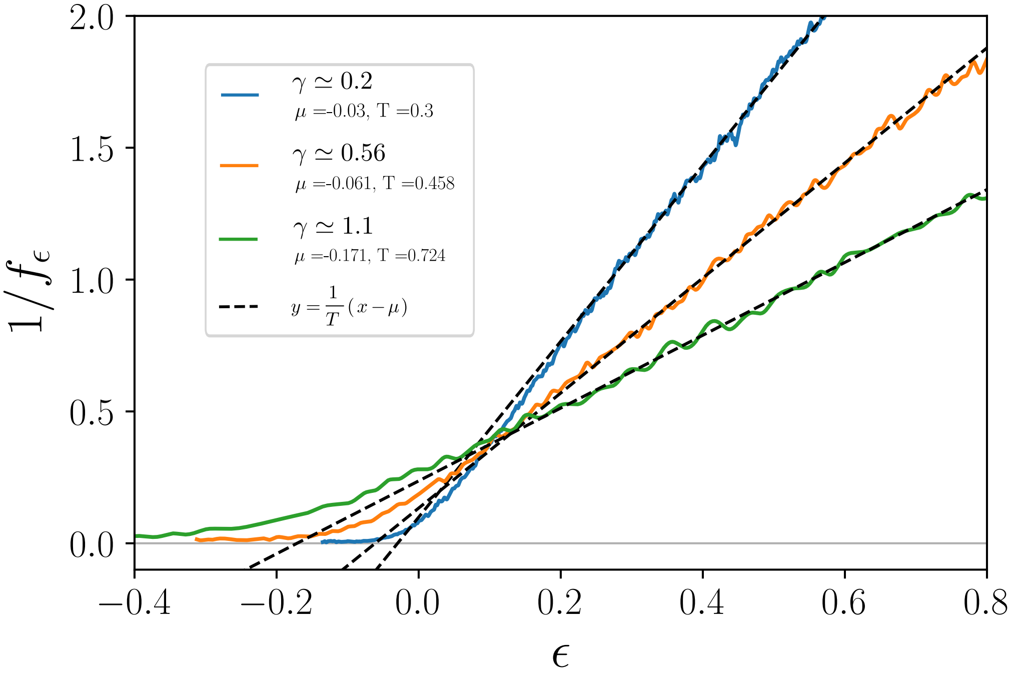

Figure 5.5 – Examples of simulated inverse occupation numbers f_ϵ^{-1} at thermal equilibrium, with fixed initial parameters $k_0 = 0.45$ and $g\rho_0 = 0.1$ and for different values of the disorder strength γ. At high energies, the data are perfectly fit by a Rayleigh-Jeans distribution. Note that we are here in the superfluid region of the phase diagram, such that, according to equation (5.8), the measured chemical potential is equal to $-2g\rho_0 + \mu$, where μ is the chemical potential introduced in the Bogoliubov description of the gas.

time t. Once we obtain the propagated state $|\psi(t)\rangle$, we use it as the initial state for a new propagation, this time with $g = 0$. We then compute the Fourier transform with respect to time of the real part of the autocorrelation function obtained for this propagation, as we did in chapter 3 to compute spectral functions. One can show that this procedure yields the energy distribution of the gas at time t. Then, to extract the occupation number f_ϵ from the numerical energy distribution $f_\epsilon(t)\nu_\epsilon$, we cannot simply divide it by the simulated density of states ν_ϵ. Indeed, on the edges of the energy spectrum, the latter takes values very close to 0, of the order of the precision of our algorithm. Thus, the ratio $f_\epsilon(t)\nu_\epsilon/\nu_\epsilon$ is not well-controlled, and displays very large fluctuations. In practice, we prefer to plot the inverse occupation number $f_\epsilon(t)^{-1}$ obtained by the product $\nu_\epsilon \times (\nu_\epsilon f_\epsilon)^{-1}$. At large enough energy, this quantity always scales like $\epsilon/T - \mu/T$ (see the remark at the end of this section), giving access to T and μ from a simple fit. The behavior of f_ϵ at low energy is of course more complicated, but we do not need it in our approach. An illustration of this procedure in given in Fig. 5.5.

In practice, this way of extracting the final temperature and chemical potential sets a lower limit for the value of the disorder parameter γ providing reliable results. Indeed, when the mean free path of a given diffusive mode $\ell_k \sim k/\gamma$ starts to exceed the system size, the partial wave amplitudes propagating with momentum k in the medium – which typically decay as $\exp(-r/\ell_k)$, see equation (1.44)– become non-negligible as they reach the edges of the system, which causes them to self-interfere because of the boundary conditions. This makes the temporal autocorrelation of the wavefunction increase by a constant amount, which translates into parasitic oscillations in the energy distribution. This problem is all the more present when probing long times, as the momentum distribution spreads out, and modes of high momenta associated with a large mean free path are populated. A good condition for this effect to be negligible is that the mean free path associated with the maximum possible value of the momentum, $\ell_{\max} = \pi/(a\gamma)$, is smaller than $L/10$, i.e for $\gamma \geq 10\pi/(aL)$. Note that whenever this condition is fulfilled, we checked that the computed temperature and chemical potential have a very weak dependence on the size of the system, indicating that the system is very close to the true thermodynamic limit.

Remark In the above description of our numerical computation of the temperature and chemical potential, we stated that at large energies, the occupation number f_ϵ is always described by the Rayleigh-Jeans distribution. While this is obvious for the normal phase, i.e. when the amount of energy injected in the system is above the energy threshold E^* from Fig. 5.2, this result is less trivial in the phase where a quasi-condensate is present, as we do not know a priori the expression of the energy distribution. We present here a very succinct justification of this statement. The phenomenon of quasi-condensation in two dimensions is predicted by the Bogoliubov theory [256, 279], which describes the interacting Bose gas by a non-interacting gas of quasiparticles. Within this framework, the conservation of the number of particles is also ensured by the introduction of a chemical potential μ, and, for a continuous dispersion relation of the quasiparticles, reads $\omega_k = \sqrt{\epsilon_k(\epsilon_k + 2\mu)}$, where $\epsilon_k = k^2/2m$, and $\mu = g\rho_0$ [279]. The latter equality follows from the Hugenholtz-Pines theorem which states that in a uniform system, the phononic spectrum is gapless (i.e. $\lim_{k\to 0} \omega_k \to 0$ and $\omega_k = 0$) [280], and still holds in the presence of disorder [281]. The occupation number for the Bogoliubov quasiparticles then reads

$$f^*_{\epsilon_k} = \frac{T}{\omega_k}, \tag{5.7}$$

which, at large energies $\epsilon \gg \mu$, coincides with the Rayleigh-Jeans distribution (5.2) with chemical potential equal to $-\mu$, as $\omega_k \sim \epsilon_k + \mu$. In our (non-uniform) lattice system, the value of the chemical potential is not set by $\mu = g\rho_0$, and can instead take arbitrary values. In this case, the Bogoliubov dispersion relation thus has the general form $\omega_k = \sqrt{(\epsilon + 3g\rho_0 - \mu)(\epsilon + g\rho_0 - \mu)}$ and the occupation number is still given by Eq. (5.7) [281]. Inverting the Bogoliubov transformation, we obtain the occupation number of the atoms in the limit of large energies, which is still described by the Rayleigh-Jeans distribution, this time with an effective chemical potential $-2g\rho_0 + \mu$:

$$f_{\epsilon \gg \mu} = \frac{T}{\epsilon + 2g\rho_0 - \mu}. \tag{5.8}$$

This demonstrates that the occupation number f_ϵ has the form of a Rayleigh-Jeans distribution at large energies both in the normal and in the quasi-condensate phases (see Fig. 5.5).

5.3.2 Equilibrium phase diagram

We now have everything we need to build the long-time equilibrium phase diagram originating from the quenched plane-wave state. We have performed long-time numerical propagations over a wide range of initial parameters (γ, k_0), at fixed (small) interaction strength $g\rho_0 = 0.1$, discretization $a = 1.5$ and system size $L = 400$, and measured both the coherence function and the energy distribution of the gas, up to a time of $t_{\max} = 10^4\tau_g$. At such long times, the coherence function is time independent for most choices of parameters.

To characterize the equilibrium phase reached after the evolution, we use the following empirical procedure. Starting from the somewhat arbitrary length 3ξ, where $\xi = 1/\sqrt{g\rho_0}$ is the healing length, we fit a cut of the g_1 function along the y-axis (i.e., perpendicular to the initial $\boldsymbol{k}_0$) by an algebraic law and an exponential law, up to the length $L - 20\xi$ to avoid the noise stemming from the use of periodic boundary conditions, as previously explained. If the algebraic fit is successful, i.e., with an estimated relative error on the fit parameters of less than 1%, we conclude that the gas lies in the superfluid phase, indicated in blue in Fig. 5.6. If, on the contrary, the exponential fit is not successful, then we conclude that the gas lies in the normal phase, indicated in orange. In between these two cases, the distinction becomes less clear and we are in a transition zone between superfluid and normal fluid, which in two dimensions is known as the BKT transition. As shown in Fig. 5.7, close to the transition, the g_1 function is not completely algebraic nor exponential. This defines a zone (represented in green in Fig. 5.6), where both fits may work approximately. On the normal side, we simply consider that the gas is in a normal fluid state when the exponential fit is nearly perfect, for values of g_1 above 10^{-2}. This criterion yields a precise distinction between the two phases because the characteristic decay length of the exponential diverges very sharply as we approach the critical temperature (see section 5.4.3). On the other side of the green area, where g_1 decays rather slowly, things are less clear, and relying on the accuracy of the algebraic fits yields a blurry separation between the blue and the green zone. However, we have noticed that the log-log plot of the coherence function at low values of r suddenly changes from concave to convex as it approaches the BKT transition from the superfluid size (see Fig. 5.7). We take this change of convexity as our criterion for the distinction between the blue and the green zones. This empirical procedure yields a rather wide "transition" zone, which is expected to contain the critical temperature of the BKT transition. This statement is confirmed by a good agreement with theoretical prediction of the critical temperature (or critical disorder), represented by the dotted line in Fig. 5.6. The derivation of this prediction is the topic of the next section.

The curvature of the BKT transition line shows the impact of disorder on the critical temperature. Note that the regime where prethermalization is to be expected, as in Fig. 5.3, lies far below the lower left corner of this diagram, for which the lowest value of the disorder strength we considered is $\gamma \simeq 0.023$, yielding a ratio $\gamma/g\rho_0 \simeq 0.23$. The multiple scattering regime of Fig.5.4, on the other hand, is situated very far beyond the top right corner of the diagram.

Finally, we have checked that the general shape of this diagram is unaffected by small variations of the value of the interaction strength, nor by for slight changes of the discretization.

Behavior at large disorder strength

The area void of data points in the top left corner of Fig. 5.6 is unreachable when starting from an initial plane-wave state. Indeed, at fixed k_0, we have found that the final temperature T approximately increases linearly with γ, leading to curved trajectories on the $\gamma - T$ diagram. The behavior of data points with the lowest initial kinetic (and thus total) energy, $k_0 = 0$, for increasing values of γ is indicated on the diagram and sets a limit for the lowest temperatures that can be reached. Coincidentally, we have noticed that this limit approximately coincides with the many-body localization-delocalization (MBDLT) transition line predicted in [65], which is most probably not contained within the classical-field description.

Slow thermalization area

In practice, we have been able to find a reliable, time-independent equilibrium state for almost all data points shown in the phase diagram. The exception is the zone indicated by the darker blue dots on the left side of the superfluid region. Indeed, in this region, we have observed that thermalization seems to be very long compared to the rest of the diagram. Specifically, it was not reached at $t = t_{\max}$, the g_1 function displaying an algebraic decay only in a limited region of space. This motivated us to perform simulations over even longer times for some of these points, of the order of $t = 10^6 = 10t_{\max}$. These simulations, displayed in Fig. 5.8, reveal that within this region, the dynamics of the gas is very slow, and looks almost stationary after a certain time. This suggests that if thermal equilibrium is indeed reached, it will take a very long time. Even more puzzling, this odd behavior completely vanishes for a very slight change of the initial k_0 on the left of the region. We do not currently have a satisfactory explanation for these observations.

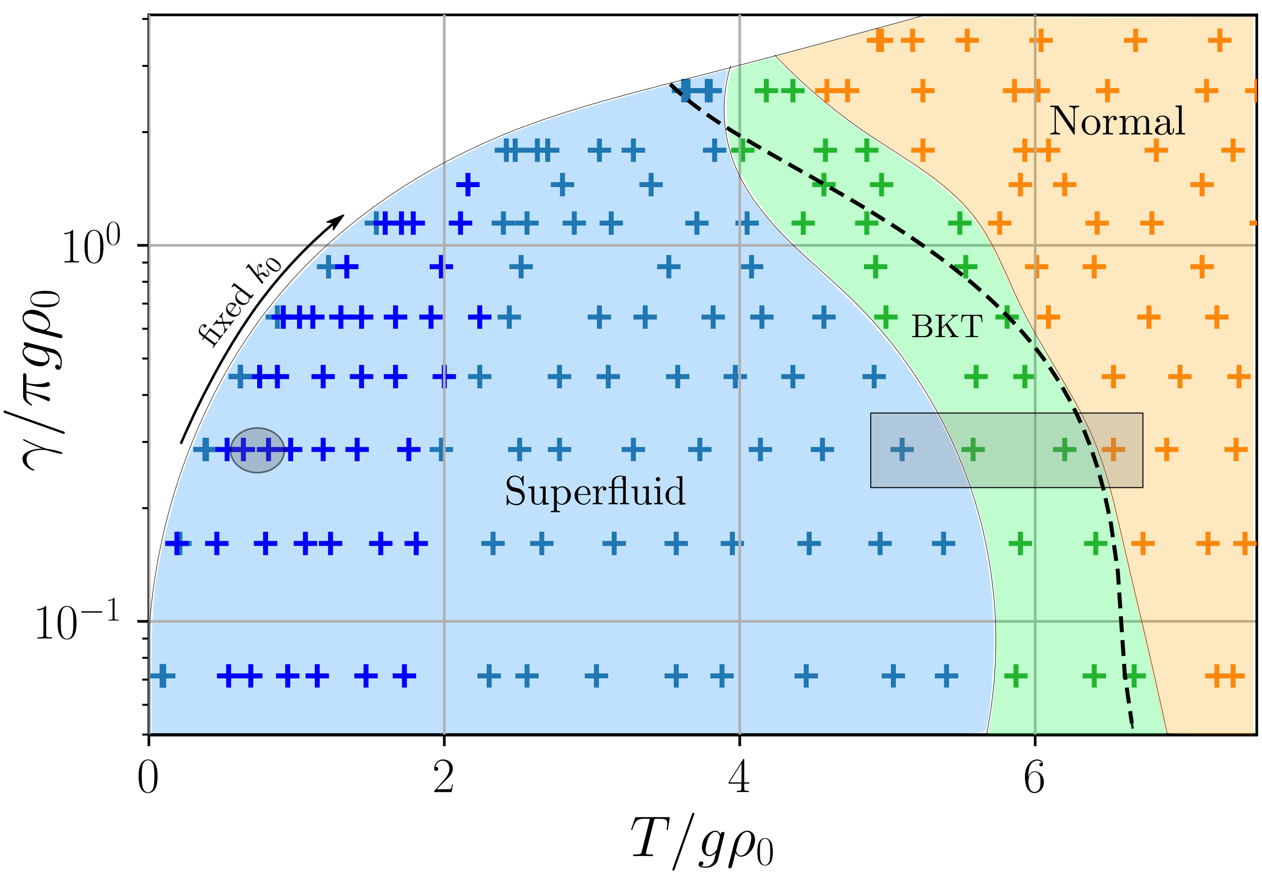

Figure 5.6 – (Quasi-)Equilibrium phase diagram of the 2d, quenched disordered Bose gas obtained after the temporal evolution is completed. Each point in the diagram is obtained by propagating an initial plane wave of wavevector $\boldsymbol{k}_0$ in a Gaussian uncorrelated disorder potential of strength γ and with an interaction strength $g\rho_0$ for a sufficiently long time, so that the g_1 spatial correlation function of the gas becomes independent of time. At this point, we assume that the system has reached thermal equilibrium, and the thermodynamic quantities T and μ are extracted from the energy distribution f_ϵ, which is assumed to follow a Rayleigh-Jeans distribution $T/(\epsilon-\mu)$ at high energy. The blue crosses refer to an algebraically decaying g_1 (the dark blue dots show cases where full thermalization has not yet been reached, dee Fig. 5.8), while orange crosses correspond to the normal phase, with exponentially decaying g_1. The green dots lie in the vicinity of the BKT transition, and fall in none of the two previous categories. The presented data are computed for values of γ comprised between 0.023 and 1.1, and values of k_0 from 0.0 to 1.0. The dashed black curve is a theoretical prediction for the BKT transition, obtained by solving implicitly Eq. (5.20). The rectangle around $\gamma = 0.3\pi g\rho_0$ and $T = 6g\rho_0$ corresponds to the plots shown in Fig. 5.7, while the small ellipsis in the superfluid zone corresponds to the plots of Fig. 5.8.

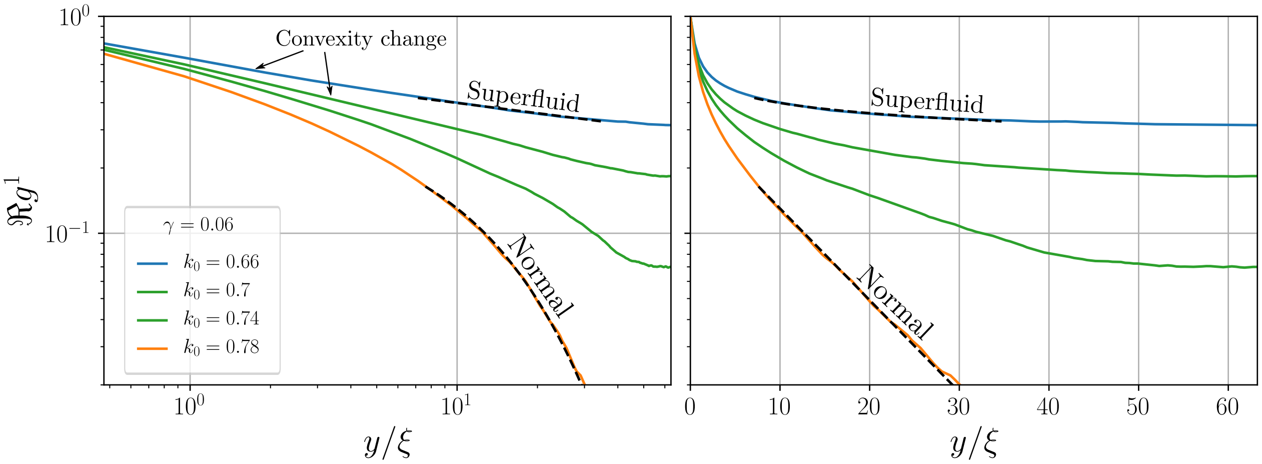

Figure 5.7 – Examples of g_1 functions of the gas at $t = t_{\max}$, in the three different phases of the phase diagram, at fixed disorder strength $\gamma = 0.14$ and for different values of k_0 indicated in the left plot (and thus different final temperatures). From top to bottom, these curves correspond to the four points (from left to right) highlighted by a grey rectangle in the phase diagram in Fig. 5.6, colors being chosen accordingly. The left plot is in log-log scale, and the right one is the same in semilog scale. One can see the change from convex to concave in the log-log representation of g_1, as we go from the superfluid to normal side.

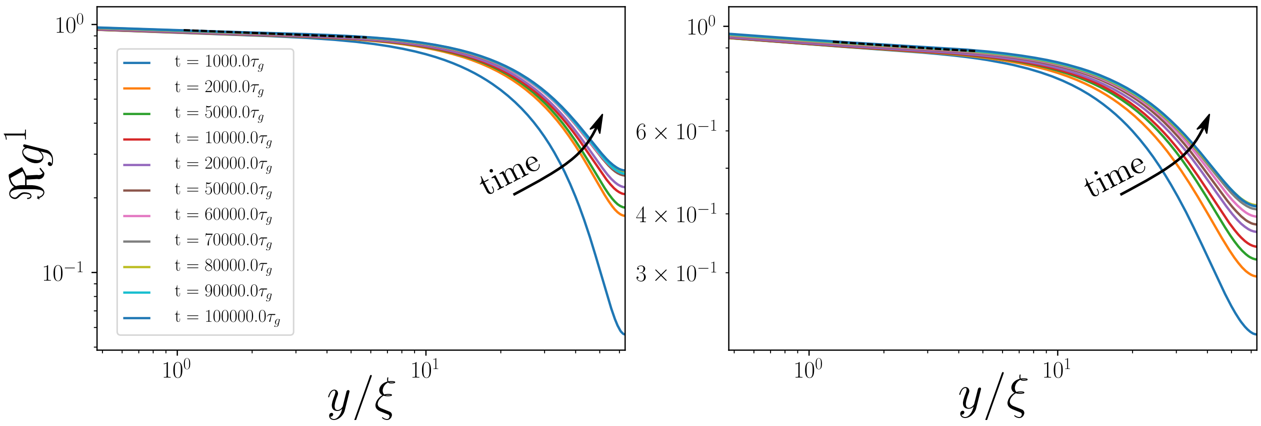

Figure 5.8 – Two examples of the time-evolution of g_1, corresponding to the circled dark blue crosses in the blue (superfluid) area of the phase diagram in Fig. 5.6. In both plots, the disorder strength is fixed at $\gamma = 0.09$, and $g\rho_0 = 0.1$. The initial momentum for the left plot is $k_0 = 0.16$, and $k_0 = 0.2$ for the right plot. Despite the algebraic behavior of g_1 over short length scales, the coherence function does not look thermal around $y = L$, even though the propagation time goes up to $10t_{\max} = 10^5\tau_g$. The dynamics of g_1 in this zone is extremely slow, suggesting a very large thermalization time. As a comparison, on the edges on the zone formed by the dark blue crosses in Fig. 5.6, the g_1 functions already look thermal (i.e. algebraic over the whole system) and time independent at times of the order of $10^4\tau_g$.

5.3.3 Thermalization time

The findings of the previous subsection are an invitation to put in perspective the equilibrium phase diagram and the dynamical evolution that precedes it. To this aim, we have tried to compute the thermalization time associated with each data point. However, finding a proper definition of the thermalization time is a difficult task, for several reasons:

- When g_1 decreases slowly in space, such that it takes non-negligible values at the edge of the system, the time at which the coherence function looks time independent heavily depends on L. For example, suppose we take as a condition for the system to be thermalized that the algebraic exponent α (measured in an intermediate spatial zone, as discussed above) does not change by more than 1% over 10% of the propagation time. Then, for a smaller system, for which the fitting zone is smaller, it is clear that this condition will be fulfilled at an earlier time (see, e.g., the shape of g_1 in the non-thermal regime in Fig. 5.8). A proper definition of the thermalization time would thus require to run simulations over system sizes such that the g_1 becomes close to 0 at the edge, while being completely algebraic over the whole space. This would require huge system sizes L, which is way beyond our computational resources. Of course, this issue is much less stringent in the normal phase, where the coherence function decays exponentially, so that we can define a reliable, size-independent thermalization time by applying a similar prescription to the decay length $\mathcal{L}$.
- We have nevertheless tried to compute thermalization times at our fixed volume $L = 400$, using the “1% over 10%” condition of the last paragraph, for both α and $\mathcal{L}$. In practice, however, we have found there are noticeable consistency issues between the thermalization times in the superfluid and normal region: the fluctuations of the values of α and $\mathcal{L}$ around their equilibrium value are different, so using the same criterion for both cases yields conflicting results.

To circumvent these issues, we have chosen another condition for thermal equilibrium, equivalent for all three phases. The thermalization time τ_{th} is assumed reached when the difference of the area under two successive curves in the fit region does not vary by more than 5% over 10% of the total propagation time. In the superfluid and normal phases, this condition is complemented by the fact that the g_1 function is well-fitted by an algebraic or exponential law. This procedure yields the values of τ_{th} in the density plot in Fig. 5.9. These results reflect the general shape of the "out-of-equilibrium" phase diagram. In particular, they show a jump of the thermalization time when going through the transition region. Then, in the normal phase, the thermalization time drops very quickly as we stray away from the BKT transition.

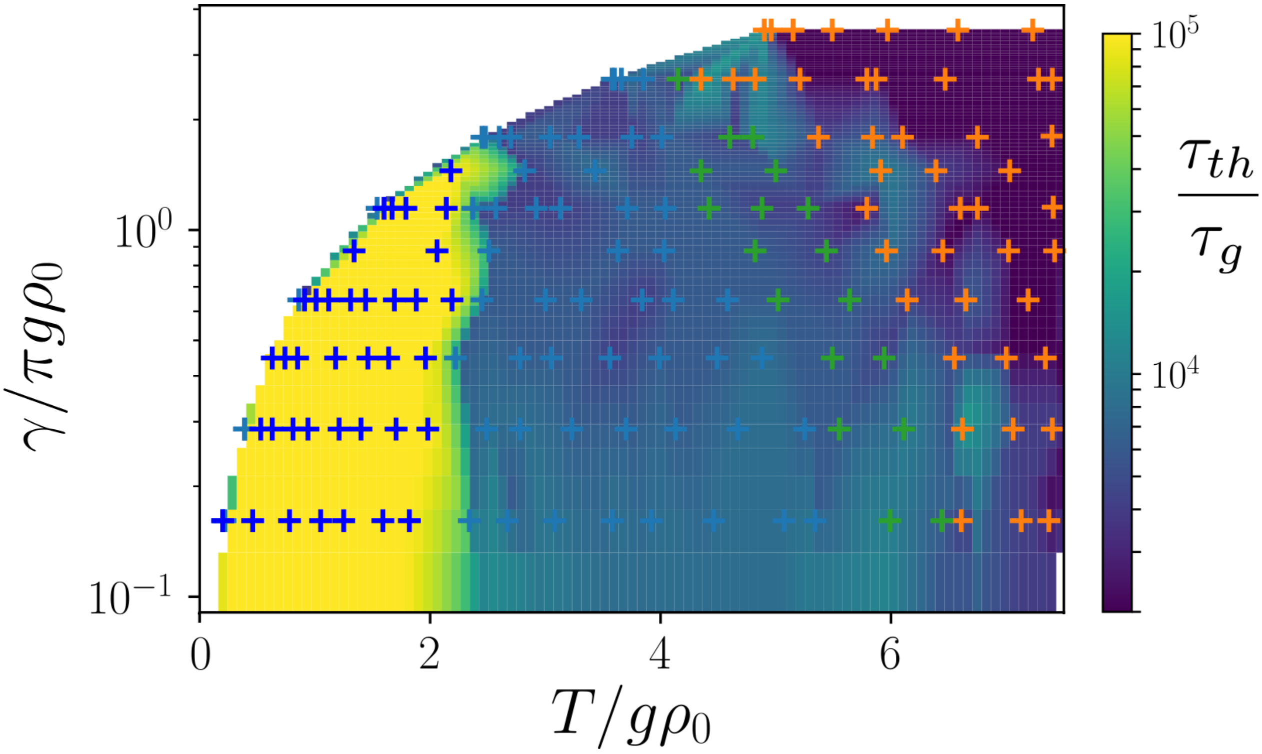

Figure 5.9 – Reduced version of the phase diagram in Fig. 5.6 with the same parameters except the lowest value of γ. On the diagram is superimposed a density plot of the thermalization times at fixed system size $L = 400$, estimated with the method described in the main text. The error on the values of τ_{th} is at least of the order of $200\tau_g$, which is the time interval between the snapshots of the g_1 functions we used. Nevertheless, the diagram shows a consistent general behavior of the thermalization time, approximately constant in the superfluid region except for the zone of very long thermalization discussed in section 5.3.2. Around the BKT transition, the thermalization time seems to increase slightly, before dropping by an order of magnitude in the bulk of the normal fluid phase.

5.4 Properties of the BKT transition in the presence of disorder

In the superfluid phase of the 2d Bose gas at finite temperature, it is well known that only a certain fraction of the gas, associated with the quasi-condensate structure, exhibits a superfluid behavior, while the thermal atoms behave as a normal fluid: the total density of the gas ρ_0 is the sum of a superfluid density ρ_s (or superfluid fraction) and a normal density ρ_n [54, 260, 282–284]. In the homogeneous case, the superfluid fraction of the gas, equal to 0 in the high-temperature normal phase, undergoes a sudden jump at the exact BKT transition, described by the Nelson-Kosterlitz relation [285]:

$$\rho_s(T_{\mathrm{BKT}}) = \frac{2m}{\pi} T_{\mathrm{BKT}}. \tag{5.9}$$

As the temperature decreases further, more and more atoms join the quasi-condensate, and the superfluid fraction is generally expected to increase [286]. Note, however, that a direct measurement of the superfluid fraction of quantum gases is a complex experimental problem, and appears to be still lacking in the 2d case [68, 283]. In this section, we give some insight on how this homogeneous picture is modified in the presence of disorder, in the context of our discrete system. We start by deriving a theoretical expression of the critical disorder as a function of the temperature (and conversely), leading to the BKT critical line that matches well the green area of the numerical phase diagram in Fig. 5.6. We then verify numerically that the Nelson-Kosterlitz relation still holds in the presence of disorder, using our estimate of the disorder dependence of the critical temperature $T_{\mathrm{BKT}}(\gamma)$ and of the superfluid fraction $\rho_s(\gamma)$ through the algebraic decay of the g_1 function. Finally, we examine another characteristic feature of the BKT transition: the sharp divergence of the characteristic coherence length $\mathcal{L}$ as we approach the transition from the normal side. This divergence appears to scale in a universal way with the disorder-modified critical temperature

5.4.1 Theory : BKT transition line in disorder

For this derivation, we closely follow the reasoning developed in [65] and [281], and adapt it to our discrete system.

Weak disorder

In the presence of a weak external disorder such that $\gamma \ll g\rho_0$, the expression for the normal (non-superfluid) density of a 2-dimensional weakly interacting Bose gas has been derived in [287], in the Bogoliubov framework, by computing the static linear response function of the system, which naturally separates into a normal and a superfluid part [288]:

$$\rho_n = \frac{\rho_0}{2}\int \frac{\mathrm{d}^2\boldsymbol{k}}{(2\pi)^2}\frac{\tilde{\mathcal{C}}(\boldsymbol{k})}{(g\rho_0+\epsilon_{\boldsymbol{k}}/2)^2} - \int \frac{\mathrm{d}^2\boldsymbol{k}}{(2\pi)^2}\epsilon_{\boldsymbol{k}}\frac{\partial f^*_{\omega_{\boldsymbol{k}}}}{\partial \omega_{\boldsymbol{k}}} \equiv \rho_n^{\mathrm{dis}} + \rho_n^{\mathrm{hom}}, \tag{5.10}$$

where ϵ_k is the kinetic energy of the particles, $\omega_k = \sqrt{(\epsilon_k + 3g\rho_0 - \mu)(\epsilon_k + g\rho_0 - \mu)}$ the Bogoliubov dispersion relation, f^* the occupation number of the quasiparticles (5.7), and $\tilde{\mathcal{C}}(\boldsymbol{k})$ the power spectrum of the disorder. We recall that for a discrete system, the kinetic energy reads

$$\epsilon_{k_x,k_y} = \frac{2-\cos(k_x a) - \cos(k_y a)}{ma^2}. \tag{5.11}$$

In what follows, we keep the integral notations for clarity, but strictly speaking they should be replaced by discrete sums over the momenta (and energies) allowed by the system. In the second equality, we defined ρ_n^{dis} and ρ_n^{hom}, respectively as the disorder and homogeneous contributions to the normal density. For a Gaussian uncorrelated potential, the disorder power spectrum from the first integral is

$$\tilde{\mathcal{C}}(\boldsymbol{k}) = \gamma. \tag{5.12}$$

Substituting this into the expression of ρ_n^{dis} in Eq. (5.10) yields, after switching from momenta to energy in the integrals,

$$\rho_n^{\mathrm{dis}} = \frac{\rho_0\gamma}{2}\int \mathrm{d}\epsilon\, \frac{\nu_\epsilon}{(g\rho_0+\frac{\epsilon}{2})^2} = \frac{m\rho_0\gamma}{4\pi g\rho_0} I_1(g\rho_0,\gamma,a,\mu) \tag{5.13}$$

$$I_1(g\rho_0,\gamma,a,\mu) = \int \mathrm{d}\epsilon\, \frac{g\rho_0\nu_\epsilon/\nu}{(g\rho_0+\frac{\epsilon}{2})^2}, \tag{5.14}$$

where the integrals run over all the energies allowed by the density of states. The quantity $\nu = m/(2\pi)$ is the free-space density of space of the *continuous* system. We have introduced the dimensionless constant I_1, which depends on the interaction strength $g\rho_0$, the spatial discretization a and the chemical potential μ. Its dependence on the disorder strength γ, through the modification of the density of states, is negligible at weak disorder. The other contribution, ρ_n^{hom}, corresponds to the normal fraction of the thermal part of the gas in the homogeneous case. The quasiparticle occupation number f^*_ϵ is given by (5.7), and the integral is taken from μ to the maximum energy set by the discretization, $\epsilon_{\max} = 4/ma^2$. The derivative is easily performed and we obtain

$$\rho_n^{\mathrm{hom}} = -\int \mathrm{d}\epsilon\, \nu_\epsilon \epsilon \frac{\partial f_\omega}{\partial \omega} = \frac{mT}{2\pi} I_2(g\rho_0,\gamma,a,\mu), \tag{5.15}$$

$$I_2(g\rho_0,\gamma,a,\mu) = \int \mathrm{d}\epsilon\, \frac{\nu_\epsilon/\nu}{\epsilon + 4g\rho_0 - 2\mu}. \tag{5.16}$$

where I_2 is another dimensionless constant, which depends on the same parameters as I_1. Using our simulated values for T, μ and for the density of states ν_ϵ, we can numerically compute I_1 and I_2, which yield the normal fraction of the gas (5.10) at each point of the phase diagram as :

$$\rho_n = \rho_n^{\text{dis}} + \rho_n^{\text{hom}} = \frac{m\rho_0\gamma}{4\pi} I_1 + \frac{mT}{2\pi} I_2, \tag{5.17}$$

To obtain an expression for the critical disorder of the BKT transition, we make the assumption that the Nelson-Kosterlitz relation (5.9) is still valid in the presence of disorder, as we approach the transition from the superfluid phase:

$$\rho_s(T) = \frac{2m}{\pi} T \quad \text{at} \quad T = T_{\text{BKT}}. \tag{5.18}$$

This assumption will be verified using simulation data in the next subsection. Using the decomposition of the gas density into a normal and a superfluid part, we obtain, at $T \sim T_{\text{BKT}}$,

$$\rho_n = \rho_0 - \rho_s = \rho_0 \left(1 - 4\frac{T}{T_d}\right), \tag{5.19}$$

where $T_d = 2\pi\rho_0/m$. From Eqs. (5.19) and (5.17), we obtain the following expression for the critical disorder strength γ^*:

$$\gamma^* = \frac{4\pi}{mI_1} \left[1 - \frac{T_{\text{BKT}}}{T_d} (4 - I_2)\right]. \tag{5.20}$$

At weak disorder, I_1 and I_2 depend very weakly in the disorder strength γ, and are easily computed at a given interaction strength $g\rho_0$ from the simulated density of states, and the numerical values for μ, using expressions (5.14) and (5.16). Then, we solve implicitely Eq. (5.20) for pairs of solutions $(\gamma^*, T_{\text{BKT}})$. This yields the lower half of the dashed transition curve in Fig. 5.6. Note that in the continuous case, $\epsilon_{\max} \simeq T$ in I_2, $\mu = g\rho_0$, and $\nu_\epsilon \simeq \nu$ (see the remark at the end of section 5.3.1), so that we recover, in the limit of weak interactions $T \gg g\rho_0$,

$$I_1 = \int_0^{+\infty} \frac{1}{(g\rho_0 + \frac{\epsilon}{2})^2} = \frac{2}{g\rho_0}, \tag{5.21}$$

$$I_2 = \int_0^{T} \mathrm{d}\epsilon \, \frac{1}{\epsilon + 2g\rho_0} \simeq \ln\left(\frac{T}{g\rho_0}\right), \tag{5.22}$$

which yields the same expression as in Ref. [65]:

$$\epsilon^*(T_{\text{BKT}}) = 2g\rho_0 \left[1 - \frac{T}{T_d} \ln\left(e^4 \frac{T}{g\rho_0}\right)\right], \tag{5.23}$$

with $\epsilon^* = m\gamma/\pi$. In the absence of disorder, $\epsilon^* = 0$, Eq. (5.23) gives for the critical temperature $T_{\rm BKT} \simeq T_d/\ln\left(e^4 T/g\rho_0\right)$, which is very close to the value obtained by Monte-Carlo simulations in [58]: $T_{\rm BKT} \simeq T_d/\ln\left(\xi T/g\rho_0\right)$, with $\xi \simeq 60$. According to Ref. [65], in the regime of weak disorder $\gamma \ll g\rho_0$, Eq. (5.23) yields values of the critical temperature which agree within 20% with the results of the Monte-Carlo numerical approach developed in [66].

Stronger disorder

As the disorder is stronger, $\gamma \sim g\rho_0$, the constants I_1 and I_2 start to depend on the disorder strength in a non-negligible way, through the modification of the density of stats ν_ϵ. As a result, equation (5.20) becomes implicit in the critical disorder strength γ^*. Another issue is the validity of our initial formula (5.10), which was derived with a Bogoliubov approach with the assumption of a weak disorder. As γ approaches $g\rho_0$, the approach must be corrected by taking into account higher-order interaction terms between quasiparticles and the random potential in the Bogoliubov Hamiltonian. This was done in the 3D case in [281], for arbitrarily strong disorder and interactions. We will not present here a full adaptation of the reasoning to the 2d case, and refer the interested reader to the paper in question. The net consequence of this approach on the formula (5.20), pushed to the next order in the disorder strength, is an effective renormalization of the interaction strength $g\rho_0$, via

$$g\rho_0 \to g\left(\rho_0 + \sigma_1\right) \tag{5.24}$$

$$\sigma_1 = \frac{\rho_0}{2}\int \frac{\mathrm{d}^2\boldsymbol{k}}{(2\pi)^2}\frac{\gamma}{(g\rho_0 + \epsilon_{\boldsymbol{k}}/2)^2} + T\int \frac{\mathrm{d}^2\boldsymbol{k}}{(2\pi)^2}\frac{g\rho_0}{\epsilon_k(\epsilon_k + 4g\rho_0 - \mu)}, \tag{5.25}$$

where σ_1 stems from the contribution of anomalous averages of the creation/anihiliation operators $\langle a_{\boldsymbol{k}} a_{-\boldsymbol{k}}\rangle$, rendered non-negligible by the presence of strong disorder. Equation (5.25) is, in fact, equal to the expression of the normal density (5.10), where the energy factor in the second integral has been replaced by $-g\rho_0$. Computing σ_1 with our numerical values of the temperature, chemical potential and density of states, and performing the replacement (5.24) into Eq. (5.20), we obtain another implicit equation for the critical disorder γ^*, which yields the full dashed line in Fig. 5.6, in reasonable agreement with the position of the BKT transition obtained from simulated data.

5.4.2 Nelson-Kosterlitz relation

In this section, we verify numerically the validity of the Nelson-Kosterlitz relation (5.9) in the presence of disorder, thus confirming our assumption of Sec. 5.4.1. To do so, we need to compute the value of the superfluid density $\rho_s(T)$ as T approaches $T_{\rm BKT}$. This can be done by looking at the algebraic decay of the g_1 function in the superfluid region. In the

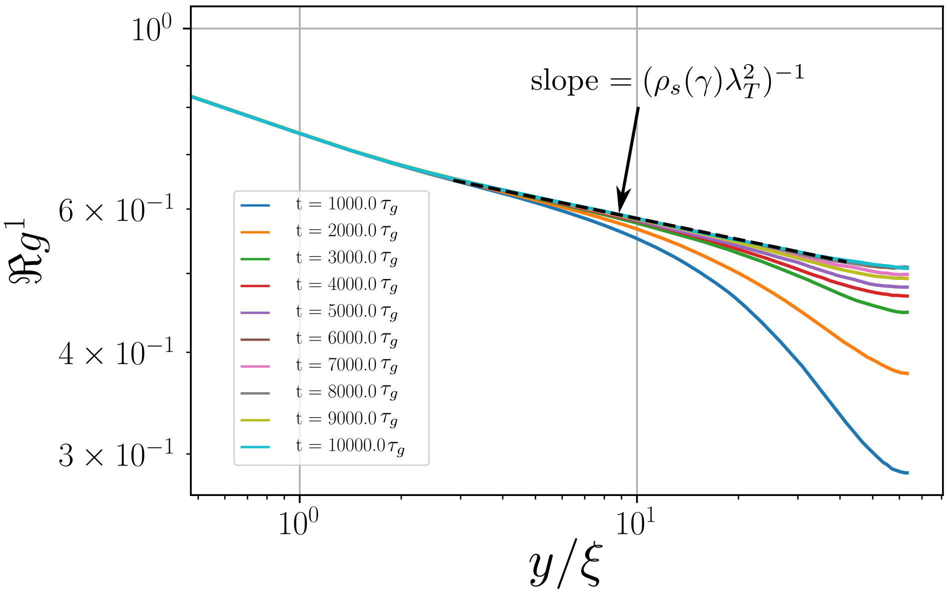

Figure 5.10 – g_1 function in the superfluid region of the phase diagram at different times. At long time, g_1 no longer depends on time, i.e., thermal equilibrium is reached. The dashed line is a fit of g_1 at the final time with formula (5.26), giving access to the superfluid density ρ_s.

homogeneous case, the equilibrium coherence function in the 2d superfluid phase is given by the expression [289]:

$$g_1(r) = \rho_s(T)\left(\frac{\xi}{r}\right)^{-1/\rho_s(T)\lambda_T^2} \tag{5.26}$$

where $\lambda_T = \sqrt{\frac{2\pi}{mT}}$ is the thermal de Broglie wavelength. The Nelson-Kosterlitz relation (5.9) can be rewritten in terms of λ_T as

$$\rho_s(T)\lambda_T^2 = 4 \quad (T = T_{\mathrm{BKT}}). \tag{5.27}$$

To extract the superfluid density ρ_s from our simulations, we make the assumption that the algebraic decay of g_1 at equilibrium in the homogeneous case (5.26) is still valid in the presence of disorder, with a disorder-dependent superfluid density $\rho_s(T,\gamma)$. By fitting the simulated g_1 in the superfluid region of the phase diagram (i.e. for each light blue point of Fig. 5.6), we can access numerically the quantity $\rho_s(T,\gamma)$. An example is displayed in Fig. 5.10.

To verify Eq. (5.27), we need a good estimate of the value of the critical temperature T_{BKT} as a function of the disorder strength γ. To do this, we simply take the average value of the temperature of all the points within the green area of Fig. 5.6 at fixed γ, and attribute it

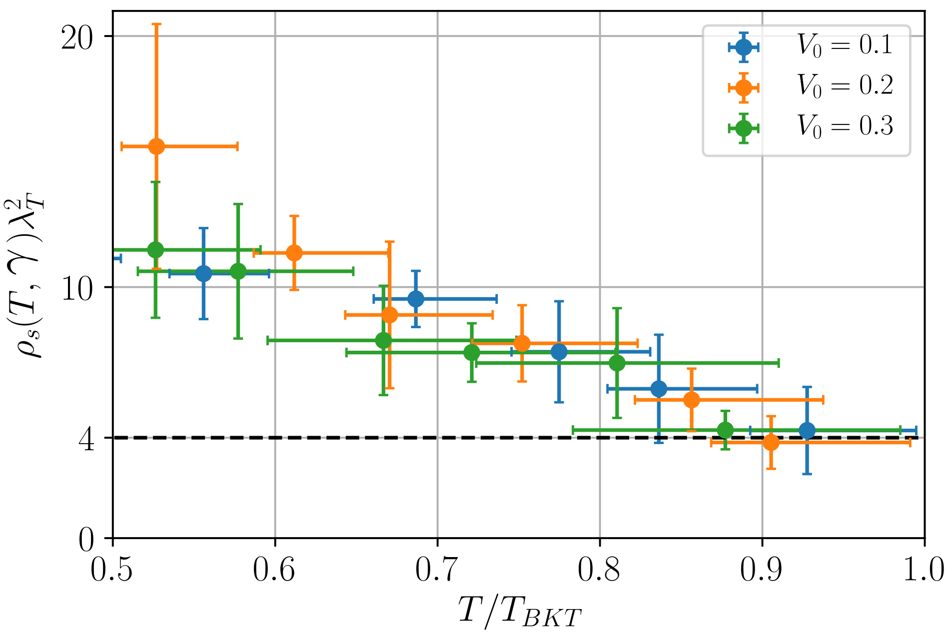

Figure 5.11 – Plot of $\rho_s(T,\gamma)\lambda_T^2$ versus T/T_{BKT} for various values of the disorder strength γ. Here the horizontal error bars stem from the determination of T_{BKT} from the green points of Fig. 5.6. All points seem to converge towards the value 4 as $T \to T_{\mathrm{BKT}}$. This shows that the Nelson-Kosterlitz relation $\rho_s(T_{\mathrm{BKT}})\lambda_{T_{\mathrm{BKT}}}^2 = 4$ is still valid in the presence of disorder, and also confirms our assumption on the expression of the g_1 on the superfluid side, Eq. (5.26).

with an error equal to the width of the area. Using these values, combined with the measured superfluid densities, we plot in Fig. 5.11 the temperature-dependence of the quantity $\rho_s(T)\lambda_T^2$. The agreement is reasonably good, within the error bars. This validates a posteriori our assumption that Eq. (5.26) is only modified by the disorder through the superfluid density and, more importantly, confirms the validity of the Nelson-Kosterlitz relation, at least in the regime of weak disorder $\gamma \ll g\rho_0$. At larger values of the disorder strength, the agreement remains approximately correct, but the error bars become significantly larger, so that additional simulations would be required to get a reliable result.

5.4.3 Normal phase

We now turn to the normal phase, where the g_1 function displays an exponential decay. An important feature of the BKT transition is the very sharp divergence of the characteristic decay length $\mathcal{L}$ of the exponential at the transition [56]. In the homogeneous case indeed, it grows as [289]:

$$\mathcal{L}(T > T_{\mathrm{BKT}}) \sim \lambda_T \exp \frac{\sqrt{\zeta T_{\mathrm{BKT}}}}{\sqrt{T - T_{\mathrm{BKT}}}}, \tag{5.28}$$

where ζ is a model-dependent dimensionless constant. Once again, we assume that the structure of this formula is not changed in the presence of disorder, and try to compute the numerical constant ζ as a function of the disorder strength γ. We start by deriving an analytical formula for the coherence function, and thus for $\mathcal{L}$, far from the transition, including the presence of weak disorder.

g_1 decay far from the transition

Far from the BKT transition, we can use the results of chapter 2 to derive g_1 at equilibrium. First, let us recall that, at all times:

$$n_{\boldsymbol{k}}(t) = \overline{|\psi(\boldsymbol{k},t)|^2} = \int_{-\infty}^{\infty} \mathrm{d}\epsilon \, A_\epsilon(\boldsymbol{k}) f_\epsilon(t), \tag{5.29}$$

where $A_\epsilon(\boldsymbol{k})$ is the spectral function and $f_\epsilon(t)$ the time-dependent occupation number of the gas.

We have seen that at long time and far above the BKT transition, $f_\epsilon(t)$ eventually reaches the equilibrium distribution of Eq. (5.2). Thus, using the Lorentzian expression for the spectral function at weak disorder, the equilibrium momentum distribution $n_{\boldsymbol{k}}$ can be written as :

$$n_{\boldsymbol{k}} = \int_0^{\infty} \mathrm{d}\epsilon \, \frac{1}{2\pi\tau} \frac{1}{(\epsilon - k^2/2m)^2 + 1/4\tau^2} \frac{T}{\epsilon - \mu}. \tag{5.30}$$

Taking the Fourier transform of this expression, we arrive at :

$$g_1(\boldsymbol{r}) = \frac{T}{2\pi\tau V} \int \frac{\mathrm{d}^2\boldsymbol{k}}{(2\pi)^2} e^{i\boldsymbol{k}.\boldsymbol{r}} \int_0^{\infty} \mathrm{d}\epsilon \, \frac{1}{(\epsilon - k^2/2m)^2 + 1/4\tau^2} \frac{1}{\epsilon - \mu}. \tag{5.31}$$

Performing the angular integral first yields :

$$g_1(\boldsymbol{r}) = \frac{T}{2\pi\tau V} \int_{-\infty}^{+\infty} \mathrm{d}\epsilon \frac{1}{\epsilon - \mu} \int_0^{+\infty} \frac{\mathrm{d}k}{2\pi} \frac{J_0(kr)k}{(\epsilon - k^2/2m)^2 + 1/4\tau^2}. \tag{5.32}$$

We now want to compute the following integral:

$$I = \int_0^{+\infty} \frac{\mathrm{d}k}{2\pi} \frac{kJ_0(kr)}{(\epsilon - k^2/2m)^2 + 1/4\tau^2}. \tag{5.33}$$

Let us first notice that the integrand is an even function of the integration variable (J_0 is even when it is defined on the negative reals by analytic continuation), so that we can extend the integration domain to $[-\infty, +\infty]$. Then, using the integral representation for the Bessel function of the first kind $J_0(x) = \frac{2}{\pi}\int_0^{+\infty} \sin(x \cosh u)$, the integral becomes:

$$I = \Im\left[\int_0^{+\infty} \mathrm{d}u \int_0^{+\infty} \frac{\mathrm{d}k}{\pi^2} \frac{k e^{irk\cosh u}}{(\epsilon - k^2/2m)^2 + 1/4\tau^2}\right]. \tag{5.34}$$

The integrand has two simple poles on the top-half of the complex plane: $\pm\sqrt{2m\epsilon \pm im/\tau}$. In the weak disorder limit $k_\epsilon \ell_\epsilon \gg 1$, we can rewrite them as $\pm k_\epsilon + i/2\ell_\epsilon$, where $k_\epsilon \equiv \sqrt{2m\epsilon}$, and we introduced the mean free path $\ell_\epsilon = k\tau/m$. The integration is performed by using the residue theorem on the usual half-circle contour, and yields:

$$\begin{aligned} I &= \frac{\tau}{2\pi}\Im\left[\int_0^{+\infty} \mathrm{d}u\, e^{i(k_\epsilon + i/2\ell_\epsilon)r\cosh u} - e^{i(-k_\epsilon+i/2\ell_\epsilon)r\cosh u}\right] \\ &= \frac{\tau}{2\pi}\int_0^{+\infty} \mathrm{d}u\, \sin\left(k_\epsilon r\cosh u\right) e^{-r/2\ell_\epsilon \cosh u} \end{aligned} \tag{5.35}$$

Let us now try to find an approximation to this integral. When $k_\epsilon r \gg 1$ first, the function $\sin\left(k_\epsilon r\cosh u\right)$ is highly oscillatory and therefore the integral is dominated by the stationary phase $u = 0$, where $\cosh u$ is minimal. This implies:

$$I \simeq \frac{\tau}{2\pi}\left[\int_0^{+\infty} \mathrm{d}u\, \sin\left(k_\epsilon r\cosh u\right)\right] e^{-r/2\ell_\epsilon} \quad (k_\epsilon r \gg 1). \tag{5.36}$$

In the opposite case $k_\epsilon r \leq 1$, again due to the oscillatory character of $\sin\left(k_\epsilon r\cosh u\right)$, only values of u such that $k_\epsilon r\cosh u \leq 1$ contribute non-vanishingly to the integral. For such values, the argument of the exponential in Eq. (5.35) is $r/2\ell_\epsilon \cosh u \leq 1/2k_\epsilon\ell_\epsilon \ll 1$, so that

$$I \simeq \frac{\tau}{2\pi}\left[\int_0^{+\infty} \mathrm{d}u\, \sin\left(k_\epsilon r\cosh u\right)\right], \quad (k_\epsilon r \leq 1), \tag{5.37}$$

which can also be seen as equal to (5.36) since $r/2\ell_\epsilon \ll k_\epsilon r \leq 1$. In other words, whatever r, we always have, in very good approximation,

$$I \simeq \frac{\tau}{2\pi}\left[\int_0^{+\infty} \mathrm{d}u\, \sin\left(k_\epsilon r\cosh u\right)\right] e^{-r/2\ell_\epsilon} = \frac{\tau}{4} J_0(k_\epsilon r)\, e^{-r/2\ell_\epsilon}. \tag{5.38}$$

Going back to our derivation of g_1, we are left with :

$$g_1(\boldsymbol{r}) = \frac{T}{8\pi V}\int_0^{+\infty} \mathrm{d}\epsilon\, \frac{J_0(k_\epsilon r) e^{-r/2\ell_\epsilon}}{\epsilon - \mu}\,. \tag{5.39}$$

The remaining integral over the energies is easily performed, and yields the final result

$$g_1(\boldsymbol{r}) = \frac{T}{4\pi V} K_0(k_\mu r) e^{-r/2\ell}. \tag{5.40}$$

At large r, this expression becomes :

$$g_1(\boldsymbol{r}) \sim \frac{T}{4\sqrt{2\pi}V}\sqrt{\frac{r}{\ell_\mu}} e^{-r/\ell_\mu} e^{-r/2\ell}, \tag{5.41}$$

where we introduced the characteristic decay length $\ell_\mu \equiv \sqrt{2m\mu}$. Equation (5.41) thus yields the expression of the exponential decay length

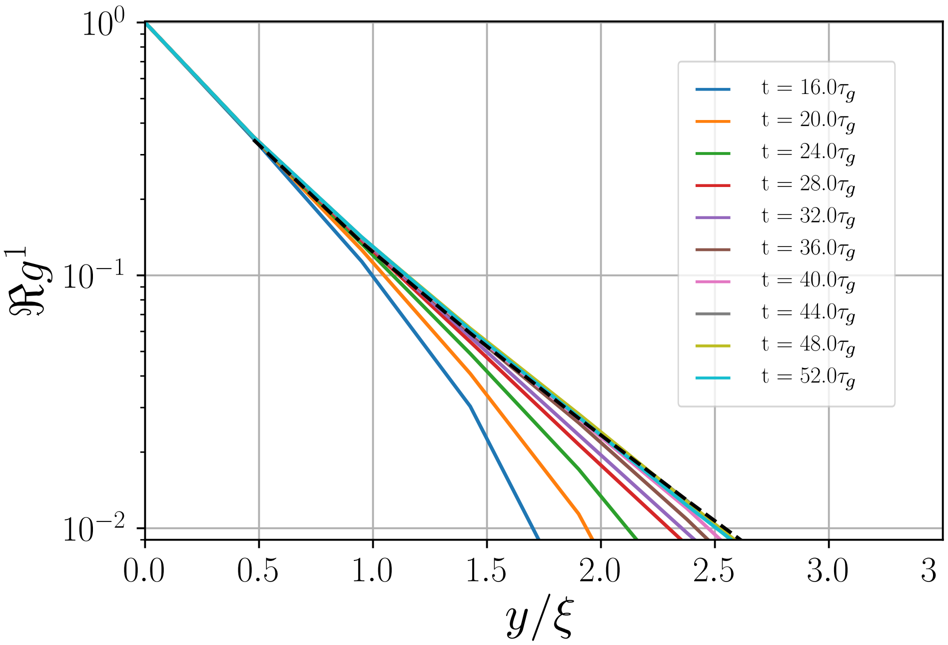

Figure 5.12 – g_1 function in the normal region of the phase diagram at different times, here far from the BKT transition. At long enough time g_1 does not evolve anymore, so we consider that thermal equilibrium is reached. The dashed line is a fit of g_1 at the final time with Eq. (5.40).

$$\frac{1}{\mathcal{L}} = \frac{1}{\ell_\mu} + \frac{1}{\ell} \tag{5.42}$$

and we recover the correct expression $\mathcal{L} = \sqrt{2m\mu}$ in the homogenous case [289]. Note that this expression can be rewritten as

$$\mathcal{L} = \sqrt{2m\mu} \simeq \frac{\lambda_T}{\sqrt{4\pi}} e^{\mathcal{D}/2}, \tag{5.43}$$

where $\mathcal{D} = \rho_s \lambda_T^2$ is the phase space density of the gas. Eq. (5.43) matches the formula (5.28) in the limit $T \gg T_{\text{BKT}}$. Using a simulated value of the chemical potential μ, expression (5.41) matches very well our simulations results, very far from the BKT transition line, as shown in Fig. 5.12.

Divergence of the characteristic decay length at the transition

As we get closer to the transition, $T \to T_{\text{BKT}}$, we can extract the characteristic decay length $\mathcal{L}$ from our simulations and check the validity of expression (5.28) for the divergence of the exponential decay length at the onset of the transition. The results (without error bars) are displayed in Fig. 5.13 and show a good agreement with the value $\zeta \simeq 2$. This

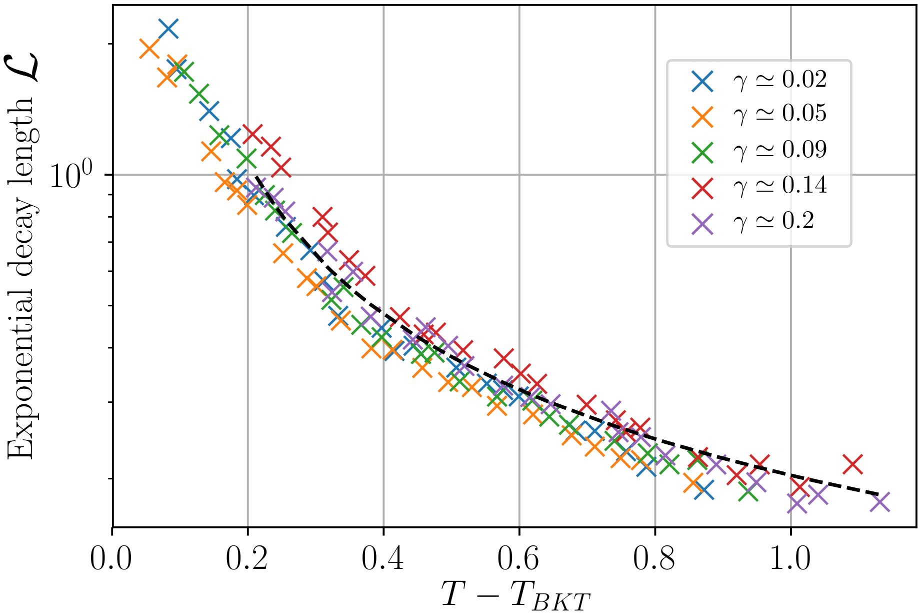

Figure 5.13 – Plot of the exponential decay length $\mathcal{L}$ of the g_1 function in the normal phase of the phase diagram, as a function of the temperature, and for different values of γ. The dashed curve is a fit of the series $\gamma = 0.2$ by the formula (5.28). For the fit, we use $\zeta \simeq 1.944$ and a prefactor $a_{fit} \simeq 0.04$. Here the leftmost blue cross corresponds to the parameters in Fig. 5.12, which can indeed be considered far from the transition.

suggests that the divergence (5.28) of the correlation function is universal, the whole effect of disorder boiling down to a renormalization of T_{BKT}.

Conclusion

In this chapter, we have presented and discussed preliminary numerical results on the equilibrium phase diagram reached by a 2d weakly interacting Bose gas in disorder a long time after a quench. The phase diagram exhibits the expected normal and superfluid phases, separated by a BKT transition. Our results show a dependence of the critical temperature on the disorder strength, which is globally consistent with previous theoretical [54, 65, 287], numerical [58, 66] and experimental [67, 68] works. We have also shown that a few of the well-known properties of the BKT mechanism, like the superfluid jump at the transition or the divergence of the coherence length on the normal side of the transition are robust in the presence of uncorrelated disorder. Note, in passing, that recent works [64] predict a significative broadening of the transition in the presence of strongly correlated disorder, a phenomenon which was also observed experimentally [67, 68]. One of the most interesting aspects of our numerical implementation of a quenched system is the possibility to relate the equilibrium phase diagram with the out-of-equilibrium evolution that precedes it, noticeably through the thermalization time τ_{th}. Another remarkable point is that in the considered regime of relatively weak interactions, the use of a classical field description in the simulations seems sufficient to encapsulate the quantum behavior of the Bose gas at low energy.

Conclusion

In this thesis, we have explored several aspects of the non-equilibrium dynamics of weakly interacting disordered Bose gases in two dimensions. In chapter 1, we have first reviewed a few core concepts associated with interference phenomena in the multiple scattering of a non-interacting matter wave, in particular Anderson localization and weak localization/coherent backscattering. Then, we have recalled the usual quantum transport theory allowing one to describe the propagation of a single particle in a random potential in the limit of weak disorder, and we have applied it to the problem of coherent backscattering of a non-equilibrium cold gas, visible in its momentum distribution. Starting from this approach, we have extended the quantum transport theory to the realm of weakly interacting Bose gases in chapter 2. Assuming particle interactions processes to be less frequent that disorder scattering events (i.e., an interaction "weaker" than the disorder), we have been able to derive, from the first principles, kinetic equations governing both the diffusive and weakly localized modes responsible for coherent backscattering. This kinetic theory constitutes a central result of the thesis and it was, to the best of our knowledge, not known so far.

In the third chapter, we have solved the kinetic equations and we have explored their predictions for the temporal evolution of the momentum distribution of a quenched disordered Bose gas in two dimensions. At short time, we have found that particle interactions essentially broaden and flatten the energy distribution of the particles. The asymmetry of the kinetic equations for diffusive and weakly localized modes, on the other hand, gives rise to a kind of breaking of reciprocity, in turn leading to a decrease of the coherent backscattering peak contrast. At the macroscopic level, this phenomenon can be interpreted as an effective decoherence mechanism for weak localization, similar in spirit to what is observed for interacting electrons in disordered conductors. All these predictions have been successfully confirmed by extensive numerical simulations of the time-dependent Gross-Pitaevskii equation in two dimensions.

The fourth chapter of thesis has been dedicated to the dynamics of a disordered Bose gas in a regime where the interaction quench is “stronger” than the disorder quench. In this limit, the temporal evolution can no longer be seen as a multiple scattering process perturbed by rare interactions processes. Rather, the disorder fluctuations are smoothed by interactions, and the Bose gas exhibits a robust, quasi long-range spatial coherence during its evolution. At the same time, the dynamics in this regime becomes much slower, the Bose gas lying in a “pre-thermal” state typical of nearly-integrable non-equilibrium systems. In the thesis, we have also provided a detailed theoretical description of this regime, based on a non-equilibrium, density-phase Bogoliubov formalism, and have again confirmed its validity by numerical simulations of the Gross-Pitaevskii equation.

In the last chapter, finally, we have characterized the equilibrium state reached by the gas a long time after the quench. As a mirror of the early-time dynamics, at long time the Bose gas can fall into two qualitatively different states, depending on the relative amplitudes of the disorder, kinetic and interaction energies. For a disorder typically stronger than interactions, for example, the gas eventually thermalizes to a normal-fluid state displaying a short-range spatial coherence. On the contrary, for a disorder smaller than interactions, the gas exhibits a quasi-condensate state on top of a thermal background, together with a finite superfluid fraction. These two phases are separated by a Kosterlitz-Thouless phase transition that dynamically emerges in time. We have verified a few emblematic signatures of this transition in the presence of disorder, such as a universal algebraic exponent of the coherence function at the transition, or a divergence of the correlation length above it.

Outlook

The results we have obtained during this PhD naturally rise a number of questions. On the behavior of coherent backscattering in the presence of interactions, while both our simulations and a qualitative analysis of the kinetic equations strongly suggest an exponential relaxation of its contrast, at this stage we cannot exclude sub-leading corrections to this observed scaling. Likewise, we have not explored the effect of interactions on the momentum width of the coherent backscattering peak. While, in the absence of interactions, the latter becomes narrower and narrower as time grows, we might expect a saturation in the presence of decoherence induced by interactions. Another obvious question is the impact of interactions on the coherent forward scattering peak, known to emerge in the momentum distribution of the non-interacting gas at the onset of the Anderson localization regime. Charactering this impact for weak interactions, however, would require to make the (Anderson) localization time – where coherent forward scattering appears – much smaller than the particle interaction time. In practice, this would require working with rather large disorder strengths, making a theoretical analysis probably challenging. From this point of view, a study in one dimension could be a first valuable step.

While we have been able to successfully characterize the short-time dynamics in the limit where disorder is weaker than interactions using a non-equilibrium Bogoliubov theory, a description of the full temporal thermalization process in this regime is lacking. In short, it would consist in developing a quantum kinetic theory, as done in chapter 2, but now starting from the basis of Bogoliubov quasi-particles (phonons). This task is currently the object of another thesis in the Complex Quantum Systems group.

The long-time thermalization process of the two-dimensional Bose gas, which we have touched upon in the last chapter of the thesis, is perhaps the subject on which most questions remain open. In the first place, our analysis of the time it takes for the Bose gas to reach its final equilibrium state, is still preliminary. We have observed rather large variations of this time scale, which we need to understand and characterize more precisely. Another open question is the long-time equilibration of the Bose gas at very low temperatures. Indeed, in practice this regime is difficult to explore since the very existence of the quench naturally involves a minimal energy initially injected into the system, and therefore a corresponding minimum equilibrium temperature at long time. Let alone that, for low equilibrium temperatures, the thermalization time tends to be very long. In fact, at low temperature, one expects the gas to fall in the famous Bose glass phase, possibly involving a tri-critical point connecting the superfluid and normal phases. At strong disorder and strong interactions, finally, a many-body localized phase could emerge as well. Describing this phenomenon in two dimensions remains, however, a very challenging task.

Bibliography

[1] M. H. Anderson, J. R. Ensher, M. R. Matthews, C. E. Wieman, and E. A. Cornell, “Observation of Bose-Einstein Condensation in a Dilute Atomic Vapor,” Science **269**, 198–201 (1995).

[2] K. B. Davis, M.-O. Mewes, M. R. Andrews, N. J. van Druten, D. S. Durfee, D. M. Kurn, and W. Ketterle, “Bose-Einstein Condensation in a Gas of Sodium Atoms,” Physical Review Letters **75**, 3969–3973 (1995).

[3] T.-L. Ho and M. Ma, “Quasi 1 and 2d Dilute Bose Gas in Magnetic Traps: existence of Off-Diagonal Order and Anomalous Quantum Fluctuations,” Journal of Low Temperature Physics **115**, 61–70 (1999).

[4] D. S. Petrov, G. V. Shlyapnikov, and J. T. M. Walraven, “Regimes of Quantum Degeneracy in Trapped 1D Gases,” Physical Review Letters **85**, 3745–3749 (2000).

[5] D. S. Petrov, D. M. Gangardt, and G. V. Shlyapnikov, “Low-dimensional trapped gases,” Journal de Physique IV **116**, 5–44 (2004).

[6] M. Greiner, O. Mandel, T. Esslinger, T. W. Hänsch, and I. Bloch, “Quantum phase transition from a superfluid to a Mott insulator in a gas of ultracold atoms,” Nature **415**, 39–44 (2002).

[7] J. W. Goodman, *Speckle Phenomena in Optics: theory and Applications, Second Edition* (Roberts & Company Publishers, 2020).

[8] R. Kuhn, “Coherent Transport of Matter Waves in Disordered Optical Potentials,” PhD thesis (Université Nice Sophia Antipolis, 2007).

[9] P. W. Anderson, “Absence of Diffusion in Certain Random Lattices,” Phys. Rev. **109**, 1492–1505 (1958).

[10] E. Abrahams, P. W. Anderson, D. C. Licciardello, and T. V. Ramakrishnan, “Scaling Theory of Localization: absence of Quantum Diffusion in Two Dimensions,” Phys. Rev. Lett. **42**, 673–676 (1979).

[11] L. P. Gor’kov, A. I. Larkin, and D. E. Khmel’nitskii, “Particle conductivity in a two-dimensional random potential,” JETP Lett. **30**, 228 (1979).

[12] E. Akkermans and R. Maynard, “Weak localization of waves,” Journal de Physique Lettres **46**, 1045–1053 (1985).

[13] J. Billy, V. Josse, Z. Zuo, A. Bernard, B. Hambrecht, P. Lugan, D. Clément, L. Sanchez-Palencia, P. Bouyer, and A. Aspect, “Direct observation of Anderson localization of matter waves in a controlled disorder,” Nature **453**, 891–894 (2008).

[14] G. Roati, C. D’Errico, L. Fallani, M. Fattori, C. Fort, M. Zaccanti, G. Modugno, M. Modugno, and M. Inguscio, “Anderson localization of a non-interacting Bose-Einstein condensate,” Nature **453**, 895–898 (2008).

[15] F. Jendrzejewski, A. Bernard, K. Müller, P. Cheinet, V. Josse, M. Piraud, L. Pezzé, L. Sanchez-Palencia, A. Aspect, and P. Bouyer, “Three-dimensional localization of ultracold atoms in an optical disordered potential,” Nature Physics **8**, 398–403 (2012).

[16] G. Semeghini, M. Landini, P. Castilho, S. Roy, G. Spagnolli, A. Trenkwalder, M. Fattori, M. Inguscio, and G. Modugno, “Measurement of the mobility edge for 3D Anderson localization,” Nature Physics **11**, 554–559 (2015).

[17] J. Chabé, G. Lemarié, B. Grémaud, D. Delande, P. Szriftgiser, and J. C. Garreau, “Experimental Observation of the Anderson Metal-Insulator Transition with Atomic Matter Waves,” Physical Review Letters **101**, 255702 (2008).

[18] G. Lemarié, H. Lignier, D. Delande, P. Szriftgiser, and J. C. Garreau, “Critical State of the Anderson Transition: between a Metal and an Insulator,” Physical Review Letters **105**, 090601 (2010).

[19] M. Lopez, J.-F. Clément, P. Szriftgiser, J. C. Garreau, and D. Delande, “Experimental Test of Universality of the Anderson Transition,” Physical Review Letters **108**, 095701 (2012).

[20] G. Labeyrie, C. A. Müller, D. S. Wiersma, C. Miniatura, and R. Kaiser, “Observation of coherent backscattering of light by cold atoms,” Journal of Optics B: Quantum and Semiclassical Optics **2**, 672–685 (2000).

[21] F. Jendrzejewski, K. Müller, J. Richard, A. Date, T. Plisson, P. Bouyer, A. Aspect, and V. Josse, “Coherent Backscattering of Ultracold Atoms,” Phys. Rev. Lett. **109**, 195302 (2012).

[22] K. Müller, J. Richard, V. V. Volchkov, V. Denechaud, P. Bouyer, A. Aspect, and V. Josse, “Suppression and Revival of Weak Localization through Control of Time-Reversal Symmetry,” Phys. Rev. Lett. **114**, 205301 (2015).

[23] C. Hainaut, I. Manai, R. Chicireanu, J.-F. Clément, S. Zemmouri, J. C. Garreau, P. Szriftgiser, G. Lemarié, N. Cherroret, and D. Delande, “Return to the Origin as a Probe of Atomic Phase Coherence,” Phys. Rev. Lett. **118**, 184101 (2017).

[24] C. Chin, R. Grimm, P. Julienne, and E. Tiesinga, "Feshbach Resonances in Ultracold Gases," Reviews of Modern Physics **82**, 1225–1286 (2010).

[25] T. Giamarchi and H. J. Schulz, "Anderson localization and interactions in one-dimensional metals," Phys. Rev. B **37**, 325–340 (1988).

[26] P. B. Weichman, "Dirty Bosons: twenty Years Later," Modern Physics Letters B **22**, 2623–2647 (2008).

[27] L. Sanchez-Palencia and M. Lewenstein, "Disordered quantum gases under control," Nature Physics **6**, 87–95 (2010).

[28] M. P. A. Fisher, P. B. Weichman, G. Grinstein, and D. S. Fisher, "Boson localization and the superfluid-insulator transition," Phys. Rev. B **40**, 546–570 (1989).

[29] S. Rapsch, U. Schollwoeck, and W. Zwerger, "Density matrix renormalization group for disordered bosons in one dimension," Europhysics Letters (EPL) **46**, 559–564 (1999).

[30] E. Altman, Y. Kafri, A. Polkovnikov, and G. Refael, "Phase Transition in a System of One-Dimensional Bosons with Strong Disorder," Phys. Rev. Lett. **93**, 150402 (2004).

[31] K. V. Krutitsky, M. Thorwart, R. Egger, and R. Graham, "Ultracold bosons in lattices with binary disorder," Phys. Rev. A **77**, 053609 (2008).

[32] P. Lugan, D. Clément, P. Bouyer, A. Aspect, M. Lewenstein, and L. Sanchez-Palencia, "Ultracold Bose Gases in 1D Disorder: from Lifshits Glass to Bose-Einstein Condensate," Phys. Rev. Lett. **98**, 170403 (2007).

[33] G. M. Falco, T. Nattermann, and V. L. Pokrovsky, "Weakly interacting Bose gas in a random environment," Phys. Rev. B **80**, 104515 (2009).

[34] I. L. Aleiner, B. L. Altshuler, and G. V. Shlyapnikov, "A finite-temperature phase transition for disordered weakly interacting bosons in one dimension," Nature Physics **6**, 900–904 (2010).

[35] N. Dupuis and R. Daviet, "Bose-glass phase of a one-dimensional disordered Bose fluid: metastable states, quantum tunneling, and droplets," Phys. Rev. E **101**, 042139 (2020).

[36] A. Priyadarshee, S. Chandrasekharan, J.-W. Lee, and H. U. Baranger, "Quantum Phase Transitions of Hard-Core Bosons in Background Potentials," Phys. Rev. Lett. **97**, 115703 (2006).

[37] V. Gurarie, L. Pollet, N. V. Prokof'ev, B. V. Svistunov, and M. Troyer, "Phase diagram of the disordered Bose-Hubbard model," Phys. Rev. B **80**, 214519 (2009).

[38] L. Pollet, N. V. Prokof'ev, B. V. Svistunov, and M. Troyer, "Absence of a Direct Superfluid to Mott Insulator Transition in Disordered Bose Systems," Phys. Rev. Lett. **103**, 140402 (2009).

[39] F. Lin, E. S. Sørensen, and D. M. Ceperley, "Superfluid-insulator transition in the disordered two-dimensional Bose-Hubbard model," Phys. Rev. B **84**, 094507 (2011).

[40] J. P. Álvarez Zúñiga, D. J. Luitz, G. Lemarié, and N. Laflorencie, "Critical Properties of the Superfluid—Bose-Glass Transition in Two Dimensions," Phys. Rev. Lett. **114**, 155301 (2015).

[41] R. Gautier, H. Yao, and L. Sanchez-Palencia, "Strongly Interacting Bosons in a Two-Dimensional Quasicrystal Lattice," Phys. Rev. Lett. **126**, 110401 (2021).

[42] M. Inguscio, "Quantum degenerate gases in optical lattices," in *Quantum-Atom Optics Downunder* (Optical Society of America, 2007), QThD4.

[43] M. White, M. Pasienski, D. McKay, S. Q. Zhou, D. Ceperley, and B. DeMarco, "Strongly Interacting Bosons in a Disordered Optical Lattice," Phys. Rev. Lett. **102**, 055301 (2009).

[44] B. Deissler, M. Zaccanti, G. Roati, C. D'Errico, M. Fattori, M. Modugno, G. Modugno, and M. Inguscio, "Delocalization of a disordered bosonic system by repulsive interactions," Nature Physics **6**, 354–358 (2010).

[45] M. Pasienski, D. McKay, M. White, and B. DeMarco, "A disordered insulator in an optical lattice," Nature Physics **6**, 677–680 (2010).

[46] Y. P. Chen, J. Hitchcock, D. Dries, M. Junker, C. Welford, and R. G. Hulet, "Phase coherence and superfluid-insulator transition in a disordered Bose-Einstein condensate," Phys. Rev. A **77**, 033632 (2008).

[47] A. Zheludev and T. Roscilde, "Dirty-boson physics with magnetic insulators," Comptes Rendus Physique **14**, 740–756 (2013).

[48] F. Yamada, H. Tanaka, T. Ono, and H. Nojiri, "Transition from Bose glass to a condensate of triplons in $\mathrm{Tl}_{1-X}\mathrm{K}_x\mathrm{CuCl}_3$," Phys. Rev. B **83**, 020409 (2011).

[49] R. Yu et al., "Bose glass and Mott glass of quasiparticles in a doped quantum magnet," Nature **489**, 379–384 (2012).

[50] A. V. Lopatin and V. M. Vinokur, "Thermodynamics of the Superfluid Dilute Bose Gas with Disorder," Phys. Rev. Lett. **88**, 235503 (2002).

[51] G. M. Falco, A. Pelster, and R. Graham, "Thermodynamics of a Bose-Einstein condensate with weak disorder," Phys. Rev. A **75**, 063619 (2007).

[52] V. I. Yukalov, E. P. Yukalova, K. V. Krutitsky, and R. Graham, "Bose-Einstein-condensed gases in arbitrarily strong random potentials," Phys. Rev. A **76**, 053623 (2007).

[53] S. Pilati, S. Giorgini, and N. Prokof'ev, "Superfluid Transition in a Bose Gas with Correlated Disorder," Physical Review Letters **102**, 150402 (2009).

[54] T. Bourdel, "Phase diagrams of 2D and 3D disordered Bose gases in the local density approximation," Physical Review A **86**, 063626 (2012).

[55] V. L. Berezinskiǐ, "Destruction of Long-range Order in One-dimensional and Two-dimensional Systems Possessing a Continuous Symmetry Group. II. Quantum Systems," Soviet Journal of Experimental and Theoretical Physics **34**, 610 (1972).

[56] J. M. Kosterlitz and D. J. Thouless, "Ordering, metastability and phase transitions in two-dimensional systems," **6**, 1181–1203 (1973).

[57] D. S. Petrov, M. Holzmann, and G. V. Shlyapnikov, "Bose-Einstein Condensation in Quasi-2D Trapped Gases," Physical Review Letters **84**, 2551–2555 (2000).

[58] N. Prokof'ev, O. Ruebenacker, and B. Svistunov, "Critical Point of a Weakly Interacting Two-Dimensional Bose Gas," Phys. Rev. Lett. **87**, 270402 (2001).

[59] N. Prokof'ev and B. Svistunov, "Two-dimensional weakly interacting Bose gas in the fluctuation region," Physical Review A **66**, 043608 (2002).

[60] P. Cladé, C. Ryu, A. Ramanathan, K. Helmerson, and W. D. Phillips, "Observation of a 2D Bose Gas: from Thermal to Quasicondensate to Superfluid," Physical Review Letters **102**, 170401 (2009).

[61] S. P. Rath, T. Yefsah, K. J. Günter, M. Cheneau, R. Desbuquois, M. Holzmann, W. Krauth, and J. Dalibard, "Equilibrium state of a trapped two-dimensional Bose gas," Physical Review A **82**, 013609 (2010).

[62] Z. Hadzibabic and J. Dalibard, "BKT Physics with Two-Dimensional Atomic Gases," in J. V. José, *40 Years of Berezinskii–Kosterlitz–Thouless Theory* (WORLD SCIENTIFIC, 2013), pp. 297–323.

[63] S. Sunami, V. P. Singh, D. Garrick, A. Beregi, A. J. Barker, K. Luksch, E. Bentine, L. Mathey, and C. J. Foot, "Observation of the BKT Transition in a 2D Bose Gas via Matter-Wave Interferometry," arxiv:2108.08840 [cond-mat] (2021).

[64] I. Maccari, L. Benfatto, and C. Castellani, "Broadening of the Berezinskii-Kosterlitz-Thouless transition by correlated disorder," Physical Review B **96**, 060508 (2017).

[65] G. Bertoli, V. P. Michal, B. L. Altshuler, and G. V. Shlyapnikov, "Finite-Temperature Disordered Bosons in Two Dimensions," Phys. Rev. Lett. **121**, 030403 (2018).

[66] G. Carleo, G. Boéris, M. Holzmann, and L. Sanchez-Palencia, "Universal Superfluid Transition and Transport Properties of Two-Dimensional Dirty Bosons," Phys. Rev. Lett. **111**, 050406 (2013).

[67] T. Plisson, B. Allard, M. Holzmann, G. Salomon, A. Aspect, P. Bouyer, and T. Bourdel, "Coherence properties of a two-dimensional trapped Bose gas around the superfluid transition," Physical Review A **84**, 061606 (2011).

[68] B. Allard, T. Plisson, M. Holzmann, G. Salomon, A. Aspect, P. Bouyer, and T. Bourdel, "Effect of disorder close to the superfluid transition in a two-dimensional Bose gas," Phys. Rev. A **85**, 033602 (2012).

[69] L. Boltzmann, *Vorlesungen über Gastheorie,* (J.A. Barth, 1896).

[70] M. Kardar, *Statistical Physics of Particles*, Higher Education from Cambridge University Press, (2007)

[71] J. Gemmer, M. Michel, and G. Mahler, "Brief Review of Pertinent Concepts," in *Quantum Thermodynamics: emergence of Thermodynamic Behavior Within Composite Quantum Systems* (Springer, 2009), pp. 41–62.

[72] J. V. Neumann, "Beweis des Ergodensatzes und des H-Theorems in der neuen Mechanik," Zeitschrift für Physik **57**, 30–70 (1929).

[73] M. Rigol, V. Dunjko, and M. Olshanii, "Thermalization and its mechanism for generic isolated quantum systems," Nature **452**, 854–858 (2008).

[74] T. Mori, T. N. Ikeda, E. Kaminishi, and M. Ueda, "Thermalization and prethermalization in isolated quantum systems: a theoretical overview," **51**, 112001 (2018).

[75] S. Trotzky, Y.-A. Chen, A. Flesch, I. P. McCulloch, U. Schollwöck, J. Eisert, and I. Bloch, "Probing the relaxation towards equilibrium in an isolated strongly correlated one-dimensional Bose gas," Nature Physics **8**, 325–330 (2012).

[76] A. M. Kaufman, M. E. Tai, A. Lukin, M. Rispoli, R. Schittko, P. M. Preiss, and M. Greiner, "Quantum thermalization through entanglement in an isolated many-body system," Science **353**, 794–800 (2016).

[77] C. Neill et al., "Ergodic dynamics and thermalization in an isolated quantum system," Nature Physics **12**, 1037–1041 (2016).

[78] L. D'Alessio, Y. Kafri, A. Polkovnikov, and M. Rigol, "From Quantum Chaos and Eigenstate Thermalization to Statistical Mechanics and Thermodynamics," Advances in Physics **65**, 239–362 (2016).

[79] J. M. Deutsch, "Eigenstate Thermalization Hypothesis," Reports on Progress in Physics **81**, 082001 (2018).

[80] M. Ueda, "Quantum equilibration, thermalization and prethermalization in ultracold atoms," Nature Reviews Physics **2**, 669–681 (2020).

[81] J. M. Deutsch, "Quantum statistical mechanics in a closed system," Physical Review A **43**, 2046–2049 (1991).

[82] M. Srednicki, "Chaos and quantum thermalization," Physical Review E **50**, 888–901 (1994).

[83] M. Rigol and M. Srednicki, “Alternatives to Eigenstate Thermalization,” Physical Review Letters **108**, 110601 (2012).

[84] L. F. Santos, F. Borgonovi, and F. M. Izrailev, “Chaos and Statistical Relaxation in Quantum Systems of Interacting Particles,” Physical Review Letters **108**, 094102 (2012).

[85] W. Beugeling, R. Moessner, and M. Haque, “Finite-size scaling of eigenstate thermalization,” Physical Review E **89**, 042112 (2014).

[86] H. Kim, T. N. Ikeda, and D. A. Huse, “Testing whether all eigenstates obey the Eigenstate Thermalization Hypothesis,” Physical Review E **90**, 052105 (2014).

[87] T. Kinoshita, T. Wenger, and D. S. Weiss, “A quantum Newton’s cradle,” Nature **440**, 900–903 (2006).

[88] S. Hofferberth, I. Lesanovsky, B. Fischer, T. Schumm, and J. Schmiedmayer, “Non-equilibrium coherence dynamics in one-dimensional Bose gases,” Nature **449**, 324–327 (2007).

[89] T. Langen, S. Erne, R. Geiger, B. Rauer, T. Schweigler, M. Kuhnert, W. Rohringer, I. E. Mazets, T. Gasenzer, and J. Schmiedmayer, “Experimental observation of a generalized Gibbs ensemble,” Science **348**, 207–211 (2015).

[90] A. Torrielli, “Lectures on Classical Integrability,” arxiv:1606.02946 [hep-th] (2016).

[91] E. H. Lieb and W. Liniger, “Exact Analysis of an Interacting Bose Gas. I. The General Solution and the Ground State,” Physical Review **130**, 1605–1616 (1963).

[92] H. A. Gersch and G. C. Knollman, “Quantum Cell Model for Bosons,” Physical Review **129**, 959–967 (1963).

[93] M. A. Olshanetsky and A. M. Perelomov, “Quantum integrable systems related to lie algebras,” Physics Reports **94**, 313–404 (1983).

[94] A. Doikou, S. Evangelisti, G. Feverati, and N. Karaiskos, “Introduction to Quantum Integrability,” International Journal of Modern Physics A **25** (2009).

[95] M. Rigol, A. Muramatsu, and M. Olshanii, “Hard-core bosons on optical superlattices: dynamics and relaxation in the superfluid and insulating regimes,” Physical Review A **74**, 053616 (2006).

[96] M. Rigol, V. Dunjko, V. Yurovsky, and M. Olshanii, “Relaxation in a Completely Integrable Many-Body Quantum System: an Ab Initio Study of the Dynamics of the Highly Excited States of 1D Lattice Hard-Core Bosons,” Physical Review Letters **98**, 050405 (2007).

[97] L. Vidmar and M. Rigol, “Generalized Gibbs ensemble in integrable lattice models,” Journal of Statistical Mechanics: Theory and Experiment **2016**, 064007 (2016).

[98] T. Langen, T. Gasenzer, and J. Schmiedmayer, "Prethermalization and universal dynamics in near-integrable quantum systems," J. Stat. Mech. **2016**, 064009 (2016).

[99] A. Polkovnikov, K. Sengupta, A. Silva, and M. Vengalattore, "Colloquium: nonequilibrium dynamics of closed interacting quantum systems," Rev. Mod. Phys. **83**, 863–883 (2011).

[100] G. Aarts, G. F. Bonini, and C. Wetterich, "Exact and truncated dynamics in nonequilibrium field theory," Physical Review D **63**, 025012 (2000).

[101] J. Berges, S. Borsányi, and C. Wetterich, "Prethermalization," Physical Review Letters **93**, 142002 (2004).

[102] M. Kollar, F. A. Wolf, and M. Eckstein, "Generalized Gibbs ensemble prediction of prethermalization plateaus and their relation to nonthermal steady states in integrable systems," Physical Review B **84**, 054304 (2011).

[103] S. A. Weidinger and M. Knap, "Floquet prethermalization and regimes of heating in a periodically driven, interacting quantum system," Scientific Reports **7**, 45382 (2017).

[104] K. Mallayya, M. Rigol, and W. De Roeck, "Prethermalization and Thermalization in Isolated Quantum Systems," Physical Review X **9**, 021027 (2019).

[105] M. Gring, M. Kuhnert, T. Langen, T. Kitagawa, B. Rauer, M. Schreitl, I. Mazets, D. A. Smith, E. Demler, and J. Schmiedmayer, "Relaxation and Prethermalization in an Isolated Quantum System," Science **337**, 1318–1322 (2012).

[106] R. Nandkishore and D. A. Huse, "Many-Body Localization and Thermalization in Quantum Statistical Mechanics," Annual Review of Condensed Matter Physics **6**, 15–38 (2015).

[107] E. Altman and R. Vosk, "Universal Dynamics and Renormalization in Many-Body-Localized Systems," Annual Review of Condensed Matter Physics **6**, 383–409 (2015).

[108] F. Alet and N. Laflorencie, "Many-body localization: an introduction and selected topics," Comptes Rendus Physique **19**, 498–525 (2018).

[109] D. A. Abanin, E. Altman, I. Bloch, and M. Serbyn, "Colloquium: many-body localization, thermalization, and entanglement," Rev. Mod. Phys. **91**, 021001 (2019).

[110] I. V. Gornyi, A. D. Mirlin, and D. G. Polyakov, "Interacting Electrons in Disordered Wires: anderson Localization and Low-T Transport," Phys. Rev. Lett. **95**, 206603 (2005).

[111] D. M. Basko, I. L. Aleiner, and B. L. Altshuler, "Metal–insulator transition in a weakly interacting many-electron system with localized single-particle states," Ann. Phys. (N.Y.) **321**, 1126–1205 (2006).

[112] M. Serbyn, M. Knap, S. Gopalakrishnan, Z. Papić, N. Y. Yao, C. R. Laumann, D. A. Abanin, M. D. Lukin, and E. A. Demler, “Interferometric Probes of Many-Body Localization,” Physical Review Letters **113**, 147204 (2014).

[113] M. Schreiber, S. S. Hodgman, P. Bordia, H. P. Lüschen, M. H. Fischer, R. Vosk, E. Altman, U. Schneider, and I. Bloch, “Observation of many-body localization of interacting fermions in a quasirandom optical lattice,” Science **349**, 842–845 (2015).

[114] P. Bordia, H. P. Lüschen, S. S. Hodgman, M. Schreiber, I. Bloch, and U. Schneider, “Coupling Identical one-dimensional Many-Body Localized Systems,” Physical Review Letters **116**, 140401 (2016).

[115] J.-y. Choi, S. Hild, J. Zeiher, P. Schauß, A. Rubio-Abadal, T. Yefsah, V. Khemani, D. A. Huse, I. Bloch, and C. Gross, “Exploring the many-body localization transition in two dimensions,” Science **352**, 1547–1552 (2016).

[116] Q. Guo et al., “Observation of energy-resolved many-body localization,” Nature Physics **17**, 234–239 (2021).

[117] G. Kopidakis, S. Komineas, S. Flach, and S. Aubry, “Absence of Wave Packet Diffusion in Disordered Nonlinear Systems,” Physical Review Letters **100**, 084103 (2008).

[118] A. S. Pikovsky and D. L. Shepelyansky, “Destruction of Anderson Localization by a Weak Nonlinearity,” Phys. Rev. Lett. **100**, 094101 (2008).

[119] N. Cherroret, B. Vermersch, J. C. Garreau, and D. Delande, “How Nonlinear Interactions Challenge the Three-Dimensional Anderson Transition,” Phys. Rev. Lett. **112**, 170603 (2014).

[120] N. Cherroret, “A self-consistent theory of localization in nonlinear random media,” Journal of Physics: Condensed Matter **29**, 024002 (2016).

[121] D. M. Basko, “Weak chaos in the disordered nonlinear Schrödinger chain: destruction of Anderson localization by Arnold diffusion,” Annals of Physics **326**, 1577–1655 (2011).

[122] P. Drude, “Zur Elektronentheorie der Metalle,” Annalen der Physik **306**, 566–613 (1900).

[123] N. Ashcroft and D. Mermin, *Solid State Physics* (Philadelphia, PA: Saunders College, 1976).

[124] S. Datta, *Electronic Transport in Mesoscopic Systems*, Cambridge Studies in Semiconductor Physics and Microelectronic Engineering (Cambridge University Press, 1995).

[125] E. Akkermans and G. Montambaux, *Mesoscopic physics of electrons and photons* (Cambridge University Press, 2007).

[126] C. A. Müller and D. Delande, “Disorder and interference: localization phenomena,” in *Lecture notes of the les houches summer school in singapore: ultracold gases and quantum information*, Vol. 91, edited by C. M. et al. (Oxford Scholarship, 2011) Chap. 9.

[127] A. Lagendijk, B. van Tiggelen, and D. S. Wiersma, "Fifty years of Anderson localization," Physics Today **62**, 24–29 (2009).

[128] G. Stolz, "An Introduction to the Mathematics of Anderson Localization," arxiv:1104.2317 [math-ph] (2011).

[129] T. Giordani, W. Schirmacher, G. Ruocco, and M. Leonetti, "Transverse and Quantum Localization of Light: a Review on Theory and Experiments," Frontiers in Physics **9**, 439 (2021).

[130] P. W. Anderson, "The question of classical localization A theory of white paint?" Philosophical Magazine B **52**, 505–509 (1985).

[131] M. Filoche and S. Mayboroda, "Universal mechanism for Anderson and weak localization," Proceedings of the National Academy of Sciences **109**, 14761–14766 (2012).

[132] M. Cutler and N. F. Mott, "Observation of Anderson Localization in an Electron Gas," Physical Review **181**, 1336–1340 (1969).

[133] P. W. Anderson, E. Abrahams, and T. V. Ramakrishnan, "Possible Explanation of Nonlinear Conductivity in Thin-Film Metal Wires," Physical Review Letters **43**, 718–720 (1979).

[134] G. Bergmann, "Weak localization in thin films: a time-of-flight experiment with conduction electrons," Physics Reports **107**, 1–58 (1984).

[135] A. Tonomura, N. Osakabe, T. Matsuda, T. Kawasaki, J. Endo, S. Yano, and H. Yamada, "Evidence for Aharonov-Bohm effect with magnetic field completely shielded from electron wave," Physical Review Letters **56**, 792–795 (1986).

[136] G. Bergmann, "Weak anti-localization—An experimental proof for the destructive interference of rotated spin 12," Solid State Communications **42**, 815–817 (1982).

[137] T. Koga, J. Nitta, T. Akazaki, and H. Takayanagi, "Rashba Spin-Orbit Coupling Probed by the Weak Antilocalization Analysis in InAlAs\InGaAs\InAlAs Quantum Wells as a Function of Quantum Well Asymmetry," Physical Review Letters **89**, 046801 (2002).

[138] H. Nakamura, D. Huang, J. Merz, E. Khalaf, P. Ostrovsky, A. Yaresko, D. Samal, and H. Takagi, "Robust weak antilocalization due to spin-orbital entanglement in Dirac material Sr_3SnO," Nature Communications **11**, 1161 (2020).

[139] G. Li, M. Chen, G. Liu, M. Wang, S. Wang, and S. Yan, "Difficulties of weak localization theory for thin metal films with magnetic impurities," Physical Review B **57**, 2683–2686 (1998).

[140] M. Liu et al., "Crossover between Weak Antilocalization and Weak Localization in a Magnetically Doped Topological Insulator," Physical Review Letters **108**, 036805 (2012).

[141] J. J. Lin, T. . Li, and Y. L. Zhong, "Electron Dephasing near Zero Temperature: an Experimental Review," Journal of the Physical Society of Japan **72**, 7–12 (2003).

[142] A. Trionfi, S. Lee, and D. Natelson, "Electronic coherence in metals: comparing weak localization and time-dependent conductance fluctuations," Physical Review B **70**, 041304 (2004).

[143] J. Berezovsky and R. M. Westervelt, "Imaging coherent transport in graphene (Part II): probing weak localization," Nanotechnology **21**, 274014 (2010).

[144] S. Shamim, S. Mahapatra, G. Scappucci, W. M. Klesse, M. Y. Simmons, and A. Ghosh, "Dephasing rates for weak localization and universal conductance fluctuations in two dimensional Si:p and Ge:p δ-layers," Scientific Reports **7**, 46670 (2017).

[145] S. John, "Electromagnetic Absorption in a Disordered Medium near a Photon Mobility Edge," Physical Review Letters **53**, 2169–2172 (1984).

[146] S. John, "Strong localization of photons in certain disordered dielectric superlattices," Physical Review Letters **58**, 2486–2489 (1987).

[147] A. A. Chabanov, M. Stoytchev, and A. Z. Genack, "Statistical signatures of photon localization," Nature **404**, 850–853 (2000).

[148] A. Peña, A. Girschik, F. Libisch, S. Rotter, and A. A. Chabanov, "The single-channel regime of transport through random media," Nature Communications **5**, 3488 (2014).

[149] H. Hu, A. Strybulevych, J. H. Page, S. E. Skipetrov, and B. A. van Tiggelen, "Localization of ultrasound in a three-dimensional elastic network," Nature Physics **4**, 945–948 (2008).

[150] L. A. Cobus, S. E. Skipetrov, A. Aubry, B. A. van Tiggelen, A. Derode, and J. H. Page, "Anderson Mobility Gap Probed by Dynamic Coherent Backscattering," Physical Review Letters **116**, 193901 (2016).

[151] T. Schwartz, G. Bartal, S. Fishman, and M. Segev, "Localization of Light in Disordered Lattices," Optics and Photonics News **18**, 35–35 (2007).

[152] Y. Lahini, A. Avidan, F. Pozzi, M. Sorel, R. Morandotti, D. N. Christodoulides, and Y. Silberberg, "Anderson Localization and Nonlinearity in One-Dimensional Disordered Photonic Lattices," Physical Review Letters **100**, 013906 (2008).

[153] Z. V. Vardeny and A. Nahata, "Anderson localization of slow light," Nature Photonics **2**, 75–76 (2008).

[154] M. Boguslawski, S. Brake, J. Armijo, F. Diebel, P. Rose, and C. Denz, "Analysis of transverse Anderson localization in refractive index structures with customized random potential," Optics Express **21**, 31713–31724 (2013).

[155] A. A. Golubentsev, "The suppression of interference effects in the multiple scattering of light," Zhurnal Eksperimentalnoi i Teoreticheskoi Fiziki **86**, 47–59 (1984).

[156] E. Akkermans, P. E. Wolf, R. Maynard, and G. Maret, "Theoretical study of the coherent backscattering of light by disordered media," Journal de Physique **49**, 77–98 (1988).

[157] M. P. Van Albada and A. Lagendijk, "Observation of Weak Localization of Light in a Random Medium," Physical Review Letters **55**, 2692–2695 (1985).

[158] P.-E. Wolf and G. Maret, "Weak Localization and Coherent Backscattering of Photons in Disordered Media," Physical Review Letters **55**, 2696–2699 (1985).

[159] C. M. Aegerter and G. Maret, "Coherent Backscattering and Anderson Localization of Light," in *Progress in Optics*, Vol. 52 (Elsevier, 2009), pp. 1–62.

[160] F. Pisani, T. Pierre, and D. Batani, "Microwave Coherent Backscattering from Acoustic or Electronic Waves in a Magnetized Plasma," Journal of Plasma Physics **59**, 69 (1998).

[161] J. S. Erkelens, V. K. C. Venema, H. W. J. Russchenberg, and L. P. Ligthart, "Coherent Scattering of Microwaves by Particles: evidence from Clouds and Smoke," Journal of the Atmospheric Sciences **58**, 1091–1102 (2001).

[162] E. Larose, O. Lobkis, and R. Weaver, "Coherent backscattering of ultrasound without a source," EPL (Europhysics Letters) **76** (2007).

[163] L. A. Cobus, B. A. van Tiggelen, A. Derode, and J. H. Page, "Dynamic coherent backscattering of ultrasound in three-dimensional strongly-scattering media," The European Physical Journal Special Topics **226**, 1549–1561 (2017).

[164] L. Kolokolova, B. Buratti, and V. Tishkovets, "Impact of coherent backscattering on the spectra of icy satellites of saturn and the implications of its effects for remote sensing," The Astrophysical Journal **711**, L71–L74 (2010).

[165] B. W. Hapke, R. M. Nelson, and W. D. Smythe, "The Opposition Effect of the Moon: the Contribution of Coherent Backscatter," Science **260**, 509–511 (1993).

[166] J. Dalibard and C. Cohen-Tannoudji, "Laser cooling below the Doppler limit by polarization gradients: simple theoretical models," Journal of the Optical Society of America B **6**, 2023 (1989).

[167] W. D. Phillips, "Laser cooling and trapping of neutral atoms," Rev. Mod. Phys. **70**, 21 (1998).

[168] S. Chu and C. Wieman, "Laser Cooling and Trapping of Atoms: introduction," JOSA B **6**, 2020–2022 (1989).

[169] N. Cherroret and T. Wellens, "Fokker-Planck equation for transport of wave packets in nonlinear disordered media," Phys. Rev. E **84**, 021114 (2011).

[170] T. Karpiuk, N. Cherroret, K. L. Lee, B. Grémaud, C. A. Müller, and C. Miniatura, "Coherent Forward Scattering Peak Induced by Anderson Localization," Phys. Rev. Lett. **109**, 190601 (2012).

[171] T. Micklitz, C. A. Müller, and A. Altland, "Echo spectroscopy of Anderson localization," Phys. Rev. B **91**, 064203 (2015).

[172] N. Cherroret, T. Karpiuk, B. Grémaud, and C. Miniatura, "Thermalization of matter waves in speckle potentials," Phys. Rev. A **92**, 063614 (2015).

[173] S. E. Skipetrov, A. Minguzzi, B. A. van Tiggelen, and B. Shapiro, "Anderson Localization of a Bose-Einstein Condensate in a 3D Random Potential," Physical Review Letters **100**, 165301 (2008).

[174] L. Sanchez-Palencia, D. Clément, P. Lugan, P. Bouyer, G. V. Shlyapnikov, and A. Aspect, "Anderson Localization of Expanding Bose-Einstein Condensates in Random Potentials," Physical Review Letters **98**, 210401 (2007).

[175] R. C. Kuhn, O. Sigwarth, C. Miniatura, D. Delande, and C. A. Müller, "Coherent matter wave transport in speckle potentials," New Journal of Physics **9**, 161–161 (2007).

[176] F. Gerbier et al., "Expansion of a quantum gas released from an optical lattice," Physical Review Letters **101**, 155303 (2008).

[177] A. F. Ioffe and A. R. Regel, *Progress in Semiconductors*, A. F. Gibson, Vol. 4 (John Wiley & Sons, Inc., New York, 1960), pp. 237–291.

[178] D. Vollhardt and P. Wölfle, "Diagrammatic, self-consistent treatment of the Anderson localization problem in $d \leq 2$ dimensions," Physical Review B **22**, 4666–4679 (1980).

[179] P. Wölfle and D. Vollhardt, "Self-Consistent Theory of Anderson Localization: general Formalism and Applications," International Journal of Modern Physics B **24**, 1526–1554 (2010).

[180] M. Störzer, P. Gross, C. M. Aegerter, and G. Maret, "Observation of the Critical Regime Near Anderson Localization of Light," Physical Review Letters **96**, 063904 (2006).

[181] C. M. Aegerter, M. Störzer, and G. Maret, "Experimental determination of critical exponents in Anderson localisation of light," EPL (Europhysics Letters) **75**, 562 (2006).

[182] I. Manai, J.-F. Clément, R. Chicireanu, C. Hainaut, J. C. Garreau, P. Szriftgiser, and D. Delande, "Experimental Observation of Two-Dimensional Anderson Localization with the Atomic Kicked Rotor," Physical Review Letters **115**, 240603 (2015).

[183] P. A. Lee and T. V. Ramakrishnan, "Disordered electronic systems," Reviews of Modern Physics **57**, 287–337 (1985).

[184] R. C. Kuhn, C. Miniatura, D. Delande, O. Sigwarth, and C. A. Müller, "Localization of Matter Waves in Two-Dimensional Disordered Optical Potentials," Phys. Rev. Lett. **95**, 250403 (2005).

[185] D. H. White, T. A. Haase, D. J. Brown, M. D. Hoogerland, M. S. Najafabadi, J. L. Helm, C. Gies, D. Schumayer, and D. A. W. Hutchinson, "Observation of two-dimensional Anderson localisation of ultracold atoms," Nature Communications **11**, 4942 (2020).

[186] M. Born, "Quantenmechanik der Stoßvorgänge," Zeitschrift für Physik **38**, 803–827 (1926).

[187] P. Lugan, A. Aspect, L. Sanchez-Palencia, D. Delande, B. Grémaud, C. A. Müller, and C. Miniatura, "One-dimensional Anderson localization in certain correlated random potentials," Physical Review A **80**, 023605 (2009).

[188] V. V. Volchkov, M. Pasek, V. Denechaud, M. Mukhtar, A. Aspect, D. Delande, and V. Josse, "Measurement of Spectral Functions of Ultracold Atoms in Disordered Potentials," Phys. Rev. Lett. **120**, 060404 (2018).

[189] E. E. Salpeter and H. A. Bethe, "A Relativistic Equation for Bound-State Problems," Physical Review **84**, 1232–1242 (1951).

[190] T. Plisson, T. Bourdel, and C. A. Müller, "Momentum isotropisation in random potentials," The European Physical Journal Special Topics **217**, 79 (2013).

[191] E. Altman, *Non equilibrium quantum dynamics in ultra-cold quantum gases*, Notes of the 2012 Les Houches Summer School of Physics "Strongly Interacting Quantum Systems Out of Equilibrium" (Oxford University Press, 2012).

[192] M. Heyl, "Dynamical quantum phase transitions: a review," **81**, 054001 (2018).

[193] A. del Campo and W. H. Zurek, "Universality of phase transition dynamics: topological defects from symmetry breaking," International Journal of Modern Physics A **29**, 1430018 (2014).

[194] C. Texier and G. Montambaux, "Altshuler-Aronov correction to the conductivity of a large metallic square network," Phys. Rev. B **76**, 094202 (2007).

[195] P. Schwab and R. Raimondi, "Quasiclassical theory of charge transport in disordered interacting electron systems," Annalen der Physik **12**, 471–516 (2003).

[196] B. L. Altshuler and A. Aronov, "Contribution to the theory of disordered metals in strongly doped semiconductors," Journal of Experimental and Theoretical Physics (1979).

[197] B. L. Altshuler, D. Khmel'nitzkii, A. I. Larkin, and P. A. Lee, "Magnetoresistance and Hall effect in a disordered two-dimensional electron gas," Phys. Rev. B **22**, 5142–5153 (1980).

[198] B. L. Altshuler and A. G. Aronov, "Fermi-liquid theory of the electron-electron interaction effects in disordered metals," Solid State Communications **46**, 429–435 (1983).

[199] A. E. White, M. Tinkham, W. J. Skocpol, and D. C. Flanders, "Evidence for Interaction Effects in the Low-Temperature Resistance Rise in Ultrathin Metallic Wires," Phys. Rev. Lett. **48**, 1752–1755 (1982).

[200] P. M. Echternach, M. E. Gershenson, H. M. Bozler, A. L. Bogdanov, and B. Nilsson, "Temperature dependence of the resistance of one-dimensional metal films with dominant Nyquist phase breaking," Phys. Rev. B **50**, 5748–5751 (1994).

[201] F. Pierre, A. B. Gougam, A. Anthore, H. Pothier, D. Esteve, and N. O. Birge, "Dephasing of electrons in mesoscopic metal wires," Phys. Rev. B **68**, 085413 (2003).

[202] F. Schopfer, C. Bäuerle, W. Rabaud, and L. Saminadayar, "Anomalous temperature dependence of the dephasing time in mesoscopic Kondo wires," Physical Review Letters **90**, 056801 (2003).

[203] V. M. Agranovich and V. E. Kravtsov, "Nonlinear backscattering from opaque media," Phys. Rev. B **43**, 13691–13694 (1991).

[204] T. Wellens and B. Grémaud, "Nonlinear coherent transport of waves in disordered media," Phys. Rev. Lett. **100** (2008).

[205] T. Wellens, "Nonlinear coherent backscattering," Applied Physics B **95**, 189 (2009).

[206] T. Chanelière, D. Wilkowski, Y. Bidel, R. Kaiser, and C. Miniatura, "Saturation-induced coherence loss in coherent backscattering of light," Phys. Rev. E **70**, 036602 (2004).

[207] T. Wellens, B. Grémaud, D. Delande, and C. Miniatura, "Coherent backscattering of light by nonlinear scatterers," Phys. Rev. E **71**, 055603 (2005).

[208] B. Grémaud, T. Wellens, D. Delande, and C. Miniatura, "Coherent backscattering in nonlinear atomic media: quantum Langevin approach," Phys. Rev. A **74**, 033808 (2006).

[209] M. Hartung, T. Wellens, C. A. Müller, K. Richter, and P. Schlagheck, "Coherent Backscattering of Bose-Einstein Condensates in Two-Dimensional Disorder Potentials," Phys. Rev. Lett. **101**, 020603 (2008).

[210] T. Geiger, T. Wellens, and A. Buchleitner, "Inelastic Multiple Scattering of Interacting Bosons in Weak Random Potentials," Phys. Rev. Lett. **109**, 030601 (2012).

[211] T. Hartmann, J. Michl, C. Petitjean, T. Wellens, J.-D. Urbina, K. Richter, and P. Schlagheck, “Weak localization with nonlinear bosonic matter waves,” Annals of Physics **327**, 1998–2049 (2012).

[212] T. Geiger, A. Buchleitner, and T. Wellens, “Microscopic scattering theory for interacting bosons in weak random potentials,” New Journal of Physics **15**, 115015 (2013).

[213] R. Chrétien and P. Schlagheck, “Inversion of coherent backscattering with interacting Bose-Einstein condensates in two-dimensional disorder: a truncated Wigner approach,” Phys. Rev. A **103**, 033319 (2021).

[214] G. Schwiete and A. M. Finkel’stein, “Nonlinear Wave-Packet Dynamics in a Disordered Medium,” Phys. Rev. Lett. **104**, 103904 (2010).

[215] G. Schwiete and A. M. Finkel’stein, “Effective theory for the propagation of a wave packet in a disordered and nonlinear medium,” Phys. Rev. A **87**, 043636 (2013).

[216] G. Schwiete and A. M. Finkel’stein, “Kinetics of the disordered Bose gas with collisions,” Phys. Rev. A **88**, 053611 (2013).

[217] J. Dalibard, “Collisional Dynamics of Ultra-Cold Atomic Gases,” in *Proceeding of the international school of physics - enrico fermi* (IOS press, Amsterdam, 1999), p. 321.

[218] E. Fermi, “Motion of neutrons in hydrogenous substances,” Ricerca Scientifica **7**, 13–52 (1936).

[219] F. Dalfovo, S. Giorgini, L. P. Pitaevskii, and S. Stringari, “Theory of Bose-Einstein condensation in trapped gases,” Reviews of Modern Physics **71**, 463–512 (1999).

[220] L. Pitaevskii and S. Stringari, *Bose-Einstein Condensation and Superfluidity*, International Series of Monographs on Physics (Oxford University Press, 2016).

[221] L. Erdős, B. Schlein, and H.-T. Yau, “Derivation of the Gross-Pitaevskii equation for the dynamics of Bose-Einstein condensate,” Ann. of Math. **2**, 291–370 (2010).

[222] C. J. Pethick and H. Smith, *Bose–Einstein Condensation in Dilute Gases* (Cambridge University Press, 2001).

[223] L. Sanchez-Palencia, “Smoothing effect and delocalization of interacting Bose-Einstein condensates in random potentials,” Phys. Rev. A **74**, 053625 (2006).

[224] T. N. A. Griffin and E. Zaremba, *Bose-Condensed Gases at Finite Temperatures* (Cambridge University Press, Cambridge, 2009).

[225] G. N. Watson, *A Treatise on the Theory of Bessel Functions, 2nd ed.* (Cambridge, England: Cambridge University Press, 1966).

[226] B. L. Altshuler and A. G. Aronov, *Electron-electron interaction in disordered conductors, in Electron-electron Interactions in Disordered Systems* (Amsterdam: Elsevier, 1985).

[227] A. Knothe and T. Wellens, “Flux conservation in coherent backscattering and weak localization of light,” Journal of Physics A: Mathematical and Theoretical **46**, 315101 (2013).

[228] D. Clément, A. F. Varón, J. A. Retter, L. Sanchez-Palencia, A. Aspect, and P. Bouyer, “Experimental study of the transport of coherent interacting matter-waves in a 1D random potential induced by laser speckle,” New Journal of Physics **8**, 165–165 (2006).

[229] D. F. Griffiths and D. J. Higham, *Numerical Methods for Ordinary Differential Equations: initial Value Problems*, Springer Undergraduate Mathematics Series (Springer, 2010).

[230] J. Crank and P. Nicolson, “A practical method for numerical evaluation of solutions of partial differential equations of the heat-conduction type,” Mathematical Proceedings of the Cambridge Philosophical Society **43** (1947).

[231] H. Tal-Ezer and R. Kosloff, “An accurate and efficient scheme for propagating the time dependent Schrödinger equation,” J. Chem. Phys. **81**, 3967 (1984).

[232] C. Leforestier et al., “A comparison of different propagation schemes for the time dependent Schrödinger equation,” J. Comput. Phys. **94**, 59 (1991).

[233] S. Roche and D. Mayou, “Conductivity of Quasiperiodic Systems: a Numerical Study,” Phys. Rev. Lett. **79**, 2518–2521 (1997).

[234] H. Fehske, J. Schleede, G. Schubert, G. Wellein, V. S. Filinov, and A. R. Bishop, “Numerical approaches to time evolution of complex quantum systems,” Physics Letters A **373**, 2182–2188 (2009).

[235] M. Abramowitz, *Handbook of Mathematical Functions, With Formulas, Graphs, and Mathematical Tables,* (Dover Publications, Inc., 1974).

[236] C. W. Clenshaw, “Chebyshev Series for Mathematical Functions,” in *National Physical Laboratory Mathematical Tables*, Vol. 5 (Department of Scientific and Industrial Research, London, 1962).

[237] X. Antoine, W. Bao, and C. Besse, “Computational methods for the dynamics of the nonlinear Schrödinger/Gross–Pitaevskii equations,” Computer Physics Communications **184**, 2621–2633 (2013).

[238] C. F. Barenghi, *Quantized Vortex Dynamics and Superfluid Turbulence* (Springer Berlin Heidelberg, 2001).

[239] M. Abid, C. Huepe, S. Metens, C. Nore, C. T. Pham, L. S. Tuckerman, and M. E. Brachet, “Gross–Pitaevskii dynamics of Bose–Einstein condensates and superfluid turbulence,” Fluid Dynamics Research **33**, 509–544 (2003).

[240] M. I. Trappe, D. Delande, and C. A. Müller, "Semiclassical spectral function for matter waves in random potentials," Journal of Physics A: Mathematical and Theoretical **48**, 245102 (2015).

[241] L. Van Hove, "The Occurrence of Singularities in the Elastic Frequency Distribution of a Crystal," Phys. Rev. **89**, 1189–1193 (1953).

[242] P. Virtanen et al., "SciPy 1.0: fundamental Algorithms for Scientific Computing in Python," Nature Methods **17**, 261–272 (2020).

[243] G. Montambaux and E. Akkermans, "Nonexponential Quasiparticle Decay and Phase Relaxation in Low-Dimensional Conductors," Phys. Rev. Lett. **95**, 016403 (2005).

[244] T. Prat, N. Cherroret, and D. Delande, "Semiclassical spectral function and density of states in speckle potentials," Phys. Rev. A **94**, 022114 (2016).

[245] Y. Imry, *Introduction to Mesoscopic Physics* (Oxford, 2002).

[246] I. L. Aleiner, B. L. Altshuler, and M. E. Gershenson, "Interaction effects and phase relaxation in disordered systems," Waves in Random Media **9**, 201–239 (1999).

[247] C. Texier and G. Montambaux, "Dephasing due to electron-electron interaction in a diffusive ring," Phys. Rev. B **72**, 115327 (2005).

[248] D. Delande and G. Orso, "Mobility Edge for Cold Atoms in Laser Speckle Potentials," Physical Review Letters **113**, 060601 (2014).

[249] C. F. Barenghi and N. G. Parker, "Waves and Solitons," in *A Primer on Quantum Fluids*, SpringerBriefs in Physics (Springer International Publishing, 2016), pp. 53–78.

[250] N. Cherroret and S. E. Skipetrov, "Long-Range Correlations of Density in a Bose-Einstein Condensate Expanding in a Random Potential," Physical Review Letters **101**, 190406 (2008).

[251] D. P. Sankovich, "Bogolyubov's theory of superfluidity," Physics of Particles and Nuclei **41**, 1068–1070 (2010).

[252] N. D. Mermin and H. Wagner, "Absence of Ferromagnetism or Antiferromagnetism in One- or Two-Dimensional Isotropic Heisenberg Models," Physical Review Letters **17**, 1133–1136 (1966).

[253] N. Dupuis, "Unified Picture of Superfluidity: from Bogoliubov's Approximation to Popov's Hydrodynamic Theory," Physical Review Letters **102**, 190401 (2009).

[254] J. O. Andersen, U. Al Khawaja, and H. T. C. Stoof, "Phase Fluctuations in Atomic Bose Gases," Physical Review Letters **88**, 070407 (2002).

[255] U. Al Khawaja, J. O. Andersen, N. P. Proukakis, and H. T. C. Stoof, "Low dimensional Bose gases," Physical Review A **66**, 013615 (2002).

[256] C. Mora and Y. Castin, "Extension of Bogoliubov theory to quasi-condensates," Physical Review A **67**, 053615 (2003).

[257] V. N. Popov, *Functional integrals and collective excitations* (Cambridge University Press, 1987).

[258] J.-X. Zhu, *Bogoliubov-de Gennes Method and Its Applications* (Springer International Publishing, 2016).

[259] "Superfluid Flow Around an Obstacle," in *Vortices in Bose—Einstein Condensates*, Progress in Nonlinear Differential Equations and Their Applications (Birkhäuser, 2006), pp. 157–193.

[260] R. Desbuquois, L. Chomaz, T. Yefsah, J. Léonard, J. Beugnon, C. Weitenberg, and J. Dalibard, "Superfluid behaviour of a two-dimensional Bose gas," Nature Physics **8**, 645–648 (2012).

[261] M. Syafwan, P. Kevrekidis, A. Paris-Mandoki, I. Lesanovsky, P. Krüger, L. Hackermüller, and H. Susanto, "Superfluid flow past an obstacle in annular Bose–Einstein condensates," **49**, 235301 (2016).

[262] C. Michel, O. Boughdad, M. Albert, P.-É. Larré, and M. Bellec, "Superfluid motion and drag-force cancellation in a fluid of light," Nature Communications **9**, 2108 (2018).

[263] T. Bardon-brun, S. Pigeon, and N. Cherroret, "Classical Casimir force from a quasi-condensate of light," Physical Review Research **2**, 013297 (2020).

[264] M. Cheneau, P. Barmettler, D. Poletti, M. Endres, P. Schauß, T. Fukuhara, C. Gross, I. Bloch, C. Kollath, and S. Kuhr, "Light-cone-like spreading of correlations in a quantum many-body system," Nature **481**, 484–487 (2012).

[265] G. I. Martone, P.-É. Larré, A. Fabbri, and N. Pavloff, "Momentum distribution and coherence of a weakly interacting Bose gas after a quench," Physical Review A **98**, 063617 (2018).

[266] Y. Kagan and B. V. Svistunov, "Evolution of large-scale correlations in a strongly nonequilibrium Bose condensation process," Journal of Experimental and Theoretical Physics Letters **67**, 521–527 (1998).

[267] Z. Hadzibabic, P. Krüger, M. Cheneau, B. Battelier, and J. Dalibard, "Berezinskii-Kosterlitz-Thouless Crossover in a Trapped Atomic Gas," Nature **441**, 1118 (2006).

[268] S. Tung, G. Lamporesi, D. Lobser, L. Xia, and E. A. Cornell, "Observation of the Presuperfluid Regime in a Two-Dimensional Bose Gas," Physical Review Letters **105**, 230408 (2010).

[269] M. Buchhold and S. Diehl, "Kinetic Theory for Interacting Luttinger Liquids," The European Physical Journal D **69**, 224 (2015).

[270] J. Berges and T. Gasenzer, "Quantum versus classical statistical dynamics of an ultracold Bose gas," Phys. Rev. A **76**, 033604 (2007).

[271] M. Kuhnert, R. Geiger, T. Langen, M. Gring, B. Rauer, T. Kitagawa, E. Demler, D. Adu Smith, and J. Schmiedmayer, "Multimode Dynamics and Emergence of a Characteristic Length Scale in a One-Dimensional Quantum System," Phys. Rev. Lett. **110**, 090405 (2013).

[272] T. Langen, R. Geiger, M. Kuhnert, B. Rauer, and J. Schmiedmayer, "Local emergence of thermal correlations in an isolated quantum many-body system," Nature Physics **9**, 640–643 (2013).

[273] J. Dalibard, *Fluides quantiques de basse dimension et transition de Kosterlitz-Thouless* (Cours du Collège de France, 2016).

[274] V. L. Berezinskiĭ, "Destruction of Long-range Order in One-dimensional and Two-dimensional Systems having a Continuous Symmetry Group I. Classical Systems," Soviet Journal of Experimental and Theoretical Physics **32**, 493 (1971).

[275] Rayleigh, "The Dynamical Theory of Gases and of Radiation," Nature **72**, 54–55 (1905).

[276] J. H. Jeans, "A Comparison between Two Theories of Radiation," Nature **72**, 293–294 (1905).

[277] M. Planck, "On the Theory of the Energy Distribution Law of the Normal Spectrum," in *The Old Quantum Theory* (Elsevier, 1967), pp. 82–90.

[278] I. M. Lifshitz, "Energy spectrum structure and quantum states of disordered condensed systems," Soviet Physics Uspekhi **7**, 549 (1965).

[279] D. S. Petrov, "Bose-Einstein Condensation in Low-Dimensional Trapped Gases," PhD thesis (University of Amsterdam, 2003).

[280] N. M. Hugenholtz and D. Pines, "Ground-State Energy and Excitation Spectrum of a System of Interacting Bosons," Physical Review **116**, 489–506 (1959).

[281] V. I. Yukalov and R. Graham, "Bose-Einstein-condensed systems in random potentials," Physical Review A **75**, 023619 (2007).

[282] E. Strepparola, A. Minguzzi, and M. P. Tosi, "Quasicondensate and superfluid fraction in the two-dimensional charged boson gas at finite temperature," Physical Review B **63**, 104509 (2001).

[283] N. R. Cooper and Z. Hadzibabic, "Measuring the Superfluid Fraction of an Ultracold Atomic Gas," Physical Review Letters **104**, 030401 (2010).

[284] C. De Rossi, R. Dubessy, K. Merloti, M. De Goër De Herve, T. Badr, A. Perrin, L. Longchambon, and H. Perrin, "Probing superfluidity in a quasi two-dimensional Bose gas through its local dynamics," New Journal of Physics **18**, 062001 (2016).

[285] D. R. Nelson and J. M. Kosterlitz, “Universal Jump in the Superfluid Density of Two-Dimensional Superfluids,” Physical Review Letters **39**, 1201–1205 (1977).

[286] K. Huang and H.-F. Meng, “Hard-sphere Bose gas in random external potentials,” Phys. Rev. Lett. **69**, 644–647 (1992).

[287] H.-F. Meng, “Quantum theory of the two-dimensional interacting-boson system,” Physical Review B **49**, 1205–1210 (1994).

[288] J. Keeling, “Response functions and superfluid density in a weakly interacting Bose gas with nonquadratic dispersion,” Physical Review B **74**, 155325 (2006).

[289] Z. Hadzibabic and J. Dalibard, “Two-dimensional Bose fluids: an atomic physics perspective,” La Rivista del Nuovo Cimento **34**, 389–434 (2011).